THE ENDOTHELIAL GLYCOCALYX AS A PROTECTIVE BARRIER: AN IN VITRO STUDY ON NANOPARTICLE UPTAKE, SUBSTANCE TRANSPORT, AND VESICLE ADHESION

Dissertation

zur Erlangung des akademischen Grades

Dr. rer. nat.

eingereicht an der

Mathematisch-Naturwissenschaftlichen-Technischen Fakultät

der Universität Augsburg

von

Manuel Marcel Sirch

Augsburg, den 27. Januar 2025

Universität Augsburg University

Erstgutachter: Prof. Dr. Christoph Westerhausen

Zweitgutachter: Prof. Dr. Janina Bahnemann

Termin der mündlichen Prüfung: 03.04.2025

TABLE OF CONTENT

1. MOTIVATION

The endothelial glycocalyx, a complex and dynamic layer of carbohydrates and proteins coating the surface of virtually all mammalian cells, has long captivated the curiosity of scientists across disciplines. Its intricate structure and multifaceted functions remain enigmatic, yet its significance in various physiological and pathological processes cannot be overstated [1][2].

The glycocalyx serves as the first point of contact between cells and their external environment, playing pivotal roles in cellular adhesion, signaling, and protection. Composed of an array of glycoproteins, glycolipids, and proteoglycans, this dynamic structure acts as a molecular sieve, selectively allowing the passage of molecules and ions while shielding the cell from mechanical and chemical insults. Despite its seemingly delicate nature, the glycocalyx exerts profound influences on cellular behavior and function, impacting processes ranging from immune response modulation to vascular homeostasis [3][4].

Additionally, the role of the glycocalyx in vascular health is of paramount importance. This layer helps regulate blood flow and shear stress, preventing excessive permeability and maintaining the integrity of the vascular endothelium. Damage or degradation of the glycocalyx is often associated with conditions such as atherosclerosis, diabetes, and sepsis, where the protective barrier is compromised, leading to increased vulnerability to vascular inflammation and injury [5][6].

The glycocalyx also plays a critical role in the immune system. It contributes in the recognition and clearance of pathogens, as well as the regulation of leukocyte adhesion and migration. Understanding how the glycocalyx interacts with immune cells can provide valuable insights into immune evasion strategies employed by pathogens and tumor cells, potentially guiding the development of immunotherapies and anti-cancer treatments [7][8].

Of particular interest is the intersection between the glycocalyx and drug delivery systems, notably nanoparticles. The glycocalyx serves as a formidable barrier to nanoparticle penetration, presenting a significant challenge for effective drug delivery to target cells and tissues. However, exploiting the unique properties of the glycocalyx holds promise for enhancing the specificity, efficacy, and safety of drug delivery systems. By understanding the intricate interplay between nanoparticles and the glycocalyx, researchers can engineer tailored delivery platforms capable of traversing this biological barrier with precision, unlocking new frontiers in targeted therapeutics [9][10].

In this doctoral thesis, a comprehensive investigation into the intricate role of the glycocalyx as a barrier in cellular physiology is conducted, with a particular focus on the impact of flow cultivation, the resulting changes to the cell membrane, and its implications for targeted drug delivery systems. The research involves a series of carefully designed experiments conducted with Human Umbilical Vein Endothelial Cells (HUVEC) and HeLa cells as reference in vitro.

Flow cultivation is expected to induce significant alterations in the structure and composition of the cell membrane, particularly in the glycocalyx layer. These membrane changes are crucial as they can influence various cellular functions, including permeability, mechanotransduction, and cellular signaling pathways.

The investigation delves into how these dynamic alterations impact the overall barrier function of the endothelial cells and their ability to regulate the passage of molecules [11][12][13].

Additionally, the role of cell junctions, such as tight junctions, adherens junctions, and gap junctions, is examined to comprehend their interplay with the glycocalyx in maintaining the integrity and functionality of the endothelial barrier. Understanding these junctions is essential as they contribute significantly to the cohesive barrier that regulates cellular permeability and communication [14][15].

The specific questions regarding the glycocalyx and subsequent research objectives of this thesis include:

1. **Does an intact glycocalyx, as observed under physiological conditions, occur under the in vitro culture conditions used in this research?** Wheat Germ Agglutinin (WGA) staining will be employed to visualize and verify the state of the glycocalyx in HUVEC cultures. This validation step is crucial for ensuring the reliability and reproducibility of experimental findings regarding glycocalyx modulation and its impact on cellular behavior.

2. **Does an intact glycocalyx affect the uptake of nanoparticles into endothelial cells?** The influence of the glycocalyx on the endocytic uptake of nanoparticles is examined using 50 nm SiO_2 nanoparticles. Fluorescence microscopy is employed to indirectly quantify the number of nanoparticles internalized by endothelial cells with an intact glycocalyx, as well as those with a compromised or degenerated glycocalyx.

3. **Does an intact glycocalyx affect the uptake of molecules by diffusion through the cell membrane into endothelial cells?** The experiment will assess the diffusion of Hoechst 33342 dye through the cell membrane to quantify how treatments or conditions impact the integrity and functionality of the glycocalyx in HUVEC. By evaluating changes in dye uptake, this study aims to determine the extent to which the glycocalyx influences membrane permeability.

4. **Has the presence or absence of an intact glycocalyx an effect on the phase state of the membrane?** To assess the effect of the glycocalyx on the phase state of the cell membrane, the HUVEC will be stained with Laurdan, a dye sensitive to lipid packing and membrane fluidity. By measuring the generalized polarization of Laurdan, the influence of the presence or absence of an intact glycocalyx on membrane phase behavior will be quantified. The same experiments will be performed on HeLa cells as a reference. This approach is particularly important to differentiate whether observed changes in membrane properties arise directly from the glycocalyx or are a consequence of cultivation under flow conditions.

5. **Is the adhesion of lipid vesicles to the cell membrane dependent on the electrical charge of the membrane and the glycocalyx?** The adhesion dynamics of vesicles, made of positively charged and uncharged lipid, mimicking drug delivery carriers or circulating tumor cells, to HUVEC (and HeLa as a references) with varying glycocalyx states will be investigated. Therefore, DOTAP-DMPC and DMPC vesicles are produced and the adhesion to the cell layer in dependance of the culture condition is measured.

6. **Does the glycocalyx affect the diffusion of macromolecules beyond the endothelium in a blood vessel model?** The objective is to establish a 3D hydrogel-HUVEC model by creating a 3D channel and populating it with HUVEC to form an endothelial layer. Once the model is established, the diffusion of FITC-Dextran of varying sizes will be studied to measure differences in macromolecule diffusion across the endothelial layer.

7. **Does the existence of the glycocalyx affect the cell-cell-contacts?** VE-cadherin is employed to stain and visualize the cell-cell contacts of HUVEC. This staining allows for a detailed analysis of the solidity and integrity of these contacts, highlighting any variations that may arise due to different culture conditions. By comparing static, dynamic, and shedding culture methods, the experiment aims to elucidate how each method impacts the structural cohesiveness of endothelial cell junctions.

The methodology, as illustrated in figure 1.1 involves conducting experiments on three fundamental types of cell cultures:

- Statically cultured cells: Cells grown in a stationary environment without shearflow.
- Dynamically cultured cells: Cells exposed to continuous shearflow, so a glycocalyx can be formed.
- Shedding cells: Cells initially under dynamic conditions, followed by a one-hour flow stop to induce glycocalyx degradation.

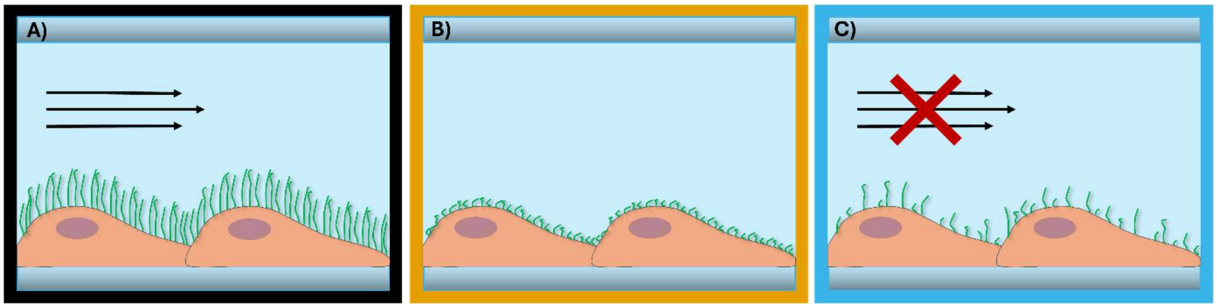

Figure 1.1: ***Culture Methods and Impact on HUVEC.*** *A) Dynamic culture. Cells are constantly exposed to a distinct shear stress. HUVEC will synthesize a robust glycocalyx. B) Static culture. Cells are not exposed to shear stress and the glycocalyx in HUVEC is only minimal. C) Shedding. Cells are dynamically cultured, and the shear stress is stopped. HUVEC begin to shed their glycocalyx.*

Based on these research questions and objectives, the following hypotheses are proposed for this thesis:

1. HUVEC cultured under dynamic conditions exhibit higher binding of Alexa Fluor 555-conjugated WGA compared to statically cultured cells or cells under the shedding condition.

2. HUVEC cultured under dynamic conditions show a reduced endocytic uptake of nanoparticles compared to statically cultured cells or cells under the shedding condition.

3. HUVEC cultured under dynamic conditions impede the diffusion of dye molecules into the cells compared to statically cultured cells or cells under the shedding condition.

4. The cultivation method of HUVEC and HeLa influences the cell membrane's phase state, making it either more fluid or gel-like depending on whether the cells are cultured statically, dynamically, or under shedding conditions.

5. HUVEC cultured under dynamic conditions exhibit decreased adhesion of positively charged lipid vesicles compared to statically cultured cells or cells under the shedding condition.

6. HUVEC cultured under dynamic conditions show decreased diffusion of FITC-dextran through the cell layer into the hydrogel, particularly for smaller molecular sizes, compared to statically cultured cells or cells under the shedding condition.

7. HUVEC cultured under dynamic conditions demonstrate improved solidity and form factor of cell-cell contacts compared to statically cultured cells or cells under the shedding condition.

2. BASIC PRINCIPLES

The fundamental principles of cell physiology and -physics form the basis for understanding complex biological processes and are essential for the study of specific cellular structures such as the glycocalyx. This Chapter will elaborate on the basic mechanisms and components of the endothelium, the glycocalyx, and cell junctions, highlighting their physiological aspects and theoretical foundations that underpin the experimental investigations [16].

Particular focus is given to the cell membrane and lipid order, which are crucial for understanding models and mechanisms of uptake and transport from a physical perspective. The complex organization and dynamic nature of the cell membrane play a pivotal role in maintaining cellular integrity and facilitating various cellular processes. Understanding the lipid order and phase transitions within the membrane is essential for comprehending how cells regulate transport mechanisms and interact with their environment [17].

Subsequently, the Chapter will delve into fundamental processes such as nanoparticle uptake, membrane transport, and trans endothelial diffusion, providing a comprehensive understanding of these phenomena from a biophysical point of view. The uptake of nanoparticles by cells is a complex process influenced by the physical properties of the particles and the characteristics of the cell membrane [18].

The principles of shear flow in cylindrical and rectangular channels will also be briefly revisited, as such flow conditions are used to mimic physiological conditions and variations that endothelial cells experience in vivo and in vitro. Studying shear flow in controlled environments allows for precise manipulation of flow parameters, facilitating the investigation of endothelial responses to different shear stress levels [19].

2.1. Endothelium and Glycocalyx

The human endothelium, composed of endothelial cells forming a delicate monolayer along blood vessel walls, stands as a vital interface mediating intricate interactions between circulating blood components and the vascular environment. Endothelial cells exhibit remarkable morphological diversity across various vascular beds, yet they commonly present a flattened and elongated morphology aligned with blood flow, showcasing an adaptation to hemodynamic forces [20][21].

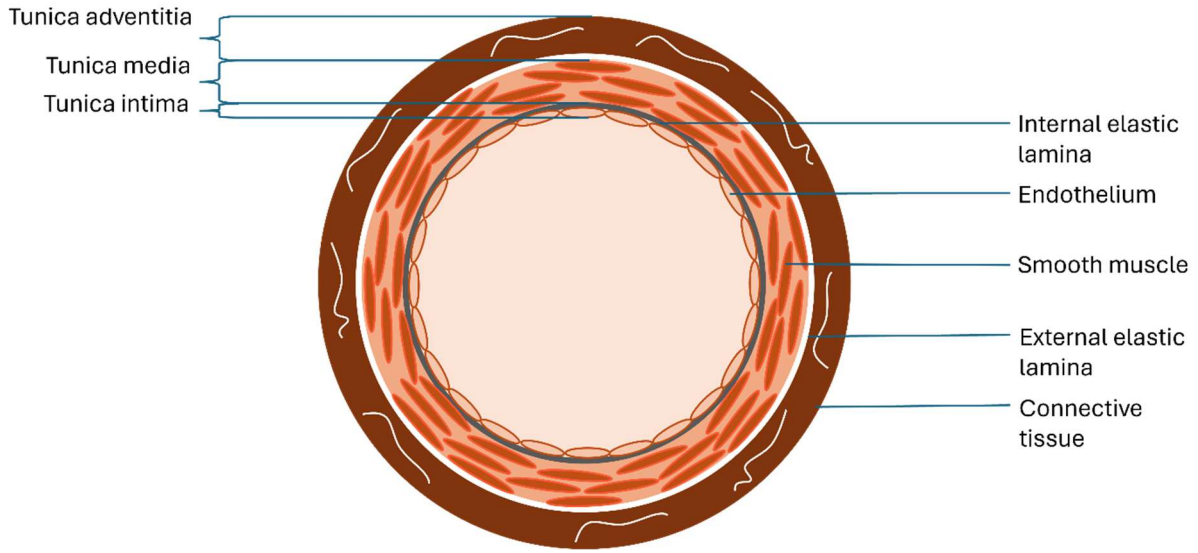

Figure 2.1: ***Cross-Sectional Anatomy of a Blood Vessel.*** *Blood vessels consist of three main layers: the tunica adventitia, tunica media, and tunica intima. The tunica adventitia is made up of connective tissue. The tunica media is primarily composed of smooth muscle cells and includes the external elastic lamina. The tunica intima contains the endothelium and is supported by the internal elastic lamina. Derived from [22].*

Endothelial cells are highly specialized and differ depending on their location within the vascular system. For example, arterial endothelial cells are adapted to withstand high pressure and shear stress, whereas venous endothelial cells are more involved in regulating the exchange of substances between blood and tissues. Microvascular endothelial cells, found in capillaries, are key players in nutrient and gas exchange and are often characterized by their ability to form tight junctions to regulate permeability [23][24].

Furthermore, endothelial cells are involved in a variety of physiological processes, including the regulation of blood flow and pressure through the production of vasoactive substances such as nitric oxide and endothelin. They also play a critical role in angiogenesis, the formation of new blood vessels, which is essential for growth, development, and wound healing. In addition, endothelial cells contribute to the immune response by controlling the passage of immune cells into tissues and presenting antigens [25][26][27].

Endothelial cell morphology and function can be significantly influenced by pathological conditions. For instance, in atherosclerosis, endothelial cells become dysfunctional, leading to increased permeability, inflammation, and the formation of plaques. Similarly, in diabetes, high glucose levels can damage endothelial cells, resulting in impaired vascular function and increased risk of complications [28][29].

Endothelial Cell Junctions

Critical for maintaining vascular integrity, endothelial cell junctions, including tight junctions, adherens junctions, and gap junctions, establish a cohesive barrier between adjacent endothelial cells. These junctions are integral to the endothelial barrier function and play crucial roles in cellular communication, mechanotransduction, and the regulation of vascular permeability [30].

- Tight junctions are composed of proteins such as claudins, occludin, and junctional adhesion molecules (JAMs), form a continuous seal along endothelial borders, tightly regulating paracellular permeability. These junctions are crucial in maintaining the selective barrier of the endothelium, controlling the passage of ions, proteins, and other solutes between the bloodstream and surrounding tissues. The integrity of tight junctions is influenced by various signaling pathways and can be dynamically regulated in response to physiological and pathological stimuli [31][32].

- Adherens junctions, primarily formed by the cadherin-catenin complex, provide structural support and facilitate intercellular communication. The main component, VE-cadherin (vascular endothelial cadherin), is linked to the actin cytoskeleton through catenins, which not only ensures mechanical cohesion between cells but also transduces signals that regulate cell growth, migration, and survival. Adherens junctions play a pivotal role in endothelial barrier function and are involved in the remodeling of blood vessels during angiogenesis [33].

- Gap junctions, composed of connexin proteins, enable direct exchange of ions and small molecules between neighboring endothelial cells, further integrating cellular responses within the endothelial monolayer. These junctions allow for rapid intercellular communication and coordination of cellular activities, such as synchronization of endothelial cell responses to shear stress and the propagation of calcium waves, which are essential for maintaining vascular tone and homeostasis [34].

- In addition to these primary junctions, other adhesive structures, such as desmosomes and focal adhesions, contribute to the endothelial barrier's integrity and the mechanical stability of the endothelium. Desmosomes provide strong intercellular adhesion by connecting intermediate filaments between cells, while focal adhesions anchor endothelial cells to the extracellular matrix and facilitate signal transduction from the extracellular environment to the cell interior [35][36][37].

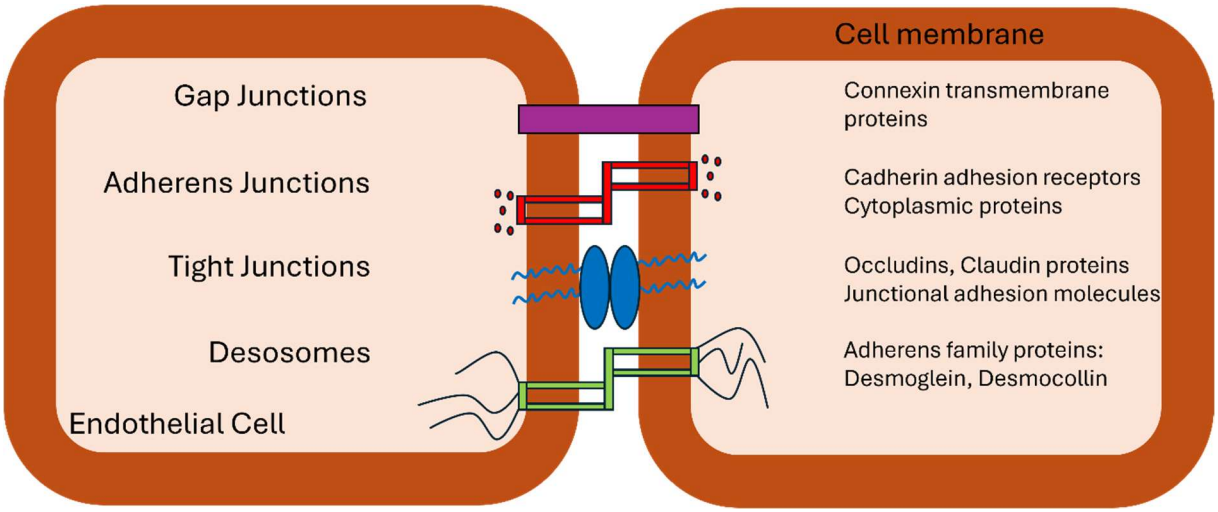

Figure 2.2: ***Cell Junctions in Endothelial Cells.*** *Gap junctions are composed of connexin transmembrane proteins that facilitate cell-to-cell communication. Adherens junctions are formed by cadherin adhesion receptors and associated cytoplasmic proteins, connecting the actin cytoskeletons of adjacent cells. Tight junctions consist of occludin, claudin proteins, and junctional adhesion molecules, sealing the spaces between cells. Desmosomes, formed by adherens family proteins such as desmoglein and desmocollin, provide additional adhesion and structural stability between cells. Derived from [38].*

The endothelial glycocalyx

The endothelial glycocalyx is a dense and intricate layer comprised of a diverse array of macromolecules lining the luminal surface of endothelial cells. It serves as a dynamic interface between circulating blood and the endothelium. This mesh-like structure extends from the endothelial cell membrane into the bloodstream [39].

This complex architecture imparts the glycocalyx with unique properties such as a negative charge, selective permeability, and mechanosensory capabilities. Key components of the glycocalyx and their roles include [40]:

- Syndecans and Glypicans: These proteoglycans are integral membrane proteins that anchor the glycocalyx to the endothelial cell surface, playing a crucial role in maintaining the structural integrity of the glycocalyx [41][42].

- Heparan Sulfate Proteoglycans: These molecules extend into the vascular lumen and interact with a variety of circulating molecules, contributing to the anticoagulant properties of the endothelium and influencing blood coagulation and fibrinolysis. Heparan sulfate proteoglycans are highly sulfated, imparting a strong negative charge [43].

- Hyaluronan: A large negatively charged glycosaminoglycan that forms a hydrated gel-like matrix, providing a cushioning effect and contributing to the mechanical properties of the glycocalyx [44].

- Chondroitin Sulfate: A sulfated glycosaminoglycan that integrates into the extracellular matrix of the glycocalyx, contributing to its structural integrity and mechanical properties. It also forms a

hydrated gel-like substance that provides cushioning and viscoelasticity, resists compressive forces, and enhances the selective permeability of the glycocalyx [45].

- Adherent Plasma Proteins: These proteins, including albumin and fibrinogen, bind to the glycocalyx, forming an additional protective layer that influences vascular permeability and enhances the barrier function of the endothelium. They help maintain an anti-coagulant surface, prevent platelet aggregation and leukocyte adhesion, and play roles in mechanotransduction, inflammatory responses, and tissue repair [46].

Due to the presence of heparan sulfate proteoglycans, hyaluronan, and chondroitin sulfate, the glycocalyx exhibits an overall negative charge. This negative charge is crucial as it repels negatively charged molecules, including albumin and various inflammatory mediators. By preventing the adhesion of these negatively charged molecules, the glycocalyx plays a pivotal role in maintaining vascular homeostasis. This selective barrier function is essential for regulating vascular permeability, ensuring that the endothelium remains a controlled interface between the blood and the underlying tissues [47].

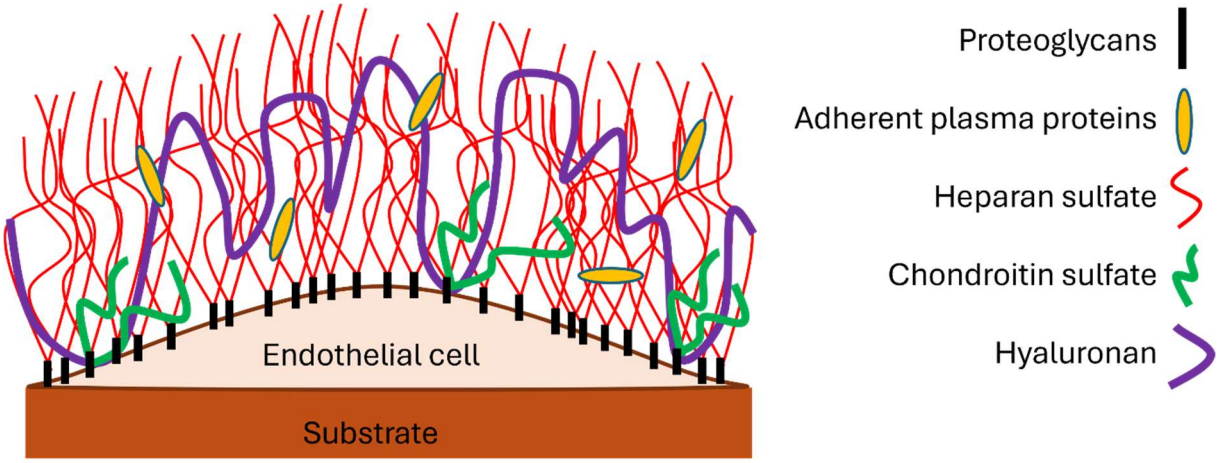

Figure 2.3: ***Components of the Endothelial Glycocalyx.*** *The endothelial glycocalyx consists of various components, including proteoglycans, which are the core structures of the glycocalyx. Adherent plasma proteins attach to these proteoglycans, contributing to the layer's functionality. Heparan sulfate and chondroitin sulfate are glycosaminoglycans associated with the proteoglycans, playing a role in maintaining the structure and charge of the glycocalyx. Hyaluronan, another key glycosaminoglycan, is also present, contributing to the overall thickness and protective function of the glycocalyx. Derived from [47][48].*

Mechanotransduction

The endothelial glycocalyx plays a pivotal role in mechanotransduction, the process by which cells convert mechanical stimuli into biochemical signals. Shear stress, exerted by blood flow on the endothelial surface, induces deformation of the glycocalyx, triggering a cascade of intracellular signaling pathways. Key mechanosensitive molecules within the glycocalyx, including the already mentioned syndecans and glypicans, function as mechanoreceptors, transducing mechanical forces into biochemical signals [49].

Upon experiencing shear stress, the deformation of the glycocalyx activates several downstream signaling pathways. This includes the activation of protein kinase C (PKC), mitogen-activated protein kinases (MAPKs), and transcription factors such as nuclear factor kappa B (NF-κB). These pathways collectively modulate endothelial function and gene expression, influencing various physiological processes. Syndecans and glypicans are critical for detecting mechanical changes in the environment, initiating signaling cascades that lead to cellular responses. Heparan sulfate proteoglycans contribute not only to the structural integrity of the glycocalyx but also participate in mechanotransduction by interacting with growth factors and cytokines [50][51].

PKC is activated by mechanotransductive signals from the glycocalyx, leading to alterations in endothelial cell permeability and inflammatory responses. MAPKs play a significant role in cellular responses to stress; their activation leads to changes in gene expression, affecting cell growth, differentiation, and apoptosis. NF-κB is crucial for inflammatory responses, with shear stress-induced activation resulting in the expression of pro-inflammatory genes that can affect vascular tone and inflammation [52][53].

The mechanotransductive properties of the glycocalyx influence the production of nitric oxide (NO) and other vasoactive substances, regulating vascular tone and blood pressure. Additionally, mechanotransduction pathways modulated by the glycocalyx can either promote or inhibit inflammatory responses, depending on the context. This regulation is vital in maintaining vascular homeostasis and responding to injury or infection [54][55].

Selective Barrier of the Glycocalyx

A key feature of the glycocalyx is its ability to discriminate between molecules based on size and charge. The negatively charged components of the glycocalyx, mostly heparan sulfate proteoglycans and glycosaminoglycans, create an electrostatic barrier that repels other negatively charged molecules, including albumin and various inflammatory mediators. Conversely, this negative charge facilitates the passage of positively charged ions and small solutes, ensuring that essential nutrients and electrolytes can traverse the endothelial layer efficiently [56][57].

The size selectivity of the glycocalyx is equally important. The dense, gel-like matrix of the glycocalyx acts as a molecular sieve, allowing small solutes and water to pass through while restricting larger molecules. This sieving effect is crucial for preventing the leakage of plasma proteins and other macromolecules into the interstitial space, thereby maintaining the colloid osmotic pressure necessary for proper fluid balance within the vascular system [58][59].

In addition to its intrinsic properties, the glycocalyx also interacts with endothelial cell junctions, enhancing its barrier function. By influencing the assembly and maintenance of tight junctions, adherens junctions, and gap junctions, the glycocalyx helps regulate the overall permeability of the endothelial monolayer. This interaction ensures that the endothelial barrier remains selectively permeable and can dynamically adjust to varying physiological demands and stressors [14][60][61].

The barrier function of the glycocalyx is not static; it can be compromised under pathological conditions. Enzymatic degradation, oxidative stress, and inflammatory responses can disrupt the glycocalyx, leading to increased vascular permeability. This disruption allows for the uncontrolled passage of proteins, solutes,

and inflammatory mediators into the surrounding tissues, contributing to conditions such as tissue edema and inflammation [62][63].

Synthesis of the Endothelial Glycocalyx Under Shear Flow

Under physiological conditions, shear flow exerted by circulating blood plays a crucial role in the synthesis and maintenance of the endothelial glycocalyx. Shear stress, generated by laminar blood flow, stimulates endothelial cells to produce and release glycocalyx components, promoting glycocalyx buildup and structural integrity. Mechanotransduction pathways activated by shear stress, such as those involving endothelial nitric oxide synthase (eNOS), enhance glycocalyx synthesis and assembly [64][65][66].

Additionally, shear-induced activation of transcription factors, including Krüppel-like factors (KLFs) and NF-κB, upregulates the expression of glycocalyx-related genes, facilitating glycocalyx formation. Furthermore, shear flow promotes the recruitment and binding of glycocalyx-producing enzymes, such as glycosyltransferases and sulfotransferases, to the luminal surface of endothelial cells, facilitating glycosylation and sulfation of glycocalyx components. Overall, shear flow serves as a potent stimulus for glycocalyx synthesis, contributing to the maintenance of vascular homeostasis and endothelial function [67][19][68].

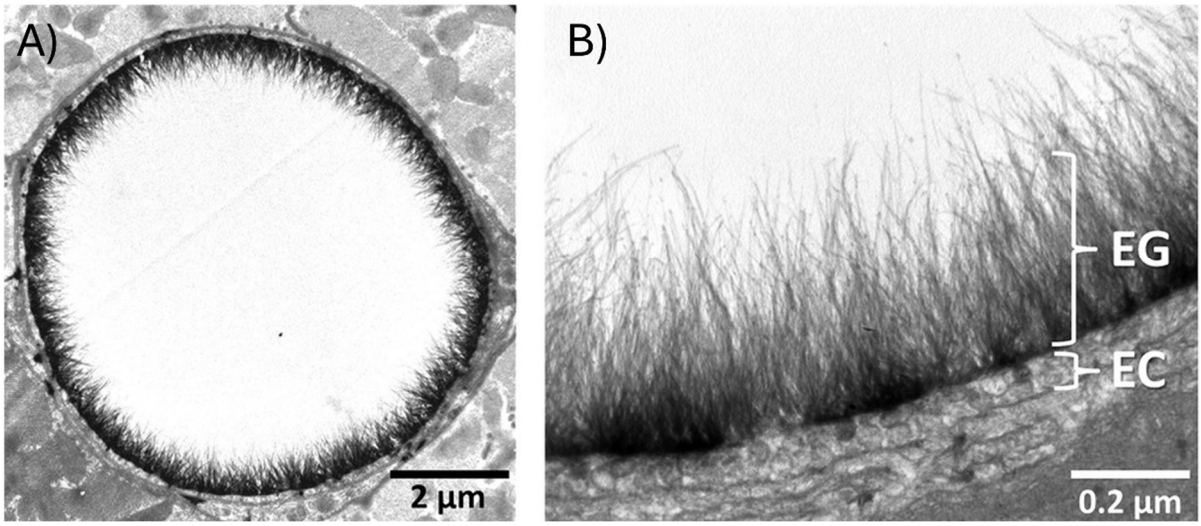

Figure 2.4: ***Electron micrographs showcasing the glycocalyx of goat capillaries.*** *A) Cross-sectional view of the entire capillary. B) 10x magnified image compared to A). Endothelial cells and the endothelial glycocalyx are clearly distinguishable. The endothelial glycocalyx is partially many times larger than the cell itself. Adapted and modified from [69], with permission from B. van den Berg and John Wiley and Sons (Licensce Number 5815831100201).*

The thickness of the endothelial glycocalyx can vary depending on several factors, including the vascular bed, shear stress levels, and physiological conditions. In larger vessels such as arterioles and arteries, the glycocalyx typically ranges from 0.2 to 1 µm, up to 3 µm in extreme cases. The time required to build a glycocalyx can also vary depending on several factors, including the rate of synthesis, turnover, and shear stress levels. Under physiological conditions with optimal shear stress, endothelial cells continuously

synthesize and replenish the glycocalyx, with studies suggesting that glycocalyx turnover occurs within days [67][69][70][71].

Degradation of the Endothelial Glycocalyx

The endothelial glycocalyx, despite its continuous synthesis, is susceptible to degradation under various pathological conditions and physiological stimuli. Inflammatory cytokines, such as tumor necrosis factor-alpha (TNF-α) and interleukin-1β (IL-1β), play a significant role in this process by upregulating the expression of glycocalyx-degrading enzymes, including matrix metalloproteinases (MMPs) and hyaluronidases. These enzymes specifically target glycocalyx components, such as glycoproteins and proteoglycans, leading to their cleavage and subsequent shedding from the endothelial surface [72][73][74].

When blood flow is stopped or reduced, creating conditions of low or disturbed flow, the shedding of the glycocalyx can occur rapidly. Studies have demonstrated that within minutes to hours of flow cessation or reduction, glycocalyx shedding becomes evident. This rapid shedding is attributed to elevated levels of inflammatory cytokines, increased oxidative stress, and mechanical stress on the endothelial surface. These factors collectively promote the release of glycocalyx components into the circulation [75][76][77][78].

Oxidative stress, marked by the increased production of reactive oxygen species (ROS), further aggravates glycocalyx degradation. ROS cause oxidative damage to glycocalyx components, compromising the structure and function of the glycocalyx. In addition to local factors, systemic conditions such as hyperglycemia and hyperlipidemia can worsen glycocalyx degradation [79][80][81].

2.2. Cell Membranes and Lipid Order

The cellular membrane is a dynamic structure in the form of a bilayer that plays an important role in maintaining the integrity and functionality of cells and is composed primarily of proteins, phospholipids, cholesterol, and glycolipids. Phospholipids are the most abundant lipids and are characterized by a hydrophilic head and two hydrophobic tails. These molecules spontaneously organize themselves into a bilayer structure in an aqueous environment, with the hydrophobic tails facing inward and the hydrophilic heads facing outward towards the aqueous surroundings [82][83]. This thesis focuses on the lipid components of the membrane, with the following theory addressing their specific properties and roles.

Cholesterol molecules are interspersed within the phospholipid bilayer. They are vital for the regulation of membrane fluidity and stability by modulating the packing of phospholipids. Additionally, glycolipids, which have a carbohydrate moiety attached to a lipid tail, are found predominantly in the outer leaflet of the membrane and are involved in cell recognition and adhesion processes [84][85].

Lipid Order

The arrangement of lipids within the bilayer can vary in terms of order and fluidity. Lipid order refers to the degree of packing and organization of lipid molecules within the membrane. It is influenced by factors such as lipid composition, temperature, and the presence of cholesterol [86][87].

At low temperatures, lipid molecules are packed tightly together, resulting in a highly ordered, gel-like state known as the gel phase. In this phase, lateral movement of lipid molecules is restricted, and the membrane exhibits decreased fluidity. Conversely, at higher temperatures, lipid molecules become more disordered, leading to a fluid state called the fluid phase. In this phase, lipid molecules can move laterally within the membrane, allowing for increased flexibility and permeability [87][88].

Phase State

The lipid bilayer can exist in different phase states depending on its lipid composition and environmental conditions. These phase states include the liquid-disordered (Ld), liquid-ordered (Lo), and gel phases. The Ld phase is characterized by high fluidity and minimal lipid packing, whereas the Lo phase exhibits lower fluidity and increased lipid ordering due to the presence of cholesterol and sphingolipids [89][90].

The distribution of lipids between these phases is not uniform and can vary depending on the specific lipid species present in the membrane. For instance, saturated phospholipids tend to favor the gel phase, while unsaturated phospholipids prefer the fluid phase. Cholesterol and sphingolipids promote the formation of Lo domains within the membrane, which are enriched in certain lipid species and associated proteins [87][91].

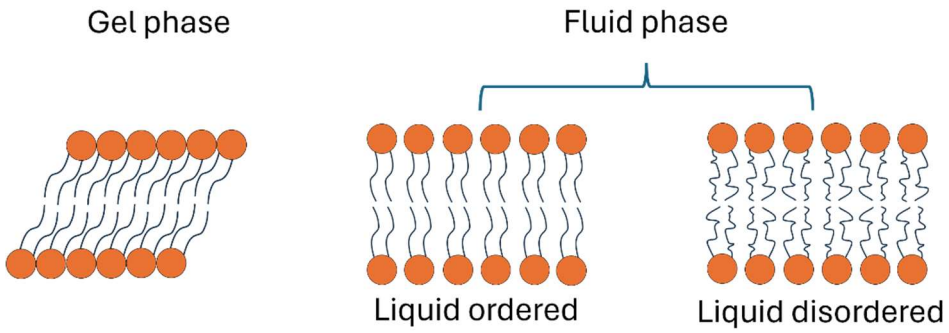

Figure 2.5: ***Phases of Lipid Bilayers: Gel Phase and Fluid Phase****. Lipid bilayers can exist in different phases. The gel phase is characterized by tightly packed lipids with limited movement, resulting in a more rigid and ordered structure. In contrast, the fluid phase includes two sub-phases: the liquid-ordered phase, where lipids are more loosely packed yet maintain some order due to cholesterol presence, and the liquid-disordered phase, where lipids are more randomly distributed and have greater mobility, leading to a highly fluid and flexible membrane. Derived from [92][93].*

Phase Transitions

During a phase transition, such as the transition from a gel phase to a fluid phase, the specific excess heat capacity plays a crucial role. As the temperature increases, the specific heat capacity, defined as

$$c_{\mathrm{p}} = \left.\frac{\mathrm{d}H}{\mathrm{d}T}\right|_{p} \tag{2.1}$$

determines the amount of heat energy needed to disrupt the interactions between lipid molecules and facilitate the transition to a more disordered state. This process involves breaking the intermolecular forces that hold lipid molecules in a particular arrangement, such as van der Waals forces and hydrogen bonding [94].

At the phase transition temperature, the specific heat capacity may exhibit a peak or discontinuity, indicating the absorption or release of heat energy as the membrane undergoes a change in phase. This phenomenon, known as a heat capacity anomaly, reflects the energy required to overcome the energetic barriers associated with transitioning between different lipid packing arrangements [87][95][96].

The heat capacity model, while informative for understanding the thermodynamic behavior of lipid membranes, differs in application to real cell membranes due to several factors. Real cell membranes are complex structures characterized by a diverse lipid composition including not only phospholipids, cholesterol and glycolipids, but also proteins. Also, the diversity in lipid composition results in broad, less cooperative phase transitions that are challenging to measure accurately [97][98].

The specific arrangement and interactions among these lipid components significantly influence the membrane's excess heat capacity. Moreover, cell membranes also host integral and peripheral membrane proteins, which play crucial roles in cellular function. Protein-lipid interactions, protein conformational changes, and modulation of lipid packing by these proteins can further alter the membrane's heat capacity.

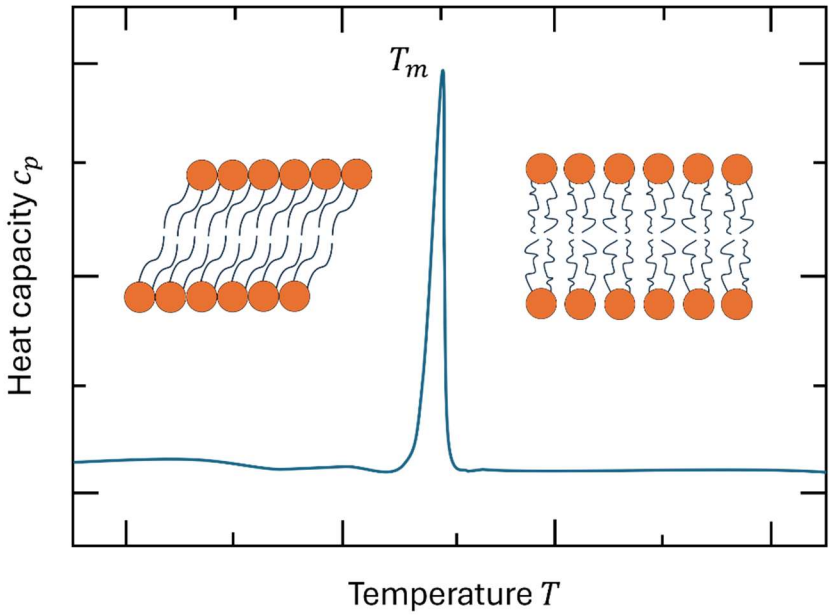

Figure 2.6: ***Phase Transition Diagram of a Lipid Bilayer.*** *As the temperature increases, the lipid bilayer undergoes a phase transition from the gel phase to the fluid phase. The transition temperature T_m , marks the point at which this change occurs, typically represented by a peak in the heat capacity c_p. Before T_m, the bilayer is in the gel phase, and after T_m, it transitions into the fluid phase, characterized by increased lipid mobility and fluidity. Derived from [87].*

Variations in lipid composition and the abundance of membrane proteins across different cell types and organelles contribute to the variability in heat capacity profiles observed among real cell membranes [87][94][99].

Optical Spectroscopy as an Alternative to Differential Scanning Calorimetry

To overcome the difficulties of determining phase transitions and changes in phase states in biological cell membranes, e.g. Laurdan can be used. Laurdan (6-dodecanoyl-2-dimethylaminonaphthalene) is a highly useful sovatochromic dye widely employed to study membrane order and dynamics in biological membranes. It exhibits a high sensitivity to the polarity of its environment, making it an excellent probe for assessing the lipid packing and phase state of membranes. The unique property of Laurdan lies in its fluorescence emission, which shifts depending on the lipid environment. This characteristic allows for the distinction between ordered (gel) and disordered (liquid-crystalline) membrane phases [100][101].

When incorporated into biological membranes, Laurdan is typically excited at a wavelength of around 350-380 nm. Its emission spectrum undergoes significant changes depending on the phase of the membrane it is embedded in. In ordered (gel) phases, Laurdan exhibits an emission peak at approximately 440 nm, whereas in disordered (liquid-crystalline) phases, the emission peak shifts to around 490 nm. This spectral shift arises from differences in membrane hydration between the phases, which influence the relaxation dynamics of the dye and, consequently, the energy of the emitted light. These changes reflect variations in the local lipid environment and packing densities in the membrane [102].

To quantify these changes in the fluorescence emission spectra of the Laurdan, the generalized polarization (GP) value can be utilized. It is calculated based on the ratio of Laurdan's emission intensities at two distinct wavelengths, typically around 440 nm and 490 nm:

$$GP = \frac{I_{440\,\mathrm{nm}} - I_{490\,\mathrm{nm}}}{I_{440\,\mathrm{nm}} + I_{490\,\mathrm{nm}}} \tag{2.2}$$

The GP-value approaches 1 for a completely ordered membrane and -1 for a maximally disordered membrane, changing proportionally with the order of the hydrocarbon chains. Higher GP values indicate more ordered, tightly packed membranes, whereas lower GP values suggest a more disordered, fluid membrane state. These properties can be exploited using classical spectroscopy or fluorescence microscopy, where emission filters in the two wavelength ranges are used to capture phase-dependent fluorescence images [103].

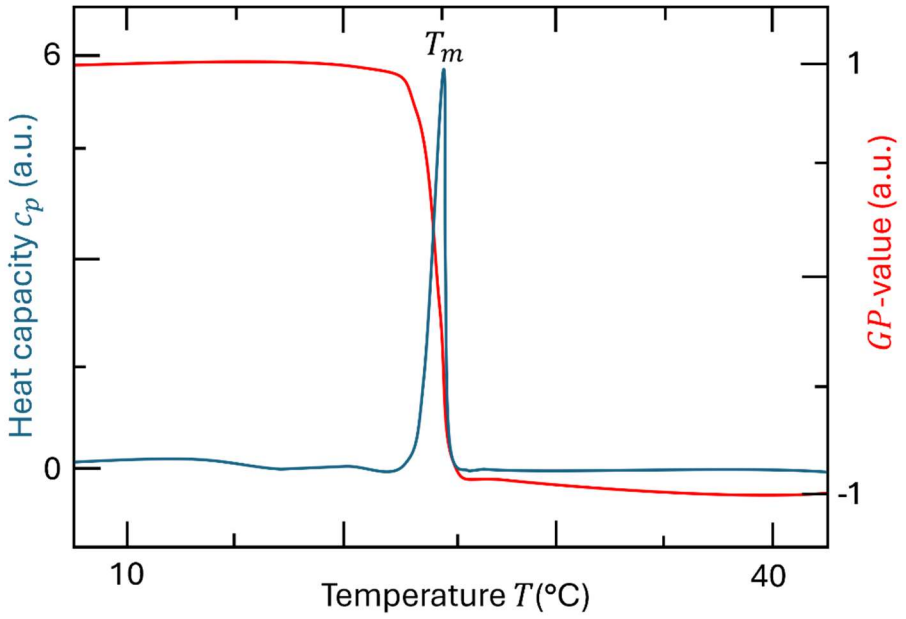

Figure 2.7: ***Generalized Polarization of Laurdan embedded in a Lipid Membrane around the Main Phase Transisiton.*** *As the temperature increases, the GP value typically decreases, reflecting the transition from a more ordered gel phase to a less ordered fluid phase. The transition temperature, T_m, marks the point where GP=0 or shows the highest slope, indicating the shift in lipid packing and membrane fluidity during the phase transition. Before T_m, the GP value is higher, corresponding to the gel phase, and it decreases after T_m, corresponding to the fluid phase. Derived from [104].*

2.3. Nanoparticle Uptake

Nanoparticles have garnered significant interest in various fields, including medicine, electronics, and environmental science. Their unique properties, such as large surface area-to-volume ratio, tunable surface chemistry, and ability to encapsulate or carry payloads, make them promising candidates for drug delivery, imaging, sensing, and other applications. One critical aspect of utilizing nanoparticles in biomedical applications is understanding how they interact with cell membranes and are internalized by cells [105][106].

Interaction Mechanisms of Nanoparticles and Cell Membranes

Nanoparticles interact with cell membranes through various mechanisms, including adsorption, penetration, endocytosis, and membrane fusion. The specific interaction mechanism depends on factors such as nanoparticle size, shape, surface chemistry, and the properties of the cell membrane [107][108]:

- Adsorption: Nanoparticles can adsorb onto the surface of the cell membrane through electrostatic, hydrophobic, or van der Waals interactions. This initial adsorption can influence subsequent uptake processes [109].

- Penetration: Small nanoparticles have the ability to penetrate the cell membrane directly, either by disrupting the lipid bilayer or by traversing through transient defects or nanopores in the membrane [110].

- Endocytosis: Endocytosis is a common mechanism by which cells internalize extracellular material. Nanoparticles can be engulfed by the cell through various endocytic pathways, such as clathrin-mediated endocytosis, caveolae-mediated endocytosis, macropinocytosis, or phagocytosis, depending on their size, shape, and surface properties [111].

- Membrane Fusion: Certain nanoparticles, particularly lipid-based or viral nanoparticles, can fuse with the cell membrane, releasing their cargo directly into the cytoplasm [112].

Factors Influencing Uptake of Nanoparticles

Several physical and biological factors can influence the uptake of nanoparticles into cell membranes. The most important are:

- Nanoparticle Properties: Size, shape, surface charge, surface chemistry, and composition of nanoparticles play crucial roles in determining their interaction with cell membranes and subsequent internalization. For example, smaller nanoparticles typically exhibit higher cellular uptake due to their increased surface area-to-volume ratio [105][113][114].

- Cellular Factors: Cell type, membrane composition, membrane fluidity, expression of specific receptors or transporters, and metabolic activity of cells can all influence nanoparticle uptake. Different cell types may exhibit varying degrees of nanoparticle internalization [115][116].

- External Conditions: External factors such as temperature, pH, presence of serum proteins, and mechanical forces can affect nanoparticle-cell membrane interactions and uptake kinetics [17][18].

- Nanoparticle Coatings: Surface modifications, such as the addition of targeting ligands, polymers, or stealth coatings, can enhance nanoparticle stability, biocompatibility, and cellular uptake efficiency [106][119][120].

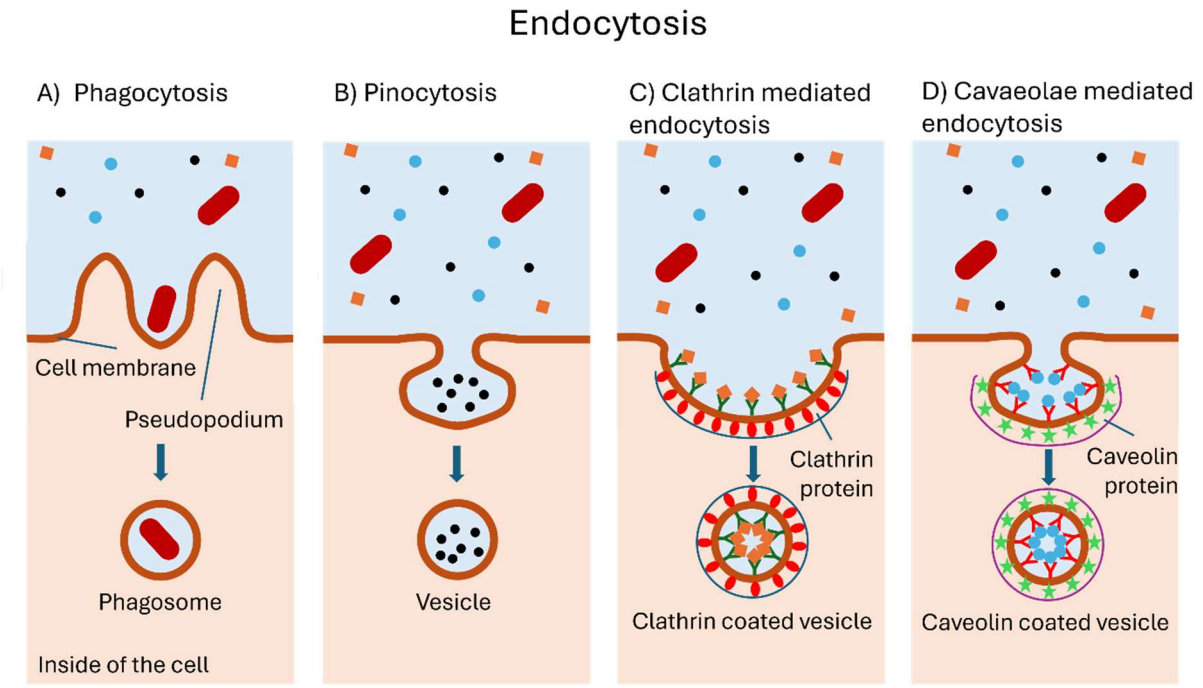

Figure 2.8: ***Types of Endocytosis in Cells.*** *A) Phagocytosis: A process where the cell engulfs large particles or microorganisms by extending its membrane to form phagosomes. B) Pinocytosis: The cell engulfs extracellular fluid and dissolved substances into small vesicles. C) Clathrin-Mediated Endocytosis: Involves the formation of vesicles with the help of clathrin protein coats, specifically for the uptake of specific molecules bound to receptors. D) Caveolae-Mediated Endocytosis: A type of endocytosis involving flask-shaped invaginations called caveolae, rich in cholesterol and caveolin proteins, often associated with the uptake of specific lipid-bound molecules. Derived from [121][122].*

Endocytic Uptake of Nanoparticles

The size of nanoparticles plays a crucial role in determining their uptake mechanism, particularly through endocytosis. Generally, nanoparticles with sizes ranging from a range of 10 nm to around 200 nm are efficiently internalized by cells via various endocytic pathways [114].

For instance, smaller nanoparticles (typically less than 200 nanometers) are often taken up via clathrin-mediated endocytosis or caveolae-mediated endocytosis. These pathways involve the formation of vesicles

coated with clathrin or caveolin proteins, respectively, which bud off from the cell membrane to engulf the nanoparticles [114][121].

On the other hand, larger nanoparticles (ranging from 200 nm) may be internalized through macropinocytosis, a process where the cell membrane forms large, non-specific invaginations called macropinosomes to engulf extracellular material [122].

However, the relationship between nanoparticle size and endocytosis is not strictly defined, and it can vary depending on cell type, nanoparticle composition, and surface properties. Additionally, larger nanoparticles may face challenges in cellular uptake due to their size, as they may be too large to enter cells efficiently via endocytosis and instead may require alternative mechanisms such as phagocytosis by specialized cells like macrophages [123].

For silica nanoparticles, the uptake mechanisms and predominant endocytic pathways are size-dependent, as observed for other nanoparticle types. Smaller silica nanoparticles (less than 200 nm) are primarily internalized via clathrin-mediated endocytosis or caveolae-mediated endocytosis, aligning with the general behavior of nanoparticles of this size range. In contrast, larger silica nanoparticles (over 200 nm) are more likely to undergo macropinocytosis or, in specialized cells such as macrophages, phagocytosis. However, the endocytic pathway can be influenced by the formation of a protein corona, which occurs when nanoparticles are incubated in biological media supplemented with proteins, such as fetal bovine serum (FBS). This protein corona can alter the surface properties of the nanoparticles, potentially modifying their interaction with the cellular membrane and favoring different uptake pathways. For instance, studies involving albumin-coated silica nanoparticles suggest that the protein corona can enhance cellular uptake efficiency and alter the specificity of the endocytic mechanism [201][202].

Fundamental Energetic Principles

Lipid vesicles serve as excellent model systems for studying nanoparticle uptake mechanics due to their simplified and well-defined structure, which closely mimics the basic properties of cellular membranes. These vesicles, composed of lipid bilayers, provide a controllable environment where variables such as membrane composition can be precisely manipulated [124][125].

When viewed through a physicist's point of view, the model for nanoparticle uptake into lipid vesicles involves a series of interrelated energy considerations. This process can be broken down into three main stages [126]:

1. Adhesion of the nanoparticle to the membrane
2. Invagination of the membrane around the nanoparticle
3. Detachment of the membrane-enclosed nanoparticle

This process encompasses the adhesion of an object to the membrane, subsequent invagination of the membrane, and final detachment of the membrane-enclosed object. The driving force behind this process is the change in adhesion energy E_{adh} upon the object's envelopment. The energy behind this force must overcome the bending energy E_{ben},required to enclose the object, and the surface tension energy E_{ten}, which accrues due to membrane consumption. The object is only taken up if

$$E_{\mathrm{adh}} > E_{\mathrm{ben}} + E_{\mathrm{ten}} \tag{2.3}$$

This provides a framework primarily applicable to artificial lipid systems such as lipid vesicles. However, when applied to real cells, this model only partially captures the complexity of the uptake process [126][127][128].

Application to real Cells

While the presence of proteins, glycoproteins, and other biomolecules on the cell surface can modulate the adhesion, they do not negate the basic energetic requirements for nanoparticle uptake. Instead, they may enhance or inhibit adhesion, altering E_{adh}, but not changing the fundamental relationship among E_{adh}, E_{ben} and E_{ten} [129][130].

Moreover, the dynamic nature of the cytoskeleton and cellular protrusions can influence membrane curvature and tension, affecting the energetics of nanoparticle uptake. Real cell membranes, like lipid vesicles, undergo invagination and other shape changes. The cell membrane's intrinsic properties, such as flexibility and ability to curve, are still governed by E_{ben}, which must be overcome for successful nanoparticle encapsulation. The cytoskeleton's role in influencing membrane curvature and tension affects the energetics of nanoparticle uptake by potentially altering E_{ben} and E_{ten} [131][132].

Also in lipid vesicles, E_{ten} would consequently increase due to the uptake of nanoparticles and therefore decreasing membrane area. However, cells have a lot of excess membrane area which means, that compared to lipid vesicles, E_{ten} would increase significantly slower or even stay constant, although the energetic principle still holds [131][133][134].

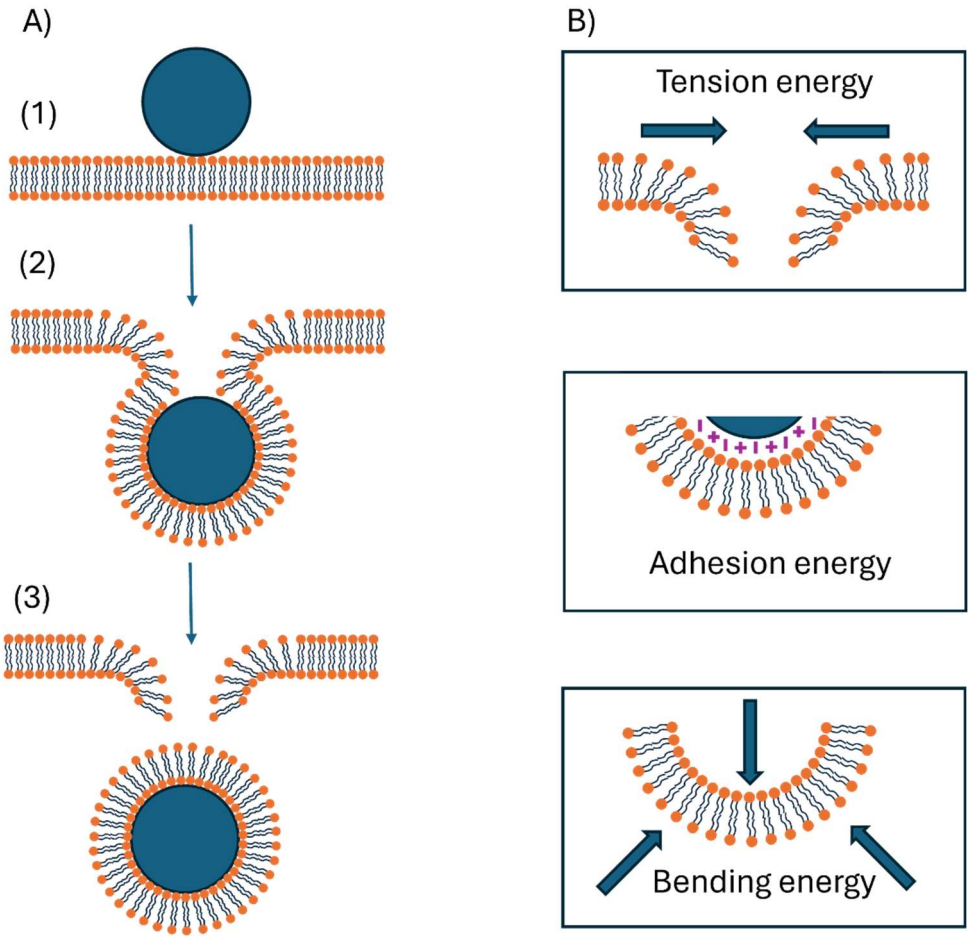

Figure 2.9: ***Endocytosis-like Uptake of Nanoparticles into Lipid Membranes.*** *A) Steps of the uptake mechanism. (1) Adhesion of a particle onto the membrane. (2) Engulfment of the particle by the lipid membrane. (3) Rupture, internalization, and pore formation within the membrane. B) Energies involved in the uptake process. Tension Energy: Arises from the membrane's surface tension as it deforms to engulf the nanoparticle. Adhesion Energy: Generated through interactions between the nanoparticle and the membrane, typically mediated by van der Waals forces or electrostatic interactions. Bending Energy: Related to the membrane's curvature, reflecting the membrane's resistance to bending and deformation. Derived from [128][135].*

2.4. Membrane Transport

Passive diffusion is a spontaneous process by which molecules move across the cell membrane from an area of higher concentration to an area of lower concentration. This movement is driven solely by the concentration gradient, without the expenditure of cellular energy. Small, nonpolar molecules such as oxygen and carbon dioxide can readily diffuse through the lipid bilayer due to their solubility in the hydrophobic core of the membrane. In contrast, polar molecules and ions, which are not readily soluble in the lipid bilayer, often require assistance from channel proteins or carrier proteins to traverse the membrane efficiently. These proteins provide specific pathways or mechanisms that facilitate the transport of such molecules, ensuring the cell's proper function and homeostasis [136][137][138][139].

Physical Model for Membrane Transport

Substance exchange in passive diffusion occurs through porous substance transport. In artificial lipid membranes the required energy ΔW to form a pore of diameter d in a membrane with an area of A_m is given by:

$$\Delta W(d) = \frac{1}{2\kappa_T^A}\left(\frac{d}{A_\mathrm{m}}\right)^2 A_\mathrm{m} + \pi d\gamma \tag{2.4}$$

Here, κ_T^A describes the isothermal area compressibility of the membrane and γ the line tension of the pore. Furthermore, κ_T^A is described by the change of area caused by the lateral pressure Π:

$$\kappa_T^A = -\frac{1}{A}\frac{\partial A}{\partial \Pi}\bigg|_T \tag{2.5}$$

Through this expression and the fact that the isothermal area compressibility κ_T^A is directly proportional to the specific heat capacity c_p of the membrane one can conclude that both have their maximum at the phase transition of the membrane. As a result, the energy required for pore formation is minimized at the membrane's melting point, leading to a maximum in membrane permeability. This increased permeability at the phase transition facilitates the passive diffusion of molecules, making it easier for substances to cross the membrane through these transient pores [87][97][216].

Application to real Cells

As already mentioned, real cell membranes are more complex consisting of various proteins, lipids, and other biomolecules that influence substance exchange beyond simple diffusion. While some aspects of the physical model still apply, real cell membranes introduce additional factors and regulatory mechanisms, including [139][140][141]:

- Selective Transport: Facilitated by specific channels or transporters.
- Active Transport: Driven by ATP hydrolysis.

- Membrane-Bound Compartments: Such as organelles, which further regulate substance exchange.

Despite these complexities, certain similarities exist between artificial lipid membranes and real cells regarding basic membrane properties and behavior. Both systems exhibit phase transitions and changes in permeability associated with temperature or lipid composition alterations. Additionally, the principle of concentration gradients driving passive diffusion is a fundamental concept applicable to both artificial lipid membranes and real cells [139][141][142][143].

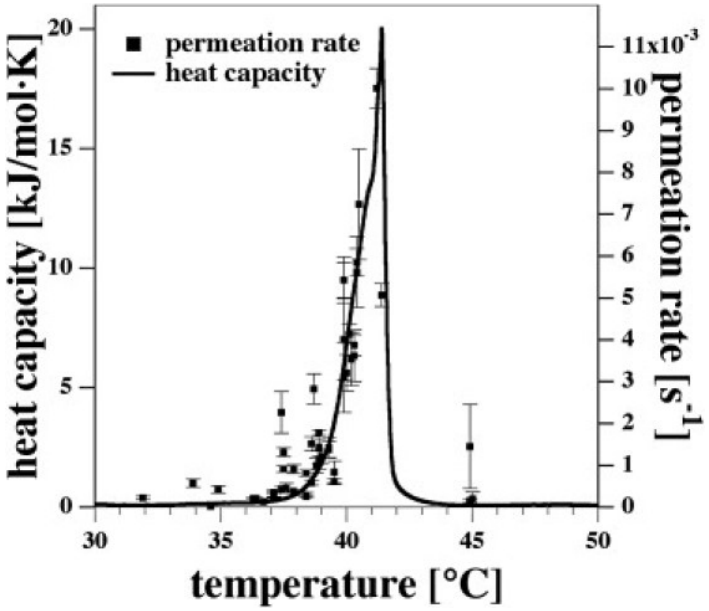

Figure 2.10: ***Temperature-Dependent Permeation Rate in Lipid Membranes.*** *Permeation rate of the dye R6G through DPPC/DPPG (95:5) LUVs (200 mM NaCl) as a function of temperature, compared with the heat capacity profile of the same sample. The permeation rate shows a strong correlation with the heat capacity. Extracted from [142]. With permission from Elsevier (License Number 5815931036945).*

The process of pore formation in membranes, when considered without the influence of tension, is governed primarily by γ and κ_T^A. In real cell membranes, compressibility is lower than in pure lipid bilayers due to the presence of proteins, cholesterol, and other biomolecules, which reduces the dominance of line tension as the driving factor. This results in altered energy landscapes for pore formation compared to artificial membranes. Depending on the uptake pathway, membrane bending rigidity also varies; for example, macropinocytosis likely requires higher bending rigidity due to the large-scale deformations involved, whereas clathrin- and caveolae-mediated pathways, with their structured protein-coated pits, reduce the influence of intrinsic membrane mechanical properties. Furthermore, the heterogeneous nature of cell membranes, such as lipid rafts or other microdomains, creates regions with varying physical parameters like line tension and compressibility [203][204].

2.5. Trans Endothelial Diffusion

Trans endothelial diffusion can occur via two main routes: paracellular and transcellular pathways. In the paracellular pathway, substances pass between adjacent endothelial cells through the intercellular spaces sealed by tight junctions. This route is selective and primarily allows for the diffusion of small hydrophilic molecules and ions. In contrast, the transcellular pathway involves the transport of substances across endothelial cells themselves, either through passive diffusion or facilitated transport mediated by transmembrane proteins such as transporters and channels. Lipid-soluble molecules can diffuse directly through the lipid bilayer of endothelial cell membranes, while larger or polar molecules may require specific transport mechanisms [23][30][33][144][145].

Factors Influencing Trans Endothelial Diffusion

Several factors influence the rate and selectivity of trans endothelial diffusion. Molecular size, shape, charge, lipophilicity, and solubility play critical roles in determining the permeability of substances across endothelial barriers. Additionally, the presence of transporters, receptors, and enzymatic pathways on endothelial cell surfaces can actively regulate the transport of specific molecules. Physical forces such as hydrostatic pressure, osmotic gradients, and shear stress exerted by blood flow also influence trans endothelial diffusion by affecting endothelial cell morphology and junctional integrity [23][50][146].

Trans Endothelial Fluid Sieving

Trans endothelial fluid sieving involves the special role in filtration of molecules of varying sizes and charges across the endothelial layer and in the kidney, driven by hemodynamic forces. This process is governed by the endothelial barrier and other components of the vessel wall. The selective sieving of plasma by these barriers significantly influences the composition of tissue fluid and lymph. By regulating which molecules pass through, the endothelial barrier maintains the balance of fluids and solutes within tissues, ensuring proper physiological function and response to changes in the vascular environment [147][148][149][150].

Physical Model for Trans Endothelial Diffusion

In a simplified model of trans endothelial diffusion, the endothelial barrier is envisioned as a thin layer comprising interconnected endothelial cells forming the inner lining of a blood vessel. This layer is conceptualized as a porous medium, wherein the endothelial cells serve as obstacles through which molecules traverse to transit between the blood vessel and the adjacent tissue. By linking the endothelial barrier to a porous medium, the model acknowledges the intricate network of endothelial cells [150][151].

In expanding upon the conceptualization of trans endothelial diffusion, it is plausible to consider the tissue situated behind the endothelial cells as akin to a hydrogel matrix. A hydrogel is a three-dimensional network of hydrophilic polymer chains capable of retaining large amounts of water. In this analogy, the tissue matrix exhibits properties similar to a hydrogel due to its water-retaining capacity and ability to swell in response

to environmental stimuli. Just as a hydrogel provides a supportive structure for cellular growth and molecular transport, the tissue behind the endothelial cells serves as a scaffold for various cellular components and facilitates the diffusion of molecules from the blood vessel into the surrounding interstitial space [150][151][152][153][154].

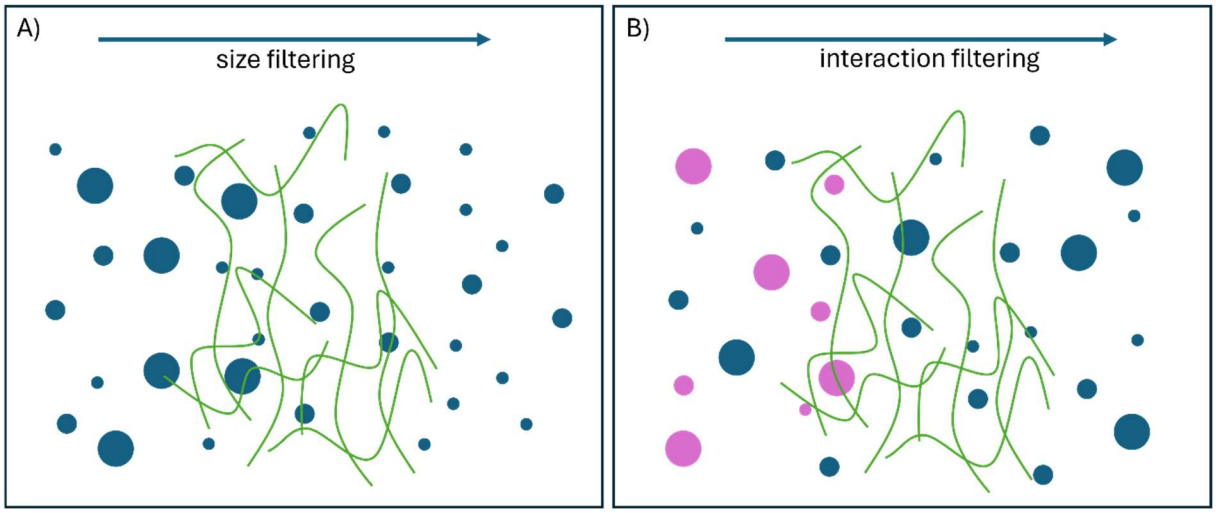

Figure 2.11: ***Size and Interaction Filtering Mechanisms in Hydrogels.*** *A) Size filtering: This method allows particles that are smaller than the hydrogel's cut-off size to pass through, while larger particles are rejected. B) Interaction filtering: In this approach, particles are distinguished based on their surface properties. Particles that strongly interact with the polymer matrix of the hydrogel are trapped, whereas those with weak interactions are permitted to pass. Derived from [150].*

Considering a cross-section of a hydrogel where a solute can diffuse exclusively from a single side, the solute's concentration across the length of the cross-section can be approximated using a one-dimensional diffusion model. For this scenario, the first Fick's law in the one-dimensional case states:

$$J = -D\frac{\partial c}{\partial x} \tag{2.6}$$

In this context, J represents the diffusion flux along the x coordinate, D the diffusion constant and c the concentration of the dissolved solute in the gel. If one also considers the temporal change, the second Fick's law must be considered:

$$\frac{\partial c}{\partial t} = D\frac{\partial^2 c}{\partial x^2} \tag{2.7}$$

Assuming in the model used here that an infinite reservoir of the dissolved solute is maintained at a constant initial concentration c_0, the partial differential equation is represented by the nontrivial standard solution

$$c\,(x) = c_0\left[1 - \mathrm{erf}\left(\frac{x}{(Dt)^2}\right)\right] \tag{2.8}$$

whereas $\mathrm{erf}\,(x)$ is

$$\mathrm{erf}(x) = \frac{2}{\pi^{\frac{1}{2}}} \int_0^x e^{-\acute{x}^2} \, \mathrm{d}\acute{x} \tag{2.9}$$

Given that x and t are known, the solution obtained can be effectively used as a fitting function. The resulting curves are each the shape of a Gaussian distribution and are characterized by the diffusion length [151][155][156]:

$$\lambda = (Dt)^{1/2} \tag{2.10}$$

Typical diffusion lengths of macromolecules in polyacrylamide hydrogels range from approximately 10 µm for small proteins (e.g., 20 kDa) to 4.5 µm for large proteins (e.g., IgG, 150 kDa) over a 1-second timescale. Similar to biological tissues, these values depend on factors such as molecule size, hydrogel crosslinking density, and polymer concentration [205][206].

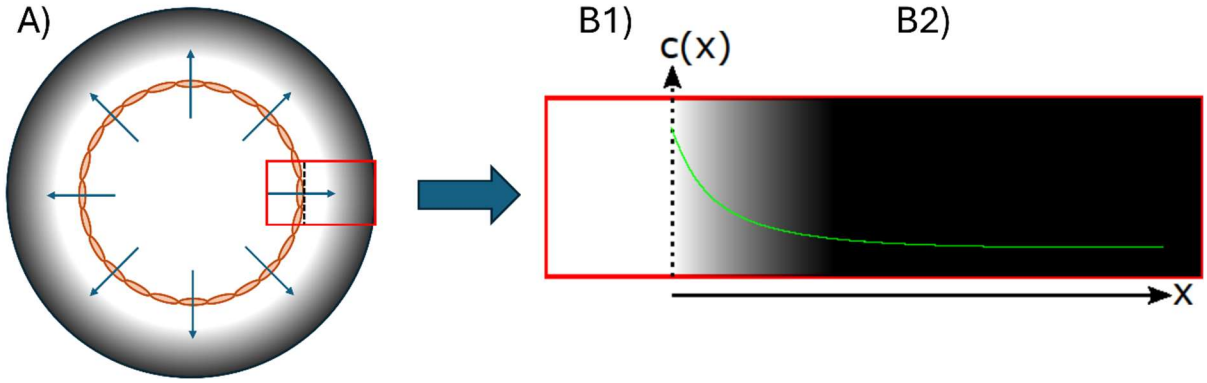

Figure 2.12: ***An Example of a Diffusion Gradient in a 3D Hydrogel Channel.*** *A) Illustration of a blood vessel with the endothelial layer, where the diffusible substance (white) flows through the vessel. B) Diffusion gradient of a substance, abstracted into one dimension, diffusing through the endothelium into the tissue. B1) An infinite reservoir of a dissolved substance with a normalized concentration. B2) The entry of the dissolved substance occurs only on one side (dotted line) and then diffuses into the tissue. Light areas indicate high concentration, while dark areas indicate low concentration. The intensity profiles of the actual measurements ideally match the profile shown in this example.*

2.6. Shear Flow in Cylindrical and Rectangular Channels

Shear stress is present wherever there is fluid flow. In living organisms, this shear stress primarily arises from the frictional force of blood moving along the walls of blood vessels. To cultivate and maintain an intact glycocalyx in blood vessels and artificial blood vessels, there must be a flow present in blood vessels and artificial cultures. When fluids flow along a wall, friction effects lead to an exchange of momentum and thus a force exerted by the fluid elements on the wall and vice versa [78][157].

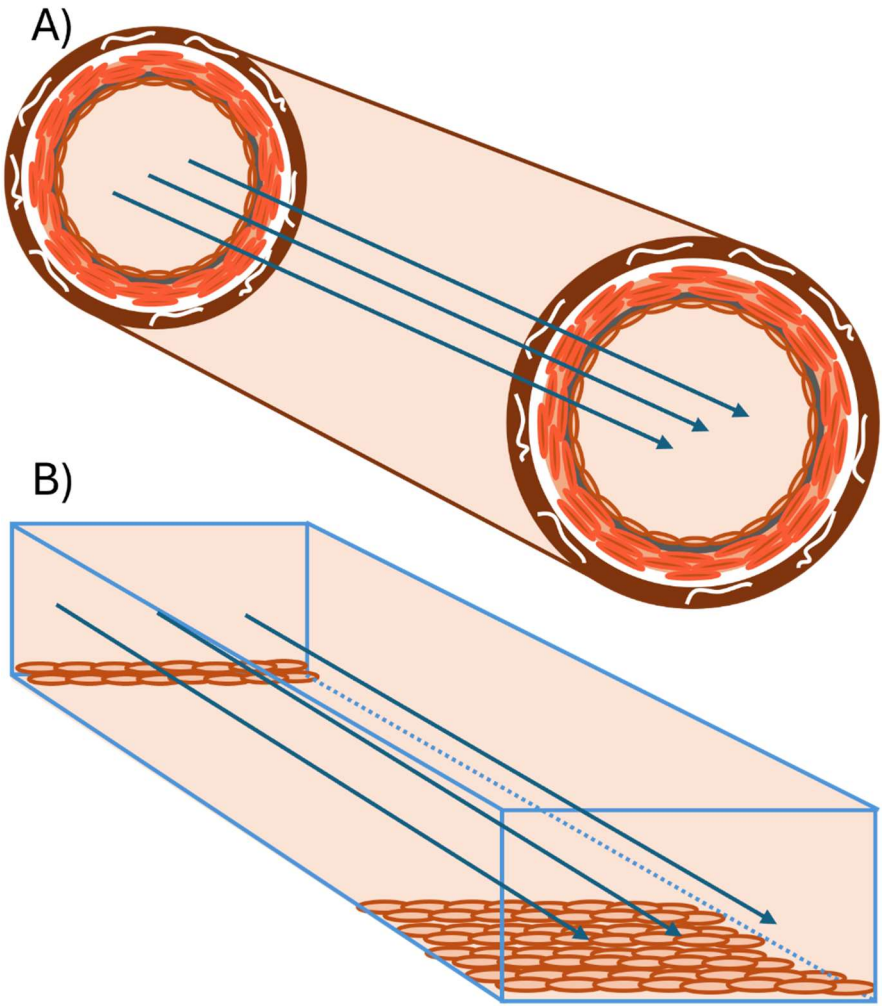

Figure 2.13: ***Dynamic Cell Culture in a Channel Slide.*** *A) Illustration of a blood vessel with its different tunicae and cylindrical geometry. B) A rectangular channel slide for in-vitro culture of endothelial cells under dynamic conditions.*

Shear Stress in Laminar Flow

Laminar flow occurs in distinct layers. Viscosity creates drag both between these layers and with the stationary surface. The quotient of the force F acting per unit area A is referred to as wall shear stress

$$\tau = \frac{F}{A} \tag{2.11}$$

For Newtonian fluids like water, the wall shear stress can be described as

$$\tau = \eta\dot{\gamma} \tag{2.12}$$

where η is the viscosity and $\dot{\gamma}$ is the shear rate. The shear rate is in turn defined by the gradient of the flow velocity $\vec{v}$ [157][158][159]:

$$\dot{\gamma} = \text{grad}\,(\vec{v}) \tag{2.13}$$

Although blood is a non-Newtonian fluid, the aqueous cell culture medium used in this context can be considered a Newtonian fluid. Consequently, η the depends solely on temperature and remains constant across the experiments.

Cylindrical Channels

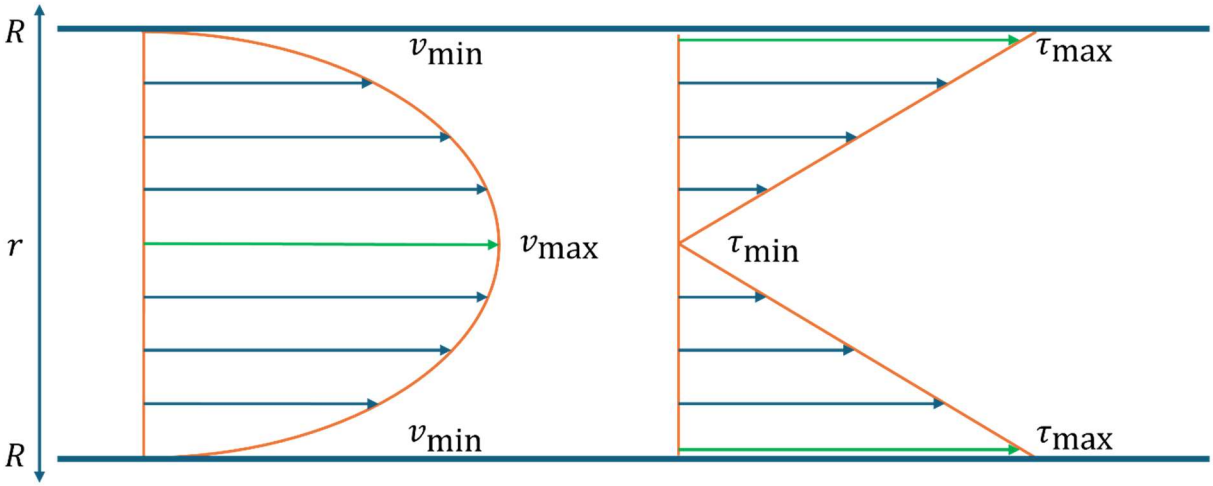

Figure 2.14: ***Flow Profile in a Cylindrical Channel.*** *The flow velocity is highest at the center of the cylinder and decreases towards the walls, creating a parabolic velocity profile typical of laminar flow.*

For cylindrical geometry and laminar flow, which can be simplified for blood vessels, for example, it holds that the flow velocity is greatest at the center of the cylinder and becomes zero at the cylinder's edge with radius R:

$$v(r) = v_{\max}\left(1 - \frac{r^2}{R^2}\right) \tag{2.14}$$

If the volumetric flow rate $\dot{V}$ is known, the equation can be rewritten as follows:

$$v(r) = \frac{2\dot{V}}{R^2\pi}\left(1 - \frac{r^2}{R^2}\right) \tag{2.15}$$

If this expression is differentiated and substituted in τ it can be formulated as:

$$\tau(r) = \frac{4\eta\,\dot{V}r}{\pi R^4} \tag{2.16}$$

Accordingly, the wall shear stress decreases linearly towards the center of the vessel [157][158][159].

Rectangular Channels

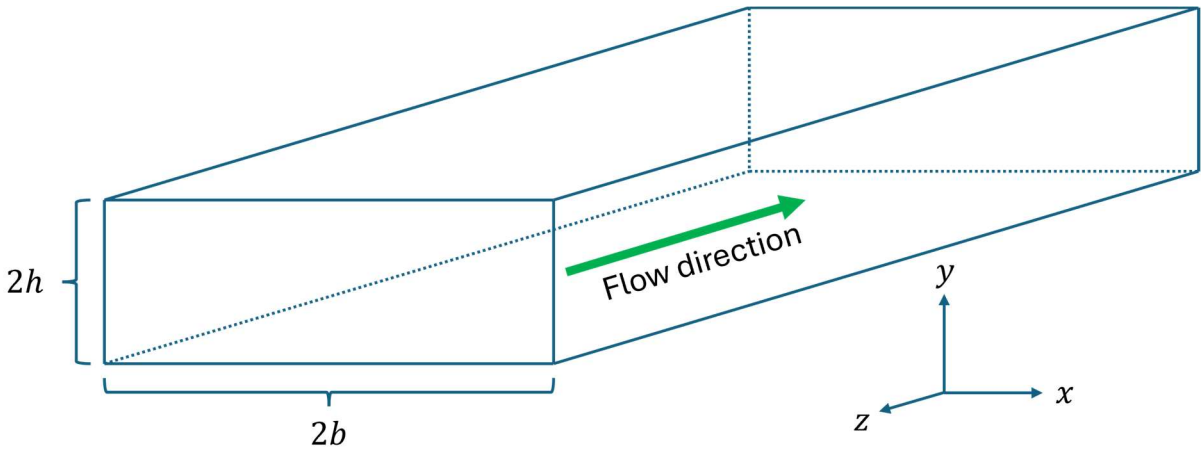

Figure 2.15: ***Flow Profile in a Rectangular Channel.*** *The coordinate cross is positioned at the center of the channel. The y-axis is oriented vertically, the x-axis is horizontal and perpendicular to the flow direction, and the z-axis runs parallel to the flow direction. The flow velocity is highest at the center and decreases towards the channel walls, creating a characteristic flow profile.*

While cylindrical channels offer a more physiological representation of in vivo conditions, rectangular channels are prevalent in in vitro cell culture due to their compatibility with essential laboratory equipment such as microscopes and incubators. This compatibility makes rectangular channels a practical choice for researchers despite their departure from physiological accuracy. Therefore, understanding the theory of shear flow in rectangular channels becomes paramount, as it directly influences cellular responses and experimental outcomes in these commonly used setups [157][158][159].

The shear flow in rectangular channels is described as

$$\tau(x,y) = \eta \frac{\partial v(x,y)}{\partial y} = \alpha \dot{V} \tag{2.17}$$

Whereas $v(x,y)$ is the flow velocity and $\alpha = \frac{\alpha_1}{\alpha_2}$ is a geometrical factor dependent on the dimensions of the channel.

The flow velocity $u(x,y)$ and the flow rate $\dot{V}$ can be written as [157][158][159][160]:

$$v(x,y) = -\frac{1}{\eta}\frac{\mathrm{d}p}{\mathrm{d}z}\left\{\frac{b^2 - x^2}{2} - \sum_{n=0}^{\infty} \frac{b\pi(-1)^n}{(2n+1)^3}\left(\frac{2}{\pi}\right)^3 \frac{\cosh\left[(2n+1)\left(\frac{\pi y}{2b}\right)\right]}{\cosh\left[(2n+1)\left(\frac{\pi y}{2h}\right)\right]} \cos\left[(2n+1)\left(\frac{\pi x}{2b}\right)\right]\right\} \tag{2.18}$$

$$\dot{V} = -\frac{1}{\eta}\frac{\mathrm{d}p}{\mathrm{d}z}\underbrace{\left\{\frac{4hb^3}{3} - 8b^4\left(\frac{2}{\pi}\right)^5 \sum_{n=0}^{\infty} \frac{1}{(2n+1)^5} \tanh\left[\frac{\pi h(2n+1)}{2b}\right]\right\}}_{\alpha_1} \tag{2.19}$$

Here, $2h$ is the height in y-direction, $2b$ the width in x-direction and $\frac{\mathrm{d}p}{\mathrm{d}z}$ the change of pressure in z-direction. Solving the equation for $\frac{\mathrm{d}p}{\mathrm{d}z}$ yields:

$$\frac{\mathrm{d}p}{\mathrm{d}z} = -\frac{\eta \dot{V}}{\alpha_1} \tag{2.20}$$

Since the cells adhere and grow on the bottom of the channels, one can now say that $y = -h$. For the middle of the channel surface the shear stress is then.

$$\tau(x = 0, y = -h) = \frac{\eta \dot{V}}{\alpha_1}\underbrace{\left\{\sum_{n=0}^{\infty} \frac{b\pi(-1)^n}{(2n+1)^2}\left(\frac{2}{\pi}\right)^5 \tanh\left[\frac{\pi h(2n+1)}{2b}\right]\right\}}_{\alpha_2} \tag{2.21}$$

With these equations α_1 and α_2 and therefore α can be calculated if the dimensions of the channel are known. For example, a commonly used channel with a height of 800 µm and a width of 5000 µm the geometrical factor is

$$\alpha = 34.7 \tag{2.22}$$

3. METHODS

This Chapter explains the methodologies employed in the performed experiments.

Initially, the cell culture techniques are elucidated, detailing static, dynamic, and shed cultivation methods to establish diverse cellular environments. Following this, the glycocalyx staining experiments are described to verify the presence or absence of the glycocalyx under different cultivation conditions.

Nanoparticle uptake experiments are then outlined, followed by dye uptake experiments through membrane diffusion. Additionally, lipid vesicle adhesion experiments on the cell surface are conducted and membrane phase state experiments using Laurdan staining and generalized polarization (GP) value measurements are included to determine membrane fluidity.

After that, trans endothelial diffusion experiments are performed in an artificial 3D hydrogel channel that simulates the endothelial surface layer.

Finally, cell-cell contact staining experiments in dependance of the cultivation method are detailed.

Each method is systematically detailed to ensure the reproducibility and reliability of the results. All works were performed under safety regulations S1 GenTSV. A complete table of the used materials and instruments, as well as detailed information about the excitation and emission of the used dyes is provided in the Appendix A2.

3.1. Cell Culture

Human Umbilical Vein Endothelial Cells (HUVEC) are extensively utilized in in vitro cell culture studies as a representative model for human endothelial cells. Derived from the umbilical vein, HUVEC cells possess primary endothelial characteristics and exhibit similar behaviors and responses to physiological stimuli. These cells express a variety of endothelial markers and are responsive to mechanical forces such as shear stress, making them ideal for studying vascular biology and pathophysiology. Additionally, HUVEC cells have the ability to form functional monolayers and develop a glycocalyx under flow conditions in vitro, allowing researchers to mimic aspects of the vascular microenvironment [161][162].

Primary cells, including Human Umbilical Vein Endothelial Cells (HUVEC), exhibit a finite lifespan in culture and gradually lose their characteristic features with each passage. Typically, after around passage 10, primary cells undergo senescence and exhibit altered morphology, reduced proliferation rates, and diminished responsiveness to stimuli. This loss of attributes compromises the reliability of experimental results and may lead to misinterpretations. Therefore, it is generally recommended to avoid prolonged cultivation of primary cells beyond passage 10 to maintain their physiological relevance and ensure the validity of research findings [162][163][164].

For the experiments of this thesis, only HUVEC with passages 2 to 8 were used. The cells were split when they reached 70-80% confluency in their culture flasks. The cell culture medium used was supplemented with 1% penicillin/streptomycin.

To investigate the effects of vesicle adhesion or membrane interactions in the absence of an intact glycocalyx, HeLa cells were chosen as an alternative to HUVEC. This substitution was made because HeLa cells have a structurally weaker glycocalyx in comparison to endothelial cells cultured under flow, making them a sufficient model system for studying cellular interactions that occur without the influence of the glycocalyx layer. Because of this, for HeLa the condition is referred to as “flow interruption” instead of “shedding” [165].

The cell culture medium used for HeLa cells was supplemented with 10% fetal bovine serum (FBS) and 1% penicillin/streptomycin.

Thawing Protocol for HUVEC and HeLa

1. The cell culture medium and DPBS were warmed to room temperature.
2. Three T75 flasks were filled with 15 ml medium.
3. Cryopreserved cells were taken out of the -80°C refrigerator and thawed at room temperature under the sterile bench.
4. A 15 ml Centrifuge tube was filled with 4 ml cell medium.
5. As soon as the cells were thawed, the contents (1 ml) were pipetted into the Centrifuge tube with cell medium.
6. The centrifuge tube was centrifuged for 10 minutes at a force of 200 g, so that a cell pellet was formed at the bottom.

7. The medium was removed, disposed and resuspended with 5 ml fresh medium.
8. The contents of the tube were then split equally into the T75 flasks and stored in an incubator at 37°C and 5% CO_2.

Splitting Protocol for HUVEC and HeLa

1. The cell culture medium and DPBS were warmed to 37°C.
2. The old medium of the cell culture flask was removed and disposed.
3. 15 ml DPBS was pipetted into the flask to wash the cells and then removed and disposed.
4. 3 ml Accutase or Trypsin was added and left in the flask for 10 minutes to detach the cells from the bottom of the flask. To control this process, a microscope was used.
5. 7 ml of fresh medium was filled into the flask to neutralize the Accutase.
6. The cells were counted with a cell counter.
7. The full content of the flask was pipetted into a Centrifuge tube and centrifuged for 10 minutes at a force of 200 g, so that a cell pellet was formed at the bottom.
8. The cell culture medium was removed, disposed and resuspended with 15 ml fresh medium if the cells were split into another passage or if used for an experiment, with an individual amount of medium that was calculated beforehand.
9. If split, a new T75 flask was filled with 15 ml medium. 5 ml of the resuspended Falco tube were pipetted into the new flask and stored in an incubator at 37°C and 5% CO_2.

Dynamic Cell Culture

To achieve an intact glycocalyx in dynamic in *vitro cell* culture, an Ibidi pump system was used. The ibidi pump system is a tool used in cell biology research to control fluid flow in microfluidic experiments. It offers precise control over flow rates and is compatible with microfluidic plates, designed for various cell culture applications. In this case it is used to mimic shear flow in blood vessels by pumping cell culture medium in a unidirectional flow through µ-channel slides in which HUVEC, or in some cases HeLa cells, are cultured.

Since µ-channels of 800 µm and 400 µm height were used, the values in the parenthesis in the protocols indicate the parameters for 400 µm channels. If only one value is listed, it applies for both.

Preparation of the Channels

The channels were coated with rat tail collagen Type I at a 145 µg/ml concentration dissolved in 17.5 mM acidic acid before seeding the cells to ensure better adhesion.

1. 200 µl (100 µl) of the collagen solution was pipetted into the channel so that the surface is fully covered.
2. The channels slides were incubated at room temperature under the sterile bench for 1 hour.
3. The channel slides were rinsed with 1 ml DPBS three times.
4. If not used, the channel slides were stored in a sterile box in the refrigerator at 8 °C for a maximum of 1 day.

Static Cultivation in Channel Slides

1. The cells were split as already written in the **Splitting protocol.**
2. 200 µl (100 µl) medium with a cell concentration of 2 x 10^5 cells/ml (4 x 10^5 cells/ml) was pipetted into the channel.
3. The channel slide was incubated for 1 hour at 37°C and 5% CO2 for the cells to adhere to the channel.
4. The medium reservoirs of the channel slide were filled with medium
5. Two 5 ml syringes were filled with 2 ml medium in each syringe were connected to the channel slide carefully without bringing air bubbles into the channel.
6. The syringe plunger was removed and replaced with a filter on each syringe. The cells were cultivated for 6 days.
7. The medium was replaced every 2 days.

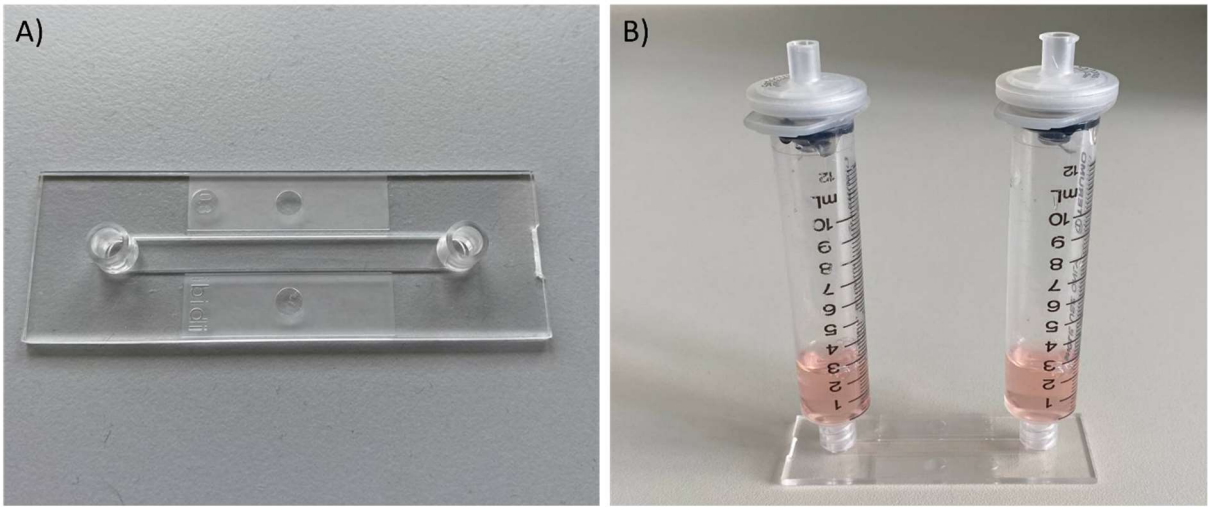

Figure 3.1: ***Statical Cell Culture in Channel Slides.*** *A) An 800 µm channel slide, where cells are pipetted into the channel, which can later be connected to a pump for dynamic culture. B) To ensure that statically cultured cells receive sufficient cell medium, two syringes filled with medium and equipped with filters to prevent contamination are connected to the reservoirs of the channel slide.*

Dynamic Cultivation in Channel Slides

1. A RED perfusion set (length 15 cm, inner diameter 1.6 mm, 10 ml reservoirs) was connected to fluidic unit and the pump system and filled with 6 ml cell medium in each reservoir.
2. The pump system was started with a shear flow of 10 dyn/cm², 3 hours before the cells were connected, to remove air bubbles from the system.
3. The cells were split as already written in the **Splitting protocol.**
4. 200 µl (100 µl) medium with a cell concentration of 1 x 10^6 cells/ml (2 x 10^6 cells/ml) was pipetted into the channel.
5. The channel slide was incubated for 1 hour at 37°C and 5% CO2 for the cells to adhere to the channel.
6. The medium reservoirs of the channel slide were filled with medium.

7. The channel was carefully connected to the perfusion set without bringing air bubbles into the system.
8. The pump was started with a shear flow of 2 dyn/cm² for 1 hour.
9. The shear flow was adjusted to 6 dyn/cm² and the cells cultivated for 6 days.
10. The medium was replaced every 2 days. Therefore, the pump was disconnected from the fluidic unit for about 1 minute.
11. If shed samples were used, the slides were disconnected from the flow for 2 hours before the experiment.

In some special cases, a shear flow of 2 dyn/cm² or 10 dyn/cm² was used for cultivation.

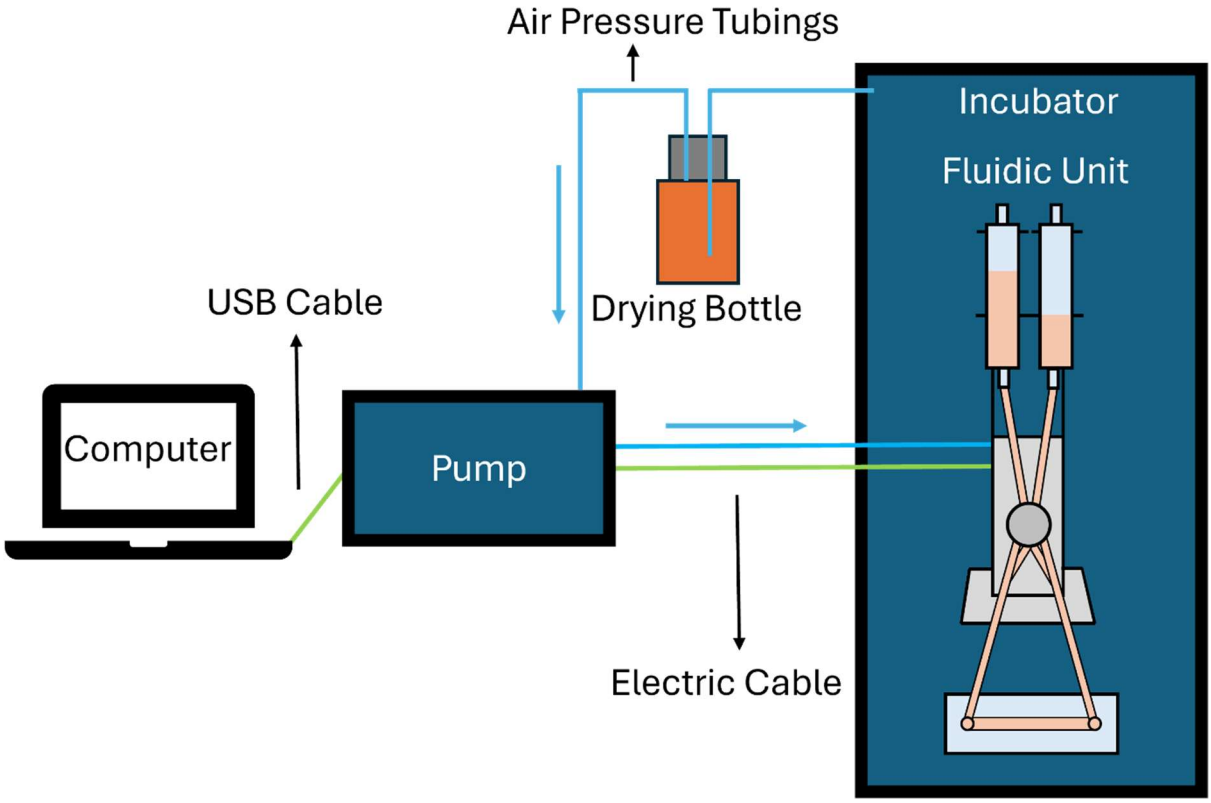

Figure 3.2: ***Experimental Setup for Cell Culture under Dynamic Conditions.*** *The computer and pump are placed on a stable surface, such as a workbench, next to the incubator. The Fluidic Unit with the mounted Perfusion Set is positioned inside the incubator, while the pump remains outside, connected to the Fluidic Unit via an electrical cable and air pressure tubing. The setup uses positive pressure, as recommended. Derived from the manual of the ibidi pump system.*

Laurdan Staining of Cells

For confocal microscopy, membrane fluorescence microscopy, and GP-value experiments, cells were stained using Laurdan. The detailed preparation of the Laurdan solution and the staining procedure are described in this Chapter and serve as a reference for subsequent sections. All steps were performed with very low and indirect light, to minimize photobleaching of the dye.

Preparation of the Laurdan Dye

1. Laurdan solution, consisting of 100 µl with a concentration of 5 mg/ml dissolved in chloroform, was pipetted into an opaque glass vial.
2. The vial was exposed to a continuous flow of nitrogen for 30 minutes to evaporate the chloroform.
3. 500 µl DMSO was added to the vial and placed in the ultrasonic bath for 30 minutes at a temperature of 50°C.
4. The Laurdan-DMSO solution was mixed with 50 ml HUVEC medium in a Centrifuge Tube wrapped in aluminum foil to prevent bleaching.

Staining the Cells

Cells of all culture conditions were stained with Laurdan using the ibidi pump system. If the cells were cultured statically, they were connected to an ibidi pump system for the staining. If shed cells were needed, the flow was stopped 2 hours before the staining.

1. The flow was stopped and the medium in the reservoirs was disposed and replaced with the Laurdan dye.
2. The flow was restarted at 6 dyn/cm², and the cells incubated for another 2 hours.
3. The channel slide was rinsed with 2 ml DPBS and 2 ml medium afterwards.

3.2. Glycocalyx Staining Experiments

The existence or absence of the glycocalyx was verified via Alexa Fluor 555 conjugated WGA staining. After the cells were split, a set of dynamically, statically and shed specimen from the same source were cultured in 400 µm channels slides. A Zeiss Axio Observer 7 featuring an objective with 10x magnification was used to take images.

All steps were performed with very low and indirect light, to minimize photobleaching of the dye.

Preparation of the WGA Solution

1. A 500 ml stock solution with a concentration of 1.0 mg/ml WGA dissolved in DPBS was produced and stored at -20°C.
2. The stock solution was further diluted to a concentration of 5.0 µg/ml in DPBS.

Staining the Cells

If the cells were cultured statically, they were connected to an ibidi pump system for the staining. If shed cells were needed, the flow was stopped 2 hours before the staining.

1. The flow was stopped and the medium in the reservoirs was disposed and replaced with the WGA.
2. The flow was restarted, and the cells incubated for another 2 hours.
3. The channel slide was rinsed with 2 ml DPBS afterwards.

Preparation of the Experimental Setup

All steps were performed with very low and indirect light, to minimize photobleaching of the dye.

1. A stage incubator was pre heated to 37°C.
2. The channel slide was disconnected from the pump system and quickly put on the microscope stage and connected to the syringe tube. It was made sure that no air bubbles were brought into the channels and that the flow has the same direction as in the cultivation.
3. Another tube was connected to the other end of the channel slide and lead into a collection container.
4. The microscope's objective was located at the middle of the channel and an image of the cells in phase contrast was taken.
5. The microscope shutter was closed and the Alexa Fluor 555 filter used.
6. The exposure time was set to 7 s at an intensity of 30%.

Execution of the Experiment

1. An image was taken in phase contrast for reference.
2. An image was taken in the Alexa Fluor 555 fluorescence channel.

Confocal Image Measurement

A Stellaris 5 confocal microscope with a 63x magnification was used to gather additional data about the position and morphology of the vesicles. Therefore, a set of channel slides where vesicle adhesion had already been measured was used.

1. The staining of the cells follows the same protocol as in the cell culture section.
2. The Laurdan stained cells were illuminated using a 405 nm laser, while a white light laser with an excitation wavelength of 569 nm was utilized for the Texas Red fluorescent nanoparticles.
3. The channel slides were mounted onto the microscope stage, and cells were located using a 20x magnification.
4. The bottom of the slides was precisely identified using a 63x magnification.
5. A z-scan was initiated, capturing images at 0.1 µm intervals from the slide bottom upwards until a z-position of 20 µm above the channel bottom was reached.

3.3. Nanoparticle Uptake Experiments

Negatively charged Texas Red fluorescent Silica nanoparticles with a diameter of 50 nm were used in the experiments to measure the endocytic uptake over time into cells in dependance of the existence of an intact glycocalyx and the method of cultivation. After the cells were split, a set of dynamically, statically and shed specimen from the same source were cultured in 800 µm channels slides. A Zeiss Axiovert 200M microscope with a 10x magnification and a Hamamatsu Orca C8484-05G01 camera was used to take images.

Preparation of the Nanoparticle Solution

1. The nanoparticle stock solution was put in an ultrasonic bath for 30 minutes.
2. The nanoparticles were diluted by a factor of 1:250 in cell medium in a 50 ml Centrifuge Tube to a concentration of 100 µg/ml. This is equal to a surface concentration of 4.54 m^2/l.
3. The Centrifuge Tube was wrapped with tin foil to prevent photobleaching.
4. The solution was used the same day. 30 minutes before the experiment, the solution was again put in an ultrasonic bath at 37°C.

Preparation of the Experimental Setup

All steps were performed with very low and indirect light, to minimize photobleaching of the nanoparticles.

1. 20 ml of the nanoparticle solution was filled into a syringe and a 1 m tube with an inner diameter of 1.6 mm was connected to the syringe.
2. The syringe was placed in a syringe pump, and a flow rate of 50 µl/min was set which is equal to a flow velocity of 12,5 mm/min in the channel slide.
3. A stage incubator was pre heated to 37°C.
4. The channel slide was disconnected from the pump system and quickly put on the microscope stage and connected to the syringe tube. It was made sure that no air bubbles were brought into the channels and that the flow has the same direction as in the cultivation.
5. Another tube was connected to the other end of the channel slide and lead into a collection container.
6. The microscope's objective was located at the middle of the channel and an image of the cells in phase contrast was taken.
7. The microscope shutter was closed and the Texas Red filter set.
8. The exposure time was set to 500 ms.

Execution of the Experiment

1. The syringe pump was started and as soon as the nanoparticle solution filled the channel a timer was started.
2. For 40 minutes every 300 s, a fluorescence image of the cells in the Texas Red channel was taken. The shutter was opened only very briefly before taking the image.
3. The Z-focus was readjusted if needed.

Confocal Image Measurement

A Stellaris 5 confocal microscope with a 63x magnification was used on one set of cells to verify whether the nanoparticles were internalized or only adherent at the outside of the plasma membrane. Therefore, a set of channel slides where the nanoparticle uptake kinetic had already been measured was used.

1. Hoechst 33342 was diluted to a concentration of 100 µl/ml in cell medium in a 50 ml Centrifuge Tube.
2. The channels were flushed with 600 µl of the Hoechst 33342 solution and then incubated for 20 minutes at 37°C with 5% CO2.
3. The stained nuclei were illuminated using a 405 nm laser, while a white light laser with an excitation wavelength of 569 nm was utilized for the Texas Red fluorescent nanoparticles.
4. The channel slides were mounted onto the microscope stage, and cells were located using a 20x magnification.
5. The bottom of the slides was precisely identified using a 63x magnification.
6. A z-scan was initiated, capturing images at 0.5 µm intervals from the slide bottom upwards until the nuclei were no longer visible.

3.4. Hoechst 33342 Uptake Experiments

Hoechst 33342 dye was used to stain the cells and measure the uptake into the cells through the cell membrane membrane over time in dependance of the existence of an intact glycocalyx and the cultivation method. After the cells were split, a set of dynamically, statically and shed specimen from the same source were cultured in 800 µm channels slides. A Zeiss Axio Observer 7 featuring an objective with 10x magnification was used to take images.

Preparation of the Hoechst 33342 Solution

1. Hoechst 33342 was diluted to a concentration of 100 µl/ml in cell medium in a 50 ml Centrifuge Tube.
2. The Centrifuge Tube was wrapped with tin foil to prevent photobleaching.

Preparation of the Experimental Setup

All steps were performed with very low and indirect light, to minimize photobleaching of the dye.

1. 20 ml of the dye solution was filled into a syringe and a 1 m tube with an inner diameter of 1.6 mm was connected to the syringe.
2. The syringe was placed in a syringe pump, and a flow rate of 50 µl/min was set which is equal to a flow velocity of 12,5 mm/min in the channel slide.
3. A stage incubator was pre heated to 37°C.
4. The channel slide was disconnected from the pump system and quickly put on the microscope stage and connected to the syringe tube. It was made sure that no air bubbles were brought into the channels and that the flow has the same direction as in the cultivation.
5. Another tube was connected to the other end of the channel slide and lead into a collection container.
6. The microscope's objective was located at the middle of the channel and an image of the cells in phase contrast was taken.
7. The microscope shutter was closed and the DAPI filter set.
8. The exposure time was set to 250 ms.

Execution of the Experiment

1. The syringe pump was started and as soon as the dye solution filled the channel a timer was started.
2. For 40 minutes every 300 s, a fluorescence image of the cells in the DAPI channel was taken. The shutter was opened only very briefly before taking the image.
3. The Z-focus was readjusted if needed.

3.5. Membrane Phase State Experiments

The phase state of HUVEC membranes was assessed by measuring changes in the GP-value of Laurdan stained membranes across varying temperatures, with consideration given to the presence of an intact glycocalyx and the cultivation method employed. Imaging was conducted using a custom-built temperature control device compatible with a Zeiss Axio Observer 7 microscope equipped with a 10x magnification objective. After the cells were split, a set of dynamically, statically and shed samples from the same source were cultured in 400 µm channels slides.

In a complementary experiment, HeLa cells were used in place of HUVEC to further validate the results. To rule out potential systemic errors with the temperature control, a 3D-printed heat bath insert, compatible with the microscopes stage, was employed. Imaging of the HeLa cell membranes was performed using a Zeiss Axiovert 200M microscope equipped with a 10x magnification objective.

The Laurdan staining procedure, previously detailed in the cell culture section, was applied.

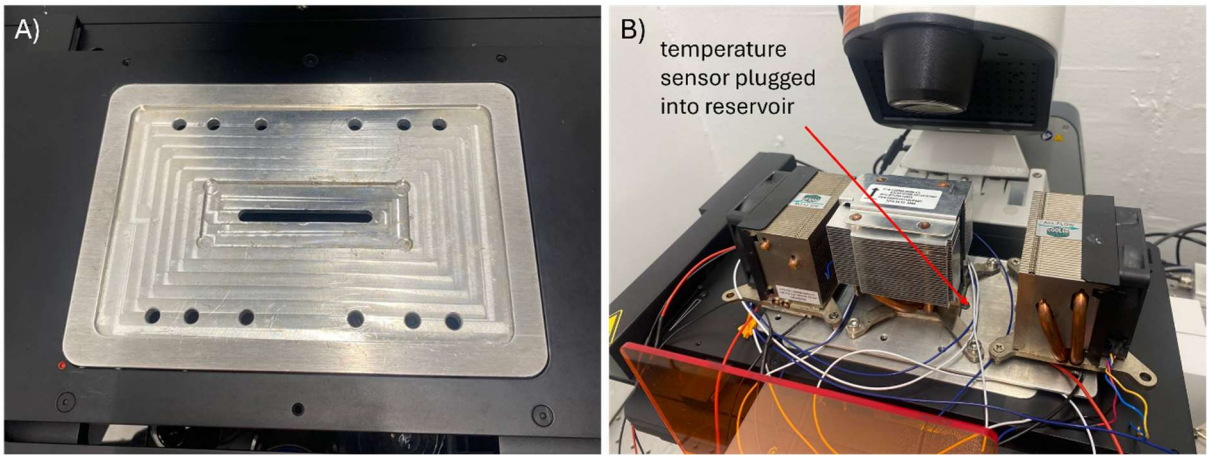

Figure 3.3: ***Temperature Control Device for GP-Measurements.*** *A) An aluminum plate with an inlet for the channel slides, mounted onto the microscope stage. B) A second aluminum plate is positioned on top of the channel slides, equipped with three Peltier elements and CPU coolers. The temperature sensor is inserted into the reservoir of the channel slide, accessible from the top.*

Preparation of the Experimental Setup

1. The temperature device was installed on the microscope stage and pre heated to 45°C.
2. The exposure time for the images was set to 300 ms.
3. The filters for 440 nm and 490 nm emission were set.
4. The channel slide was placed on the microscope stage and the temperature sensor inserted into the reservoir.

Execution of the Experiment

Conducting the membrane phase state experiment required swift action to preserve the integrity of the glycocalyx. Typically completed within a timeframe of less than 20 minutes, speed was essential to prevent degradation.

1. The cells were initially focused with minimal intensity and subsequently adjusted to 30% intensity.
2. Images were captured in both the 440 nm and 490 nm spectra.
3. The temperature was systematically decreased to 5°C, with images taken at intervals of 3 K in the 440 nm and 490 nm spectra.

Reference Experiments with HeLa Cells

The protocol of the experiment is identical to the protocol with HUVECs, with only the following differences, that the HeLa cells cultured under flow conditions were exposed to 2 dyn/cm², 6 dyn/cm², and 10 dyn/cm², respectively.

The temperature control device used in the experiment was originally designed by Nicolas Färber for similar research purposes. It features a 3D-printed channel that is affixed to a metallic insert on the microscope stage using silicone paste. The 3D-printed channel is connected to tubes from a heat bath, which regulates the temperature. To ensure accuracy, the temperature is monitored using both the heat bath and an additional sensor placed in one of the reservoirs of the channel slide.

However, measuring temperatures across the range of 10°C to 45°C takes approximately one hour due to the slow rate of temperature change. This makes the method unsuitable for experiments involving HUVECs with an intact glycocalyx but viable for use with HeLa cells.

Bleaching Correction

A bleaching correction was applied to normalize the fluorescence intensity over the illumination period. For data acquisition, Laurdan stained samples of statically cultured cells were measured according to the protocol in the normal experiment but at a constant temperature. For HUVEC, the samples were measured with constant temperatures of $T = \{22.0°C, 22.0°C, 27.0°C\}$, for HeLa with $T = \{22.0°C, 22.0°C, 45.0°C\}$.

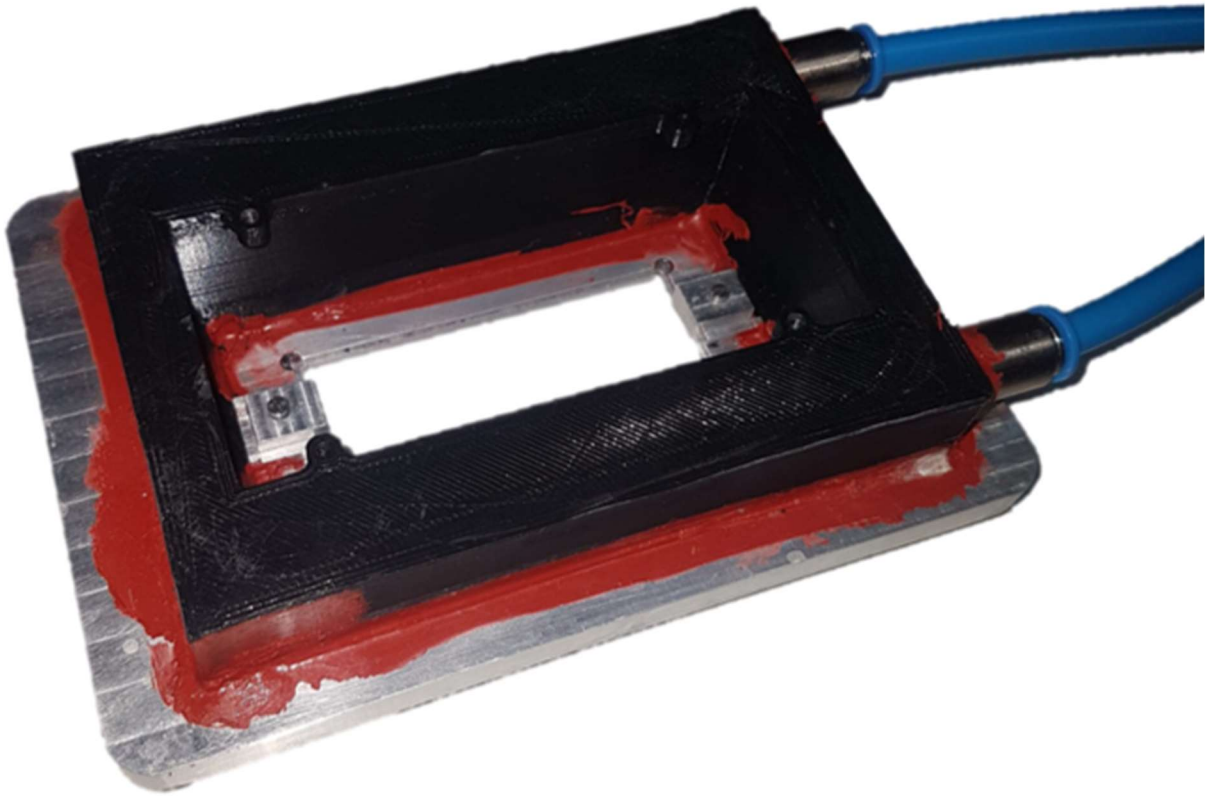

Figure 3.4: ***Alternative Temperature Control Device for GP-Measurments.*** *The device features a 3D-printed channel affixed to a metallic insert on the microscope stage using silicone paste. The channel is connected to tubes from a heat bath, which regulates the temperature. Temperature accuracy is maintained by monitoring with both the heat bath and an additional sensor placed in one of the channel slide reservoirs.*

3.6. Lipid Vesicle Adhesion Experiments

Positively and neutrally charged Giant Unilamellar Vesicles (GUV) stained with Texas Red dye were produced by using electroformation and used to measure the adhesion of the GUV on the cell surface in dependance of the existence of an intact glycocalyx and the method of cultivation. After the cells were split, a set of dynamically, statically and shed samples from the same source were cultured in 800 µm channels slides. A Zeiss Axio Observer 7 featuring an objective with 10x magnification was used to take images.

Additional experiments were carried out using HeLa cells, where positively charged Multilamellar Vesicles (MLV) were produced through ultrasonication. These MLV were then employed to assess their adhesion to the cell surface, focusing on how this interaction varies with the duration and intensity of shear flow during dynamic cultivation. Following cell splitting, a series of samples, including dynamically cultivated and statically cultivated samples from the same source, were grown in 800 µm channel slides. Imaging was performed using a Zeiss Axiovert 200M microscope equipped with a 10x magnification objective to capture detailed observations of MLV adhesion under these different conditions.

GUV Adhesion Experiments

Preparation of the GUV

A self-built incubation chamber, made of two zinc-oxide glass slides, coated on one side and a Teflon spacer, was used to produce the GUV. Proper cleaning of the equipment is crucial for ensuring the quality of the produced GUVs, which is why the process is explained here in detail.

1. The glasses and the teflon spacers were put in a glass jar and filled with isopropyl alcohol. The jar was then put in the ultrasonic bath for 30 minutes.
2. The coated glasses and the spacer were rinsed with ultrapure water, dried with a nitrogen airflow, and stored in a clean container with the uncoated surface facing upwards.
3. An opaque 1 ml glass bottle was filled with chloroform and then briefly mixed with the vortex mixer. The chloroform was disposed afterwards.
4. The lipids were filled into the cleaned bottle and diluted with chloroform to a concentration of 10 mg/ml at a volume of 120 µl. A pure DMPC and an 80:20 DMPC-DOTAP mix was produced.
5. 5% Texas Red DHPE at a 1 mg/ml concentration in chloroform was added to the solution.
6. The solution was briefly mixed with a vortex mixer.
7. A volume of 50 µl of the solution was applied onto the uncoated surface of one of the glass slides. The other slide was then put on top of the other glass, also with the uncoated surface facing the lipid.
8. The glasses were then pulled apart, so that a thin film of lipids wetted the surface of both slides.
9. The glass slides were put in an opaque box with the wetted surface facing upwards. The box was placed in a vacuum desiccator for 10 minutes, so that the chloroform can evaporate.
10. The spacer was placed between the glass slides, with the lipid wetted surfaces facing inwards. Two clamps were used to keep the chamber together.

11. A sucrose solution with an osmolarity of DPBS was injected through a hole in the spacer until the incubation-chamber was full.
12. The chamber was placed in a pre-heated heat bath (about 10°C above the phase transition temperature of the lipids).
13. A frequency generator was connected to both glass slides. The generator was set to a peak to peak 1 V square wave signal at 10 Hz for 15 minutes. After that the voltage was adjusted to 4 V for another 2 hours.
14. The chamber was disconnected from the generator and carefully opened. The vesicle suspension was pipetted from the chamber into a 1.5 ml Eppendorf tube. The tube was wrapped in tin foil to prevent photobleaching.
15. The vesicles could be stored up to several weeks in the refrigerator at 8°C.

Preparation of the Experimental Setup

1. A 2 cm diameter syringe was cut to serve as a funnel that can be screwed into one side of the channel slides. The syringe was previously cleaned with ethanol.
2. The other side of the channel slide was connected to a tube with an inner diameter of 1.6 mm that was connected to another syringe.
3. The syringe was placed in a syringe pump, and a flow rate of 20 µl/min was set which is equal to a flow velocity of 5 mm/min in the channel slide. The pump was used in reverse mode so that the fluid gets sucked into the syringe.
4. A stage incubator was pre heated to 37°C.
5. The microscope's objective was located at the middle of the channel and an image of the cells in phase contrast was taken.
6. The microscope shutter was closed and the Texas Red filter set.
7. The exposure time was set to automatically adjust.
8. The vesicle solution was diluted at 1:25 with DPBS at a final volume of 2.5 ml in a centrifuge tube.
9. The solution was inserted into the reservoir.

Execution of the Experiment

1. The vesicle solution was manually pumped into the channel until it reached the area where the objective was.
2. The focus was recalibrated so that the vesicles on the cell surfaces were visible. An image for reference was taken.
3. The pump was started. Every 30 s an image was taken until a set of 25 images was complete.

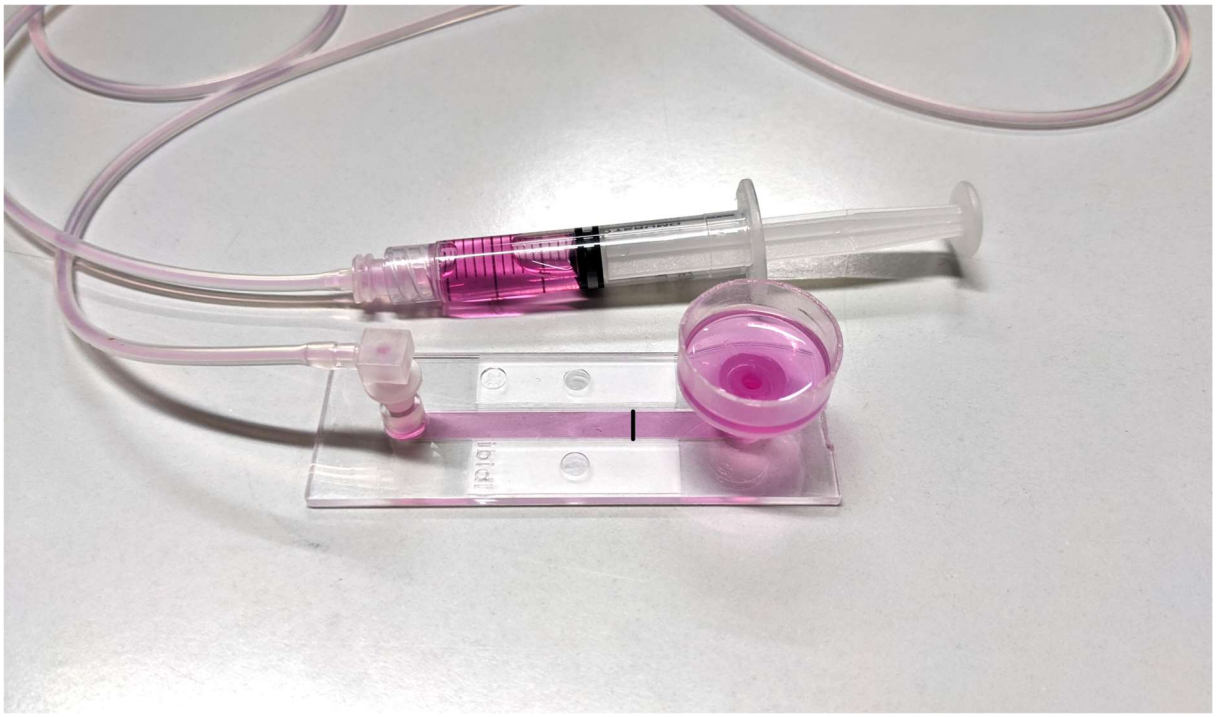

Figure 3.5: ***Vesicle Reservoir for Adhesion Measurements.*** *A reservoir made from a syringe is connected to one end of a channel slide, filled with a vesicle solution. A tube on the other end of the channel slide is connected to a syringe placed in a syringe pump. The pump operates in reverse mode, sucking the vesicle solution from the reservoir through the channel slide into the syringe.*

Confocal Image Measurement

A Stellaris 5 confocal microscope with a 63x magnification was used to gather additional data about the position and morphology of the vesicles. Therefore, a set of channel slides where vesicle adhesion had already been measured was used.

1. The staining of the cells follows the same protocol as in the cell culture section.
2. The adhesion experiments were conducted as usual.
3. The Laurdan stained cells were illuminated using a 405 nm laser, while a white light laser with an excitation wavelength of 569 nm was utilized for the Texas Red fluorescent nanoparticles.
4. The channel slides were mounted onto the microscope stage, and cells were located using a 20x magnification.
5. The bottom of the slides was precisely identified using a 63x magnification.
6. A z-scan was initiated, capturing images at 0.5 µm intervals from the slide bottom upwards until neither cells nor vesicles were visible.

DOTAP-MLV Adhesion Measurement

Preparation of the MLV

1. An opaque 1 ml glass bottle was filled with chloroform and then briefly mixed with the vortex mixer. The chloroform was disposed afterwards.
2. Pure DOTAP was filled into the cleaned bottle and diluted with chloroform to a concentration of 10 mg/ml at a volume of 53 µl.
3. 5% Texas Red DHPE at a 1 mg/ml concentration was added to the solution.
4. The chloroform was vaporized by drying the solution for 3 hours in the desiccator.
5. 1 ml DPBS was added.
6. The glass bottle was put in the ultrasonic bath for 30 min.
7. The MLV can now be stored in the refrigerator for several weeks.

Preparation of the Experimental Setup

The preparation of the experimental setup is identical to the setup of the GUV measurement. The exposure time in the fluorescence channel was calculated automatically for each measurement with the software HCImage.

Execution of the Experiment

1. The vesicle solution was manually pumped into the channel until it reached the area where the objective was.
2. The focus was recalibrated so that the vesicles on the cell surfaces were visible. An image for reference was taken.
3. The pump was started and an image in the Texas Red channel was taken.
4. After 5 minutes another image in phase contrast and in the fluorescence channel was taken.

Cytometry for Vesicle Size Analysis

The size of the GUV was assessed using a Beckman Coulter CytoFlex cytometer. Forward Scatter Area (FSC-A) measurements were recorded to evaluate the vesicle dimensions. A 100 µl aliquot of the vesicle solution was introduced into the cytometer, operating at a flow rate of 30 µl/min.

Zeta Potential Measurement

The surface charge characteristics of the GUVs were determined by measuring the zeta potential using a Zetasizer Ultra. Measurements were conducted at 37°C to reflect experimental conditions. Three independent runs were performed for both DMPC and DOTAP-DMPC GUVs to ensure accuracy and reproducibility.

3.7. Macromolecule Diffusion through the Endothelial Layer

A durable, transparent 3D hydrogel channel was fabricated by molding an amalgam of acrylamide and collagen. Within this channel HUVEC were cultured, forming an artificial endothelial layer. To gauge the diffusion across this layer into the gel, a solution of FITC-dextran was actively pumped through the channel. Cultures containing dynamically, statically, and shed cells from identical sources were seeded within the channel and perfused with the ibidi Pump System. Additionally, control measurements devoid of cellular presence were conducted. Images were captured using a Zeiss Axiovert 200M microscope at a magnification of 5x. A 3D printed frame with the dimensions 30x25x2 mm with inlets on two sides was used to cast the hydrogel.

Preparation of the Chamber

1. Frame, cover slips, cannulas and clamps were cleaned with isopropyl alcohol and UV sterilized.
2. A small film of hydrophobic silicon paste was spread between the frame and the cover slips. Clamps were used to give it additional stability.
3. The shorter 1.6 mm diameter cannulas were inserted into the inlets, the long 1.1 mm diameter spinal cannula was inserted through both other cannulas.

Preparation of the Hydrogel

1. 60 mg ammonium peroxide sulphate (APS) was dissolved in 1 ml in ultra-pure water.
2. 100 mg gelatin powder was dissolved in 4.5 ml ultra-pure water and 0.5 ml 10x PBS. For better solubility, the solution was warmed to 37°C for 30 minutes and mixed with a vortex mixer.
3. The following chemicals were added into a 50 ml Centrifuge Tube:
    - 2 ml acrylamide solution (40%)
    - 2 ml bisacrylamide solution (2%)
    - 1 ml gelatin solution
    - 50 µl APS
4. 50 µl N',N',N'-Tetramethylethylenediamine (TEMED) was added. Adding TEMED and APS starts the polymerization reaction.
5. The solution was briefly shaken and then pipetted into the prepared chamber until it was filled completely.
6. The gel was left to polymerize for 30 minutes. Then the spinal cannula was carefully removed.
7. The channel was rinsed with 1 ml DPBS and connected to the Ibidi pump system to equilibrate at a flow rate of 1 ml/h for 24 hours with HUVEC medium.

Cultivation of HUVEC inside the 3D Channel

1. The chamber was disconnected from the Ibidi system.
2. HUVEC in a 70% confluent T75 flask were detached from the flask, centrifuged, and resuspended to 300 µl new medium.
3. The cell suspension was pulled into a 1 ml.
4. A spinal cannula with a diameter of 0.9 mm was used to inject the cells evenly into the 3D channel.
5. The inlets were closed with a Luer-plug and the chamber placed in the incubator at 37°C and 5% CO_2.
6. After 30 minutes the chamber was rotated, so that the cells could also adhere to the other side of the channel.
7. The following chemicals were added into a 50 ml Centrifuge Tube:
   - If cultured dynamically, the pressure was set to 15 mbar which is equal to 3 dyn/cm² in the 800 µm channel slides. The cells were then cultured for 4 days. For shed specimen, the flow was stopped 2 hours before the experiments.
   - If cultured statically, the medium was changed daily.

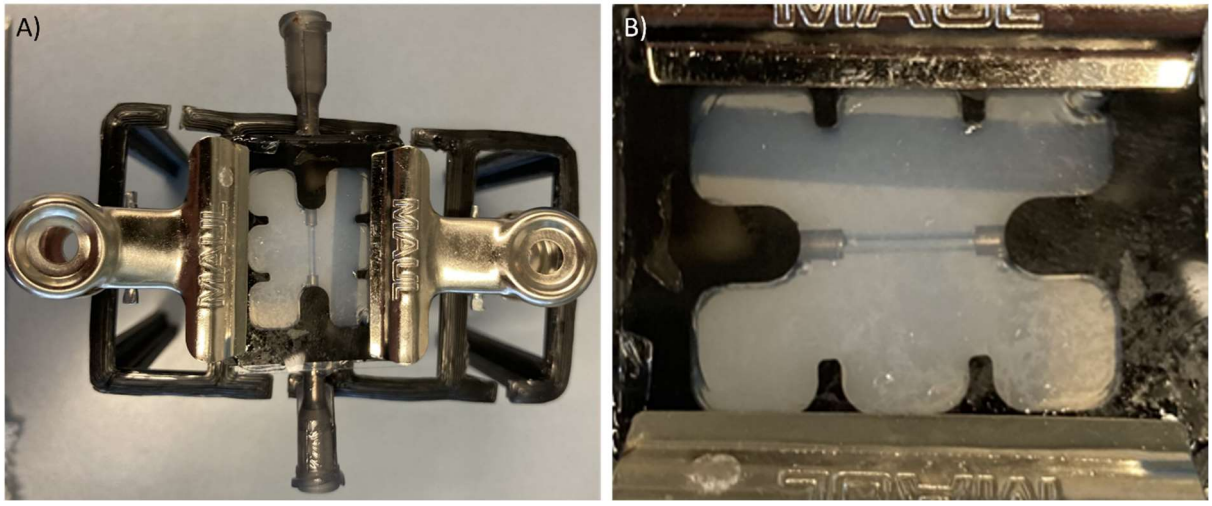

Figure 3.6: ***3D-Hydrogel Channel as a Blood Vessel Model.*** *A) The housing consists of a plastic frame and glass slides that are held together with clamps. Two needles are inserted at the ends that connect to the 3D channel. B) The channel is approximately 1 mm in diameter.*

Preparation of the FITC-Dextran Solution

4. A solution containing 20 ml of FITC-dextran at a concentration of 5 µM in DPBS was prepared inside a 50 ml Centrifuge tube, with the option of using either 4 kDa or 10 kDa dextran size.
5. The tube was wrapped with tin foil to prevent photobleaching.
6. The solution was used the same day. 30 minutes before the experiment, the solution was again put in an ultrasonic bath at 37°C.

Preparation of the Experimental Setup

All steps were performed with very low and indirect light, to minimize photobleaching of the FITC-dextran.

1. 20 ml of the FITC-dextran solution was filled into a syringe and a 1 m tube with an inner diameter of 1.6 mm was connected to the syringe.
2. The syringe was placed in a syringe pump, and a flow rate of 50 µl/min was set.
3. A stage incubator was pre heated to 37°C.
4. The chamber was disconnected from the pump system and quickly put on the microscope stage and connected to the syringe tube. It was made sure that no air bubbles were brought into the channels and that the flow has the same direction as in the cultivation.
5. Another tube was connected to the other end of the channel slide and lead into a collection container.
6. The image was adjusted so that the center of the channel aligned with the bottom edge of the image. The focus was adjusted so that the center of the channel wall towards the gel was visible.
7. An image in the phase contrast was taken. The microscope shutter was closed and the FITC filter set.

Execution of the Experiment

1. The syringe pump was started and as soon as the FITC-dextran solution filled the channel a timer was started.
2. For 40 minutes every 300 s, a fluorescence image of the channel in the FITC fluorescence channel was taken. The shutter was only opened for 1 s to prevent bleaching, before taking the image.
3. The Z-focus was readjusted if needed.

Z-Scans to Verify the Adhesion of Cells

To verify if the cells adhered to the channel surface, the cells were stained with Hoechst 33342 and imaged with the Zeiss Axiovert 200M microscope at a magnification of 10x. 200 µl Hoechst 33342 dye was diluted in 2 ml medium and pumped into a fully cultivated channel. Images of different z-regions were taken in the DAPI channel in the middle of the channel.

3.8. Cell-Cell-Contact Staining Experiments

VE-cadherin antibodies conjugated with the fluorescent dye Alexa Fluor™ 674 were used label VE-cadherin proteins of the cell-cell contact in dependance of an existing glycocalyx and the cultivation method of the cells. After the cells were split, a set of dynamically, statically and shed specimen from the same source were cultured in 400 µm channels slides. To avoid a dry flow channel between the labeling steps, the liquid exchange is performed by rinsing three times with 100 µl each of the new reagent. This corresponds to three times the volume of the channel. A Zeiss Axio Observer 7 featuring an objective with 63x magnification was used to take images.

Staining the Cells

1. The channels were rinsed with DPBS.
2. The cells were fixed with 4% paraformaldehyde solution in DPBS for 10 minutes at room temperature.
3. The channels were rinsed with DPBS again.
4. The cells were permeabilized with a 0.2% Triton-X-100 solution in DPBS for 10 minutes at room temperature.
5. The channels were rinsed with DPBS again.
6. The nonspecific bindings were blocked with a 1% Bovine Serum Albumin (BSA)-solution in DPBS for 60 minutes at room temperature.
7. The channels were rinsed with DPBS again.
8. The cell contacts were marked with VE-Cadherin antibodies that were diluted to a concentration of 0.5% in the 1% BSA-DPBS-solution for 12 hours at 4°C.
9. The channels were rinsed with 2 ml DPBS.

Preparation of the Experimental Setup

1. The channel slide was put on the microscope stage.
2. The cells were located with the 10x magnification in phase contrast mode.
3. The Alexa Fluor 674 fluorescence filter was used.
4. The exposure time as set to 500 ms at an intensity of 20%.

Execution of the Experiment

10 images per slide of the cell-cell-contacts were taken with a 63x magnification in different positions of the channel.

4. RESULTS AND DISCUSSION

In the subsequent Chapter the questions and hypothesis of the first Chapter will be revisited. It will be explored whether various cellular transport processes are significantly influenced by the presence of an intact glycocalyx and by the dynamic or static culture conditions.

Firstly, it will be analyzed whether a sufficient growth of an intact glycocalyx could be achieved using the dynamic culture method compared to static culture. Additionally, it will be investigated whether the degradation and shedding of the glycocalyx occurred upon cessation of shear flow.

Following the investigation into glycocalyx growth and shedding under dynamic and static culture conditions, the subsequent analysis will focus on measuring the change in the phase state of the membrane. This aims to determine whether the cultivation method influences membrane properties and whether the presence or shedding of the glycocalyx induces alterations. Understanding these membrane dynamics is crucial to understand their potential impact on the cellular uptake mechanisms and trans endothelial transport.

Next, the analysis will focus onto the adhesion of vesicles, made from positively and uncharged lipids, on endothelial cells, investigating the influence of an intact glycocalyx and the cultivation method on adhesion forces. This examination seeks to discern whether adhesion dynamics are affected by glycocalyx integrity and if adhesion is mainly contingent upon vesicle charge. The findings from this investigation will then be used to further examine the already mentioned uptake mechanics.

Subsequently, the endocytic uptake experiments of nanoparticles and the uptake of dye molecules into HUVEC through the cell membrane via diffusion will be analyzed and compared with the findings discussed above. This comparative analysis aims to identify differences and seek explanations for observed phenomena. By correlating the results from these experiments with the earlier investigations into glycocalyx integrity, membrane phase state, and changes of the adhesive forces, a comprehensive understanding of how these factors collectively influence cellular uptake mechanisms can be achieved.

Eventually, the trans endothelial diffusion of macromolecules to determine how different culture conditions affect the permeability of the endothelial cell layer. Additionally, the changes in cell-cell contacts depending on the culture method, particularly under shedding conditions, will be analyzed. This analysis will focus on the impact of these methods on the integrity and stability of endothelial junctions. By investigating these aspects, the goal is to identify key factors and mechanisms that influence endothelial barrier function and to understand how culture conditions can modulate these processes.

4.1. Cell Segmentation of Microscopy Images

For the analysis of the nanoparticle uptake, the Hoechst 33342 uptake and the lipid vesicle adhesion, the Cellpose 2.0 algorithm was employed. Cellpose is a generalist algorithm for segmenting cells and cell nuclei in images. This deep learning-based algorithm utilizes multilayer neural networks to segment and identify cells across a variety of images, without specializing in just one type of cell or cell shape. Initially trained on a diverse set of images containing over 70,000 segmented objects, Cellpose can effectively segment cells in most cases without the need for custom training on specific image data. However, it is possible to train your own model and contribute data to further improve the algorithm [166][167].

The Cellpose algorithm segments input images and provides masks containing only the detected cell objects. The outcome can be influenced in advance by choosing various parameters, including the average diameter of the objects to be segmented, which can also be determined automatically, as well as the parameters "flow threshold" and "cellprob threshold."

In this study, satisfactory results were achieved by training the algorithm with the images taken in phase contrast. An existing model was selected, and the mask was manually adjusted. Using the "Train New Model" function, a custom model was created and then automatically applied to a second image in the dataset, with the mask manually adjusted again. This process was repeated until Cellpose satisfactorily recognized the cells.

A master script for cell segmentation, primarily developed by David Wörle and Manuel Sirch as part of David Wörle's thesis under the supervision of Manuel Sirch, was utilized for the analysis presented in Chapters 4.3, 4.4, 4.5, and 4.6 (see Appendix A4).

4.2. Verification of the Glycocalyx of HUVEC in Vitro

Verifying the glycocalyx status in these in vitro experiments is essential to distinguish whether the glycocalyx was truly shed or successfully rebuilt, as this differentiation is critical for accurately interpreting the cellular responses and experimental outcomes.

As described in Chapter 3.2, epifluorescence images were captured for all three conditions: static, dynamic, and shedding environments. In this process, the glycocalyx and membrane structures of endothelial cells were stained using WGA-conjugated antibodies and Laurdan, enabling detailed analysis of their fluorescence properties.

To quantitatively compare fluorescence images of endothelial cells cultured under different conditions, a histogram-based analysis is utilized, employing a custom Python script (see Appendix A3) to generate normalized histograms from the fluorescence images. Initially, the images are converted to grayscale, with gray values ranging from 0 to 255, linearly related to the fluorescence intensity of the WGA conjugate. The pixel count for each gray value is normalized to the total pixel count and presented as a percentage frequency distribution.

The following results were obtained in close collaboration with Marina Huber as part of her master's thesis, which was supervised by Manuel Sirch. A publication on this is currently under review [P3].

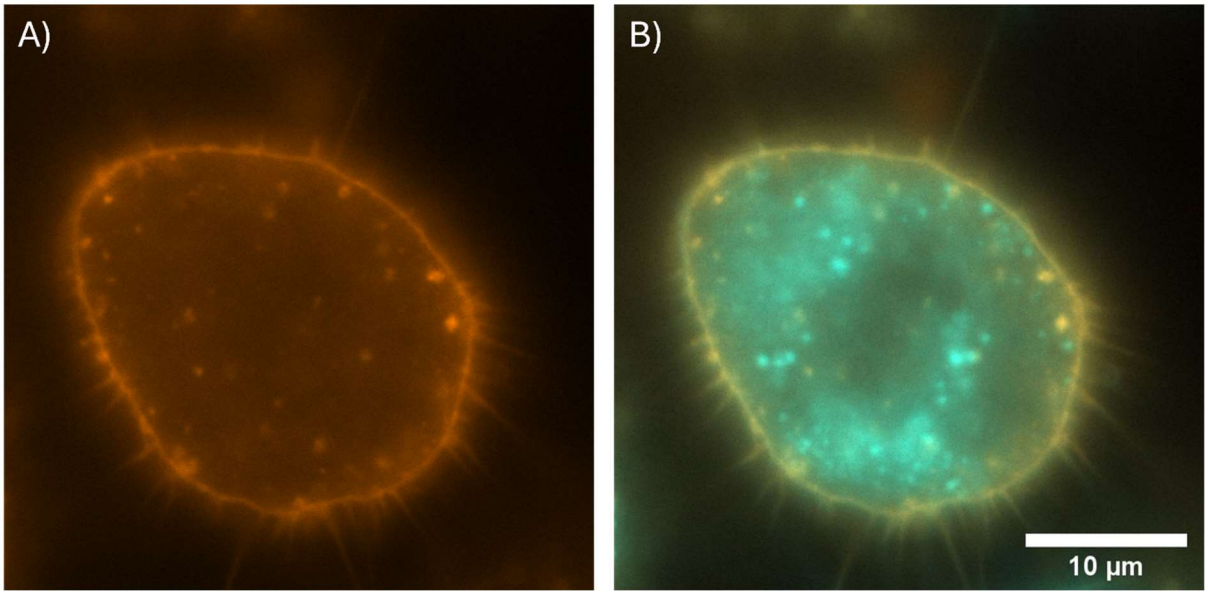

Figure 4.1: ***WGA and Laurdan Staining of an Endothelial Cell.*** *A) Image of a statically cultured HUVEC stained with Alexa Fluor 555-conjugated WGA, showing that even a statically cultured cell possesses a very thin glycocalyx. B) Image of the same cell stained with Laurdan, which integrates into the membrane, and merged with the Alexa Fluor 555 channel. The outlines of the glycocalyx are clearly visible.*

The fluorescence images of dynamically cultured cells are aligned so that the flow direction is to the right. Background fluorescence, which can be measured using images of statically cultured cells or slides coated with collagen but without cells, have to be taken into account. Gray values are assigned based on

representative fluorescence images to identify and classify the various components of the images according to their fluorescence signals. As shown in figure 4.2, gray values from 0 to 30 are attributed to the background, gray values from 30 to 100 represent the labeled glycocalyx of adherent cells, and gray values from 100 to 255 correspond to cells that are detaching, as indicated in previous studies.

The average fluorescence intensity in a histogram is not a suitable method for comparing the fluorescence intensity of the glycocalyx between statically and dynamically cultured cells. This is because, as seen in figure 4.1, even statically cultured cells possess an underdeveloped glycocalyx. Also, the cell-free areas in the statically cultured flow channels could skew the average value.

Therefore, to compare the fluorescence intensities of the glycocalyx, a peak analysis as seen in figure 4.3 is conducted in the region of adherent cells. The peak center represents the most frequent gray value in the region of the adherent cells and thus serves as an appropriate metric for comparing fluorescence intensity and the extent of the glycocalyx.

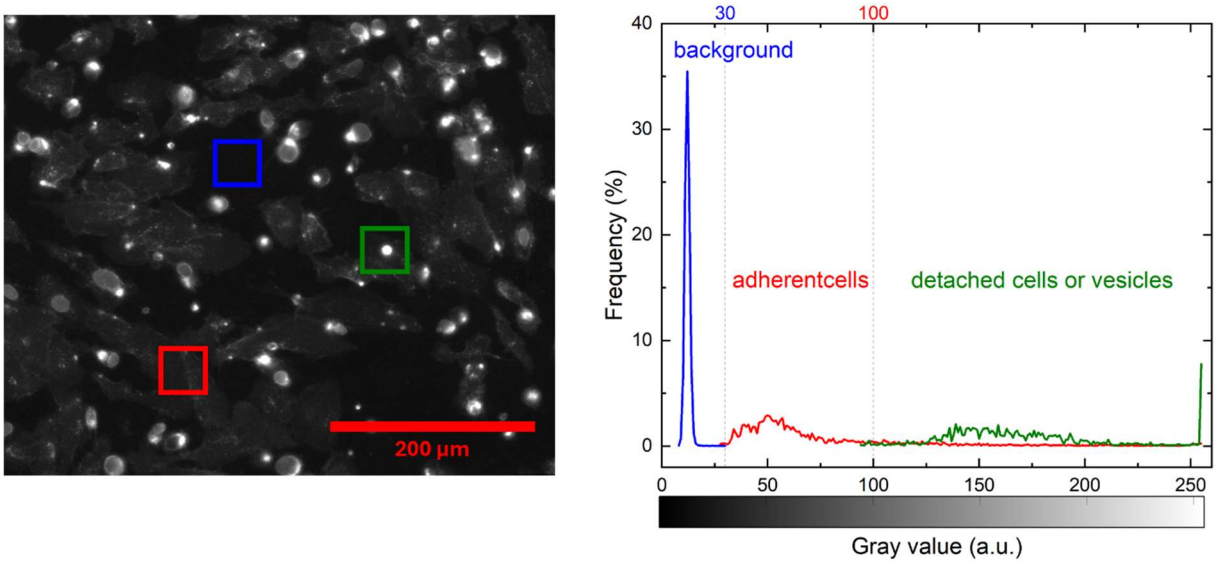

Figure 4.2: ***Exemplary Gray Value Classification of Fluorescence Images for HUVEC Cultured under Static Conditions.*** *Gray values are assigned to representative fluorescence images to identify and classify various image components based on their fluorescence signals. Gray values from 0 to 30 correspond to the background, values from 30 to 100 represent the labeled glycocalyx of adherent cells, and values from 100 to 255 indicate cells that are detaching.*

The Python script shifts the grey values by -30 a.u. and converts the peak values of individual measurements into a histogram. This is achieved by dividing the range of peak values into equal-sized bins. The frequency H_k of values within each bin $[b_k, b_{k+1})$is calculated as:

$$H_k = \sum_{i=1}^{n} \delta(x_i \epsilon\, [b_k, b_{k+1})) \tag{3.1}$$

where x_i are the individual peak values, b_k represents the bin edges, and δ is an indicator function that equals 1 if x_i falls within the bin range, and 0 otherwise. This results in a histogram showing the distribution of peak values as intensities with arbitrary units.

Subsequently, the peak values of the individual measurements for each cultivation method are aggregated, an average value is calculated, and these averages are plotted against each other. Finally, the mean and standard deviation for all measurements under each flow condition were determined and an ANOVA with a Tukey's post-hoc test was performed to assess the significance of differences between conditions.

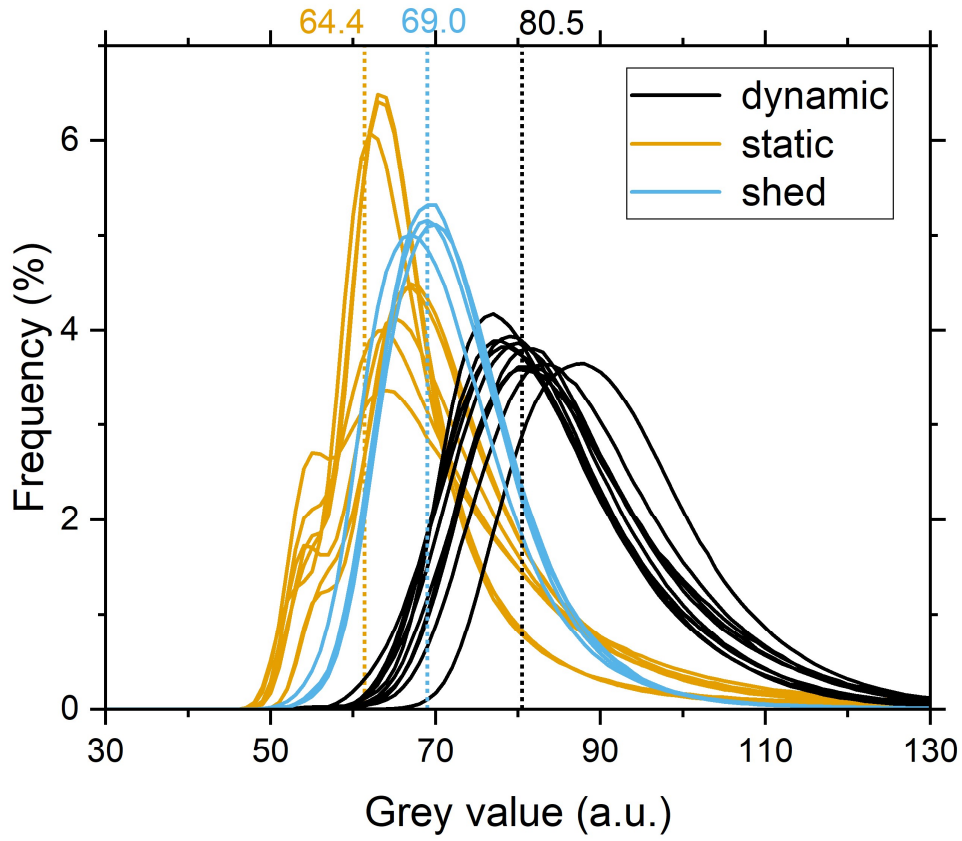

Figure 4.3: ***Peak Center Analysis of WGA Staining.*** *The result reveals mean grey value distributions for different sample conditions: dynamic samples exhibit a mean gray value of approximately 80.5, static samples show a value of 64.4, and samples under shedding conditions have a mean value of 69.0. The staining was performed using Alexa Fluor 555-conjugated WGA. The sample size were N=10 for dynamic conditions, N=8 for static conditions and N=4 for the shedding conditions.*

Figure 4.4 presents a histogram of the Alexa Fluor 555 intensities resulting from WGA staining, showing mean fluorescence values across different cell culture conditions. Dynamically cultured cells exhibited a significantly higher fluorescence intensity (20.5 ± 3.2 a.u.) compared to both statically cultured cells (4.4 ± 1.8 a.u.) and cells under shedding conditions (9.0 ± 1.4 a.u.), with $p<0.001$ for both comparisons. Additionally, a significant difference was observed between statically cultured cells and shed cells ($p<0.01$).

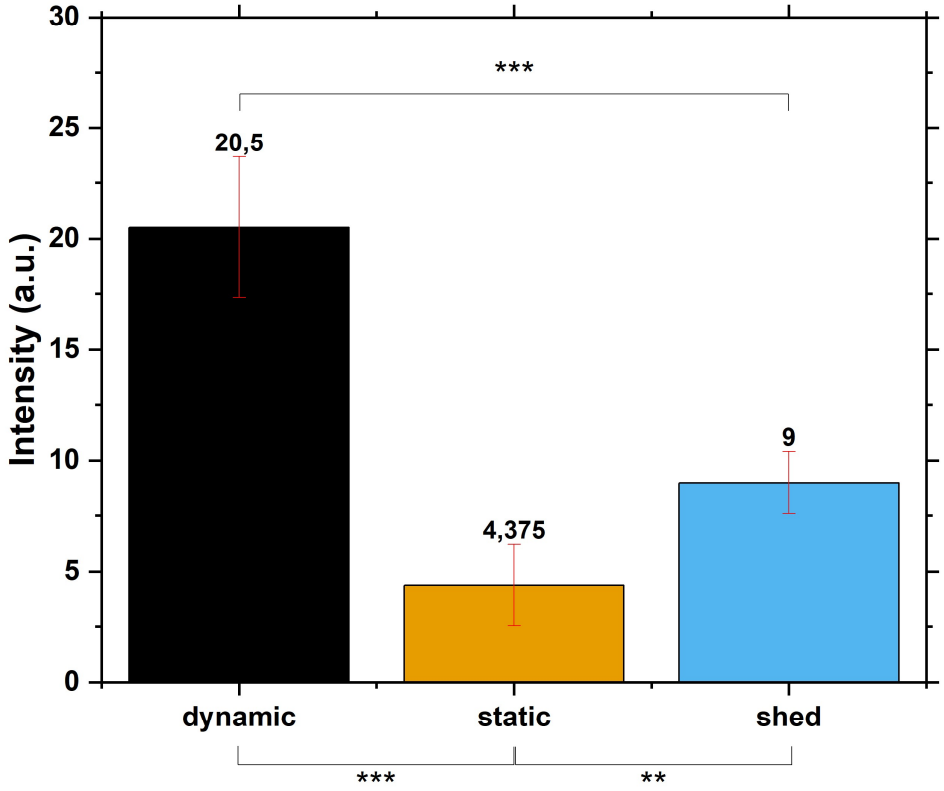

Figure 4.4: ***Mean Intensity Values of the WGA Staining.*** *Dynamically cultured cells exhibit a mean intensity of 20.5, which is significantly higher than that of statically cultured cells (mean intensity of 4.375) and cells under shedding conditions (mean intensity of 9). Additionally, there is a significant difference between the mean intensities of statically cultured cells and those under shedding conditions. Error bars are standard deviation. ***: p<0.001, **: p<0.01.*

To additionally obtain detailed insights into the vertical expression of the glycocalyx, the images of the z-stacks obtained with the confocal microscope were analyzed by extracting and plotting the average fluorescence intensity for each z-position within the stack. Each image in the z-stack, containing approximately 15 cells, was assessed to determine its average fluorescence intensity. To ensure the resulting profiles were comparable, the baseline intensity was subtracted, and the z-position of the peak center was standardized to z = 0.

Figure 4.5 presents exemplary fluorescence images from a z-stack of dynamically cultured HUVEC. It has to be noted, that this has been done with a sample size N = 1 for every cultivation method.

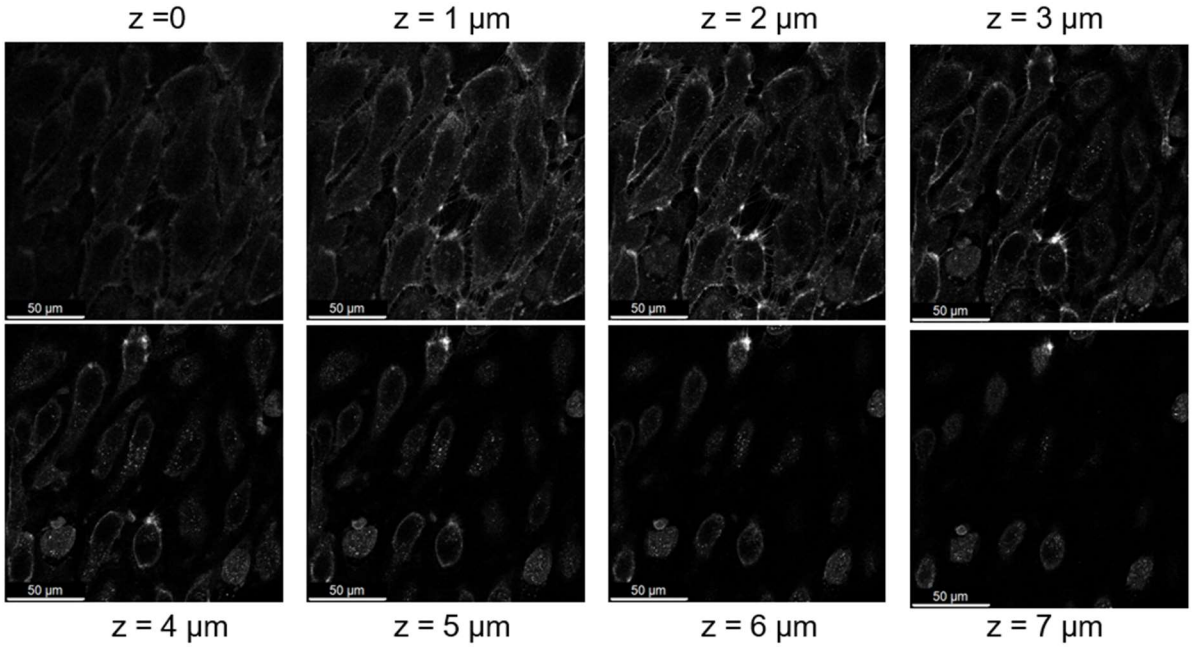

Figure 4.5: ***Confocal Z-Scans of Alexa Fluor 555 Conjugated WGA Staining on HUVEC.*** *Exemplary images from a z-stack captured with a confocal microscope. Every 10th image of the measured z-stack is shown, resulting in the displayed fluorescence images having a vertical distance of 1 µm from each other.*

In Figure 4.6, the vertical profiles of HUVEC cultured under unidirectional flow, with and without shedding, are shown. The profiles exhibit an asymmetric geometry, necessitating a Voigt function fit to determine the Full Width at Half Maximum (FWHM). The FWHM is used to compare the heights of glycocalyx expression, with the standard error of the fit adjustment included for accuracy.

The fluorescence intensity of statically cultured cells is significantly lower than that of dynamically cultured, consistent with the observations from the epifluorescence microscope experiments. Moreover, the FWHM for static culture is 3.31 ± 0.29 µm, while that for dynamic culture is 3.82 ± 0.06 µm. The vertical glycocalyx expression in dynamically cultured cells is 0.51 ± 0.30 µm greater than in statically cultured cells. For the shed specimen, there is a reduction in the vertical glycocalyx expression from 3.82 ± 0.06 µm to 3.58 ± 0.26 µm, supporting the earlier findings.

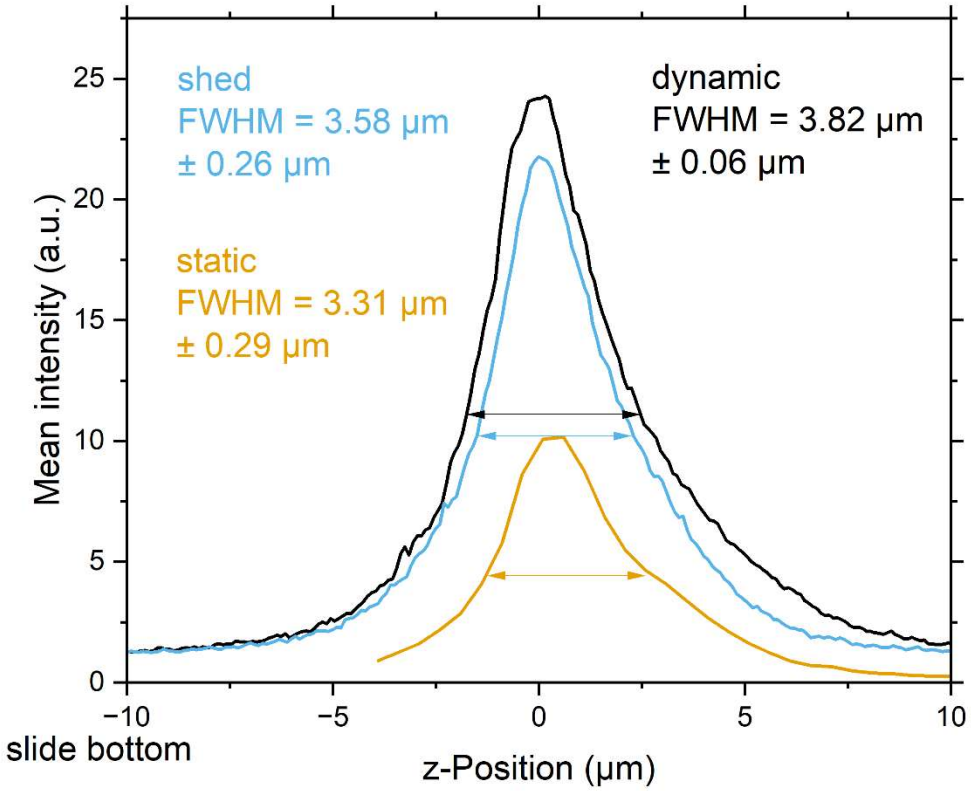

Figure 4.6: ***Vertical Extent of the Glycocalyx Quantified using Alexa Fluor 555 Conjugated WGA.*** *Vertical profiles of the mean fluorescence intensity measured with a confocal microscope, comparing different cultivation conditions: dynamic versus static cultivation, dynamic versus shedding conditions, and unidirectional versus pulsatile flow. The vertical distribution of the glycocalyx is determined by the half-width at half-maximum (HWHM) of a fitted Voigt function. The position of the peak center is normalized to z = 0 for all profiles, with the channel bottom located in the negative z-direction. The sample size was N=1.*

Discussion

The results align with previous studies, which have shown that HUVECs, even under static conditions, can develop a small but detectable glycocalyx. This finding underscores the inherent ability of HUVECs to maintain a minimal glycocalyx structure under non-dynamic conditions [207][208][209].

However, the much higher fluorescence intensity observed in dynamically cultured cells clearly indicates a more robust and well-developed glycocalyx, which is likely due to the shear stress conditions that promote both glycocalyx synthesis and maintenance. The dynamic flow environment evidently plays a crucial role in enhancing the structural integrity and presence of the glycocalyx compared to static conditions.

Furthermore, the significant difference between statically cultured cells and cells that have undergone the shedding process, as well as the sample that was measured during the shedding process, suggest that while the shedding process does reduce the glycocalyx, it does not completely remove it to the level observed in statically cultured cells. The presence of residual fluorescence in shed cells indicates that either the

glycocalyx is not fully shed, or parts of it may have been internalized post-shedding, as some studies on glycocalyx dynamics have suggested.

This residual presence highlights the resilience of the glycocalyx and suggests that a longer shedding period might be required for more thorough removal, or it could imply that certain components of the glycocalyx are more resistant to shedding.

This observation supports the notion that even in the absence of dynamic flow, HUVECs retain a baseline level of glycocalyx. The persistence of some glycocalyx components after shedding indicates that extended shedding periods might be necessary for more complete removal, or it could imply an inherent resistance of some glycocalyx elements to the shedding process.

The FWHM of the glycocalyx after the shedding process is observed to be between the FWHM values of dynamically cultured cells and statically cultured cells. This intermediate FWHM and the results of the histogram-based approach suggests that the glycocalyx undergoes a partial thinning in density as well as a degradation in height as a result of the shedding process.

Overall, the results confirm that cells cultivated under flow conditions in this study exhibit a robust and intact glycocalyx. The hypothesis that HUVEC cultured under dynamic conditions exhibit a higher binding of Alexa Fluor 555-conjugated WGA compared to those cultured under static conditions or subjected to shedding conditions has been confirmed. The question of whether an intact glycocalyx can form under the in vitro culture conditions used in this study can therefore be answered affirmatively.

4.3. Endocytic Nanoparticle Uptake in Dependance of the Culture Condition

Endocytosis is a fundamental cellular process that enables cells to internalize extracellular materials, including nanoparticles, through pathways such as clathrin-mediated endocytosis, caveolae-mediated endocytosis, macropinocytosis, or phagocytosis, depending on the particles' size, shape, and surface properties [111].

50 nm SiO_2 nanoparticles, which are specifically taken up by endothelial cells via endocytosis, were used to investigate whether an intact glycocalyx impacts endocytic processes as explained in Chapter 3.3. Understanding this relationship is crucial for optimizing experimental approaches to quantify cellular uptake under varying culture conditions. The following results were obtained in close collaboration with Serap Demir as part of her bachelor's thesis, supervised by Manuel Sirch. A publication on this is currently under review [P3].

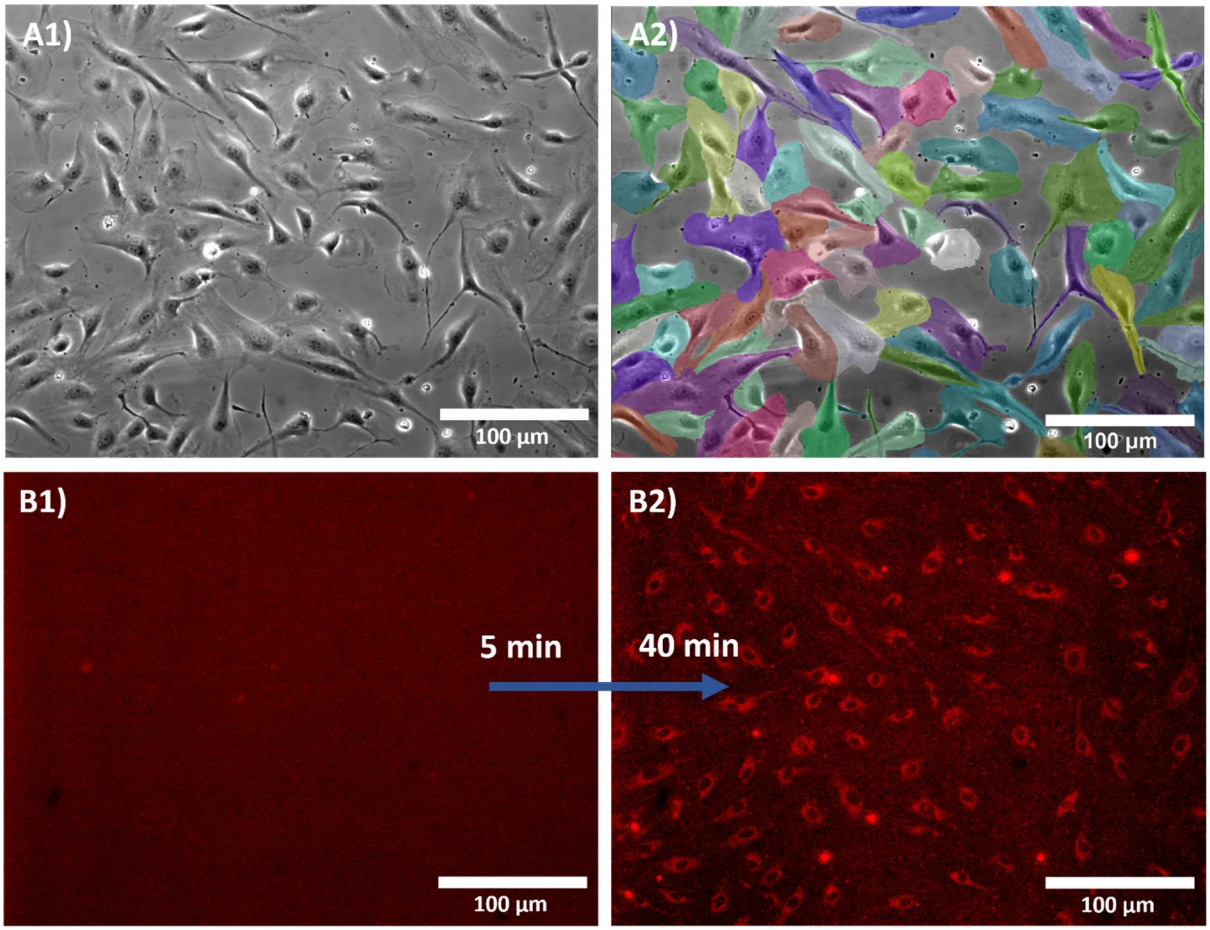

Figure 4.6: ***Method of Nanoparticle Uptake Analysis. A1****) Phase contrast image of cells before the perfusion with nanoparticles. A2) Segmentation of the phase contrast images with Cellpose 2.0. B1) Cells perfused with fluorescent nanoparticles in the Texas Red channel after 5 minutes. B2) Cells perfused with fluorescent nanoparticles in the Texas Red channel after 40 minutes.*

The uptake of nanoparticles into cells was quantitatively analyzed by measuring the increase in the intensity of the Texas Red fluorescence signal over time, which means if more nanoparticles are internalized in a cell, the intensity increases. Hence, again the Cellpose 2.0 algorithm implemented in a Python script (see appendix A4) was employed to identify and segment cells within phase-contrast images captured prior to each measurement as illustrated in figure 4.6A. Subsequently, the intensity of the segmented cell areas was cumulated and divided by the total number of pixels within those segments. Moreover, the mean background intensity of areas outside the segmented cells was subtracted from this calculation. Figure 4.6B illustrates a representative increase in Texas Red channel intensity from 5 minutes to 40 minutes.

Figure 4.7 illustrates the mean absolute intensity of HUVEC over time during the internalization of fluorescent nanoparticles (N=6 per set). Statically cultured cells show a pronounced intensity increase, with a linear fit slope of 0.86 ± 0.03 a.u./min. In contrast, dynamically cultured cells display minimal change, with a linear fit slope of 0.10 ± 0.04 a.u./min and intensity remaining nearly constant. 40 minutes after the addition of the nanoparticles, the intensity in statically cultured cells is nearly four times higher than in dynamically cultured cells. Shed samples exhibit the steepest increase, with a slope of 1.12 ± 0.06 a.u./min and greater variability, particularly between 20 and 40 minutes. Significant differences were observed between all conditions, including dynamic-static (p<0.001), dynamic-shed (p<0.001), and static-shed (p=0.032).

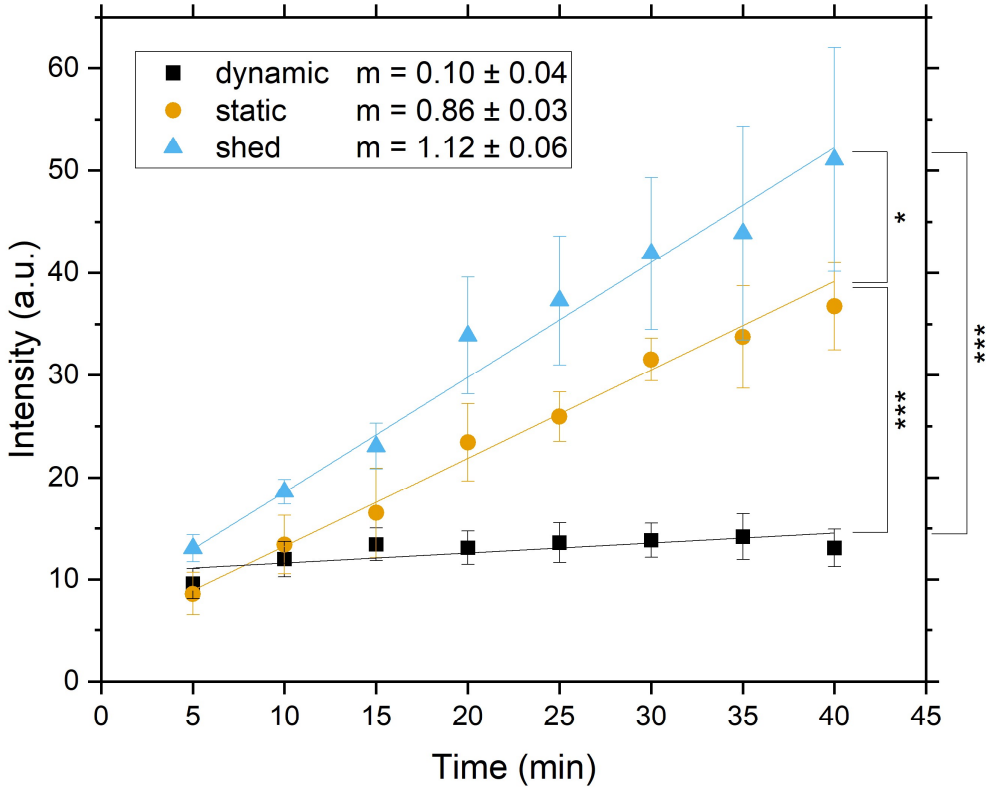

Figur4.7: ***Intensity Kinetics of the Nanoparticle Uptake.*** *Dynamically cultured cells with intact glycocalyx exhibit minimal intensity change, while statically cultured cells without glycocalyx display a consistent increase. Cells with a shed glycocalyx show a slightly steeper slope and a slight offset compared to other conditions. Intensity kinetics of the cells for each culture*

*method over time, demonstrating the rate of nanoparticle internalization. Error bars are standard deviation. ***: p<0.001, **: p<0.01, *: p<0.05. The sample size for each condition was N=6.*

However, this data does not clarify whether the nanoparticles were internalized by the cells or simply adhered to their surface, as the measurements were limited to the intensity of the apical plane. To resolve this, as previously mentioned, confocal microscopy was employed, and z-scans through the cells were performed.

Analysis of the Confocal Microscopy Data

Using the ImageJ plugin "VolumeViewer," a 3D image was constructed from the captured z-stacks. Cross-sections were taken in the xz and yz planes to better assess the position of the nanoparticles. Analysis of the data unveiled that the maximum fluorescent signal emitted by nanoparticles was localized within cellular structures, indicating penetration beyond the plasma membrane. Notably, the size range of the particle signal detected, between 0.5 µm and 1 µm, corresponds well with the height of the cells themselves. This aligns with literature suggesting that HUVEC typically range from 5 µm at the nucleus to 2 µm to 3 µm at non-nuclear regions. Furthermore, the data showed only minimal fluorescence signal around and above the nucleus region. These exploratory measurements, based on a sample size of N=1, confirm that the nanoparticles were indeed internalized into the cells, as evidenced by the localization of the maximum fluorescent signal within cellular structures and below the plasma membrane.

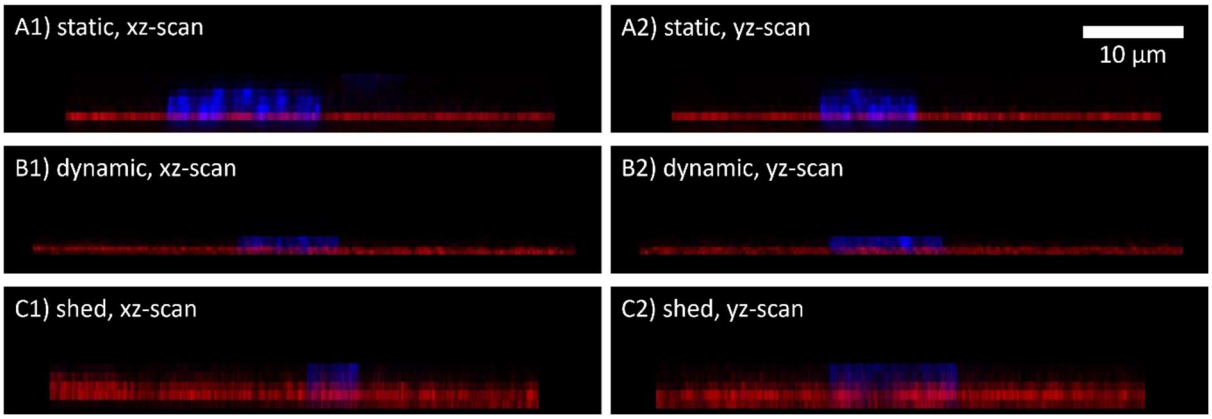

*Figure 4.8: **Confocal Scans of Nanoparticle Uptake.** The fluorescent signal emitted by nanoparticles within cells 40 minutes after addition (red) and the signal emitted from the nucleus (blue). A1 and A2 show scans of a cell cultured under static conditions. B1 and B2 show scans of a cell cultured under dynamic conditions. C1 and C2 show scans of a cell cultured under dynamic conditions with a shed glycocalyx.*

Discussion

The findings reveal consistent patterns in the uptake and permeability of nanoparticles and molecules into endothelial cells. As already mentioned in the theoretical part, endocytosis is characterized as an energy-consuming process for the cell, where the adhesion energy between particles and the cell membrane serves

as the driving factor. Consequently, higher adhesion energy enhances the efficiency of nanoparticle uptake by cells [129][168][169].

Research by Möckl et al. demonstrated that particles with both positive and negative zeta potentials exhibit significantly increased uptake in cells with a degraded glycocalyx [170].

These results, combined with the current findings, suggest that the zeta potential of particles may not be the primary driving factor for adhesion and subsequent uptake. The observation that statically cultured HUVECs also exhibit significantly higher uptake compared to dynamically cultured cells leads to the hypothesis that nanoparticle uptake is inhibited by the additional distance the glycocalyx provides between the cell membrane and the nanoparticle, thereby diminishing adhesion forces. Another possible effect could be that the glycocalyx distance hinders the efficient binding of nanoparticles to membrane structures such as clathrin-coated pits or caveolae, which, as demonstrated by Zimmer & Goepfering, also regulate nanoparticle avidity to cells [171].

However, this does not explain why cells with a degraded glycocalyx exhibit even higher nanoparticle uptake. A possible reason for the enhanced uptake in cells with a shed glycocalyx compared to statically cultured samples could be the alteration in membrane phase state and the consequent changes in membrane mechanical properties. Under flow conditions, not only is the glycocalyx synthesized, but the composition of lipids in the membrane may also be affected by an adaptation process. Yamamoto & Ando showed that endothelial cell membranes cultured under flow conditions have significantly decreased lipid order [172].

Färber et al. reported that membrane transport decreases with low lipid order and increases with high lipid order. This appears to conflict with the observation that cells with a degraded glycocalyx exhibit the highest uptake of nanoparticles [173].

However, in the same study, Färber et al. indicated that higher cell density leads to increased lipid order and, consequently, increased membrane transport. A potential explanation for the increased uptake in cells with a shed glycocalyx could be the higher cell density resulting from morphology changes. When HUVECs are cultured under flow conditions, they assume their characteristic cobblestone structure, which has a much higher density compared to statically cultured cells. However, cellular adaptation may also play a role. Yamamoto & Ando specifically investigated the effects of short-term shear stress [173][174].

Additionally, in a previous study, an increase in membrane transport with increasing lipid order was observed for $GP < 0$, while Yamamoto & Ando showed a decrease in lipid order under shear stress for $GP > 0$. A non-linear relationship between permeability and membrane state, as demonstrated for synthetic vesicles, could also explain these findings [169][172].

Recent research on the same SiO_2 nanoparticles in synthetic lipid vesicles revealed a non-linear uptake behavior related to endocytosis-like uptake, likely associated with the main phase transition and corresponding changes in membrane mechanical properties [175].

The hypothesis that dynamically cultured HUVECs exhibit reduced nanoparticle uptake compared to statically cultured or shedding-condition cells is confirmed, demonstrating that an intact glycocalyx significantly affects nanoparticle uptake in endothelial cells.

This leads directly to the next research objective of whether the observed effect is specific to nanoparticles if it also extends to smaller molecules that are taken up via diffusion through the cell membrane.

4.4. Uptake of Hoechst 33342 through the Cell Membrane

To examine the role of the glycocalyx in regulating membrane permeability, the diffusion of Hoechst 33342 dye through the cell membrane was analyzed as described in Chapter 3.4, under the three different culture conditions: static, dynamic and shedding. These findings are compared to prior observations involving nanoparticle interactions, evaluating whether the glycocalyx serves as a general barrier to diffusion across the cell membrane. A publication on this is currently under review [P3].

Figure 4.9 shows the exemplary increase of intensity in the nuclei over time. The images were processed similarly to the nanoparticle uptake experiments. In this case, only the nuclei were segmented using Cellpose 2.0. The intensity was determined by summarizing and averaging the grey values per pixel within the segmented nuclei areas. Background correction was not necessary for this analysis, allowing for a straightforward and accurate quantification of the fluorescence intensity specifically within the nuclear regions.

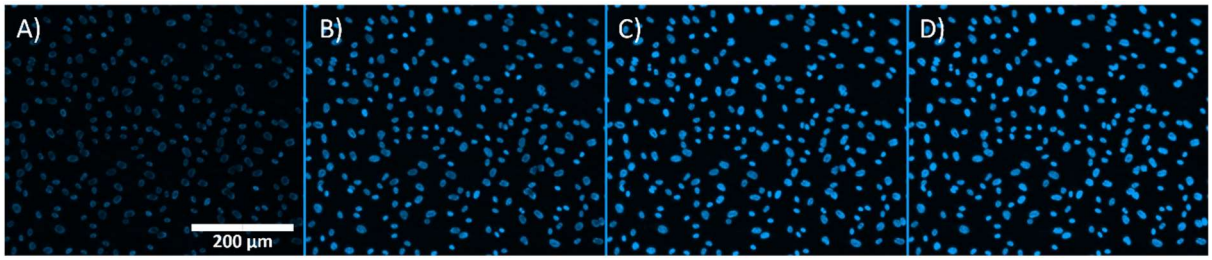

Figure 4.9: ***Intensity Increase in the Nuclei over Time due to Hoechst 33342 Uptake.*** *Panels A to D show the same cells at 10, 20, 30, and 40 minutes after addition of the Hoechst 33342 dye, respectively.*

The values from each dataset, processed using the Python script (see Appendix A4), were aggregated to calculate the mean values and standard deviations, which were plotted in Figure 4.10 to depict the diffusion kinetics of Hoechst 33342 into HUVEC over time. An ANOVA with Tukey post hoc analysis was performed to identify significant differences between the groups. Additionally, the intensity kinetic of the data sets were fitted with the equation

$$I(t) = A_0 * \left[1 - \exp\left(-\frac{t - t_0}{\tau}\right)\right] + y_0 \tag{3.2}$$

which describes a model for exponential saturation. Here, A_0 represents the amplitude, which represents the difference between the initial and the asymptotic value of the function. The parameter t_0 is a time offset that shifts the curve along the time axis and represents the time at which the exponential process effectively starts. The time constant τ determines the rate at which the function approaches its asymptotic value and is a measure of how quickly the exponential term decays. The larger the τ, the slower the approach to the asymptotic value. The offset y_0 represents the initial value of the function at $t = t_0$. For the fits of these curves, the offsets were set to $t_0 = 1.5$ min and $y_0 = 0$, for which they converge best.

The intensity of dynamically cultured cells consistently remains lower than that of cells under static and shedding conditions. While statically cultured cells and cells under the shedding condition exhibit similar intensity values 5 and 10 minutes after the addition of the dye, the intensity of cells under the shedding

condition increases thereafter. Significant differences are observed between dynamic and static conditions ($p<0.001$) as well as between dynamic and shedding conditions ($p<0.001$), with no significant difference for the comparison of cells cultured under static conditions and shedding conditions ($p = 1$).

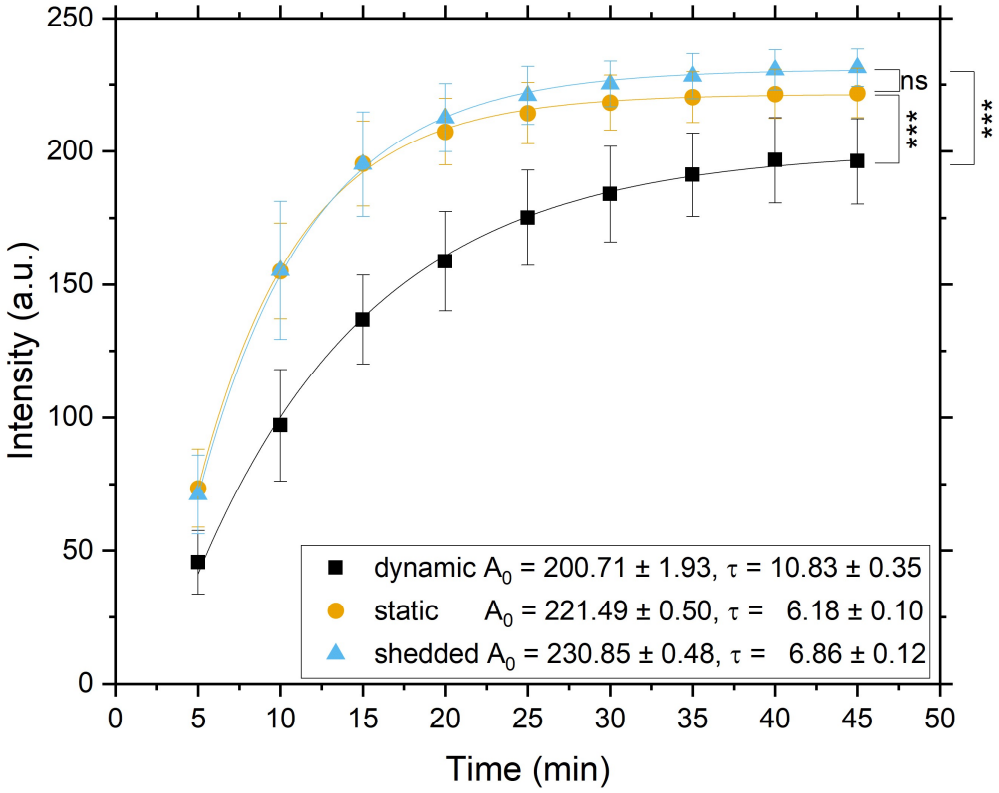

Figure 4.10: ***Hoechst 33342 Uptake Kinetics.*** *Dynamically cultured cells exhibit the lowest uptake, which is significantly lower compared to both statically cultured cells and cells under shedding conditions. No significant difference is observed between the static and shed conditions. The data have been fitted with an exponential saturation model, where A_0 represents the amplitude and τ is the decay parameter. Error bars are standard deviation. ***: p<0.001, **: p<0.01, *: p<0.05. The sample size for each culture condition was N=5.*

For dynamically cultured cells, the values $A_0 = 200.71$ a.u. and $\tau = 1083$ min indicate a slower approach to saturation and a lower intensity uptake of the dye. In statically cultured cells, the values $A_0 = 221.49$ a.u. and $\tau = 6.18$ min suggest a more rapid and higher intensity uptake compared to dynamic conditions. Cells with a degraded glycocalyx show the highest amplitude $A_0 = 230.85$ a.u. and a moderate time constant $\tau = 6.86$ min, reflecting both a rapid and elevated intensity uptake of Hoechst 33342 dye.

Discussion

The dynamic culture method utilized in the experiments apparently provides a significant barrier, effectively impeding the uptake of Hoechst 33342 molecules into the cells. This phenomenon may stem from various potential mechanisms.

Firstly, the glycocalyx may create a spatial hindrance between the cell membrane and the surrounding environment. Given that Hoechst 33342 dye molecules have a molecular weight of 561.93 g/mol, they may encounter difficulty penetrating this dense and complex structure. This hindrance impedes their access to the cell membrane and interior, consequently delaying their uptake by the cells.

Moreover, the glycocalyx often carries a net negative charge due to the presence of sialic acid residues in its composition. In contrast, Hoechst 33342 is generally considered to be a cationic dye. It contains several nitrogen atoms that can be protonated under physiological conditions, contributing to its overall positive charge. The electrostatic interaction between the positively charged Hoechst 33342 molecules and the negatively charged glycocalyx could further hinder their penetration. This electrostatic repulsion may divert the Hoechst 33342 molecules away from the cell membrane, reducing their likelihood of entering the cells [176].

Additionally, it's plausible that when a certain amount of positively charged molecules, are attracted by the glycocalyx, they contribute to an electrostatic shielding effect against further positively charged molecules. This shielding effect could limit the penetration of Hoechst 33342 molecules into the cells, as they are repelled by the accumulated positive charge at the glycocalyx interface [177].

However, given that no significant difference in Hoechst 33342 uptake was found between shed samples and those cultured under dynamic flow conditions, it is more likely that this effect is related to membrane changes induced by shear flow during cultivation. Culturing cells under shear flow conditions can, as already mentioned, lead to various adaptations in membrane composition and structure, which can affect membrane permeability and transport properties.

The observed differences between shed and static specimens might be explained by changes in the membrane phase state. Under flow conditions, not only is the glycocalyx synthesized, but the lipid composition of the membrane can also be altered through adaptation. It can be argued, as in the discussion of nanoparticle uptake, that the findings by Yamamoto and Ando, showing decreased lipid order in endothelial cell membranes under flow conditions, can be reconciled with Färber et al.'s observation that while lower lipid order typically reduces membrane transport, the associated increase in cell density under these conditions can actually enhance transport, thereby explaining the higher dye molecule uptake in shed samples [172][173].

A broader perspective on membrane permeability can be gained by considering the biophysical properties of lipid bilayers under specific conditions. As Blicher demonstrated with artificial membranes, the permeability of lipid membranes to dyes and ions increases significantly near the chain melting regime, characterized by a transition from a solid-like to a more fluid state in the lipid bilayer. This regime is crucial as it allows the membrane to exhibit behaviors similar to protein channels, such as quantized conductances and specific lifetimes for ion permeation. Mechanical stress on the membrane can also modulate its permeability. The collective understanding of lipid membrane permeation suggests that it is fundamentally linked to lateral area fluctuations within the membrane. This insight raises the possibility that some quantized current events, traditionally attributed solely to protein channels, might also be due to lipid channels, particularly in biological membranes, which often exist near their melting transitions. While the phenomenon plays a direct role in the uptake of Hoechst 33342, it may also indirectly influence nanoparticle uptake due to the necessity of pore formation during endocytosis [97][142][178].

Overall, the results confirm that cells cultured under dynamic conditions exhibit a significant barrier to the diffusion of Hoechst 33342 dye, consistent with the presence of a robust and intact glycocalyx. The hypothesis that HUVEC cultured under dynamic conditions impede the diffusion of dye molecules into the cells compared to statically cultured cells or cells under the shedding condition has been validated. The question of whether an intact glycocalyx affects the uptake of molecules by diffusion through the cell membrane into endothelial cells can therefore be answered affirmatively.

This leads directly to the next two research objectives: investigating the impact of culture conditions on membrane order and evaluating the extent to which electrostatic charge influences adhesion and uptake processes.

4.5. Phase State of Endothelial Cell Membranes as Function of Culture Conditions

The lipid components of the cellular membrane, particularly phospholipids and cholesterol, play a central role in determining its fluidity, packing, and phase state. Membrane fluidity, which is influenced by lipid composition and environmental factors, may be affected by culturing cells under flow conditions, as this induces changes in lipid organization and glycocalyx integrity. The phase behavior of lipid bilayers—ranging from gel-like to liquid-ordered or liquid-disordered states—is influenced by factors such as lipid composition, temperature, and cholesterol content. Laurdan enables the assessment of these phase states through its spectral shifts and the calculation of GP-values [86][87][100][101].

This section presents results on how culture conditions and glycocalyx integrity impact membrane order and phase behavior, as measured by Laurdan fluorescence, as explained in Chapter 3.5.

The measurements were conducted using HUVEC cultured under the three previously described conditions: dynamic, static, and shedding. The results were obtained in close collaboration with Niklas Kugelmann as part of his bachelor's thesis, supervised by Manuel Sirch.

Additional measurements were performed on HeLa cells to with varying flow velocities and culture duration. The results on these experiments were obtained in close collaboration with Lara Clemen as part of her master's thesis, again, supervised by Manuel Sirch.

Membrane Phase State Change of HUVEC

For each acquired micrograph, 15 cells were selected for analysis, along with three additional regions devoid of cells to determine the background intensity. These selected areas were consistently applied across micrographs taken at different temperatures, ensuring uniformity and minimizing distortion in cell intensity measurements caused by detection errors. The cell and background intensity values were averaged, and the background intensity was subtracted from the cell intensity to calculate the final corrected cell intensity.

This procedure was performed for all images, after which the GP values were calculated. For each of the three different culture conditions, three measurements were obtained from the 440 nm and 490 nm channels in the micrographs, and the GP values were averaged to ensure accurate and representative results.

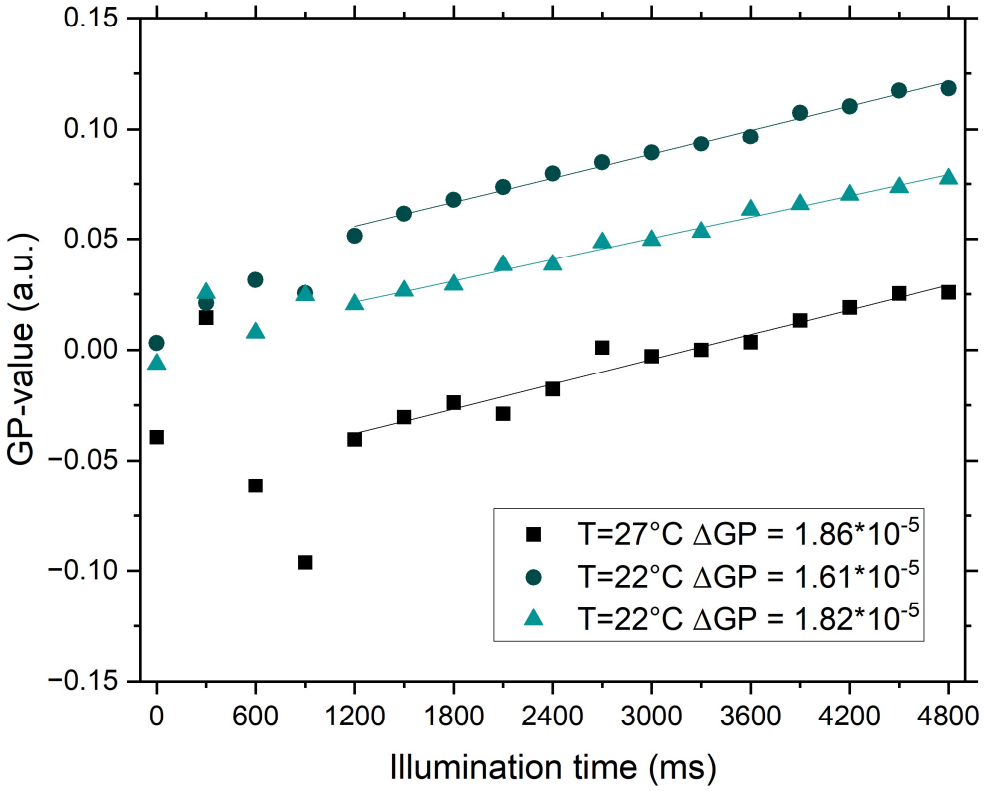

Figure 4.11: ***Laurdan Bleaching Correction for HUVEC.*** *Change in GP value due to Laurdan photobleaching at an exposure time of 300 ms for statically cultured HUVEC. The datasets were linearly fitted, and the mean change in GP value was calculated. The initial data points were identified as artifacts and excluded; only the linearly fittable data was used to calculate the mean change in GP value.*

It is essential to evaluate the bleaching correction, as previously mentioned in the experimental methods section. Figure 4.11 presents the datasets obtained at three constant temperatures, where bleaching correction was performed. The data reveal a linear trend, which has been fitted accordingly. The cumulative change in GP per unit time is calculated as $1.76*10^{-5}$ a.u./ms, equivalent to $5.29*10^{-4}$ a.u. per subsequent image. This value was taken into account for the analysis of the samples with dynamic temperature.

Figure 4.12 displays the calculated GP-values for measurements with HUVECs under different culture conditions. Both dynamic cultivation and cells under shedding conditions exhibit a trend toward slightly higher GP-values. However, the large variability, as indicated by the error bars, and the results of the ANOVA with Tukey post hoc test confirm that no statistically significant differences exist between the groups.

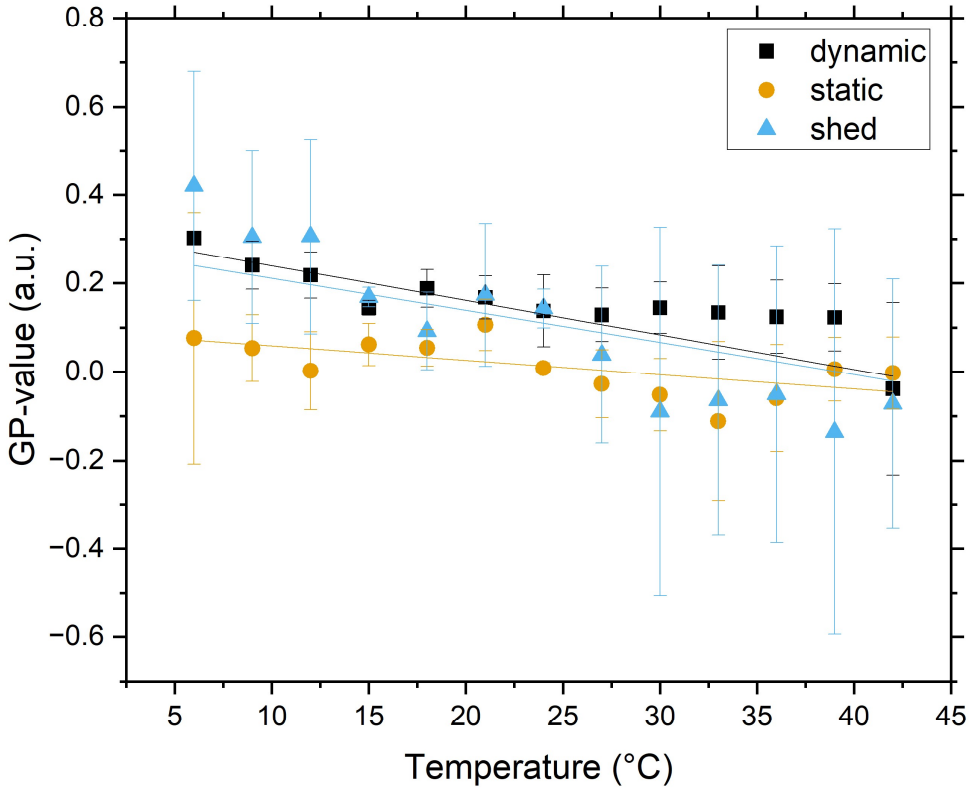

Figure 4.12: ***GP-Values for HUVEC.*** *Calculated GP-values for HUVEC measurements under different culture conditions. Both dynamic cultivation and cells under shedding conditions exhibit a shift toward slightly higher GP-values, but large error bars indicate no significant differences between the groups.*

Membrane Phase State Change of HeLa Cells

Due to the rather unusual or suboptimal results observed in the previous experiments, and to establish a reference point without the presence of glycocalyx, additional experiments were conducted using HeLa cells. These experiments aimed to provide clearer insights and serve as a control for comparison.

Cells in each image were identified using Cellpose 2.0 to create a mask of the cells (see Appendix A4). The fluorescence images with the 490 nm filter were used instead of phase contrast images due to slight drift caused by temperature changes during the measurements. Background intensity was subtracted from the previously determined cell intensities. Background intensity was measured and averaged from three cell-free areas in each image using ImageJ. The difference between cell intensity and background intensity was then used to determine the GP value. The GP value change per image due to bleaching correction averaged at $4.27*10^{-5}$ a.u./ms, which is equivalent to $2.96*10^{-4}$ a.u. per subsequent image (see figure 4.13).

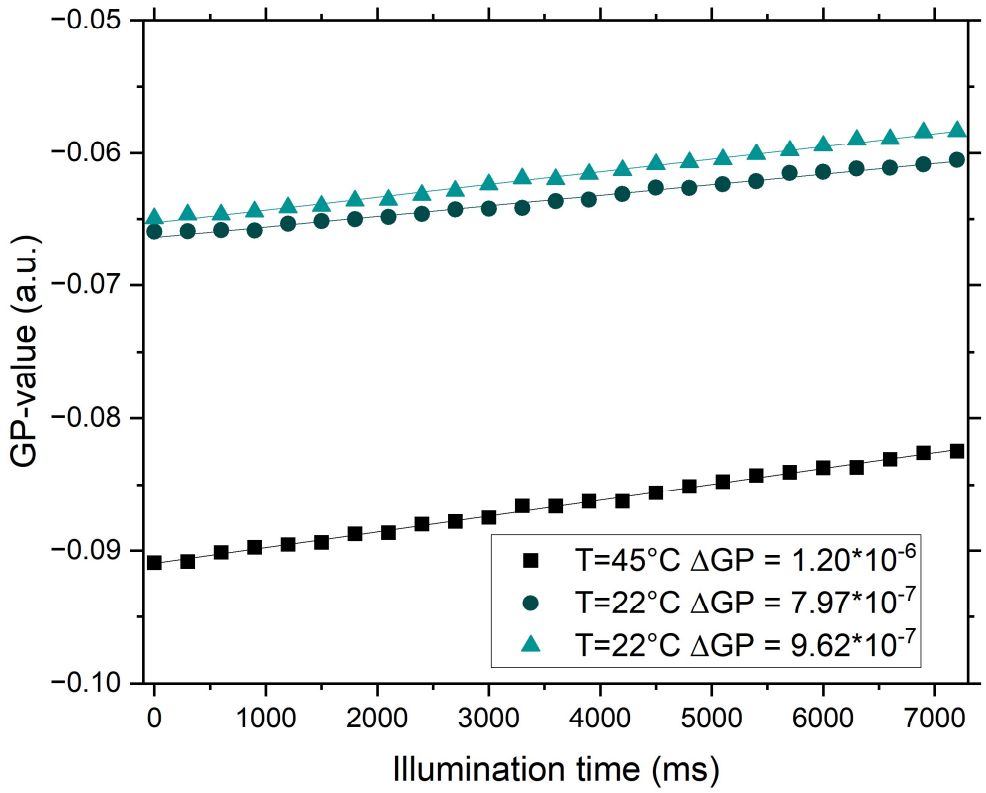

Figure 4.13: ***Laurdan Bleaching Correction for HeLa.*** *Change in GP value due to Laurdan photobleaching at an exposure time of 300 ms for statically cultured HeLa. The datasets were linearly fitted, and the mean change in GP value was calculated.*

Figure 4.14 illustrates the differences in GP values for the temperature range of 15 to 42 °C under various culture conditions for HeLa cells. At a shear stress of 2 dyn/cm², the GP values of statically cultured cells and those cultured under flow for 72 hours and 144 hours are similar. However, at shear stresses of 6 dyn/cm² and 10 dyn/cm², the GP values increase for both 72-hour and 144-hour cultures. For cells cultured at 2 dyn/cm² with a 2-hour flow interruption before the experiment, the GP value for 72-hour cultured cells is lower compared to statically cultured cells and those cultured for 144 hours. Both 72-hour and 144-hour cultured cells with a 2-hour flow interruption exhibit an increase in GP values at 6 dyn/cm². Interestingly, this shift in GP values decreases again at 10 dyn/cm².

For Figure 4.15, only the differences between flow and static conditions were considered, regardless of the duration or shear rate of the culture. Since HeLa cells do not have a glycocalyx, measurements taken under the shed condition or rather after interrupted flow were also included in the dynamic conditions. The results indicate that the linear trendline for dynamic cultivation slopes upwards, although the gradient becomes less steep.

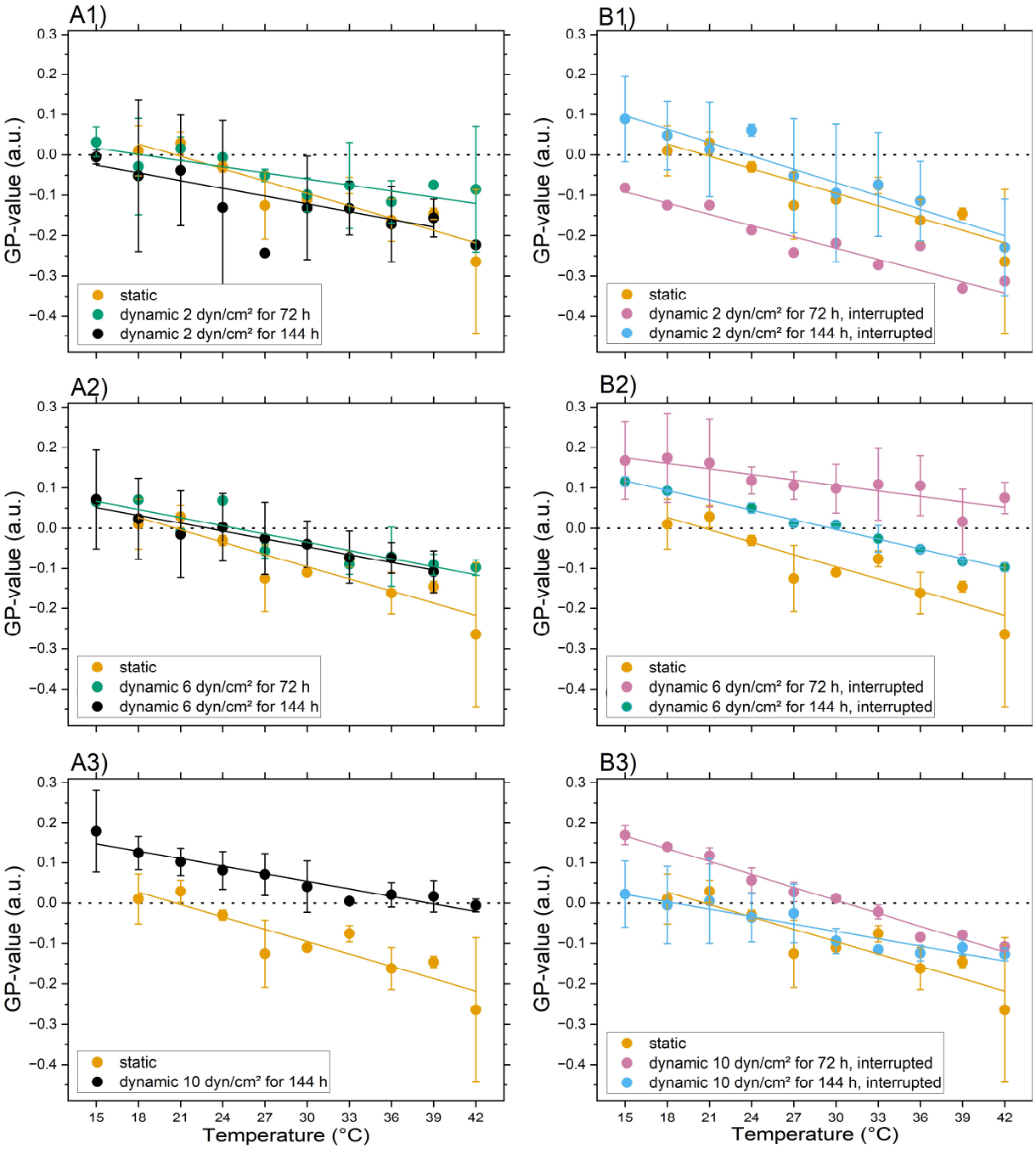

Figure 4.14: ***GP-Values for HeLa Cells.*** *GP-values of HeLa cells under different culture conditions across a temperature range of 15 to 42 °C. The static dataset, consistent across all graphs, provides a baseline for comparison. A1) At 2 dyn/cm² shear stress, GP-value changes are similar between statically cultured cells and those cultured under flow for 72 and 144 hours. A2) & A3) At 6 and 10 dyn/cm², GP values increase slightly for both 72-hour and 144-hour cultures. B1) For cells with a 2-hour flow interruption, GP values decrease at 2 dyn/cm² for 72-hour cultures compared to static and 144-hour culture. B2) & B3) The GP-values increase at 6 dyn/cm², with a subsequent decrease at 10 dyn/cm² for dynamically cultured HeLa after the 2-hour flow interruption.*

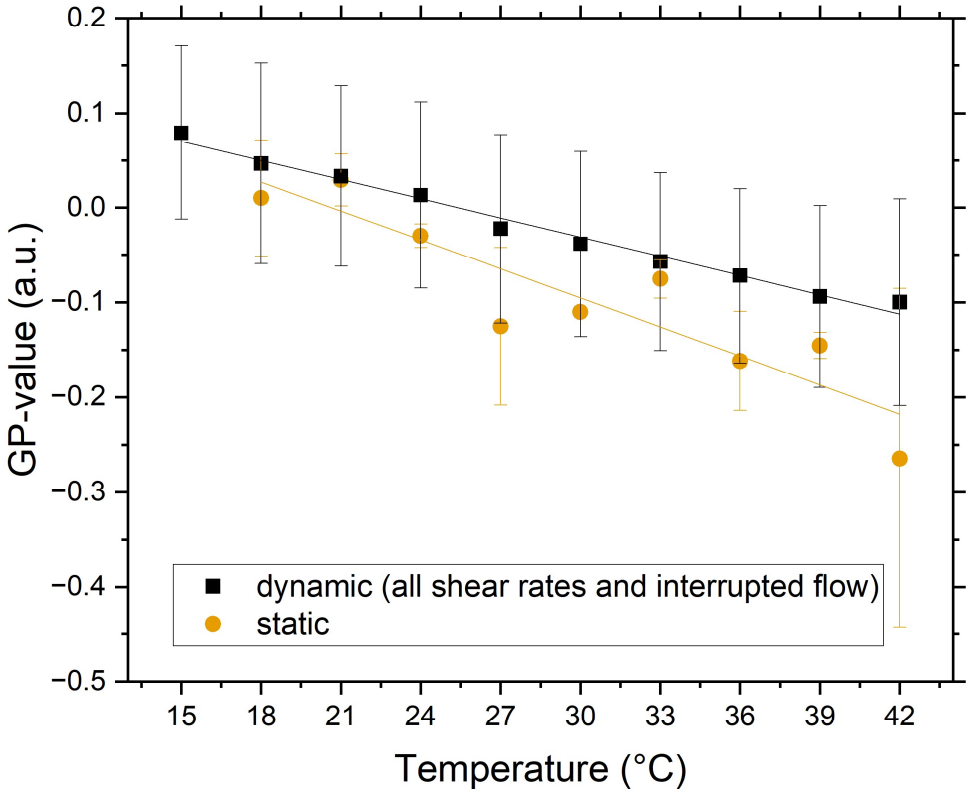

Figure 4.15: ***Summary of GP-Values for HeLa Cells****. Comparing flow versus static conditions, irrespective of culture duration or shear rate. As HeLa cells lack a glycocalyx, measurements taken under shed conditions or after interrupted flow were also categorized as dynamic conditions. The results suggest an upward-sloping linear trendline for dynamic cultivation, with a gradually decreasing gradient.*

Discussion

It is important to note that these observations are based on experiments with considerable variability, and no statistical significance was determined here. The implications and limitations of these findings, including the statistical robustness, are further discussed below.

The experiments with HUVEC reveal a distinct shift toward higher GP values for cells cultured under dynamic conditions, indicating changes in membrane phase states likely due to shear stress. Interestingly, this shift is reversed under shed conditions, where a decrease in GP values is observed, suggesting that the removal of the glycocalyx or interruptions in flow may lead to a more fluid membrane phase. This behavior underscores the sensitivity of HUVEC to mechanical stimuli and the presence of the glycocalyx in maintaining membrane integrity under dynamic conditions.

In the case of HeLa cells, the trend of increasing GP values under dynamic cultivation is also evident, supporting the notion that shear stress can induce changes in membrane phase state. However, the results are inconsistent, particularly when comparing GP values between samples subjected to flow interruptions

and continuous dynamic cultivation. This variability suggests that HeLa cells, which lack a glycocalyx, may not respond as uniformly to shear stress as HUVEC do.

The duration of cultivation (72 hours versus 144 hours) does not appear to significantly influence the GP values; instead, the magnitude of shear stress plays a more critical role. For example, at a shear rate of 10 dyn/cm², the difference in GP values between dynamic and static cultivation becomes most pronounced, particularly in HeLa cells. This finding highlights the importance of shear rate over time in determining membrane phase behavior in cells subjected to dynamic conditions.

Contrarily, these findings conflict with the results of Yamamoto & Ando, as well as older experiments by Butler et al., which demonstrate a decrease in lipid order in response to the application of shear stress Notably, in both studies, the cultivation times and shear stress application durations were significantly shorter compared to the conditions used in the present experiments [172][179][180].

The high standard deviations observed in both HUVEC and HeLa measurements, along with inconsistencies between replicates, make it challenging to draw definitive conclusions regarding the relationship between shear stress, glycocalyx presence, and membrane phase state changes. This variability suggests that additional replicates and more controlled experimental conditions are necessary to gain clearer insights.

The results could not conclusively verify the hypothesis that the cultivation method of HUVEC or HeLa influences the membrane phase state, nor could it determine whether the presence or absence of an intact glycocalyx plays a role. Despite these limitations, the observed trends are intriguing, and these research questions remain highly relevant. Future experiments, designed to reduce variability and address these methodological challenges, are essential to provide a more comprehensive understanding of these effects.

4.6. Role of Surface Charge for Adhesion to Dynamically Cultured Endothelial Cells

Cationic DOTAP vesicles are widely used in transfection to deliver genetic material into cells by forming lipoplexes through electrostatic interactions with nucleic acids. This approach enables efficient nucleic acid delivery into various cell types and is commonly applied in gene therapy research and molecular biology. As MLVs, they closely mimic the characteristics of transfection vesicles and physiologic extracellular vesicles, while as GUVs, they are more representative of cells or circulating tumor cells [210][211][212].

Here, both MLVs and GUVs are used to measure the effects of electrostatics as explained in Chapter 3.6, specifically the impact that the different culture conditions have on these effects due to variations in the glycocalyx or cell membrane.

The adhesion of DOTAP-DMPC (20:80) GUVs and DMPC GUVs to HUVEC was analyzed under static, dynamic, and shedding conditions. In addition, as a preliminary investigation, MLVs were used to study adhesion to HeLa cells under similar conditions as a reference. The results were obtained in close collaboration with David Wörle as part of his bachelor's thesis, supervised by Manuel Sirch. The datasets on HUVEC are associated with a publication that has been accepted but has not yet been published [P2].

DOTAP-MLV Adhesion to HeLa Cells

The MLVs are not detected individually. Instead, the analysis of these measurements is based on the difference in intensity between areas on the slide where cells have adhered and areas where no cells are present. To quantify the adhesion behavior, the change in this intensity difference over the course of the measurement is monitored.

Again, a Python script employing Cellpose 2.0 is used (see Appendix A4) to segment the cells in the phase contrast image, and the resulting masks are saved. The total intensity I_{seg} of all pixels in the fluorescence image that correspond to a pixel inside a segmented mask from the cell layer, as well as the total intensity I_{rest} of the remaining pixels. The intensity difference is normalized by the total intensity I_{total} of all pixels:

$$I = \frac{I_{\mathrm{seg}} - I_{\mathrm{rest}}}{I_{\mathrm{total}}} \tag{3.3}$$

In case of adhesion of the MLVs to the cells, the intensity difference

$$\Delta I = I_2 - I_1 \tag{3.4}$$

will change during the measurement, whereas I_2 and I_1 are the intensities of image 1 and 2. This quantifies the adhesion strength of the MLV to the cell surface.

In this context, comparing different cells is also important. Since the vesicle concentration is assumed to remain constant throughout the measurement, it does not affect the calculation of ΔI and, therefore, does not influence the assessment of adhesion behavior.

For adhesion under flow conditions, the flow velocity was varied. Specifically, the experiments included static conditions with flow velocities of 0.02 µm/min and 0.2 µm/min, as well as dynamic conditions with different culture durations (72 h and 144 h), shear stresses (2 dyn/cm² and 6 dyn/cm²), and flow velocities of 0.02 µm/min and 0.2 µm/min.

The intensity differences for each condition were aggregated to calculate the mean, and the standard deviation was determined. A one-way ANOVA was performed, followed by Tukey's post hoc test to identify significant differences between the groups.

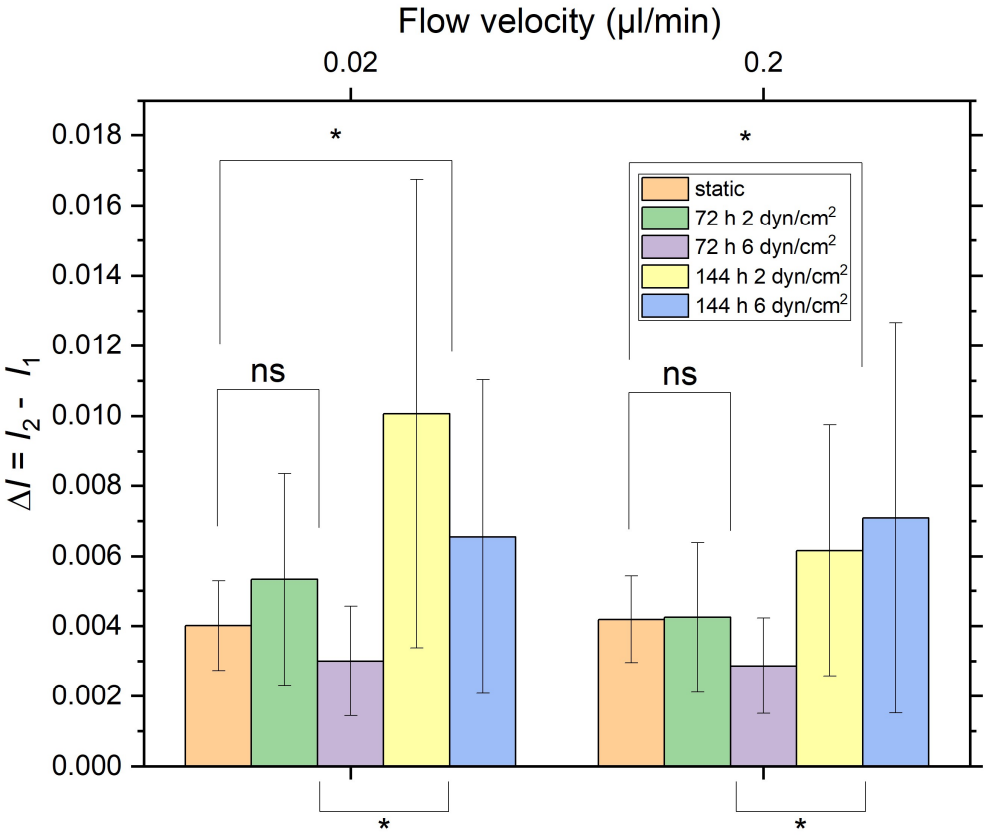

Figure 4.16: ***Adhesion of MLV to HeLa Cells.*** *The datasets of 144 h dynamic cultivation and 72 h dynamic cultivation have been summarized, regardless of the shear stress applied. The 144 h culture shows significantly higher adhesion of MLV in comparison to the 72 h culture samples and static samples. Static samples and 72 h culture samples show no significant difference. Error bars are standard deviation. *: p<0.05, ns: p>0.05. The sample sizes are listed in table 4.1.*

Figure 4.16 shows the results of the MLV adhesion to HeLa cells. Since the results in the lower flow rate range appeared to be more consistent and exhibited smaller deviations between measurements, a larger number of slides were measured in this range.

Table 4.1: Sample Sizes for the Adhesion of MLV to HeLa Cells:

Condition	Culture Duration (h)	Shear Stress (dyn/cm²)	Flow Velocity (µm/min)	Sample Size (N)
Static	-	-	0.02	6
Static	-	-	0.2	6
Dynamic	72	2	0.02	8
Dynamic	72	2	0.2	8
Dynamic	144	2	0.02	4
Dynamic	144	2	0.2	4
Dynamic	72	6	0.02	9
Dynamic	72	6	0.2	9
Dynamic	144	6	0.02	8
Dynamic	144	6	0.2	8

Each value represents the mean and standard deviation, where different samples have been cultivated on different slides, as listed in table 4.1. It can be observed that cells cultured over a longer period tend to show a larger difference in ΔI compared to statically cultured cells and those cultured under flow for a shorter period. However, cells cultured under flow for 72 h show only a slightly larger ΔI compared to static cultures at a flow rate of 2 dyn/cm², and even a smaller value at 6 dyn/cm². The standard deviations, however, are relatively large in this case, particularly for the cells cultured for 144 h.

The results from 72 h and 144 h cultures were grouped together, regardless of the shear stress level. A significant difference was found between the 144 h dynamic culture and the 72 h dynamic culture for both flow velocities ($p<0.05$). Additionally, a significant difference was observed between the 144 h dynamic culture and the static culture ($p<0.05$). However, there was no significant difference between the 72 h dynamic culture and the static culture ($p=0.50$ for 0.02 µl/min and $p=0.29$ for 0.2 µl/min).

GUV Adhesion to HUVEC

A Python script (see Appendix A4) was developed to analyze the adhesion of lipid vesicles by tracking the number of vesicles remaining on the cell layer throughout the measurement. The script's functionalities include utilizing Cellpose 2.0 to find masks and diameters on numerous images, determining the count of individually detectable adherent vesicles or cells, assessing the confluence of a cell lawn, and quantifying the adhesion of vesicles no longer individually detectable based on their intensity.

The script generates objects of a cell class from individual masks, incorporating attributes like position and radius. Position calculation involves computing the mean of all pixel positions within the mask on the image, while a simplified assumption of circular shape aids in radius calculation. These cell objects facilitate position comparison for later detection of adherent objects.

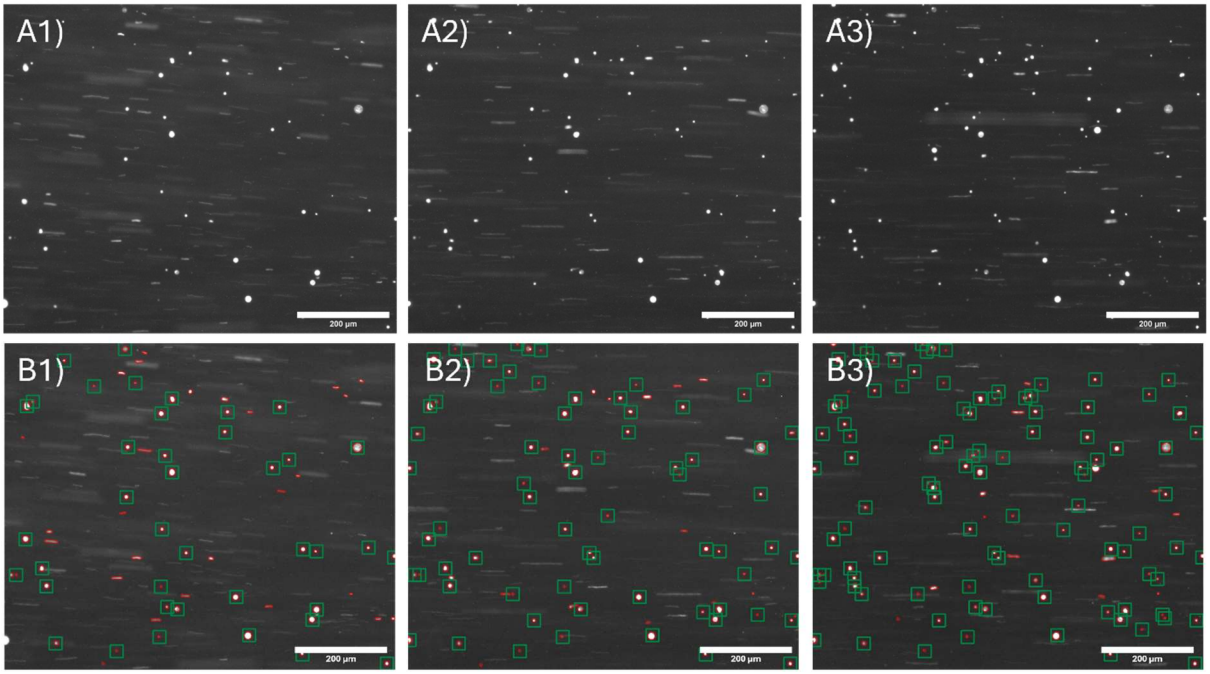

Figure 4.17: ***Fluorescence Image Analysis of Vesicles Adhering to the Cell Surface of HUVEC.*** *A1) – A3) Grayscale images showing fluorescent signals from Texas Red-stained vesicles at 30, 90, and 150 seconds. B1) Vesicle detection using Cellpose 2.0, with red circles highlighting the vesicles identified in the focal plane. B2) Adherent vesicles, defined as those that remained stationary, are marked with green squares. B3) The increasing number of adherent vesicles over time is observed.*

To discern whether a vesicle is moving with the flow or adhering to the cell surface, the script compares vesicle positions across consecutive images as exemplary shown in figure 4.17. A vesicle retains its position if it's detected in the same spot in successive images, allowing for a specified tolerance radius. Adherent vesicles, detected over a defined period, are subclassed and characterized by attributes like the initial detection image and the number of images maintaining that position.

This methodology enables the determination of the total number of adherent GUVs and vesicles per image, alongside the total and per-image count of detected objects. A normalization approach is applied to account for variations in vesicle concentration, yielding the adhesion quotient

$$A = \frac{N_{\mathrm{adh}}}{N_0} \tag{3.5}$$

as a measure of GUV adhesion. The adhesion coefficients from individual measurements for each cultivation method were aggregated, and the mean and standard deviation for all measurements under each flow condition were calculated. An ANOVA with Tukey's post-hoc test was performed to evaluate the significance of differences between the conditions.

In Figure 4.18, the adhesion behavior of both pure DMPC vesicles and 80:20 DMPC-DOTAP vesicles on the HUVEC layer is elucidated. It's necessary to consider the possibility of vesicles adhering to areas without cell growth or to coated surfaces. Only vesicles adhering to the cell lawn are relevant for analysis. Therefore, the phase-contrast image of the cell lawn is used as depicted in figure 4.19A. Only adherent vesicles whose positions align with cell lawn mask pixels are considered for analysis. Vesicles adhering to the edge of a cell are also counted as adherent to the cell lawn, based on their radius.

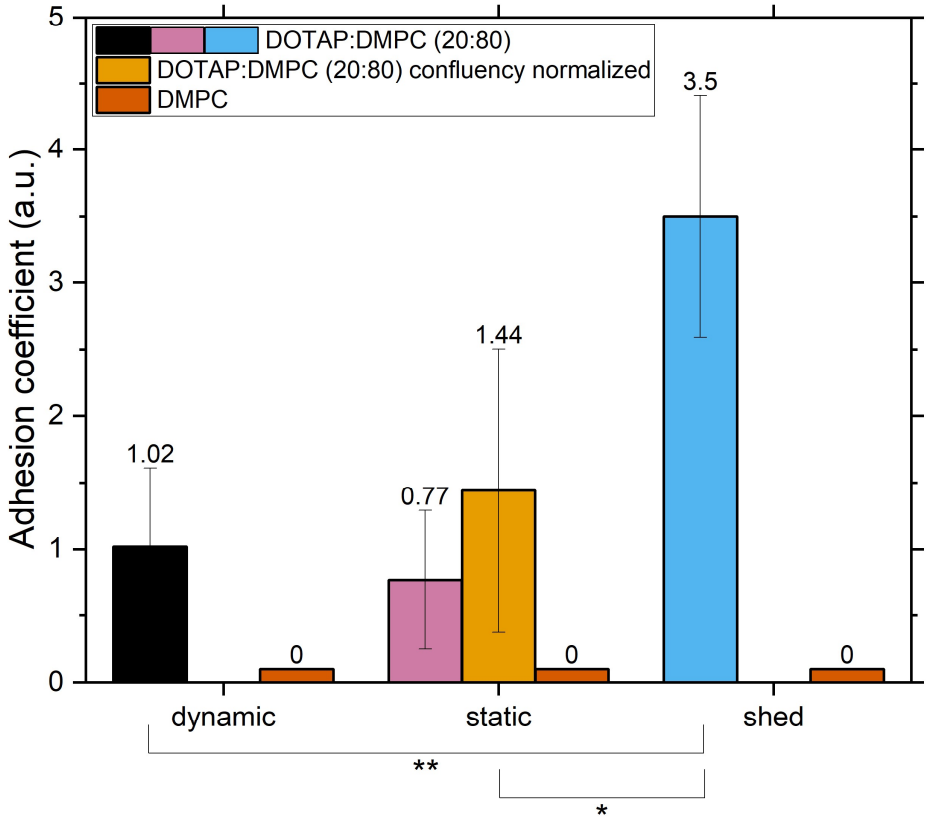

Figure 4.18: ***Adhesion Dynamics of 80:20 DMPC-DOTAP GUVs under different Conditions.*** *The adhesion coefficients for vesicles on statically and dynamically cultured cells ranged from 1 to 1.5, with a p-value of 0.343, indicating no significant difference in adhesive propensity between these two conditions. In contrast, vesicles under shedding conditions exhibited a significantly higher adhesion coefficient, averaging around 3.5, demonstrating robust adherence to the endothelial cell layer. Statistical analysis confirmed a significant difference in adhesion for shed samples compared to both static and dynamic conditions, highlighting the distinct adhesive behavior under shedding conditions. No adhesion has been measured for pure DMPC vesicles. Error bars are standard deviation. The sample size of analyzed slides was N=6 for dynamically cultured cells, N=6 for statically cultured cells and N=4 for cells under the shedding condition. **: p<0.01, *:p<0.05.*

The address the potential reduction in adhesion area in statically cultured cells, the adhesion coefficient was normalized by dividing it by the confluency percentage. Notably, the results depict a stark contrast in adhesion patterns between the two vesicle types under different culturing conditions.

For the pure DMPC vesicles, irrespective of the culturing condition—be it static, dynamic, or shed—no adhesion was observed on the HUVEC layer. This consistent lack of adhesion across varying conditions underscores the inert nature of these vesicles in interacting with the endothelial cell layer.

Conversely, examination of the 80:20 DMPC-DOTAP vesicles reveals nuanced adhesion dynamics. Both statically and dynamically cultivated cells exhibited adhesion coefficients ranging from 0.77 to 1.44, with a p-value of 0.713, suggesting no significant difference between the two conditions. This finding suggests a comparable adhesive propensity of the membranes regardless of the cell culturing environment.

However, shedding conditions elicited a markedly different response. Shed samples displayed a substantially higher adhesion coefficient, averaging around 3.5, indicating a robust adherence of the vesicles to the endothelial cell layer. Statistical analysis revealed a significant difference between HUVEC under the shedding condition and dynamic condition ($p<0.01$) as well as static condition ($p<0.05$).

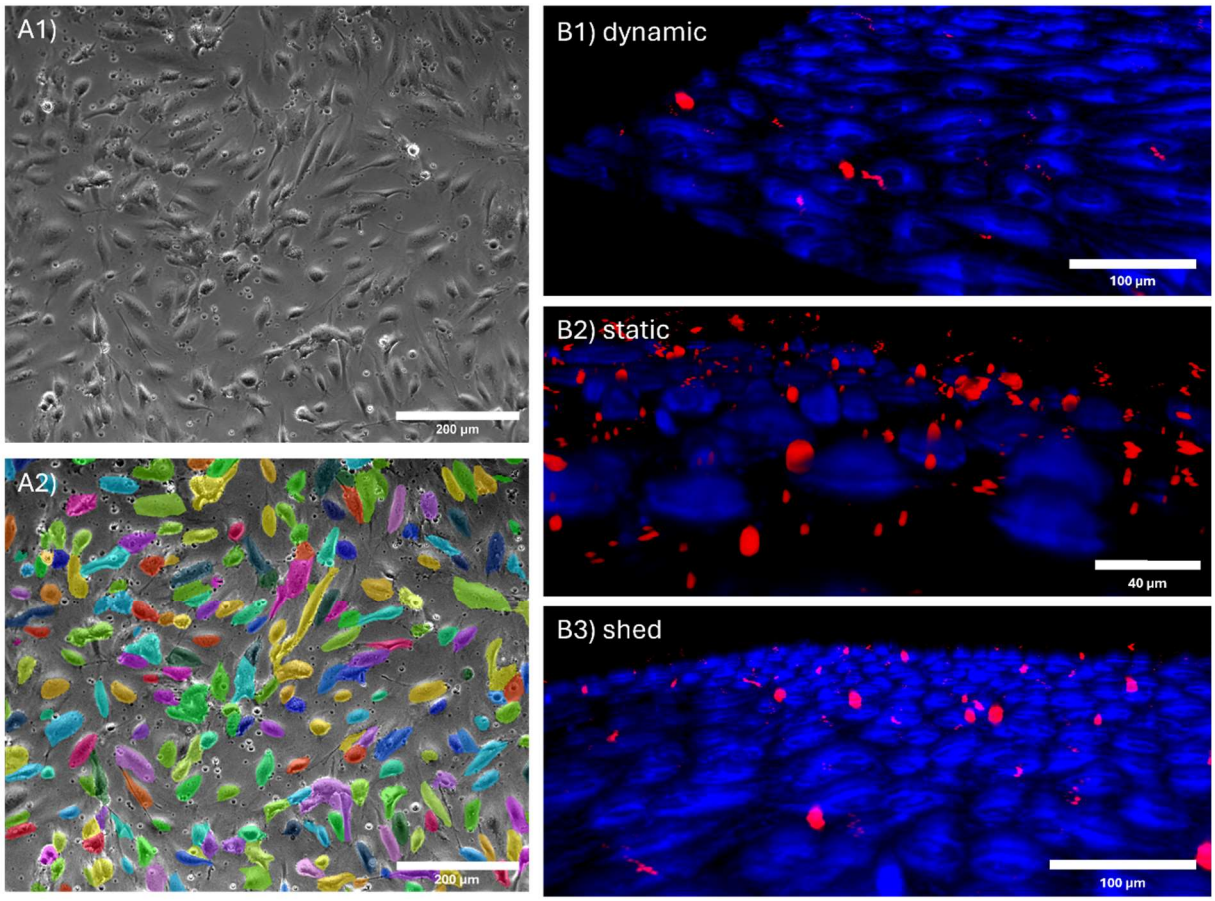

Figure 4.19: ***Phase Contrast and Confocal Image Analysis of HUVEC and Adhering Vesicles.*** *A1) Phase-contrast microscopy of statically cultured HUVEC shows loosely arranged cells lacking the cobblestone morphology of dynamically cultured cells. A2) A Cellpose 2.0 mask highlights intercellular spaces, excluding vesicles outside these regions from adherence counts. B1) Confocal microscopy of dynamically cultured HUVEC (dyed with Laurdan, depicted in blue) shows minimal vesicle adherence (red) to the confluent cell layer. B2) Statically cultured HUVEC show wider gaps, with vesicles adhering in these spaces; however, these are excluded from counts as they are not cell-bound. B3) Dynamically cultured HUVEC under shedding conditions exhibit enhanced GUV binding to a highly confluent layer.*

Confocal data as shown in figure 4.19B reveals a higher number of adhered vesicles compared to previous measurements. However, a closer examination indicates that these vesicles primarily adhere to the bottom of the slide, situated between the cells rather than directly on the cell surfaces. Consequently, they are correctly excluded from the counts of vesicles adhered to the cell surface. Measurements under dynamic and shedding conditions align with previous data, reinforcing the reliability of these observations. Interestingly, the cells seem to preferentially occupy positions at cell-cell contacts, suggesting a potential role of these junctions in influencing cellular positioning and behavior under different culture conditions.

To account for potential size differences among the various types of GUVs, two methods of size determination were employed: a micrograph-based analysis and a cytometric comparison. The data

are presented in Figure 5. The analysis of vesicle size distributions in Figure 4.20A highlights trends between non-adherent and adherent GUVs, as well as between DOTAP-DMPC and pure DMPC GUVs.

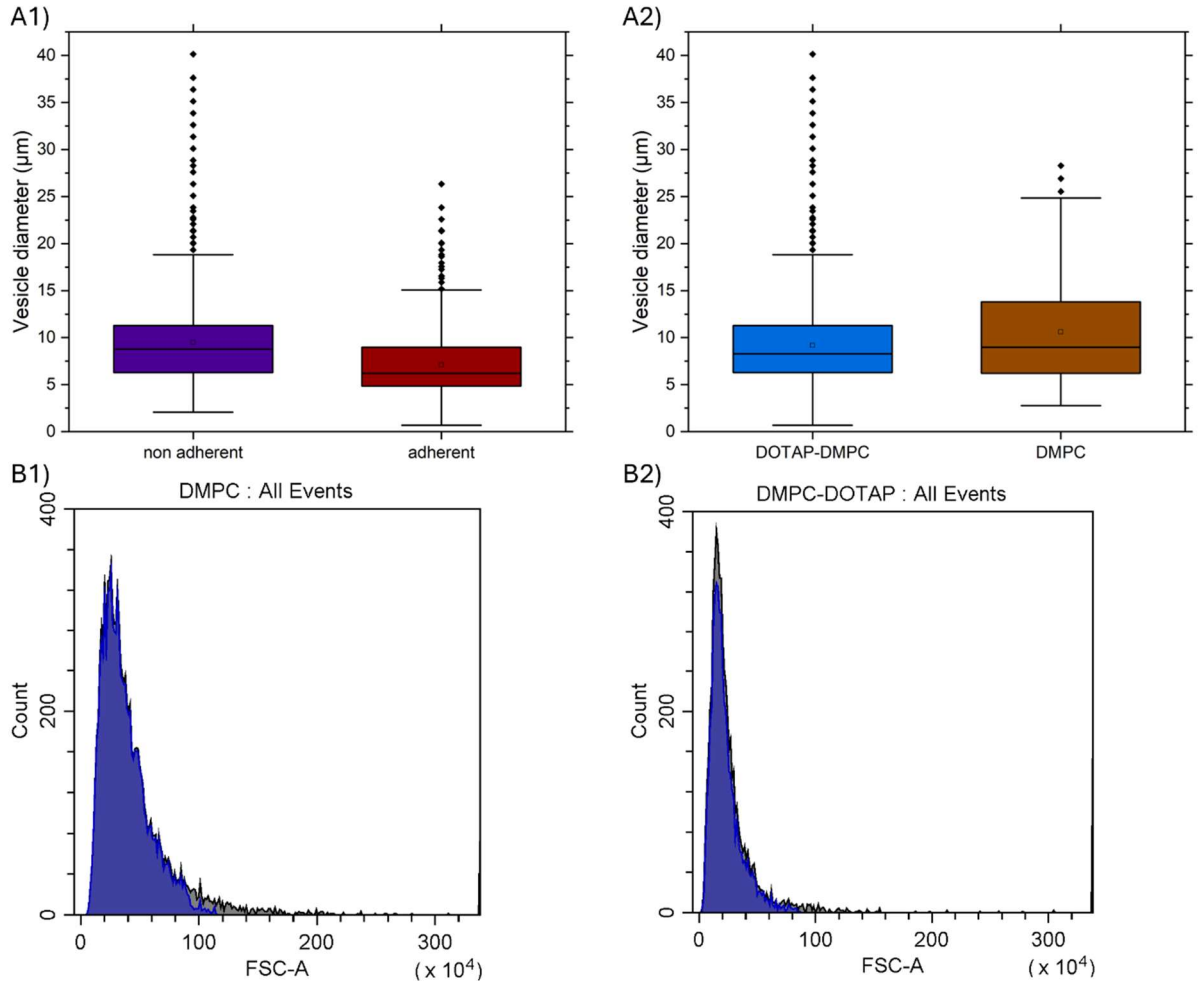

Figure 4.20: ***Boxplots and Histograms of Size Distribution of GUVs.*** *A1) Size distributions of non-adherent and adherent DOTAP-DMPC GUVs. Non-adherent GUVs have a mean diameter of 9.47 ± 4.42 µm and a median of 8.78 µm (N=12,484 vesicles). Adherent GUVs are smaller, with a mean diameter of 7.10 ± 3.78 µm and a median of 6.21 µm (N=1,876 vesicles). A2) Comparison of DOTAP-DMPC and pure DMPC GUVs. DOTAP-DMPC GUVs show a mean diameter of 9.16 ± 4.43 µm and a median of 8.28 µm (N=14,362 vesicles), while pure DMPC GUVs have a larger mean diameter of 10.61 ± 5.39 µm and a median of 8.97 µm (N=381 vesicles). Outliers are represented by dots above the whiskers. B1) FSC-A analysis of DOTAP-DMPC GUVs and B2) FSC-A analysis of pure DMPC GUVs. Both measurements included 10,000 vesicles, with higher FSC-A values indicating larger vesicles. The blue graph represents P1 (the primary gate isolating the main vesicle population, excluding debris and doublets), while the grey graph includes all recorded events.*

Non-adherent GUVs had a mean diameter of 9.47 µm (±4.42 µm) and a median of 8.78 µm, based on measurements of 12,484 vesicles. In contrast, adherent GUVs exhibited a smaller mean diameter of 7.10 µm (±3.78 µm) and a median of 6.21 µm, calculated from 1,876 vesicles.

The comparison between DOTAP-DMPC and pure DMPC GUVs also revealed size differences. DOTAP-DMPC GUVs had a mean diameter of 9.16 µm (±4.43 µm) and a median of 8.28 µm, based on measurements of 14,362 vesicles. In contrast, pure DMPC GUVs showed a larger mean diameter of 10.61 µm (±5.39 µm) and a median of 8.97 µm, though this analysis was limited to 381 vesicles. The

smaller sample size for DMPC GUVs reflects their behavior post-sedimentation, where no vesicles could be identified as adherent or temporarily adherent beyond this stage.

Figure 4.20B compares cytometric measurements of DOTAP-DMPC and DMPC GUVs, revealing a visible overlap in size distributions. However, the DMPC vesicles exhibit a broader size distribution, indicating a greater range of vesicle sizes. For each sample, data from 10,000 vesicles were recorded, with event rates of 41 events/s for DOTAP-DMPC GUVs and 54 events/s for DMPC GUVs. The higher event rate for DMPC suggests a slightly higher concentration of vesicles in the sample.

The observed overlap in size distributions, broader range, and higher concentration of DMPC GUVs suggest that the DMPC population contains sufficient vesicles of similar size to the adherent DOTAP-DMPC GUVs, as further discussed below.

To quantify differences in surface charge, zeta potential measurements were conducted. DMPC GUVs exhibited a zeta potential of -7.41 ± 0.24 mV, indicating a negatively charged surface under the experimental conditions. In contrast, DOTAP-DMPC GUVs had a zeta potential of +2.29 ± 0.17 mV, reflecting a shift to a positively charged surface due to the incorporation of DOTAP.

Discussion

The observed increase in adhesion of positively charged MLVs suggests that the significant enhancement only occurs when HeLa cells are cultured for 144 hours under shear stress conditions of 2 or 6 dyn/cm². Since HeLa cells lack a well-developed glycocalyx, this increase in adhesion must be attributed to changes in the cell membrane itself. It appears that after 144 hours of shear stress, the membrane's surface charge becomes more negative, facilitating stronger interactions with the positively charged vesicles. This effect is likely not due to changes in membrane fluidity, as membrane phase state experiments in this study showed that any such effects would have already occurred after 72 hours of dynamic culture.

A possible explanation involves the response of HeLa cells to high shear stress, where they undergo nuclear expansion. This expansion is driven by histone acetylation, which not only protects the cells from shear-induced damage but also could influence the overall net charge of the cell. The increase in nuclear size might alter the distribution of charge within the cell, potentially enhancing interactions with the extracellular environment [187].

Zeta potential measurements of DMPC GUVs show that their surface charge becomes more negative when suspended in an ionic buffer medium, such as DPBS, and maintained above their phase transition temperature, as noted by Morini et al. in their study on lipid electrostatics. This behavior suggests that pure DMPC vesicles, despite their zwitterionic composition, are not electrically neutral under these conditions. The increased negative charge enhances electrostatic repulsion between the DMPC vesicles and the negatively charged glycocalyx and cell membranes, hindering effective adhesion [213].

The inclusion of positively charged DOTAP lipids in the vesicle composition introduces electrostatic attraction between the vesicles and the negatively charged cell membrane and glycocalyx of the HUVEC layer. Under both static and dynamic culturing conditions, these electrostatic attractions facilitate the

adhesion of 80:20 DMPC-DOTAP vesicles to the endothelial cells, resulting in observed adhesion coefficients [181][182].

During shedding or degradation, proteolytic enzymes may cleave glycoproteins or proteoglycans of the glycocalyx, leading to the generation of protein fragments. These fragments may contain negatively charged amino acid residues or domains, which could interact with positively charged molecules on the vesicle surface, enhancing adhesion. Shedding of the glycocalyx may also disrupt protein-protein interactions within the glycocalyx layer, leading to the release of proteins or protein fragments that were previously involved in adhesion or signaling processes. These released proteins could potentially interact with vesicle surface proteins or receptors, promoting adhesion to the endothelial cell membrane [181][183][184].

Some membrane-associated proteins or glycolipids within the glycocalyx layer may have membrane-spanning domains or lipid anchors. Upon shedding or degradation, these anchors or domains could be exposed and retained as remnants. Depending on their composition, they could contribute to increased adhesion by providing binding sites for vesicles [181][183][184][185].

Shedding exposes surface proteins that are typically concealed beneath the glycocalyx, potentially enhancing vesicle adhesion. This phenomenon may explain why vesicles adhere more effectively even when the glycocalyx is modified or reduced. These findings suggest that the cell membrane's ability to provide multiple interaction points—beyond charge-based adhesion—plays a more significant role in vesicle adhesion than the glycocalyx alone [5][8].

In addition to these exposed proteins, the lipid composition and organization of the cell membrane, including the formation of lipid rafts—potentially induced by cultivation under shear stress—also contribute to adhesion. Lipid rafts, microdomains enriched with cholesterol and sphingolipids, may serve as preferential docking sites for vesicles by concentrating adhesion-related proteins. These specialized membrane regions could act as key platforms for vesicle interaction, enabling robust adhesion even in the absence of an intact glycocalyx [214][215].

Another factor to consider is vesicle diameter. The size distributions of adherent and non-adherent GUVs, as well as those of DMPC and DOTAP-DMPC GUVs, exhibit significant overlap, suggesting that size variations are not the primary drivers of the observed differences. Moreover, the vesicle sizes in this study closely align with the typical diameters of circulating tumor cells (CTCs), which range from 8 µm to 20 µm. This similarity is particularly noteworthy as it implies that the mechanisms governing vesicle adhesion to endothelial cells may also shed light on how CTCs interact with the endothelium during metastasis [186].

The hypothesis that HUVECs cultured under dynamic conditions exhibit decreased adhesion of positively charged lipid vesicles compared to statically cultured cells or cells under the shedding condition is confirmed partially. Notably, shedding conditions resulted in the greatest vesicle adhesion, underscoring the critical role of glycocalyx integrity. Although dynamic and static conditions showed no significant differences in adhesion for HUVECs, the comparison with shedding conditions validates the hypothesis.

The research question is answered affirmatively, as the results demonstrate that the adhesion of lipid vesicles to the cell membrane depends on both the electrical charge of the membrane and the presence or modification of the glycocalyx.

With the role of electrostatics in vesicle adhesion clarified, a new question arises: how do culture conditions and the integrity of the glycocalyx influence the permeability of the endothelial barrier to the underlying tissue? Addressing this question involves exploring how these factors affect transendothelial diffusion and the selective transport of molecules or particles across the endothelium.

4.7. Trans Endothelial Diffusion of Macromolecules in a Blood Vessel Model

Trans-endothelial diffusion plays a critical role in regulating the transport of molecules across the endothelial layer, ensuring precise control over fluid balance and molecular exchange between blood vessels and surrounding tissues. Negatively charged components of the glycocalyx repel similarly charged macromolecules, while facilitating the passage of positively charged ions and small solutes. This size and charge selectivity prevents plasma protein leakage and maintains colloid osmotic pressure [56][57][58].

Building upon this understanding, a 3D hydrogel-HUVEC model provides a biomimetic platform to study trans-endothelial diffusion. By emulating the endothelial barrier as a porous medium with HUVEC and the surrounding tissue as a hydrogel matrix, this model enables the investigation of macromolecule diffusion and fluid sieving [148][150][154].

The diffusion of FITC-Dextran into the PAA hydrogel was measured from a molded 3D channel lined with HUVECs, using Dextran molecules of varying sizes as explained in Chapter 3.7. The study was conducted under the three distinct culture conditions: static, dynamic, and glycocalyx-shedding environments. The results were obtained in close collaboration with Yannic Schmidt as part of his bachelor's thesis, supervised by Manuel Sirch.

Proof of Adhesion

Confirming successful cell adhesion and distribution is essential, as measuring diffusion beyond the endothelial layer relies on the presence of a continuous and functional cell layer. The cultivation of HUVECs within the channel yielded promising results under both static and dynamic culture conditions, as shown in Figure 4.21.

Challenges in visualizing cells using phase-contrast microscopy, due to the complex 3D architecture of the channel, were effectively addressed by Hoechst 33342 staining. This staining method enabled clear visualization of cell nuclei, facilitating detailed scanning across multiple z-levels. These scans revealed a well-distributed population of HUVECs throughout the channel, demonstrating successful adhesion to the 3D channel walls. The channel diameter, consistent at approximately 1 mm in all images, further highlights the uniformity of the model.

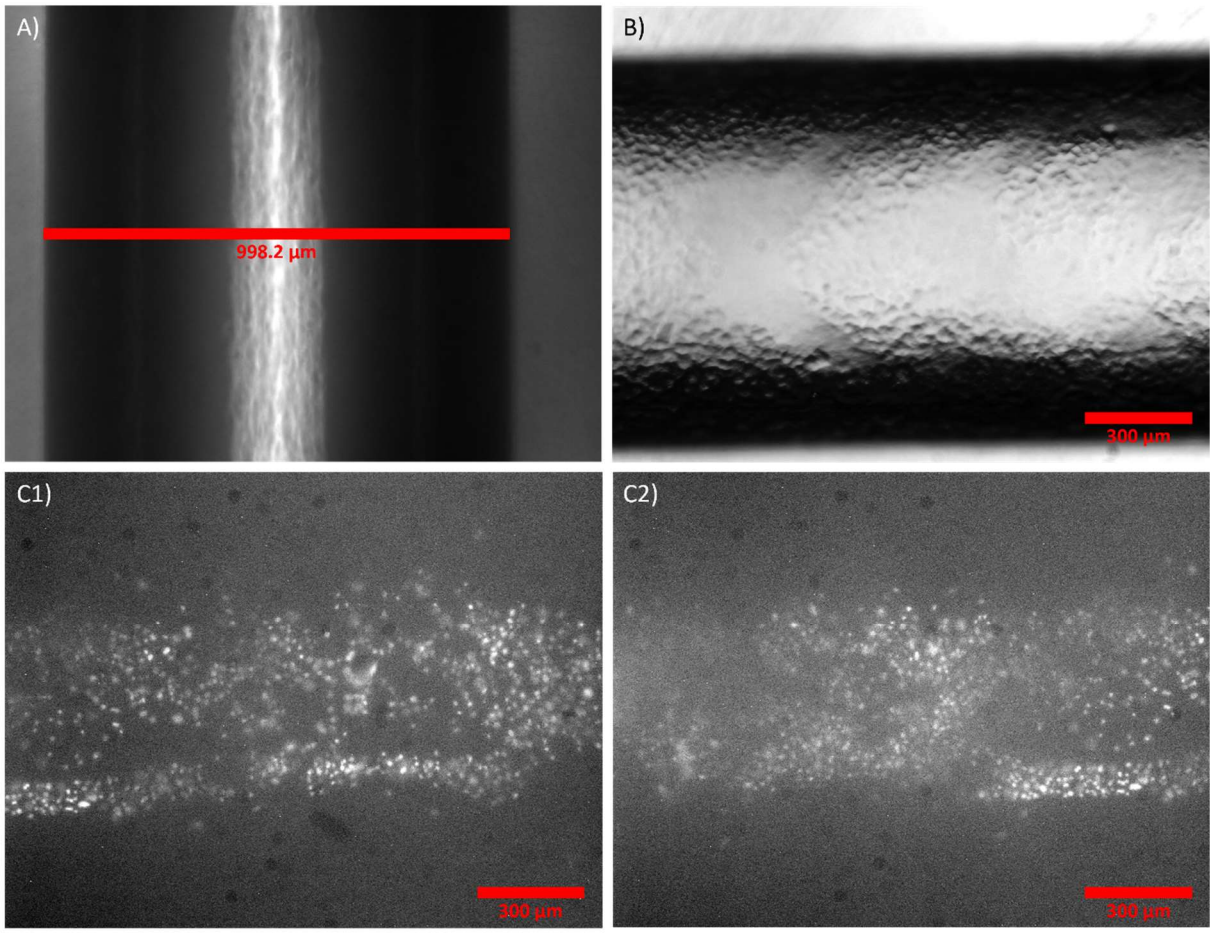

Figure 4.21: ***HUVEC in the 3D Hydrogel Channel.*** *A) An empty, stable channel after equilibration with cell medium. B) HUVEC cultured on the inside surface of the channel. C1) Hoechst 33342 stained nuclei on the lower half of the channel. C2) Hoechst 33342 stained nuclei on the upper half of the channel.*

Diffusion Measurements

A Python script (see Appendix A5) was utilized to analyze the FITC-Dextran diffusion gradient for each image. The diffusion direction was defined along the x-axis, and for each pixel column, the mean gray value was calculated. The border between the gel and the 3D channel was manually determined, and the x-axis was normalized accordingly. Additionally, pixel values were converted to a µm scale to provide accurate spatial representation. These normalized mean values were then plotted against the corresponding x-axis positions, offering a detailed depiction of the diffusion profile.

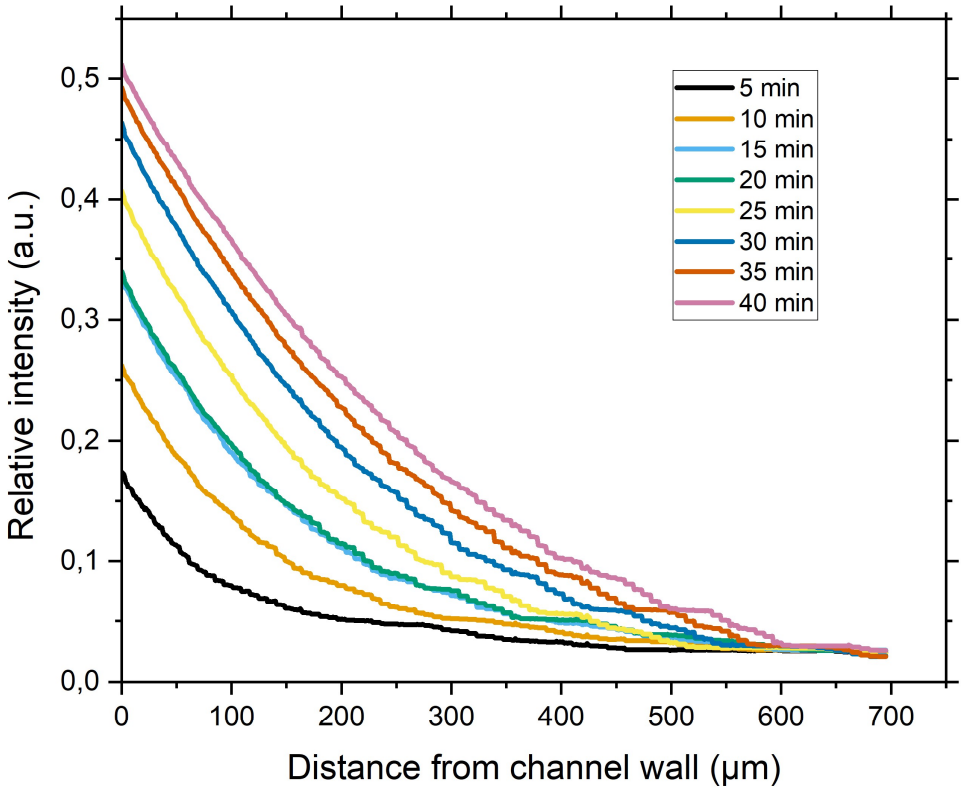

Figure 4.22: ***Example of the Diffusion into the Gel without Cells over Time.*** *Representation of image intensity versus distance from the lower edge, with the x-axis denoting the channel's position and the y-axis representing standardized intensity values (0 to 1). The maximum in the y-axis values confirms alignment with the channel.*

Figure 4.22 exemplary shows the diffusion of FITC-dextran within the gel. Over time, as FITC-dextran permeated the gel, the intensity gradually increased, indicative of its diffusion process.

To ensure consistency and facilitate comparison across diffusion experiments, all data were plotted using diagrams with identical axis ranges. As expected, the y-axis values, representing normalized image intensity, were higher in the channel region, confirming alignment with the channel structure. Intensity values were normalized on a scale from 0 to 1, where 0 indicates the lowest intensity and 1 corresponds to the highest intensity observed at the channel center. Normalization was achieved by dividing all intensity values by the maximum value at the channel center. The graphs display relative intensities smaller than 1, starting from the offset point determined by the border between the gel and the channel, allowing a clear comparison of intensity profiles across experiments and restricting analysis to data points acquired outside this demarcation.

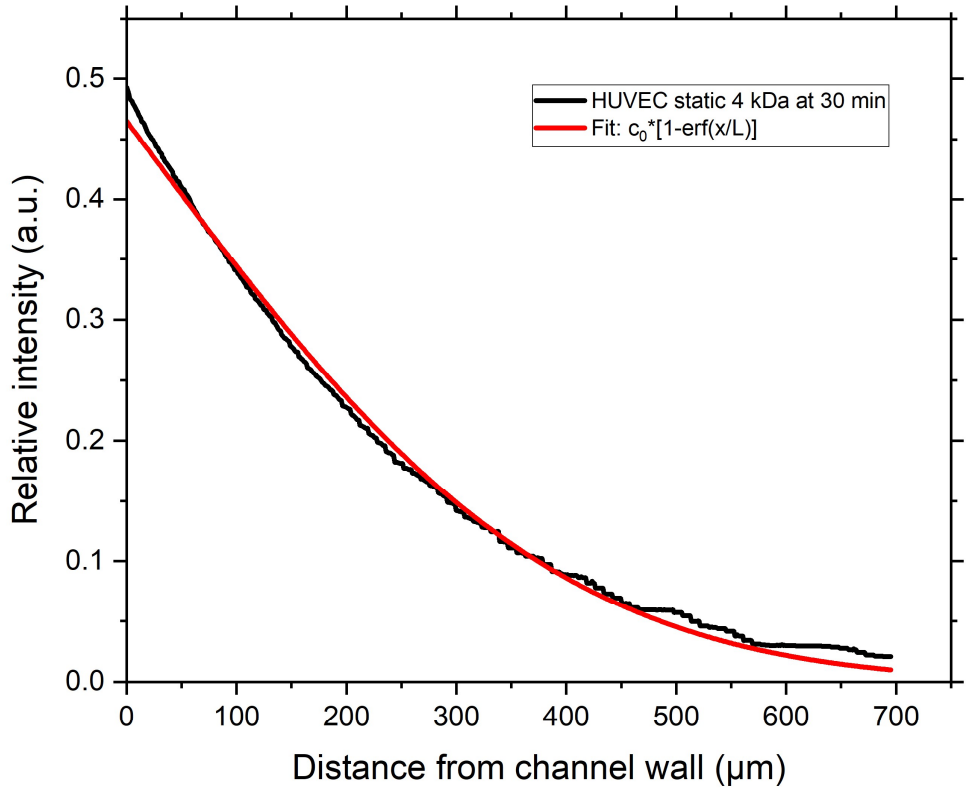

Figure 4.23: ***Example of the Diffusion Length Fit Function.*** *Fitting procedures applied to diffusion experiment data to derive qualitative assessments of diffusion characteristics. The analysis is constrained to data points outside the predefined channel boundary, which serves as the reference point for the fitting process. Fit parameters are diffusion length L and initial FITC-dextrane concentration c_0.*

To enable the derivation of qualitative assessments regarding the diffusion characteristics, the data obtained from diffusion experiments will undergo fitting procedures according to equation (2.8) $c\,(x) = c_0\left[1 - \mathrm{erf}\left(\frac{x}{(Dt)^2}\right)\right]$ for the diffusion mentioned in Chapter 2.5. This methodology facilitates the assessment, characterization, and subsequent comparison of diffusion lengths based on both the molecular dimensions of FITC-dextrans and the cellular coating of the channels. The obtained values for λ_i representing the diffusion lengths at specific time points are subsequently plotted against time and fitted using the function

$$\lambda = A + \sqrt{D} * \sqrt{t} \tag{4.6}$$

as exemplary shown in figure 4.24, whereas A is the offset. The resultant values for D, corresponding to different molecular weights of FITC-dextran and cultivation methods, are then visualized through the bar chart in figure 4.25 for comparative analysis. The bars represent the mean of the samples for each dataset, the error bars represent the standard deviation. The ANOVA could not be used because the assumption of equal variances was violated (p-value = 0.0219), the group sizes were highly unequal (ratio = 3.33), and the

test's power to detect variance differences was weak (0.17). Therefore, a double-sided t-test was used for statistical analysis.

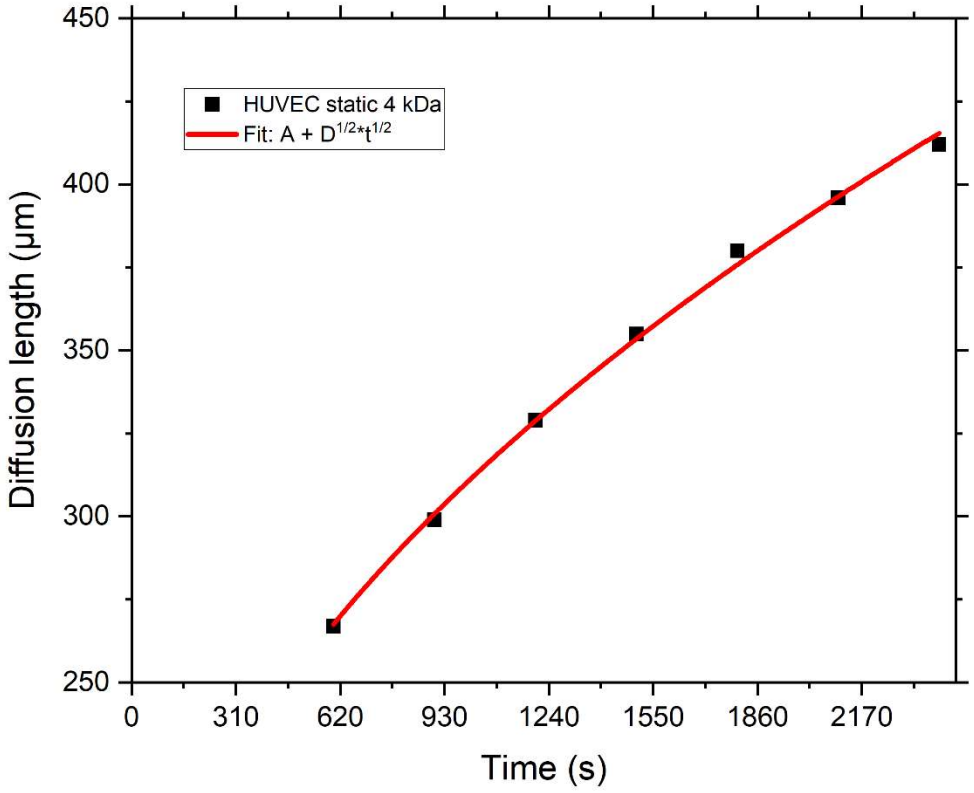

Figure 4.24: ***Example Fit Function for Determining the Diffusion Constant.*** *The previously fitted diffusion lengths are plotted against time and then fitted with the equation* $y = A + \sqrt{D} * \sqrt{t}$.

The bar chart in Figure 4.25 highlights significant differences between statically cultured cells and dynamically cultured cells, with a 41% decrease for 4kDa FITC-dextran and a 51% decrease for 10kDa dextran ($p<0.005$). A significant reduction in the diffusion coefficient was observed relative to molecular sizes across all cultivation methods and in blank channels without cells ($p<0.005$). For 4kDa FITC-dextran, no significant difference was found between the blank channel and the statically cultured channel ($p>0.005$). In contrast, a 46% decrease was noted between these two conditions with 10kDa FITC-dextran ($p>0.005$). Regarding the shed condition, measurements were solely conducted with 10kDa FITC-dextran. Although the chart depicts the average diffusion coefficient between static and dynamic culture conditions, the high standard deviation renders it not significant in comparison with both ($p>0.005$).

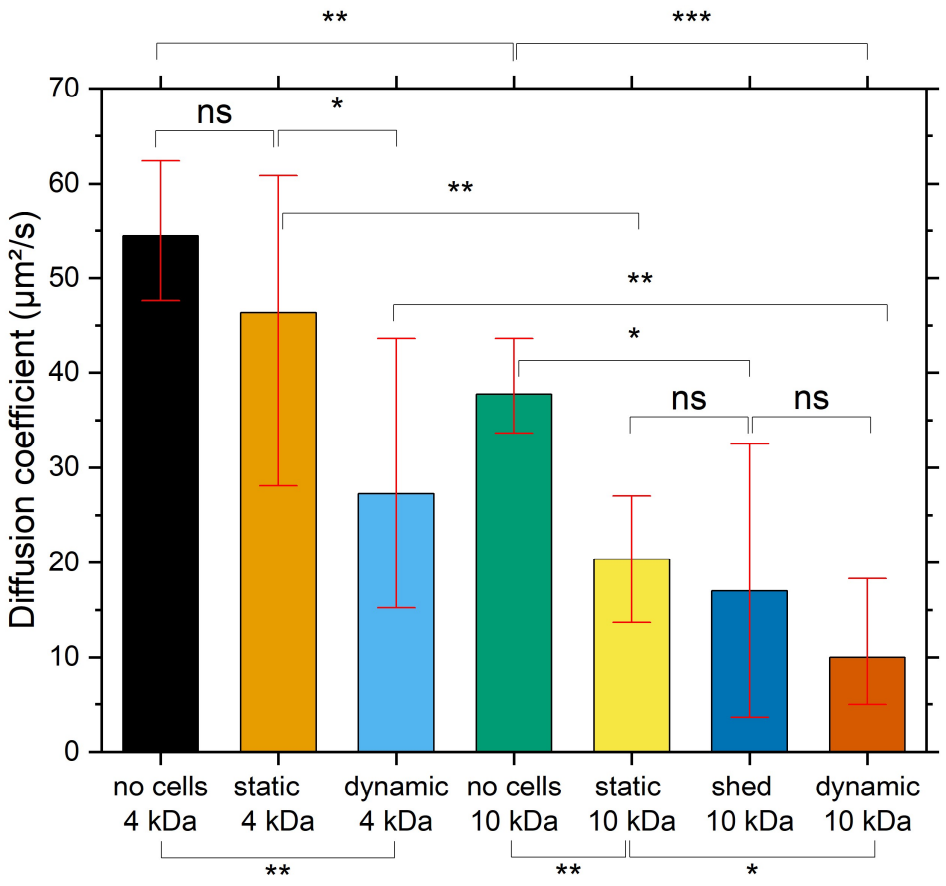

Figure 4.25: ***Comparison of the Diffusion Coefficients for Different Molecular Weights and Cell Culture Conditions.*** *Analysis of diffusion coefficients across various cultivation methods, highlighting significant decreases relative to molecular sizes. The bar chart shows a 46% decrease in the diffusion coefficient between blank channels and statically cultured channels for 10kDa FITC-dextran. Additionally, significant differences between statically cultured and dynamically cultured cells are illustrated, with decreases of about 41% for 4kDa FITC-dextran and 51% for 10kDa FITC-dextran. For the shed condition, measurements with 10kDa FITC-dextran were conducted, showing an average diffusion coefficient between static and dynamic culture conditions, though the high standard deviation rendered the difference non-significant. ***: p<0.001, **: p<0.01, *: p<0.05, ns:p>0.05. The sample sizes were N=3, N=6, N=9, N=3, N=5, N=8, N=10 from left to right.*

Discussion

The difference in permeability between the molecular sizes without cells can be attributed to the size filtering effect of the hydrogel itself [150].

Notably, the lack of significant difference in permeability between the blank channel and the statically cultured HUVEC for 4 kDa FITC-dextran suggests that molecules of this size can pass nearly unhindered between the cells into the hydrogel. In contrast, 10 kDa molecules appear to be too large to do so effectively. This indicates that 4 kDa molecules can diffuse through the intercellular spaces, as the cells do not form a tight cobblestone structure, and the molecules are able to partially pass between adherens junctions and tight junctions. For smaller molecules like those around 4 kDa, tight junctions may be sufficiently permeable to allow diffusion. However, larger molecules like those around 10 kDa are often impeded by these junctions due to their size, resulting in less efficient diffusion [188].

The observed decrease in permeability for both molecular sizes under dynamic culture conditions could be attributed to several factors, including the formation of the cobblestone structure, enhanced gap junction formation, and the development of the glycocalyx. Gap junctions are channels that directly connect the cytoplasm of adjacent endothelial cells, allowing for the transfer of small molecules and ions. These channels are highly selective and generally allow the passage of molecules less than 1 kDa, thus not significantly contributing to the diffusion of 4 kDa or 10 kDa molecules across the endothelial layer. Shear stress influences the expression levels of connexin proteins, such as connexin 43 (Cx43), which are critical components of gap junctions [188][189][190].

Studies have shown that physiological levels of shear stress can upregulate the expression of connexins in endothelial cells. Shear stress induces endothelial cell alignment in the direction of flow, which can affect the spatial organization and distribution of gap junctions. This alignment optimizes the formation and function of gap junctions between neighboring cells. The morphological changes induced by shear stress, such as elongation and reorganization of the cytoskeleton, also contribute to the stabilization and functionality of gap junctions [188][189][190][191].

As observed in the results for the shed conditions, the presence of significantly high error bars suggests notable variability in the permeability measurements. This variability potentially points towards the involvement of the glycocalyx. When the glycocalyx is shed or degraded, either due to physiological processes or pathological conditions, endothelial cells may undergo morphological changes. These changes can include alterations in cell shape, surface roughness, and protrusion formation. Without the glycocalyx, endothelial cells may appear flatter and less elongated, potentially affecting their interaction with blood flow and neighboring cells. As stated, the glycocalyx plays a crucial role in maintaining the integrity of cell junctions, including tight junctions, adherens junctions, and gap junctions. Therefore, it might be possible, that shedding of the glycocalyx can disrupt these junctions by exposing them to mechanical stress. This disruption can lead to increased permeability of the endothelial barrier, allowing the passage of macromolecules [192][193].

An important aspect to consider in this discussion is the confluence of the endothelial model and how it impacts the observed properties of the endothelial layer under different culture conditions. While dynamically cultured cells are more likely to achieve and maintain confluence due to the effects of shear stress, it remains uncertain whether the model is fully confluent, particularly under static conditions. This uncertainty limits the reliability of conclusions drawn from the static cultures and underscores the need for further verification of confluence to better understand the observed permeability differences. For future experiments confocal microscopy could be employed to verify the confluency of the endothelial layer. However, the hydrogel model used in this study was not suited for such an approach due to its current design. To enable the use of confocal microscopy, a rework of the 3D hydrogel channel slide is necessary. The revised design would need to ensure a thinner structure with tightly sealed connections to prevent damage to the microscope and facilitate accurate imaging of the endothelial cells within the hydrogel.

As of now, and considering that the model is still under development, the hypothesis that dynamically cultured HUVECs exhibit decreased diffusion of FITC-dextran through the endothelial layer into the hydrogel, particularly for larger molecular sizes, compared to statically cultured cells, can be partially supported. However, the role of confluence in influencing these diffusion differences remains uncertain,

particularly under static conditions. Additionally, the impact of the glycocalyx on the permeability of macromolecules beyond the endothelial layer cannot be definitively determined, as the observed differences were not statistically significant.

Nonetheless, it is important to explore the modulation of cell-cell contacts in dependence on the applied culture methods, as this might play a crucial role in shaping the permeability and functionality of the endothelial barrier.

4.8. Modulation of Cell-Cell Contacts under Dynamic Flow Conditions

Cell-cell contacts are essential structural and functional components of endothelial cells, playing a critical role in maintaining vascular integrity and regulating barrier function. Among these, adherens junctions, which are prominently marked by vascular endothelial (VE)-cadherin, are particularly significant. VE-cadherin is a transmembrane protein that forms homophilic interactions between adjacent endothelial cells, creating a cohesive and mechanically stable endothelial layer [33].

Building on the theoretical foundation of these adherens junctions, the analysis focuses on how different culture methods influence these critical structures. The permeability of the endothelial layer and the localization of VE-cadherin at cell-cell contacts were examined, with particular emphasis on the impact of the glycocalyx and cultivation conditions. The following results were obtained in close collaboration with Marina Huber as part of her master's thesis, which was supervised by Manuel Sirch. A publication on this is currently in preparation.

The Analysis of the cell morphology of HUVEC through shape characteristics of cell-cell contacts was performed using CellProfiler. To utilize this tool, the images acquired as described in Chapter 3.2 and exemplary shown in figure 4.26, were first imported into the software. CellProfiler, much like Cellpose, can identify and segment cells. Once the cells are accurately segmented, the objects and their outlines can be exported for detailed analysis, as shown in figure 4.27. This allows for a comprehensive examination of area and shape features, providing valuable insights into the structural characteristics of the cell-cell contacts. For the analysis, both the principles of solidity and form factor were utilized [194].

Solidity is a shape descriptor defined as the ratio of an object's area A_{cell} to the area of its convex hull $A_{\text{hull, convex}}$ (see figure 4.28A). Mathematically, it is expressed as:

$$S = \frac{A_{\text{cell}}}{A_{\text{hull, convex}}} \tag{4.7}$$

This metric quantifies how closely an object's shape approximates a convex shape. A solidity value of 1 indicates that the object is perfectly convex, with no indentations or irregularities along its boundary. Values less than 1 indicate the presence of concavities or other deviations from a convex shape. In the context of cell-cell contacts, higher solidity values typically indicate smoother, more contiguous boundaries, suggestive of healthy and stable interactions between cells. Conversely, lower solidity values can reveal irregularities, protrusions, or indentations in the cell membrane, which may signal dynamic remodeling processes, pathological conditions, or responses to external stimuli [195][196].

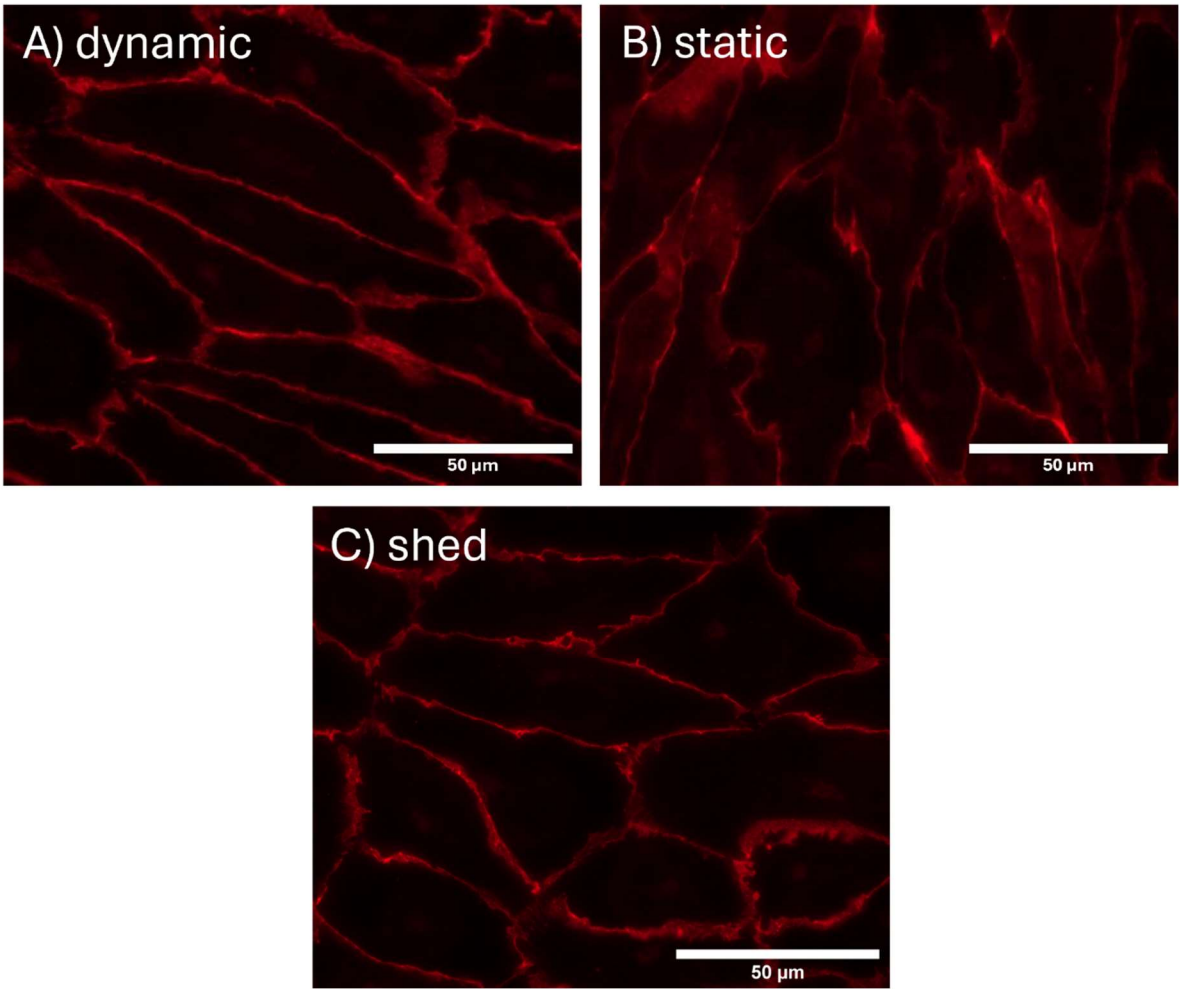

Figure 4.26: ***VE-Cadherin Proteins at Cell-Cell Contacts in HUVEC Stained with Antibodies.*** *A) Dynamically cultured cells. B) Statically cultured cells. C) Cells under the shedding condition. Differences in form factor and solidity are visibly distinguishable.*

The form factor is a shape descriptor that quantifies the roundness or circularity of an object (see figure 4.28B). It is defined as the ratio of the object's area to the area of a circle with the same perimeter U_{cell}. Mathematically, it can be expressed as:

$$F = \frac{4\pi * A_{\text{cell}}}{U_{\text{cell}}^2} \tag{4.8}$$

A form factor value of 1 indicates a perfect circle, with values decreasing as the shape becomes more elongated or irregular. This metric is particularly useful in image analysis for assessing the regularity and compactness of shapes, helping to distinguish between different morphological characteristics of cells. In the context of cellular analysis, a higher form factor suggests a more regular and rounded cell shape, which can be indicative of healthy, unstressed cells. Conversely, a lower form factor may indicate elongated, irregular, or deformed cells, which could be a result of cellular stress, pathological conditions, or morphological changes during various biological processes [195][196].

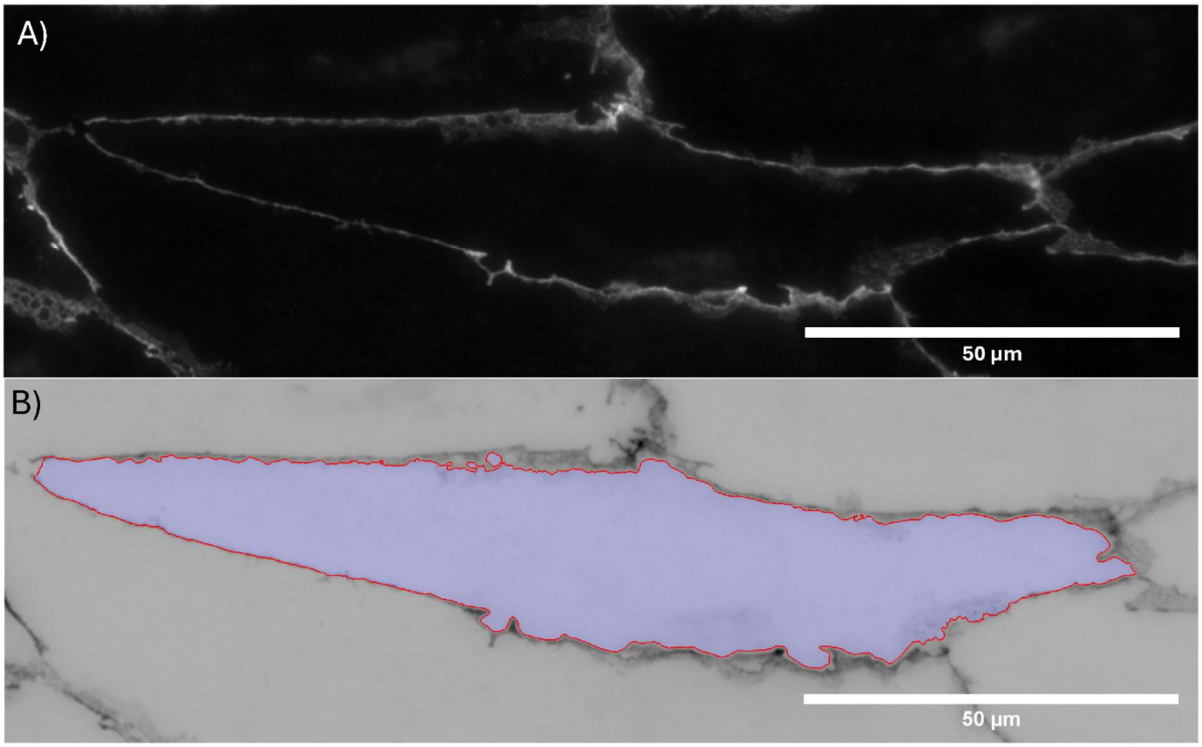

Figure 4.27: ***Method of Analysis with CellProfiler.*** *A) Inverted grayscale image displaying cell-cell contacts. B) Cell-cell contact outlines processed using CellProfiler.*

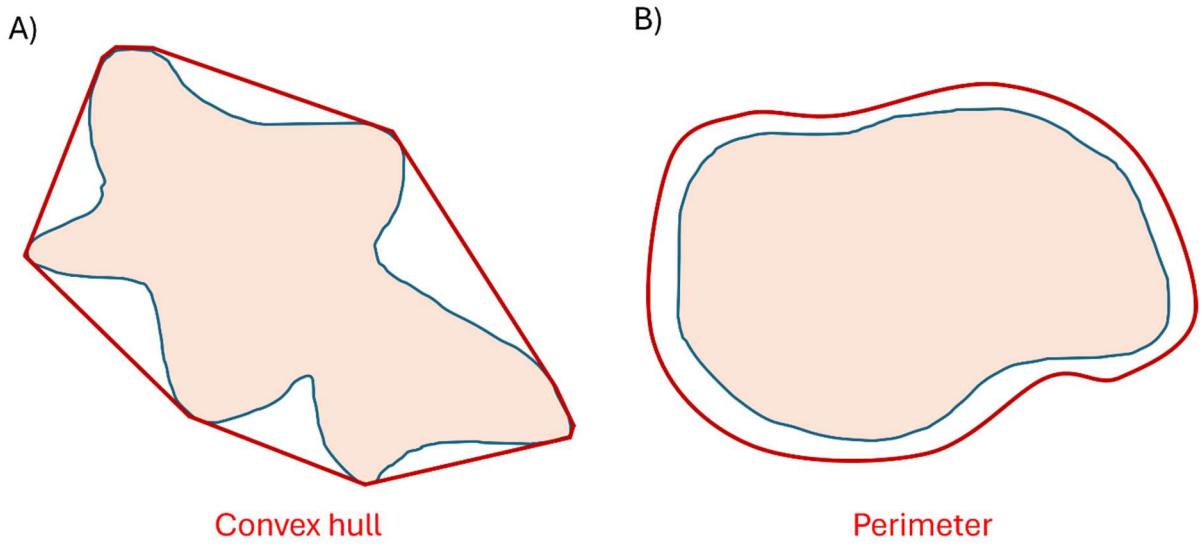

Figure 4.28: ***Solidity and Formfactor.*** *A) The Solidity showcased with the red line marking the convex hull encircling the cell. B) The Perimeter surrounding the cell, crucial for calculating the form factor. Derived from* [195][196].

The form factor and solidity data of the cells were analyzed, with mean values and standard deviations determined for each culture condition. The results are presented as boxplots in Figures 4.29 and 4.30. Group comparisons were performed using ANOVA, followed by a Tukey post-hoc test for pairwise analysis.

In figure 4.29, dynamically cultured cells stand out with the highest solidity, recorded at $S = 0.9$. This suggests that dynamically cultured cells are not only more compact but also exhibit a more regular and streamlined shape, indicative of a highly organized structural integrity.

In stark contrast, statically cultured cells demonstrate the lowest solidity, $S = 0.8$. These values imply that statically cultured cells are less dense and have a more irregular shape, reflecting a less organized cellular structure.

Shed cells display a solidity of $S = 0.75$. While this value is lower than that of dynamically cultured cells, it is significantly higher than that of statically cultured cells, suggesting that shed cells retain some structural integrity despite the shedding process. The solidity value of shed cells is positioned between the others at approximately 8.5, highlighting their intermediate characteristics.

The ANOVA confirmed that the solidity values of statically cultured cells, dynamically cultured cells, and shed cells differ significantly from each other ($p<0.05$).

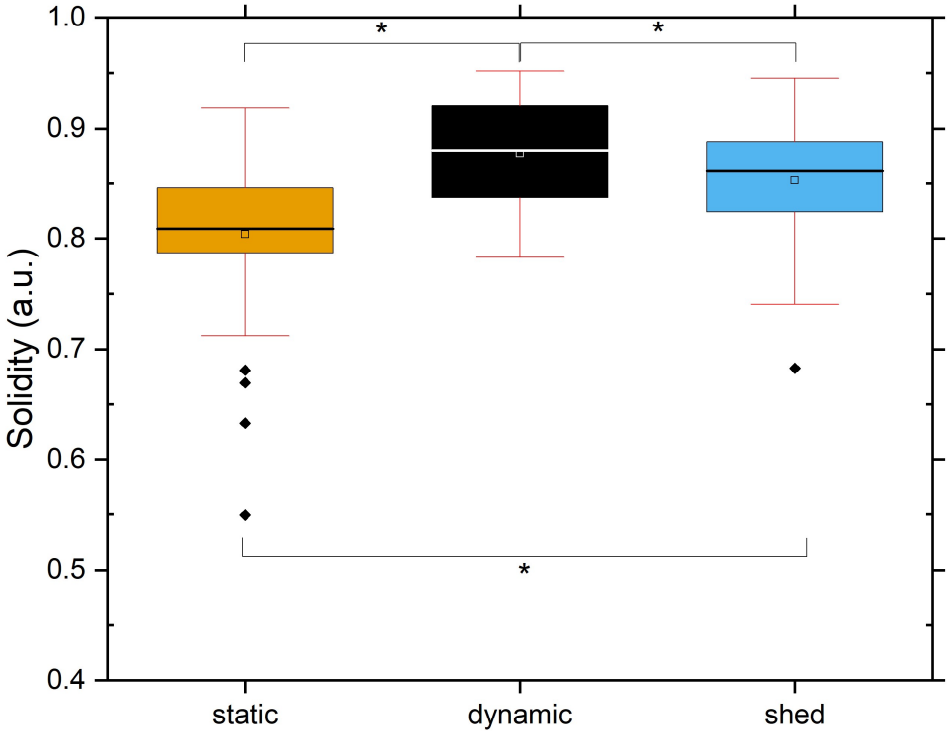

Figure 4.29: ***Solidity of HUVEC for different Cell Culture Conditions.*** *Dynamically cultured cells exhibit the highest solidity at S = 0.9, indicating a more compact, regular, and highly organized structure. In contrast, statically cultured cells have the lowest solidity, S = 0.8, reflecting a less dense and more irregular shape with lower structural organization. Shed cells, with a solidity of S = 0.75, retain some structural integrity despite the shedding process, placing their solidity between the other two types at approximately 8.5. The differences in solidity among statically cultured, dynamically cultured, and shed cells are statistically significant, highlighting their distinct structural characteristics. Error bars are standard deviation. *: p<0.05. The sample size was N=9 for each culture condition.*

In Figure 4.30, dynamically cultured cells exhibit the highest form factor, $F = 0.35$, reinforcing the observation that these cells have a more regular and streamlined shape.

Statically cultured cells demonstrate the lowest form factor, $F = 0.2$, indicating a more irregular shape and less organized structure.

Shed cells show a form factor of $F = 0.3$, which, while lower than that of dynamically cultured cells, is significantly higher than that of statically cultured cells. This suggests that shed cells maintain some degree of regularity in shape, even after the shedding process.

The ANOVA also confirms that the form factor values of statically cultured cells, dynamically cultured cells, and shed cells differ significantly from each other ($p < 0.05$).

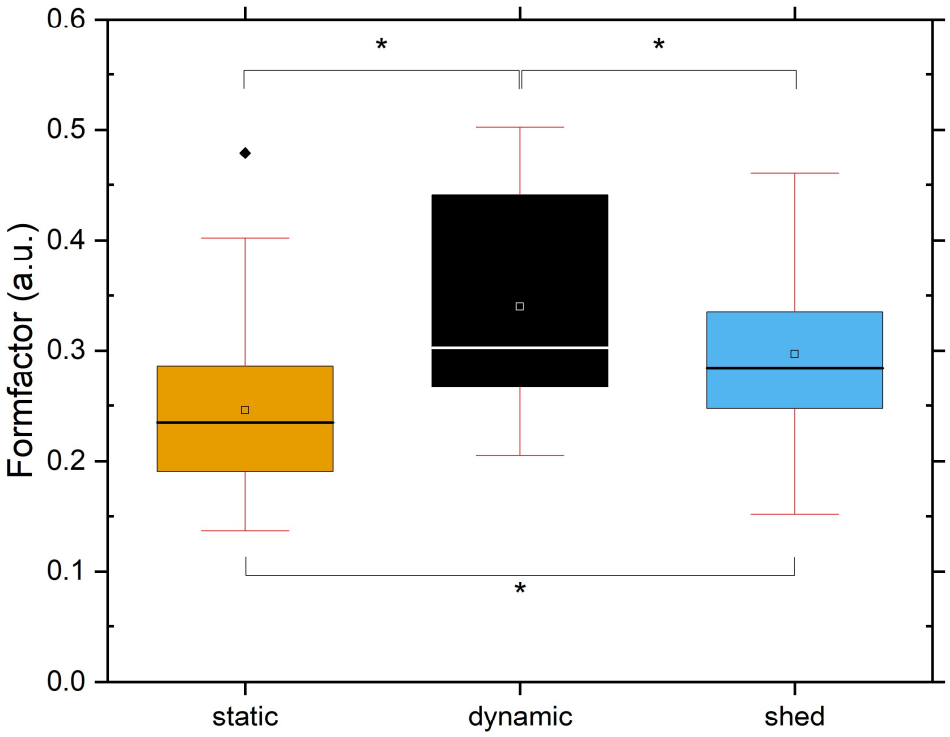

Figure 4:30: ***Formfactor of HUVEC for different Cell Culture Conditions.*** *Dynamically cultured cells have the highest form factor, F = 0.35, indicating a more regular and streamlined shape. Statically cultured cells have the lowest form factor, F = 0.2, reflecting a more irregular shape and less organized structure. Shed cells show a form factor of F = 0.3, which, while lower than that of dynamically cultured cells, is significantly higher than that of statically cultured cells. This suggests that shed cells maintain some degree of regularity in shape even after the shedding process. The differences in form factor among statically cultured, dynamically cultured, and shed cells are statistically significant, emphasizing their distinct structural characteristics. Error bars are standard deviation. *: p<0.05. The sample size was N=9 for each culture condition.*

Discussion

The observed differences in solidity and form factor among dynamically cultured cells, statically cultured cells, and cells under the shedding condition could be attributed to the distinct mechanical and biochemical environments, as well as the presence or absence of the glycocalyx layer for several reasons.

The dynamic environment promotes cytoskeletal rearrangements and could strengthen cell-cell junctions, leading to more regular and rounded cell shapes. The fluid shear stress likely enhances cell-cell contact integrity and reduces irregularities, contributing to these higher metrics, as it has already been discussed in Chapter 4.7 [188][189][190][191].

The partial removal of the glycocalyx layer in these shed cells appears to significantly affect their morphology and mechanical properties. This may likely compromise the integrity of the cell surface, leading to a slight reduction in solidity and form factor compared to dynamically cultured cells. The absence of the glycocalyx may also exacerbate cell membrane irregularities and weaken cell-cell adhesion, contributing to the observed changes in shape metrics.

The glycocalyx is intrinsically connected to the cytoskeleton through transmembrane proteins such as integrins and syndecans, which interact with cytoskeletal components like actin filaments via adaptor proteins such as ezrin, radixin, and moesin. These linkages are essential for maintaining cellular structure and transmitting mechanical and chemical signals. Shedding of the glycocalyx likely disrupts these critical connections, altering cytoskeletal organization and dynamics, which in turn impacts cell morphology and mechanical properties [192].

Even without the glycocalyx, cells can undergo morphological changes due to various factors such as changes in cell-cell and cell-matrix adhesion, and mechanical forces. Other studies have shown that the cessation of shear flow can lead to rapid morphological changes in cells as well. When shear flow is stopped, these cells can revert to a more rounded and less aligned morphology. This reversion can occur relatively quickly, within hours or even minutes, as the cells respond to the sudden change in mechanical environment [199][200].

The hypothesis that HUVEC cultured under dynamic conditions demonstrate improved solidity and form factor of cell-cell contacts compared to those cultured under static conditions or subjected to glycocalyx shedding can be supported. The question of whether the existence of the glycocalyx affects cell-cell contacts can therefore be answered affirmatively.

These findings align with the broader discussion in Chapter 4.7, highlighting how distinctions in cell-cell contacts under different culture conditions contribute to enhanced or decreased endothelial barrier functionality. The improved solidity and form factor of cell-cell contacts observed in dynamically cultured HUVEC, facilitated by the presence of an intact glycocalyx, underscore its pivotal role in strengthening barrier integrity and reducing permeability. Conversely, disruptions to the glycocalyx, as seen under shedding conditions, seem to correlate with weakened cell-cell junctions and compromised barrier functionality.

5. CONCLUSION AND OUTLOOK

The goal of this thesis was to shed light on the various aspects of transport mechanisms into and beyond HUVEC, with a focus on the influence of an existing glycocalyx and its connection to secondary effects, such as changes in membrane phase state due to cultivation under flow conditions. The findings can be summarized as follows:

- A glycocalyx was successfully synthesized in vitro under dynamic conditions, with a shear stress of 6 dyn/cm² over 144 hours. Notably, the glycocalyx partially degrades when the flow is stopped. The rate of nanoparticle uptake via endocytosis is significantly higher in statically cultured endothelial cells compared to dynamically cultured cells with an intact glycocalyx. Additionally, cells with a shed glycocalyx exhibit an even significantly higher uptake rate compared to statically cultured cells.
  The hypothesis that HUVEC cultured under dynamic conditions exhibit higher binding of Alexa Fluor 555-conjugated WGA compared to statically cultured cells or cells under the shedding condition is supported by the data, and the research question of whether an intact glycocalyx occurs under the in vitro culture conditions used in this research can be answered with yes.

- The uptake of 50 nm SiO_2 nanoparticles is significantly inhibited in HUVECs cultured under dynamic conditions with an intact glycocalyx compared to statically cultured cells or cells with a shed glycocalyx. In the shed glycocalyx condition, the uptake is even significantly higher than in statically cultured cells, emphasizing the critical role of glycocalyx integrity in regulating nanoparticle internalization. Additionally, it was verified that the nanoparticles are internalized by the cells rather than merely adhering to the membrane surface, confirming actual uptake.
  The hypothesis that HUVEC cultured under dynamic conditions show a reduced endocytic uptake of nanoparticles compared to statically cultured cells or cells under the shedding condition has been confirmed. The research question regarding whether an intact glycocalyx impacts nanoparticle internalization is answered positively.

- The uptake of Hoechst 33342 molecules through the cell membrane is significantly higher in statically cultured endothelial cells than in dynamically cultured cells with an intact glycocalyx. However, the difference in uptake between cells with an intact and a degraded glycocalyx is not significant.
  The hypothesis that HUVEC cultured under dynamic conditions impede the diffusion of dye molecules into the cells compared to statically cultured cells or cells under the shedding condition has been confirmed. The research question of whether an intact glycocalyx affects molecular diffusion through the cell membrane can be answered with answered yes.

- The GP-value of dynamically cultured cells appears to shift to higher values compared to statically cultured cells, suggesting increased membrane fluidity. However, these results were inconsistent, indicating that the methods may need refinement.

The hypothesis that the cultivation method of HUVEC and HeLa influences the cell membrane's phase state, making it either more fluid or gel-like depending on whether the cells are cultured statically, dynamically, or under shedding conditions, has not been fully supported due to inconsistent results. The research question of whether the glycocalyx affects membrane phase behavior cannot be conclusively answered

- The adhesion of positively charged DMPC-DOTAP GUVs to the surface of endothelial cells with a degraded glycocalyx is significantly higher than to dynamically cultured cells with an intact glycocalyx or statically cultured cells. Similarly, the adhesion of MLVs to dynamically cultured HeLa cells (cultured for 144 hours) is significantly higher than to cells cultured statically or for only 72 hours under flow, regardless of whether the shear flow is 2 or 6 dyn/cm².
  The hypothesis that HUVEC cultured under dynamic conditions exhibit decreased adhesion of positively charged lipid vesicles compared to statically cultured cells or cells under the shedding condition has been confirmed. Consequently, the research question regarding the glycocalyx's role in vesicle adhesion can be answered affirmatively.

- A sufficient in vitro model of the endothelial layer was successfully created using a 3D channel molded from polyacrylamide hydrogel, in which HUVECs were seeded and cultured. It was demonstrated that the diffusion of FITC-dextran beyond the endothelial layer is significantly higher for 4kDA molecules compared to 10kDA molecules. Furthermore, diffusion decreases for both molecule sizes when cells are adherent inside the 3D channel, and further decreases when cells are cultured under dynamic rather than static conditions.
  The hypothesis that HUVEC cultured under dynamic conditions show decreased diffusion of FITC-dextran through the cell layer into the hydrogel, particularly for smaller molecular sizes, compared to statically cultured cells or cells under the shedding condition, can be partially supported. However, the role of confluence and the glycocalyx in influencing macromolecule diffusion remains uncertain due to the lack of statistically significant differences. The research question of whether the glycocalyx affects the diffusion of macromolecules beyond the endothelial layer cannot yet be definitively answered

- VE-cadherin antibody staining revealed distinct differences in solidity and form factor among dynamically cultured, statically cultured, and shed cells. Dynamically cultured cells exhibited the significantly highest solidity ($S = 0.9$) and form factor ($F = 0.35$), indicating a more compact, regular, and organized structure. In contrast, statically cultured cells showed the significantly lowest solidity ($S = 0.8$) and form factor ($F = 0.2$), reflecting a less dense and more irregular shape. Shed cells exhibited intermediate values, with significant differences compared to the other culture methods, showing a solidity of $S = 0.75$ and a form factor of $F = 0.3$, suggesting they retain some structural integrity and regularity despite the shedding process.
  The hypothesis that HUVEC cultured under dynamic conditions demonstrate improved solidity and form factor of cell-cell contacts compared to statically cultured cells or cells under the shedding condition has been confirmed. The research question of whether the existence of the glycocalyx affects cell-cell contacts can therefore be answered with yes.

The findings from this thesis provide a valuable contribution to the fields of drug delivery and the development of 3D models in vascular research. The observed effects of dynamic cultivation on endothelial cells and the synthesis of an in vitro glycocalyx offer insights into how flow conditions and membrane characteristics can influence drug transport. These insights suggest that further investigation could enhance our understanding of how to optimize drug delivery systems, particularly in targeting specific areas within the vascular system.

In drug delivery, the differential uptake of nanoparticles and other molecules into endothelial cells, as well as the adhesion dynamics of vesicles, depending on the glycocalyx state and membrane fluidity highlights potential strategies for improving the specificity and efficiency of transfection and therapeutic delivery. By carefully modulating flow conditions or glycocalyx integrity, there may be opportunities to enhance the targeting of drugs, particularly in the treatment of vascular diseases where endothelial function is affected. Further research in this area could help in developing more precise and effective delivery methods, potentially offering benefits in clinical applications.

The creation of a 3D endothelial model represents an important step toward more physiologically relevant in vitro systems. These models, which better replicate the complex environment of blood vessels, hold promise for studying drug transport and endothelial behavior under conditions that more closely resemble those in vivo. This approach could contribute to a more accurate understanding of drug interactions with the endothelial barrier, which is crucial for the preclinical evaluation of new therapeutics.

While the results of this research are promising, there remains much to explore. Continued work in refining these models and deepening the understanding of the underlying mechanisms could lead to significant advancements in drug delivery and vascular research, with the hope of translating these findings into practical applications.

6. LITERATURE

1. Reitsma, S., Slaaf, D. W., Vink, H., van Zandvoort, M. A. M. J., & oude Egbrink, M. G. A. (2007). The endothelial glycocalyx: composition, functions, and visualization. *Pflügers Archiv - European Journal of Physiology*, 454(3), 345-359. DOI: https://doi.org/10.1007/s00424-007-0212-8.

2. Pries, A.R., Secomb, T.W., & Gaehtgens, P. (2000). The endothelial surface layer. *Pflügers Archiv - European Journal of Physiology*, 440:653-666. DOI: https://doi.org/10.1007/s004240000307.

3. Yilmaz, O., Afsar, B., Ortiz, A., & Kanbay, M. (2019). The role of endothelial glycocalyx in health and disease. *Clinical Kidney Journal*, 12(5), 611-619. DOI: https://doi.org/10.1093/ckj/sfz042.

4. Li, L., & Bonventre, J. V. (2016). Endothelial Glycocalyx: Not Just a Sugar Coat. *American Journal of Respiratory and Critical Care Medicine*, 194(4), 390-393. DOI: https://doi.org/10.1164/rccm.201603-0624ED.

5. Milusev, A., Rieben, R., & Sorvillo, N. (2022). The Endothelial Glycocalyx: A Possible Therapeutic Target in Cardiovascular Disorders. *Frontiers in Cardiovascular Medicine*, 9, 897087. DOI: https://doi.org/10.3389/fcvm.2022.897087.

6. Potje, S. R., Dal-Cin Paula, T., Paulo, M., & Bendhack, L. M. (2021). The Role of Glycocalyx and Caveolae in Vascular Homeostasis and Diseases. *Frontiers in Physiology*, 11, 620840. DOI: https://doi.org/10.3389/fphys.2020.620840.

7. Targosz-Korecka, M., Kubisiak, A., Kloska, D., Kopacz, A., Grochot-Przeczek, A., & Szymonski, M. (2021). Endothelial glycocalyx shields the interaction of SARS-CoV-2 spike protein with ACE2 receptors. *Scientific Reports*, 11, 12157. DOI: https://doi.org/10.1038/s41598-021-91231-1.

8. Möckl, L. (2020). The Emerging Role of the Mammalian Glycocalyx in Functional Membrane Organization and Immune System Regulation. *Frontiers in Cell and Developmental Biology*, 8, 253. DOI: https://doi.org/10.3389/fcell.2020.00253.

9. Fu, L., Kim, H. N., Sterling, J. D., Baker, S. M., & Lord, M. S. (2022). The role of the cell surface glycocalyx in drug delivery to and through the endothelium. *Advanced Drug Delivery Reviews*, 184, 114195. DOI: https://doi.org/10.1016/j.addr.2022.114195.

10. Zha, D., Fu, M., & Qian, Y. (2022). Vascular Endothelial Glycocalyx Damage and Potential Targeted Therapy in COVID-19. *Cells*, 11(12), 1972. DOI: https://doi.org/10.3390/cells11121972.

11. Bai, K., & Wang, W. (2014). Shear stress-induced redistribution of the glycocalyx on endothelial cells in vitro. *Biomechanics and Modeling in Mechanobiology*, 13(2), 303-311. DOI: https://doi.org/10.1007/s10237-013-0502-3.

12. Haidekker, M. A., L'Heureux, N., & Frangos, J. A. (2000). Fluid shear stress increases membrane fluidity in endothelial cells: a study with DCVJ fluorescence. *American Journal of Physiology-Heart and Circulatory Physiology*, 278(4), H1401-H1406. DOI: https://doi.org/10.1152/ajpheart.2000.278.4.H1401.

13. Gerhold, K. A., & Schwartz, M. A. (2016). Ion Channels in Endothelial Responses to Fluid Shear Stress. *Physiology (Bethesda)*, 31(5), 359-369. DOI: https://doi.org/10.1152/physiol.00007.2016.

14. Mensah, S. A., Nersesyan, A. A., & Ebong, E. E. (2021). Endothelial Glycocalyx-Mediated Intercellular Interactions: Mechanisms and Implications for Atherosclerosis and Cancer Metastasis. *Cardiovascular Engineering and Technology*, 12(1), 72-90. DOI: https://doi.org/10.1007/s13239-020-00487-7.

15. Dull, R. O., & Hahn, R. G. (2022). The glycocalyx as a permeability barrier: basic science and clinical evidence. *Critical Care*, 26(1), 273. DOI: https://doi.org/10.1186/s13054-022-04154-2.

16. Sugihara-Seki, M., & Fu, B. M. (2005). Blood flow and permeability in microvessels. *Fluid Dynamics Research*, 37(1-2), 82-132. DOI: https://doi.org/10.1016/j.fluiddyn.2004.03.006.

17. Simons, K., & Gerl, M. J. (2010). Revitalizing membrane rafts: new tools and insights. *Nature Reviews Molecular Cell Biology*, 11(10), 688-699. DOI: https://doi.org/10.1038/nrm2977.

18. Nel, A. E., Mädler, L., Velegol, D., Xia, T., Hoek, E. M. V., Somasundaran, P., Klaessig, F., Castranova, V., & Thompson, M. (2009). Understanding biophysicochemical interactions at the nano–bio interface. *Nature Materials*, 8, 543-557. DOI: https://doi.org/10.1038/nmat2442.

19. Chiu, J. J., & Chien, S. (2011). Effects of disturbed flow on vascular endothelium: pathophysiological basis and clinical perspectives. *Physiological Reviews*, 91(1), 327-387. DOI: https://doi.org/10.1152/physrev.00047.2009.

20. Cines, D. B., Pollak, E. S., Buck, C. A., Loscalzo, J., Zimmerman, G. A., McEver, R. P., Pober, J. S., Wick, T. M., Konkle, B. A., Schwartz, B. S., Barnathan, E. S., McCrae, K. R., Hug, B. A., Schmidt, A. M., & Stern, D. M. (1998). Endothelial Cells in Physiology and in the Pathophysiology of Vascular Disorders. *Blood*, 91(10), 3527-3561. DOI: https://doi.org/10.1182/blood.V91.10.3527.

21. D'Alessio, A. (2023). Role of Endothelial Cell Metabolism in Normal and Tumor Vasculature. *Cancers*, 15(7), 1921. DOI: https://doi.org/10.3390/cancers15071921.

22. Zhao, Y., Vanhoutte, P. M., & Leung, S. W. S. (2015). Vascular nitric oxide: Beyond eNOS. *Journal of Pharmacological Sciences*, 129(2), 83-94. DOI: https://doi.org/10.1016/j.jphs.2015.09.002.

23. Aird, W. C. (2012). Endothelial Cell Heterogeneity. *Cold Spring Harbor Perspectives in Medicine*, 2(1), a006429. DOI: https://doi.org/10.1101/cshperspect.a006429.

24. Aghajanian, A., Wittchen, E. S., Allingham, M. J., Garrett, T. A., & Burridge, K. (2008). Endothelial cell junctions and the regulation of vascular permeability and leukocyte transmigration. *Journal of Thrombosis and Haemostasis*, 6(9), 1453-1460. DOI: https://doi.org/10.1111/j.1538-7836.2008.03087.x.

25. Moncada, S., & Higgs, E. A. (2006). The discovery of nitric oxide and its role in vascular biology. *British Journal of Pharmacology*, 147(Suppl 1), S193-S201. DOI: https://doi.org/10.1038/sj.bjp.0706458.

26. Carmeliet, P. (2005). Angiogenesis in life, disease and medicine. *Nature*, 438(7070), 932-936. DOI: https://doi.org/10.1038/nature04478.

27. Pober, J. S., & Sessa, W. C. (2007). Evolving functions of endothelial cells in inflammation. *Nature Reviews Immunology*, 7(10), 803-815. DOI: https://doi.org/10.1038/nri2171.

28. Gimbrone, M. A. Jr., & García-Cardeña, G. (2016). Endothelial Cell Dysfunction and the Pathobiology of Atherosclerosis. *Circulation Research*, 118(4), 620-636. DOI: https://doi.org/10.1161/CIRCRESAHA.115.306301.

29. Tabit, C. E., Chung, W. B., Hamburg, N. M., & Vita, J. A. (2010). Endothelial dysfunction in diabetes mellitus: molecular mechanisms and clinical implications. *Reviews in Endocrine and Metabolic Disorders*, 11(1), 61-74. DOI: https://doi.org/10.1007/s11154-010-9134-4.

30. Dejana, E., & Orsenigo, F. (2013). Endothelial adherens junctions at a glance. *Journal of Cell Science*, 126(Pt 12), 2545-2549. DOI: https://doi.org/10.1242/jcs.124529.

31. Wallez, Y., & Huber, P. (2008). Endothelial adherens and tight junctions in vascular homeostasis, inflammation and angiogenesis. *Biochimica et Biophysica Acta (BBA) - Biomembranes*, 1778(3), 794-809. DOI: https://doi.org/10.1016/j.bbamem.2007.09.003.

32. Günzel, D., & Fromm, M. (2012). Claudins and other tight junction proteins. *Comprehensive Physiology*, 2(3), 1819-1852. DOI: https://doi.org/10.1002/cphy.c110045.

33. Dejana, E., Orsenigo, F., & Lampugnani, M. G. (2008). The role of adherens junctions and VE-cadherin in the control of vascular permeability. *Journal of Cell Science*, 121(13), 2115-2122. DOI: https://doi.org/10.1242/jcs.017897.

34. Nielsen, M. S., Axelsen, L. N., Sorgen, P. L., Verma, V., Delmar, M., & Holstein-Rathlou, N.-H. (2012). Gap Junctions. *Comprehensive Physiology*, 2(3), 1981-2035. DOI: https://doi.org/10.1002/cphy.c110051.

35. Hatzfeld, M., Keil, R., & Magin, T. M. (2017). Desmosomes and Intermediate Filaments: Their Consequences for Tissue Mechanics. *Cold Spring Harbor Perspectives in Biology*, 9(6), a029157. DOI: https://doi.org/10.1101/cshperspect.a029157.

36. Saito, M., Tucker, D. K., Kohlhorst, D., Niessen, C. M., & Kowalczyk, A. P. (2012). Classical and desmosomal cadherins at a glance. *Journal of Cell Science*, 125(11), 2547-2552. DOI: https://doi.org/10.1242/jcs.066654.

37. Chau, T. C. Y., Keyser, M. S., Da Silva, J. A., Morris, E. K., Yordanov, T. E., Duscyz, K. P., Paterson, S., Yap, A. S., Hogan, B. M., & Lagendijk, A. K. (2023). Dynamically regulated focal adhesions coordinate endothelial cell remodelling in developing vasculature. *Development*, 150(1), dev200454. DOI: https://doi.org/10.1242/dev.200454.

38. Bhat, A. A., Uppada, S., Achkar, I. W., Hashem, S., Yadav, S. K., Shanmugakonar, M., Al-Naemi, H. A., Haris, M., & Uddin, S. (2019). Tight Junction Proteins and Signaling Pathways in Cancer and Inflammation: A Functional Crosstalk. *Frontiers in Physiology*, 9: 1942. DOI: https://doi.org/10.3389/fphys.2018.01942.

39. Suzuki, A., Tomita, H., & Okada, H. (2022). Form follows function: The endothelial glycocalyx. *Translational Research*, 244:14-26. DOI: https://doi.org/10.1016/j.trsl.2022.03.014.

40. Jin, J., Fang, F., Gao, W., Chen, H., Wen, J., Wen, X., & Chen, J. (2021). The Structure and Function of the Glycocalyx and Its Connection With Blood-Brain Barrier. *Frontiers in Cellular Neuroscience*, 15, 739699. DOI: https://doi.org/10.3389/fncel.2021.739699.

41. Mahmoud, M., Mayer, M., Cancel, L. M., Bartosch, A. M., Mathews, R., & Tarbell, J. M. (2021). The glycocalyx core protein Glypican 1 protects vessel wall endothelial cells from stiffness-mediated dysfunction and disease. *Cardiovascular Research*, 117(6), 1592-1605. DOI: https://doi.org/10.1093/cvr/cvaa201.

42. Chignalia, A. Z., Yetimakman, F., Christiaans, S. C., Unal, S., Bayrakci, B., Wagener, B. M., Russell, R. T., Kerby, J. D., Pittet, J. F., & Dull, R. O. (2016). The glycocalyx and Trauma: A Review. *Shock*, 45(4), 338-348. DOI: https://doi.org/10.1097/SHK.0000000000000513.

43. Pretorius, D., Richter, R. P., Anand, T., Cardenas, J. C., & Richter, J. R. (2022). Alterations in heparan sulfate proteoglycan synthesis and sulfation and the impact on vascular endothelial function. *Medical Blood Plasma and Platelet Resuscitation*, 100121. DOI: https://doi.org/10.1016/j.mbplus.2022.100121.

44. Lim, J., Machin, D. R., & Donato, A. J. (2023). The role of hyaluronan in endothelial glycocalyx and potential preventative lifestyle strategy with advancing age. *Current Topics in Membranes*, 91, 139-156. DOI: https://doi.org/10.1016/bs.ctm.2023.02.006.

45. Moore, K. H., Murphy, H. A., & George, E. M. (2021). The glycocalyx: a central regulator of vascular function. *American Journal of Physiology-Regulatory, Integrative and Comparative Physiology*, 320(4), R508-R518. DOI: https://doi.org/10.1152/ajpregu.00340.2020.

46. Uchimido, R., Schmidt, E. P., & Shapiro, N. I. (2019). The glycocalyx: a novel diagnostic and therapeutic target in sepsis. *Critical Care*, 23, 16. DOI: https://doi.org/10.1186/s13054-018-2292-6.

47. Weinbaum, S., Tarbell, J. M., & Damiano, E. R. (2007). The structure and function of the endothelial glycocalyx layer. *Annual Review of Biomedical Engineering*, 9, 121-167. DOI: https://doi.org/10.1146/annurev.bioeng.9.060906.151959.

48. Yang, Y., & Schmidt, E. P. (2013). The endothelial glycocalyx: An important regulator of the pulmonary vascular barrier. *Tissue Barriers*, 1(1), e23494. DOI: https://doi.org/10.4161/tisb.23494.

49. Fels, B., & Kusche-Vihrog, K. (2020). It takes more than two to tango: mechanosignaling of the endothelial surface. *Pflugers Archiv - European Journal of Physiology*, 472(4), 419-433. DOI: https://doi.org/10.1007/s00424-020-02369-2.

50. Tarbell, J. M., & Pahakis, M. Y. (2006). Mechanotransduction and the glycocalyx. *Journal of Internal Medicine*, 259(4), 339-350. DOI: https://doi.org/10.1111/j.1365-2796.2006.01620.x.

51. Penc, S. F., Pomahac, B., Eriksson, E., Detmar, M., & Gallo, R. L. (1999). Dermatan sulfate activates nuclear factor-κB and induces endothelial and circulating intercellular adhesion molecule-1. *Journal of Clinical Investigation*, 103(9), 1329-1335. DOI: https://doi.org/10.1172/JCI4742.

52. Moore, K. H., Murphy, H. A., & George, E. M. (2021). The glycocalyx: a central regulator of vascular function. *American Journal of Physiology-Regulatory, Integrative and Comparative Physiology*, 320(4), R508-R518. DOI: https://doi.org/10.1152/ajpregu.00340.2020.

53. Chatterjee, S., & Fisher, A. B. (2014). Mechanotransduction in the Endothelium: Role of Membrane Proteins and Reactive Oxygen Species in Sensing, Transduction, and Transmission of the Signal with Altered Blood Flow. *Antioxidants & Redox Signaling*, 20(6), 899-913. DOI: https://doi.org/10.1089/ars.2013.5624.

54. Di, X., Gao, X., Peng, L., et al. (2023). Cellular mechanotransduction in health and diseases: from molecular mechanism to therapeutic targets. *Signal Transduction and Targeted Therapy*, 8, 282. DOI: https://doi.org/10.1038/s41392-023-01501-9.

55. Villalba, N., Baby, S., & Yuan, S. Y. (2021). The Endothelial Glycocalyx as a Double-Edged Sword in Microvascular Homeostasis and Pathogenesis. *Frontiers in Cell and Developmental Biology*, 9, 711003. DOI: https://doi.org/10.3389/fcell.2021.711003.

56. Foote, C. A., Soares, R. N., Ramirez-Perez, F. I., Ghiarone, T., Aroor, A., Manrique-Acevedo, C., Padilla, J., & Martinez-Lemus, L. A. (2022). Endothelial Glycocalyx. *Comprehensive Physiology*, 12(4), 3781-3811. DOI: https://doi.org/10.1002/cphy.c210029.

57. Zhao, F., Zhong, L., & Luo, Y. (2021). Endothelial glycocalyx as an important factor in composition of blood-brain barrier. *CNS Neuroscience & Therapeutics*, 27(1), 26-35. DOI: https://doi.org/10.1111/cns.13560.

58. Fan, J., Sun, Y., Xia, Y., Tarbell, J. M., & Fu, B. M. (2019). Endothelial surface glycocalyx (ESG) components and ultra-structure revealed by stochastic optical reconstruction microscopy (STORM). *Biorheology*, 56(2-3), 77-88. DOI: https://doi.org/10.3233/BIR-180204.

59. Curry, F. E., & Michel, C. C. (2021). The Colloid Osmotic Pressure Across the Glycocalyx: Role of Interstitial Fluid Sub-Compartments in Trans-Vascular Fluid Exchange in Skeletal Muscle. *Frontiers in Cell and Developmental Biology*, 9, 729873. DOI: https://doi.org/10.3389/fcell.2021.729873.

60. Tarbell, J. M., Simon, S. I., & Curry, F. E. (2014). Mechanosensing at the Vascular Interface. *Annual Review of Biomedical Engineering*, 16, 505-532. DOI: https://doi.org/10.1146/annurev-bioeng-071813-104908.

61. Thi, M. M., Tarbell, J. M., Weinbaum, S., & Spray, D. C. (2004). The role of the glycocalyx in reorganization of the actin cytoskeleton under fluid shear stress: a 'bumper-car' model. *Proceedings of the National Academy of Sciences of the United States of America (PNAS)*, 101(47), 16483-16488. DOI: https://doi.org/10.1073/pnas.0407474101.

62. Kolářová, H., Ambrůzová, B., Švihálková Šindlerová, L., Klinke, A., & Kubala, L. (2014). Modulation of Endothelial Glycocalyx Structure under Inflammatory Conditions. *Mediators of Inflammation*, 2014, 694312. DOI: https://doi.org/10.1155/2014/694312.

63. Gao, L., & Lipowsky, H. H. (2010). Composition of the endothelial glycocalyx and its relation to its thickness and diffusion of small solutes. *Microvascular Research*, 80(3), 394-401. DOI: https://doi.org/10.1016/j.mvr.2010.06.005.

64. Zeng, Y., & Tarbell, J. M. (2014). The Adaptive Remodeling of Endothelial Glycocalyx in Response to Fluid Shear Stress. *PLoS One*, 9(1), e86249. DOI: https://doi.org/10.1371/journal.pone.0086249.

65. Kumagai, R., Lu, X., & Kassab, G. S. (2009). Role of Glycocalyx in Flow-Induced Production of Nitric Oxide and Reactive Oxygen Species. *Free Radical Biology and Medicine*, 47(5), 600-607. DOI: https://doi.org/10.1016/j.freeradbiomed.2009.05.034.

66. Yao, Y., Rabodzey, A., & Dewey, C. F. Jr. (2007). Glycocalyx modulates the motility and proliferative response of vascular endothelium to fluid shear stress. *American Journal of Physiology-Heart and Circulatory Physiology*, 293(2), H1023-H1030. DOI: https://doi.org/10.1152/ajpheart.00162.2007.

67. Wang, G., Kostidis, S., Tiemeier, G. L., Sol, W. M. P. J., de Vries, M. R., Giera, M., Carmeliet, P., van den Berg, B. M., & Rabelink, T. J. (2020). Shear Stress Regulation of Endothelial Glycocalyx Structure Is Determined by Glucobiosynthesis. *Arteriosclerosis, Thrombosis, and Vascular Biology*, 40(2), 350-364. DOI: https://doi.org/10.1161/ATVBAHA.119.313399.

68. Nieuwdorp, M., Meuwese, M. C., Vink, H., Hoekstra, J. B. L., Kastelein, J. J. P., & Stroes, E. S. G. (2005). The endothelial glycocalyx: a potential barrier between health and vascular disease. *Current Opinion in Lipidology*, 16(5), 507-511. DOI: https://doi.org/10.1097/01.mol.0000181325.08926.9c.

69. Gouverneur, M., van den Berg, B., Nieuwdorp, M., Stroes, E., & Vink, H. (2006). Vasculoprotective properties of the endothelial glycocalyx: effects of fluid shear stress. *Journal of Internal Medicine*, 259(4), 393-400. DOI: https://doi.org/10.1111/j.1365-2796.2006.01625.x.

70. van den Berg, B. M., Vink, H., & Spaan, J. A. E. (2003). The Endothelial Glycocalyx Protects Against Myocardial Edema. *Circulation Research*, 92(6), 592-594. DOI: https://doi.org/10.1161/01.RES.0000065917.53950.75.

71. Bai, K., & Wang, W. (2014). Shear stress-induced redistribution of the glycocalyx on endothelial cells in vitro. *Biomechanics and Modeling in Mechanobiology*, 13(2), 303-311. DOI: https://doi.org/10.1007/s10237-013-0502-3.

72. Qu, J., Cheng, Y., Wu, W., Yuan, L., & Liu, X. (2021). Glycocalyx Impairment in Vascular Disease: Focus on Inflammation. *Frontiers in Cell and Developmental Biology*, 9, 730621. DOI: https://doi.org/10.3389/fcell.2021.730621.

73. Cosgun, Z. C., Fels, B., & Kusche-Vihrog, K. (2020). Nanomechanics of the Endothelial Glycocalyx: From Structure to Function. *The American Journal of Pathology*, 190(4), 732-741. DOI: https://doi.org/10.1016/j.ajpath.2019.07.021.

74. Becker, B. F., Jacob, M., Leipert, S., Salmon, A. H. J., & Chappell, D. (2015). Degradation of the endothelial glycocalyx in clinical settings: searching for the sheddases. *British Journal of Clinical Pharmacology*, 80(3), 389-402. DOI: https://doi.org/10.1111/bcp.12629.

75. Lipowsky, H. H. (2012). The Endothelial Glycocalyx as a Barrier to Leukocyte Adhesion and its Mediation by Extracellular Proteases. *Annals of Biomedical Engineering*, 40(4), 840-848. DOI: https://doi.org/10.1007/s10439-011-0427-x.

76. Potter, D. R., Jiang, J., & Damiano, E. R. (2009). The recovery time course of the endothelial-cell glycocalyx in vivo and its implications in vitro. *Circulation Research*, 104(11), 1318-1325. DOI: https://doi.org/10.1161/CIRCRESAHA.108.191585.

77. Chappell, D., Jacob, M., Hofmann-Kiefer, K., Bruegger, D., Rehm, M., Conzen, P., Welsch, U., & Becker, B. F. (2007). Hydrocortisone Preserves the Vascular Barrier by Protecting the Endothelial Glycocalyx. *Anesthesiology*, 107(5), 776-784. DOI: https://doi.org/10.1097/01.anes.0000286984.39328.96.

78. Chappell, D., Jacob, M., Becker, B. F., et al. (2008). Expedition Glykokalyx. *Der Anaesthesist*, 57(10), 959-969. DOI: https://doi.org/10.1007/s00101-008-1445-4.

79. Singh, A., Ramnath, R. D., Foster, R. R., Wylie, E. C., Fridén, V., Dasgupta, I., Haraldsson, B., Welsh, G. I., Mathieson, P. W., & Satchell, S. C. (2013). Reactive Oxygen Species Modulate the Barrier Function of the Human Glomerular Endothelial Glycocalyx. *PLoS One*, 8(2), e55852. DOI: https://doi.org/10.1371/journal.pone.0055852.

80. Nieuwdorp, M., van Haeften, T. W., Gouverneur, M. C. L. G., Mooij, H. L., van Lieshout, M. H. P., Levi, M., Meijers, J. C. M., Holleman, F., Hoekstra, J. B. L., Vink, H., Kastelein, J. J. P., & Stroes, E. S. G. (2006). Loss of endothelial glycocalyx during acute hyperglycemia coincides with endothelial dysfunction and coagulation activation in vivo. *Diabetes*, 55(2), 480-486. DOI: https://doi.org/10.2337/diabetes.55.02.06.db05-1103.

81. Pastor-Villaescusa, B., Meier, J., Ruske, F., Prell, C., Gruenzner, J., Koenig, M., Jakob, A., Koletzko, B., & Nussbaum, C. (2023). Association between Inflammation, Glycocalyx Biomarkers, and Endothelial Function in Children with Hypercholesterolemia. *Annals of Nutrition and Metabolism*, 82(4), 260-267. DOI: https://doi.org/10.1159/000536042.

82. Yèagle, P. L. (1989). Lipid regulation of cell membrane structure and function. *The FASEB Journal*, 3(7), 1833-1842. DOI: https://doi.org/10.1096/fasebj.3.7.2469614.

83. Bloom, M., Evans, E., & Mouritsen, O. G. (1991). Physical properties of the fluid lipid-bilayer component of cell membranes: a perspective. *Quarterly Reviews of Biophysics*, 24(3), 293-397. DOI: https://doi.org/10.1017/S0033583500003735.

84. Yeagle, P. L. (1985). Cholesterol and the cell membrane. *Biochimica et Biophysica Acta (BBA) - Reviews on Biomembranes*, 822(3-4), 267-287. DOI: https://doi.org/10.1016/0304-4157(85)90011-5.

85. Paukner, K., Králová Lesná, I., & Poledne, R. (2022). Cholesterol in the Cell Membrane—An Emerging Player in Atherogenesis. *International Journal of Molecular Sciences*, 23(1), 533. DOI: https://doi.org/10.3390/ijms23010533.

86. Heimburg, T. (2000). A Model for the Lipid Pretransition: Coupling of Ripple Formation with the Chain-Melting Transition. *Biophysical Journal*, 78(3), 1154-1165. DOI: https://doi.org/10.1016/S0006-3495(00)76673-2.

87. Heimburg, T. (2007). *Thermal Biophysics of Membranes*. Wiley-VCH Verlag GmbH & Co. KGaA. DOI: https://doi.org/10.1002/9783527611591.

88. Kranenburg, M., & Smit, B. (2005). Phase Behavior of Model Lipid Bilayers. *The Journal of Physical Chemistry B*, 109(14), 6553-6563. DOI: https://doi.org/10.1021/jp0457646.

89. M'Baye, G., Mély, Y., Duportail, G., & Klymchenko, A. S. (2008). Liquid Ordered and Gel Phases of Lipid Bilayers: Fluorescent Probes Reveal Close Fluidity but Different Hydration. *Biophysical Journal*, 95(3), 1217-1225. DOI: https://doi.org/10.1529/biophysj.107.127480.

90. Lingwood, D., & Simons, K. (2010). Lipid Rafts As a Membrane-Organizing Principle. *Science*, 327(5961), 46-50. DOI: https://doi.org/10.1126/science.1174621.

91. Levental, I., Grzybek, M., & Simons, K. (2011). Raft domains of variable properties and compositions in plasma membrane vesicles. *Proceedings of the National Academy of Sciences*, 108(28), 11411-11416. DOI: https://doi.org/10.1073/pnas.1105996108.

92. Johnston, E. J., Moses, T., & Rosser, S. J. (2019). The wide-ranging phenotypes of ergosterol biosynthesis mutants, and implications for microbial cell factories. *Yeast*, 36(11), 497-512. DOI: https://doi.org/10.1002/yea.3452.

93. Johnston, E. J., Moses, T., & Rosser, S. J. (2019). TRP Channels as Sensors of Chemically-Induced Changes in Cell Membrane Mechanical Properties. *International Journal of Molecular Sciences*, 20(2), 371. DOI: https://doi.org/10.3390/ijms20020371.

94. Heimburg, T. (1998). Mechanical aspects of membrane thermodynamics. Estimation of the mechanical properties of lipid membranes close to the chain melting transition from calorimetry. *Biochimica et Biophysica Acta (BBA) - Biomembranes*, 1415(1), 147-162. DOI: https://doi.org/10.1016/S0005-2736(98)00189-8.

95. Sun, L., & Böckmann, R. A. (2018). Membrane phase transition during heating and cooling: molecular insight into reversible melting. *European Biophysics Journal*, 47(2), 151-164. DOI: https://doi.org/10.1007/s00249-017-1237-3.

96. Chapman, D. (1988). Phospholipid bilayers physical principles and models. Gregor Cevc and Derek Marsh (Eds), John Wiley and Sons Ltd. *Cell Biochemistry and Function*, 6(2), 206. DOI: https://doi.org/10.1002/cbf.290060221.

97. Heimburg, T. (2010). Lipid ion channels. *Biophysical Chemistry*, 150(1-3), 2-22. DOI: https://doi.org/10.1016/j.bpc.2010.02.018.

98. Mužić, T., Tounsi, F., Madsen, S. B., Pollakowski, D., Konrad, M., & Heimburg, T. (2019). Melting transitions in biomembranes. *Biochimica et Biophysica Acta (BBA) - Biomembranes*, 1861(10), 183026. DOI: https://doi.org/10.1016/j.bbamem.2019.07.014.

99. Lee, A. G. (2011). Biological membranes: the importance of molecular detail. *Trends in Biochemical Sciences*, 36(9), 493-500. DOI: https://doi.org/10.1016/j.tibs.2011.06.007.

100. Parasassi, T., & Gratton, E. (1995). Membrane lipid domains and dynamics as detected by Laurdan fluorescence. Journal of Fluorescence, 5(1), 59-69. DOI: https://doi.org/10.1007/BF00718783.

101. Sánchez, S. A., Gratton, E., & Hibbs, R. (2007). Laurdan generalized polarization: from cuvette to microscope. *Modern Research and Educational Topics in Microscopy*, 2, 1007-1014.

102. Parasassi, T., Gratton, E., Yu, W. M., Wilson, P., & Levi, M. (1997). Two-photon fluorescence microscopy of laurdan generalized polarization domains in model and natural membranes. *Biophysical Journal*, 72(6), 2413-2429. DOI: https://doi.org/10.1016/S0006-3495(97)78887-8.

103. Jay, A. G., & Hamilton, J. A. (2017). Disorder Amidst Membrane Order: Standardizing Laurdan Generalized Polarization and Membrane Fluidity Terms. *Journal of Fluorescence*, 27(1), 243-249. DOI: https://doi.org/10.1007/s10895-016-1951-8.

104. Färber, N., & Westerhausen, C. (2021). Broad lipid phase transitions in mammalian cell membranes measured by Laurdan fluorescence spectroscopy. *Biochimica et Biophysica Acta (BBA) - Biomembranes*, 1863(3), 183794. DOI: https://doi.org/10.1016/j.bbamem.2021.183794.

105. Zhang, L., Gu, F. X., Chan, J. M., Wang, A. Z., Langer, R. S., & Farokhzad, O. C. (2008). Nanoparticles in Medicine: Therapeutic Applications and Developments. *Clinical Pharmacology & Therapeutics*, 83(5), 761-769. DOI: https://doi.org/10.1038/sj.clpt.6100400.

106. Peer, D., Karp, J. M., Hong, S., Farokhzad, O. C., Margalit, R., & Langer, R. (2007). Nanocarriers as an emerging platform for cancer therapy. *Nature Nanotechnology*, 2(12), 751-760. DOI: https://doi.org/10.1038/nnano.2007.387.

107. Treuel, L., Jiang, X., & Nienhaus, G. U. (2013). New views on cellular uptake and trafficking of manufactured nanoparticles. *Journal of the Royal Society Interface*, 10(82), 20120939. DOI: https://doi.org/10.1098/rsif.2012.0939.

108. Verma, A., & Stellacci, F. (2010). Effect of Surface Properties on Nanoparticle–Cell Interactions. *Small*, 6(1), 12-21. DOI: https://doi.org/10.1002/smll.200901158.

109. Penman, R., Kariuki, R., Shaw, Z. L., Dekiwadia, C., Christofferson, A. J., Bryant, G., Vongsvivut, J., Bryant, S. J., & Elbourne, A. (2023). Gold nanoparticle adsorption alters the cell stiffness and cell wall bio-chemical landscape of Candida albicans fungal cells. *Journal of Colloid and Interface Science*. DOI: https://doi.org/10.1016/j.jcis.2023.10.017.

110. Behzadi, S., Serpooshan, V., Tao, W., Hamaly, M. A., Alkawareek, M. Y., Dreaden, E. C., Brown, D., Alkilany, A. M., Farokhzad, O. C., & Mahmoudi, M. (2017). Cellular Uptake of Nanoparticles: Journey Inside the Cell. *Chemical Society Reviews*, 46(14), 4218-4244. DOI: https://doi.org/10.1039/c6cs00636a.

111. Rennick, J., Johnston, A., & Parton, R. G. (2021). Key principles and methods for studying the endocytosis of biological and nanoparticle therapeutics. *Nature Nanotechnology*, 16(3), 266-276. DOI: https://doi.org/10.1038/s41565-021-00858-8.

112. Blasco, S., Sukeník, L., & Vácha, R. (2024). Nanoparticle induced fusion of lipid membranes. *Nanoscale*, 16(21), 10221-10229. DOI: https://doi.org/10.1039/d4nr00591k.

113. Huang, X., Li, L., Liu, T., Hao, N., Liu, H., Chen, D., & Tang, F. (2011). The shape effect of mesoporous silica nanoparticles on biodistribution, clearance, and biocompatibility in vivo. *ACS Nano*, 5(7), 5390-5399. DOI: https://doi.org/10.1021/nn200365a

114. Jiang, W., Kim, B., Rutka, J., & Chan, W. (2008). Nanoparticle-mediated cellular response is size-dependent. *Nature Nanotechnology*, 3, 145-150. DOI: https://doi.org/10.1038/nnano.2008.30.

115. Salvati, A., Pitek, A. S., Monopoli, M. P., Prapainop, K., Baldelli Bombelli, F., Hristov, D. R., Kelly, P. M., Åberg, C., Mahon, E., & Dawson, K. A. (2013). Transferrin-functionalized nanoparticles lose their targeting capabilities when a biomolecule corona adsorbs on the surface. *Nature Nanotechnology*, 8, 137-143. DOI: https://doi.org/10.1038/nnano.2012.237.

116. Lesniak, A., Fenaroli, F., Monopoli, M. P., Åberg, C., Dawson, K. A., & Salvati, A. (2012). Effects of the Presence or Absence of a Protein Corona on Silica Nanoparticle Uptake and Impact on Cells. *ACS Nano*, 6(7), 5845-5857. DOI: https://doi.org/10.1021/nn300223w.

117. Lundqvist, M., Stigler, J., Elia, G., Lynch, I., Cedervall, T., & Dawson, K. A. (2008). Nanoparticle size and surface properties determine the protein corona with possible implications for biological impacts. *Proceedings of the National Academy of Sciences of the United States of America*, 105(38), 14265-14270. DOI: https://doi.org/10.1073/pnas.0805135105.

118. Decuzzi, P., & Ferrari, M. (2007). The role of specific and non-specific interactions in receptor-mediated endocytosis of nanoparticles. *Biomaterials*, 28(18), 2915-2922. DOI: https://doi.org/10.1016/j.biomaterials.2007.02.013.

119. Fam, S. Y., Chee, C. F., Yong, C. Y., Ho, K. L., Mariatulqabtiah, A. R., & Tan, W. S. (2020). Stealth Coating of Nanoparticles in Drug-Delivery Systems. *Nanomaterials*, 10(4), 787. DOI: https://doi.org/10.3390/nano10040787.

120. Torchilin, V. P., & Trubetskoy, V. S. (1995). Which polymers can make nanoparticulate drug carriers long-circulating? *Advanced Drug Delivery Reviews*, 16(2-3), 141-155. DOI: https://doi.org/10.1016/0169-409X(95)00022-Y.

121. Makvandi, P., Chen, M., Sartorius, R., Zarrabi, A., Ashrafizadeh, M., Dabbagh Moghaddam, F., Ma, J., Mattoli, V., & Tay, F. R. (2021). Endocytosis of abiotic nanomaterials and nanobiovectors: Inhibition of membrane trafficking. *Nano Today*, 40, 101279. DOI: https://doi.org/10.1016/j.nantod.2021.101279.

122. Means, N., Elechalawar, C. K., Chen, W. R., Bhattacharya, R., & Mukherjee, P. (2022). Revealing macropinocytosis using nanoparticles. *Molecular Aspects of Medicine*, 83, 100993. DOI: https://doi.org/10.1016/j.mam.2021.100993.

123. dos Santos, T., Varela, J., Lynch, I., Salvati, A., & Dawson, K. A. (2011). Quantitative Assessment of the Comparative Nanoparticle-Uptake Efficiency of a Range of Cell Lines. *Small*, 7(23), 3341-3349. DOI: https://doi.org/10.1002/smll.201101076.

124. Doktorova, M., Heberle, F. A., Eicher, B., Standaert, R. F., Katsaras, J., & London, E. (2018). Preparation of asymmetric phospholipid vesicles for use as cell membrane models. *Nature Protocols*, 13(9), 2086-2101. DOI: https://doi.org/10.1038/s41596-018-0033-6.

125. Hamada, T., & Yoshikawa, K. (2012). Cell-Sized Liposomes and Droplets: Real-World Modeling of Living Cells. *Materials*, 5(11), 2292-2305. DOI: https://doi.org/10.3390/ma5112292.

126. Deserno, M., & Gelbart, W. M. (2002). Adhesion and Wrapping in Colloid−Vesicle Complexes. *The Journal of Physical Chemistry B*, 106(21), 5543-5552. DOI: https://doi.org/10.1021/jp0138476.

127. Bahrami, A. H., Raatz, M., Agudo-Canalejo, J., Michel, R., Curtis, E. M., Hall, C. K., Gradzielski, M., Lipowsky, R., & Weikl, T. R. (2014). Wrapping of nanoparticles by membranes. *Advances in Colloid and Interface Science*, 208, 214-224. DOI: https://doi.org/10.1016/j.cis.2014.02.012.

128. Strobl, F. G., Czubak, D. M., Wixforth, A., & Westerhausen, C. (2019). Ion controlled passive nanoparticle uptake in lipid vesicles in theory and experiment. *Journal of Physics D: Applied Physics*, 52(29), 294001. DOI: https://doi.org/10.1088/1361-6463/ab1994.

129. Tang, H., Ye, H., Zhang, H., & Zheng, Y. (2015). Wrapping of nanoparticles by the cell membrane: the role of interactions between the nanoparticles. *Soft Matter*, 11(44), 8667-8676. DOI: https://doi.org/10.1039/C6NR07179A.

130. Gao, H., Shi, W., & Freund, L. B. (2005). Mechanics of receptor-mediated endocytosis. *Proceedings of the National Academy of Sciences of the United States of America (PNAS)*, 102(27), 9469-9474. DOI: https://doi.org/10.1073/pnas.0503879102.

131. Kirchhausen, T. (2012). Bending membranes. *Nature Cell Biology*, 14(9), 906–908. DOI: https://doi.org/10.1038/ncb2570.

132. Simunovic, M., & Voth, G. A. (2015). Membrane tension controls the assembly of curvature-generating proteins. *Nature Communications*, 6, 7219. DOI: https://doi.org/10.1038/ncomms8219.

133. Sens, P., & Turner, M. S. (2006). Budded membrane microdomains as tension regulators. *Physical Review E Statistical, Nonlinear, and Soft Matter Physics*, 73(3 Pt 1), 031918. DOI: https://doi.org/10.1103/PhysRevE.73.031918.

134. Zhang, X., Ma, G., & Wei, W. (2021). Simulation of nanoparticles interacting with a cell membrane: probing the structural basis and potential biomedical application. *NPG Asia Materials*, 13, 52. DOI: https://doi.org/10.1038/s41427-021-00320-0.

135. Strobl, F. G., Seitz, F., Westerhausen, C., Reller, A., Torrano, A. A., Bräuchle, C., Wixforth, A., & Schneider, M. F. (2014). Intake of silica nanoparticles by giant lipid vesicles: influence of particle size and thermodynamic membrane state. *Beilstein Journal of Nanotechnology*, 5, 2468-2478. DOI: https://doi.org/10.3762/bjnano.5.256.

136. Yang, N. J., & Hinner, M. J. (2015). Getting Across the Cell Membrane: An Overview for Small Molecules, Peptides, and Proteins. *Methods in Molecular Biology*, 1266, 29-53. DOI: https://doi.org/10.1007/978-1-4939-2272-7_3.

137. Gutknecht, J., Bisson, M. A., & Tosteson, F. C. (1977). Diffusion of carbon dioxide through lipid bilayer membranes. Effects of carbonic anhydrase, bicarbonate, and unstirred layers. *The Journal of General Physiology*, 69(6), 779-794. DOI: https://doi.org/10.1085/jgp.69.6.779.

138. Subczynski, W. K., Hyde, J. S., & Kusumi, A. (1989). Oxygen permeability of phosphatidylcholine--cholesterol membranes. *Proceedings of the National Academy of Sciences of the United States of America*, 86(12), 4474-4478. DOI: https://doi.org/10.1073/pnas.86.12.4474.

139. Cooper, G. M. (2000). *The Cell: A Molecular Approach* (2nd ed.). Sunderland (MA): Sinauer Associates. ISBN-10: 0-87893-106-6.

140. Brini, M., Calì, T., Ottolini, D., & Carafoli, E. (2013). The plasma membrane calcium pump in health and disease. *The FEBS Journal*, 280(21), 5385-5397. DOI: https://doi.org/10.1111/febs.12193.

141. Alberts, B., Johnson, A., Lewis, J., Raff, M., Roberts, K., & Walter, P. (2002). *Molecular Biology of the Cell* (4th ed.). New York: Garland Science. ISBN-10: 0-8153-3218-1.

142. Blicher, A., Wodzinska, K., Fidorra, M., Winterhalter, M., & Heimburg, T. (2009). The temperature dependence of lipid membrane permeability, its quantized nature, and the influence of anesthetics. *Biophysical Journal*, 96(11), 4581-4591. DOI: https://doi.org/10.1016/j.bpj.2009.01.062.

143. Gudmand, M., Fidorra, M., Bjørnholm, T., & Heimburg, T. (2009). Diffusion and Partitioning of Fluorescent Lipid Probes in Phospholipid Monolayers. *Biophysical Journal*, 96(11), 4592-4600. DOI: https://doi.org/10.1016/j.bpj.2009.01.063.

144. Krüger-Genge, A., Blocki, A., Franke, R.-P., & Jung, F. (2019). Vascular Endothelial Cell Biology: An Update. *International Journal of Molecular Sciences*, 20(18), 4411. DOI: https://doi.org/10.3390/ijms20184411.

145. Rajendran, P., Rengarajan, T., Thangavel, J., Nishigaki, Y., Sakthisekaran, D., Sethi, G., & Nishigaki, I. (2013). The Vascular Endothelium and Human Diseases. *International Journal of Biological Sciences*, 9(10), 1057-1069. DOI: https://doi.org/10.7150/ijbs.7502.

146. Rippe, B., & Haraldsson, B. (1994). Transport of macromolecules across microvascular walls: the two-pore theory. *Physiological Reviews*, 74(1), 163-219. DOI: https://doi.org/10.1152/physrev.1994.74.1.163.

147. Dejana, E., Tournier-Lasserve, E., & Weinstein, B. M. (2009). The control of vascular integrity by endothelial cell junctions: molecular basis and pathological implications. *Developmental Cell*, 16(2), 209-221. DOI: https://doi.org/10.1016/j.devcel.2009.01.004.

148. Michel, C. C., & Curry, F. E. (1999). Microvascular permeability. *Physiological Reviews*, 79(3), 703-761. DOI: https://doi.org/10.1152/physrev.1999.79.3.703.

149. Tarbell, J. M. (2010). Shear stress and the endothelial transport barrier. *Cardiovascular Research*, 87(2), 320–330. DOI: https://doi.org/10.1093/cvr/cvq146.

150. Lieleg, O., & Ribbeck, K. (2011). Biological hydrogels as selective diffusion barriers. *Trends in Cell Biology*, 21(9), 543-551. DOI: https://doi.org/10.1016/j.tcb.2011.06.002. PMCID: PMC3164742. PMID: 21727007.

151. Peppas, N. A., & Sahlin, J. J. (1996). Hydrogels as mucoadhesive and bioadhesive materials: a review. *Biomaterials*, 17(16), 1553-1561. DOI: https://doi.org/10.1016/0142-9612(95)00307-X.

152. Gomez-Florit, M., Pardo, A., Domingues, R. M. A., Graça, A. L., Babo, P. S., Reis, R. L., & Gomes, M. E. (2020). Natural-Based Hydrogels for Tissue Engineering Applications. *Molecules*, 25(24), 5858. DOI: https://doi.org/10.3390/molecules25245858.

153. Saludas, L., Pascual-Gil, S., Prósper, F., Garbayo, E., & Blanco-Prieto, M. (2017). Hydrogel based approaches for cardiac tissue engineering. *International Journal of Pharmaceutics*, 523(2), 454-475. DOI: https://doi.org/10.1016/j.ijpharm.2016.10.061.

154. Krüger-Genge, A., Hauser, S., Neffe, A. T., Liu, Y., Lendlein, A., Pietzsch, J., & Jung, F. (2021). Response of Endothelial Cells to Gelatin-Based Hydrogels. *ACS Biomaterials Science & Engineering*, 7(2), 527-540. DOI: https://doi.org/10.1021/acsbiomaterials.0c01432.

155. Crank, J. (1979). *The Mathematics of Diffusion* (Illustrated, Reprint ed.). Clarendon Press. ISBN: 0198534116, 9780198534112.

156. Cussler, E. L. (2009). *Diffusion: Mass Transfer in Fluid Systems* (3rd ed.). Cambridge University Press. ISBN-10: 0-521-87121-2; ISBN-13: 978-0-521-87121-1.

157. Oertel Jr., H. (2022). *Prandtl - Führer Durch Die Strömungslehre: Grundlagen und Phänomene* (15th ed.). Wiesbaden: Springer Vieweg. ISBN: 978-3-658-27894-6. DOI: https://doi.org/10.1007/978-3-658-27894-6_3.

158. Meschede, D. (Ed.). (2010). *Gerthsen Physik* (24th ed.). Springer. ISBN: 978-3-642-12893-6; e-ISBN: 978-3-642-12894-3. DOI: https://doi.org/10.1007/978-3-642-12894-3.

159. Wibowo, D., Zhao, C.-X., & He, Y. (2019). Fluid properties and hydrodynamics of microfluidic systems. In *Microfluidics for Pharmaceutical Applications: From Nano/micro Systems Fabrication to Controlled Drug Delivery* (pp. 37-77). Micro and Nano Technologies, Elsevier. DOI: https://doi.org/10.1016/B978-0-12-812659-2.00002-8.

160. Cornish, R. J. (1928). Flow in a pipe of rectangular cross-section. *Proceedings of the Royal Society A: Mathematical, Physical and Engineering Sciences*, 120(786), 691-700. DOI: https://doi.org/10.1098/rspa.1928.0175.

161. Jaffe, E. A., Nachman, R. L., Becker, C. G., & Minick, C. R. (1973). Culture of human endothelial cells derived from umbilical veins. Identification by morphologic and immunologic criteria. *The Journal of Clinical Investigation*, 52(11), 2745-2756. DOI: https://doi.org/10.1172/JCI107470.

162. Medina-Leyte, D. J., Domínguez-Pérez, M., Mercado, I., Villarreal-Molina, M. T., & Jacobo-Albavera, L. (2020). Use of Human Umbilical Vein Endothelial Cells (HUVEC) as a Model to Study Cardiovascular Disease: A Review. *Applied Sciences*, 10(3), 938. DOI: https://doi.org/10.3390/app10030938.

163. Liao, H., He, H., Chen, Y., Zeng, F., Huang, J., Wu, L., & Chen, Y. (2014). Effects of long-term serial cell passaging on cell spreading, migration, and cell-surface ultrastructures of cultured vascular endothelial cells. *Cytotechnology*, 66(2), 229-238. DOI: https://doi.org/10.1007/s10616-013-9560-8.

164. Fearnley, G. W., Smith, G. A., Odell, A. F., Latham, A. M., Wheatcroft, S. B., Harrison, M. A., Tomlinson, D. C., & Ponnambalam, S. (2013). Vascular Endothelial Growth Factor A-Stimulated Signaling from Endosomes in Primary Endothelial Cells. In *Methods in Enzymology* (Vol. 535, pp. 265-290). Elsevier. DOI: https://doi.org/10.1016/B978-0-12-397925-4.00016-X.

165. Peter, B., Kanyo, N., Kovacs, K. D., Kovács, V., Szekacs, I., Pécz, B., Molnár, K., Nakanishi, H., Lagzi, I., & Horvath, R. (2023). Glycocalyx Components Detune the Cellular Uptake of Gold Nanoparticles in a Size- and Charge-Dependent Manner. *ACS Applied Bio Materials*, 6(1), 64–73. DOI: https://doi.org/10.1021/acsabm.2c00595.

166. Stringer, C., Wang, T., Michaelos, M., & Pachitariu, M. (2021). Cellpose: a generalist algorithm for cellular segmentation. *Nature Methods*, 18, 100–106. DOI: https://doi.org/10.1038/s41592-020-01018-x.

167. Pachitariu, M., & Stringer, C. (2022). Cellpose 2.0: how to train your own model. *Nature Methods*, 19, 1634–1641. DOI: https://doi.org/10.1038/s41592-022-01663-4.

168. Yi, X., & Gao, H. (2017). Kinetics of receptor-mediated endocytosis of elastic nanoparticles. *Nanoscale*, 9, 454-463. DOI: https://doi.org/10.1039/C6NR07179A.

169. Wittmann, C. G., Kamenac, A., Strobl, F. G., Czubak, D., Wixforth, A., & Westerhausen, C. (2018). Ionic Strength and the Supporting Material Strongly Influence the Adhesion of Silica to Supported Lipid Bilayers. *Advanced Biosystems*, 2(9), 1800087. DOI: https://doi.org/10.1002/adbi.201800087.

170. Möckl, L., Hirn, S., Torrano, A. A., Uhl, B., Bräuchle, C., & Krombach, F. (2017). The Glycocalyx Regulates the Uptake of Nanoparticles By Human Endothelial Cells In Vitro. *Nanomedicine*, 12(3), 207-217. DOI: https://doi.org/10.2217/nnm-2016-0332.

171. Zimmer, O., & Goepferich, A. (2023). How clathrin-coated pits control nanoparticle avidity for cells. *Nanoscale Horizons*. DOI: https://doi.org/10.1039/D2NH00543C.

172. Yamamoto, K., & Ando, J. (2013). Endothelial cell and model membranes respond to shear stress by rapidly decreasing the order of their lipid phases. *Journal of Cell Science*, 126(5), 1227-1234. DOI: https://doi.org/10.1242/jcs.119628.

173. Färber, N., Reitler, J., Schäfer, J., & Westerhausen, C. (2023). Transport Across Cell Membranes is Modulated by Lipid Order. *Advanced Biology*, 7(3), 202200282. DOI: https://doi.org/10.1002/adbi.202200282.

174. DeStefano, J. G., Williams, A., Wnorowski, A., Yimam, N., Searson, P. C., & Wong, A. D. (2017). Real-time quantification of endothelial response to shear stress and vascular modulators. *Integrative Biology*, 9(6), 362-374. DOI: https://doi.org/10.1039/c7ib00023e.

175. Sirch, M. M., Kamenac, A., Neidinger, S. V., Wixforth, A., & Westerhausen, C. (2023). Phase-State-Dependent Silica Nanoparticle Uptake of Giant Unilamellar Vesicles. *Journal of Physical Chemistry B*, 127(32), 7238-7247. DOI: https://doi.org/10.1021/acs.jpcb.4c02383.

176. Cordeiro, M. M., Filipe, H. A. L., dos Santos, P., Samelo, J., Ramalho, J. P. P., Loura, L. M. S., & Moreno, M. J. (2023). Interaction of Hoechst 33342 with POPC Membranes at Different pH Values. *Molecules*, 28(15), 5640. DOI: https://doi.org/10.3390/molecules28155640.

177. Constantinescu, A. A., Vink, H., & Spaan, J. A. E. (2003). Endothelial Cell Glycocalyx Modulates Immobilization of Leukocytes at the Endothelial Surface. *Arteriosclerosis, Thrombosis, and Vascular Biology*, 23(9), 1541–1547. DOI: https://doi.org/10.1161/01.ATV.0000085630.24353.3a.

178. Blicher, A., & Heimburg, T. (2013). Voltage-Gated Lipid Ion Channels. *PLoS One*, 8(6), e65707. DOI: https://doi.org/10.1371/journal.pone.0065707.

179. Butler, P. J., Norwich, G., Weinbaum, S., & Chien, S. (2001). Shear stress induces a time- and position-dependent increase in endothelial cell membrane fluidity. *American Journal of Physiology-Cell Physiology*, 280(4), C962–C969. DOI: https://doi.org/10.1152/ajpcell.2001.280.4.C962.

180. Butler, P. J., Norwich, G., Weinbaum, S., & Chien, S. (1999). Shear stress increases endothelial cell-membrane fluidity. *Proceedings of The First Joint BMES/EMBS Conference Serving Humanity, Advancing Technology* (Oct. 13-16, 1999, Atlanta, GA, USA), IEEE. DOI: https://doi.org/10.1109/IEMBS.1999.802024.

181. Simberg, D., Weisman, S., Talmon, Y., & Barenholz, Y. (2004). DOTAP: Chemistry, biophysics, and transfection. *Critical Reviews in Therapeutic Drug Carrier Systems*, 21(4), 257-317. DOI: https://doi.org/10.1615/CritRevTherDrugCarrierSyst.v21.i4.10.

182. Stamatatos, L., Leventis, R., Zuckermann, M. J., & Silvius, J. R. (1988). Interactions of cationic lipid vesicles with negatively charged phospholipid vesicles and biological membranes. *Biochemistry*, 27(11), 3917–3925. DOI: https://doi.org/10.1021/bi00411a005.

183. Böhringer, M., Murugaiyan, J., Eravci, M., Weise, C., Roesler, U., Neubauer, H., & Sprague, L. D. (2020). Treatment of *Yersinia similis* with the cationic lipid DOTAP enhances adhesion to and invasion into intestinal epithelial cells - A proof-of-principle study. *Biochemical and Biophysical Research Communications*, 524(2), 373-379. DOI: https://doi.org/10.1016/j.bbrc.2020.02.081.

184. Tarbell, J. M., & Ebong, E. E. (2008). The endothelial glycocalyx: a mechano-sensor and -transducer. *Science Signaling*, 1(40), pt8. DOI: https://doi.org/10.1126/scisignal.140pt8.

185. Ebong, E. E., Macaluso, F. P., Spray, D. C., & Tarbell, J. M. (2011). Imaging the endothelial glycocalyx in vitro by rapid freezing/freeze substitution transmission electron microscopy. *Arteriosclerosis, Thrombosis, and Vascular Biology*, 31(8), 1908-1915. DOI: https://doi.org/10.1161/ATVBAHA.111.225268.

186. Vasantharajan, S. S., Barnett, E., Gray, E. S., Rodger, E. J., Eccles, M. R., Pattison, S., Munro, F., & Chatterjee, A. (2022). Size-Based Method for Enrichment of Circulating Tumor Cells from Blood of Colorectal Cancer Patients. *Methods in Molecular Biology*, 978-1-0716-2780-8_15. DOI: https://doi.org/10.1007/978-1-0716-2780-8_15.

187. Liang, L., Song, X., Zhao, H., & Lim, C. T. (2024). Insights into the mechanobiology of cancer metastasis via microfluidic technologies. *APL Bioengineering*, 8(2), 021506. DOI: https://doi.org/10.1063/5.0195389.

188. Dorland, Y.L., & Huveneers, S. (2017). Cell–cell junctional mechanotransduction in endothelial remodeling. *Cellular and Molecular Life Sciences*, 74, 279–292. DOI: https://doi.org/10.1007/s00018-016-2325-8.

189. Yeh, H. I., Dupont, E., Coppen, S., Rothery, S., & Severs, N. J. (1997). Gap junction localization and connexin expression in cytochemically identified endothelial cells of arterial tissue. *Journal of Histochemistry & Cytochemistry*, 45(4), 539–549. DOI: https://doi.org/10.1177/002215549704500406.

190. DePaola, N., Davies, P. F., Pritchard Jr, W. F., Florez, L., Harbeck, N., & Polacek, D. C. (1999). Spatial and temporal regulation of gap junction connexin43 in vascular endothelial cells exposed to controlled disturbed flows in vitro. *Proceedings of the National Academy of Sciences*, 96(6), 3154–3159. DOI: https://doi.org/10.1073/pnas.96.6.3154.

191. Weber, C. R. (2012). Dynamic properties of the tight junction barrier. *Annals of the New York Academy of Sciences*, 1257, 77–84. DOI: https://doi.org/10.1111/j.1749-6632.2012.06528.x.

192. Haywood-Watson, R. J., Holcomb, J. B., Gonzalez, E. A., Peng, Z., Pati, S., Park, P. W., Wang, W., Zaske, A. M., Menge, T., & Kozar, R. A. (2011). Modulation of Syndecan-1 Shedding after Hemorrhagic Shock and Resuscitation. *PLoS One*, *6*(8), e23530. DOI: https://doi.org/10.1371/journal.pone.0023530.

193. London, N. R., Whitehead, K. J., & Li, D. Y. (2009). Endogenous endothelial cell signaling systems maintain vascular stability. *Angiogenesis*, *12*(2), 149–158. DOI: https://doi.org/10.1007/s10456-009-9130-z.

194. Stirling, D. R., Carpenter, A. E., & Cimini, B. A. (2021). CellProfiler Analyst 3.0: Accessible data exploration and machine learning for image analysis. *Bioinformatics*, 37(21), 3992–3994. https://doi.org/10.1093/bioinformatics/btab634.

195. Janssen, A. F. J., Breusegem, S. Y., & Larrieu, D. (2022). Current Methods and Pipelines for Image-Based Quantitation of Nuclear Shape and Nuclear Envelope Abnormalities. *Cells*, *11*(3), 347. DOI: https://doi.org/10.3390/cells11030347.

196. Harvey, S. E., & VandenBussche, C. J. (2023). Nuclear membrane irregularity in high-grade urothelial carcinoma cells can be measured by using circularity and solidity as morphometric shape definitions in digital image analysis of urinary tract cytology specimens. *Cancer Cytopathology*. DOI: https://doi.org/10.1002/cncy.22682.

197. Tzima, E., Irani-Tehrani, M., Kiosses, W. B., Dejana, E., Schultz, D. A., Engelhardt, B., Cao, G., DeLisser, H., & Schwartz, M. A. (2005). A mechanosensory complex that mediates the endothelial cell response to fluid shear stress. *Nature*, 437(7057), 426-431. https://doi.org/10.1038/nature03952.

198. Cheng, H., Zhong, W., Wang, L., Zhang, Q., Ma, X., Wang, Y., Wang, S., He, C., Wei, Q., & Fu, C. (2022). Effects of shear stress on vascular endothelial functions in atherosclerosis and potential therapeutic approaches. *Biomedicine & Pharmacotherapy*, 153, 114198. https://doi.org/10.1016/j.biopha.2022.114198.

199. Malek, A. M., & Izumo, S. (1996). Mechanism of endothelial cell shape change and cytoskeletal remodeling in response to fluid shear stress. *Journal of Cell Science*, 109(4), 713-726. https://doi.org/10.1242/jcs.109.4.713.

200. Pakravan, H. A., Saidi, M. S., & Firoozabadi, B. (2020). Endothelial Cells Morphology in Response to Combined WSS and Biaxial CS: Introduction of Effective Strain Ratio. *Cellular and Molecular Bioengineering*, 13, 647–657. https://doi.org/10.1007/s12195-020-00618-z.

201. Gan, Q., Dai, D., Yuan, Y., et al. (2012). Effect of size on the cellular endocytosis and controlled release of mesoporous silica nanoparticles for intracellular delivery. Biomedical Microdevices, 14, 259–270. https://doi.org/10.1007/s10544-011-9604-9.

202. Arribas Perez, M., & Beales, P. A. (2022). Protein corona alters the mechanisms of interaction between silica nanoparticles and lipid vesicles. *Soft Matter*, 18, 5021–5026. https://doi.org/10.1039/D2SM00739H.

203. Cunill-Semanat, E., & Salgado, J. (2019). Spontaneous and stress-induced pore formation in membranes: Theory, experiments and simulations. *Journal of Membrane Biology*, 252, 241–260. https://doi.org/10.1007/s00232-019-00083-4.

204. Molotkovsky, R. J., & Akimov, S. A. (2009). Calculation of line tension in various models of lipid bilayer pore edge. Biochemistry (Moscow) Supplement Series A: Membrane and Cell Biology, 3, 223–230. https://doi.org/10.1134/S1990747809020160.

205. Sandrin, D., Wagner, D., Sitta, C. E., Thoma, R., Felekyan, S., Hermes, H. E., Janiak, C., de Sousa Amadeu, N., Kühnemuth, R., Löwen, H., Egelhaaf, S. U., & Seidel, C. A. M. (2016). Diffusion of macromolecules in a polymer hydrogel: from microscopic to macroscopic scales. *Physical Chemistry Chemical Physics*, 18, 12860–12876. https://doi.org/10.1039/C5CP07781H.

206. Bonnaud, B., Miège, C., Daval, A., et al. (2022). Determination of diffusion coefficients in agarose and polyacrylamide gels for 112 organic chemicals for passive sampling by organic Diffusive Gradients in Thin films (o-DGT). *Environmental Science and Pollution Research*, 29, 25799–25809. https://doi.org/10.1007/s11356-021-17563-7.

207. Abassi, Z., Armaly, Z., & Heyman, S. N. (2020). Glycocalyx degradation in ischemia-reperfusion injury. *The American Journal of Pathology*, 190(4), 752–767. https://doi.org/10.1016/j.ajpath.2019.08.019.

208. Schött, U., Solomon, C., Fries, D., et al. (2016). The endothelial glycocalyx and its disruption, protection and regeneration: a narrative review. *Scandinavian Journal of Trauma, Resuscitation and Emergency Medicine*, 24, 48. https://doi.org/10.1186/s13049-016-0239-y.

209. Yung, S., & Chan, T. M. (2023). Endothelial cell activation and glycocalyx shedding - potential as biomarkers in patients with lupus nephritis. Frontiers in Immunology, 14, 1251876. https://doi.org/10.3389/fimmu.2023.1251876.

210. Lu, B., Lim, J. M., Yu, B., Song, S., Neeli, P., Sobhani, N., K, P., Bonam, S. R., Kurapati, R., Zheng, J., & Chai, D. (2024). The next-generation DNA vaccine platforms and delivery systems: advances, challenges and prospects. *Frontiers in Immunology*, 15. DOI: https://doi.org/10.3389/fimmu.2024.1332939.

211. Yin, H., Kanasty, R., Eltoukhy, A., Vegas, A., Dorkin, J. R., & Anderson, D. G. (2014). Non-viral vectors for gene-based therapy. *Nature Reviews Genetics*, 15(8), 541–555. DOI; https://doi.org/10.1038/nrg3763.

212. Gandek, T. B., van der Koog, L., & Nagelkerke, A. (2023). A Comparison of Cellular Uptake Mechanisms, Delivery Efficacy, and Intracellular Fate between Liposomes and Extracellular Vesicles. *Advanced Healthcare Materials*. DOI: https://doi.org/10.1002/adhm.202300319.

213. Morini, M. A., Sierra, M. B., Pedroni, V. I., Alarcon, L. M., Appignanesi, G. A., & Disalvo, E. A. (2015). Influence of temperature, anions and size distribution on the zeta potential of DMPC, DPPC and DMPE lipid vesicles. *Colloids and Surfaces B: Biointerfaces, 131*, 54–58. DOI: https://doi.org/10.1016/j.colsurfb.2015.03.054.

214. Codini, M., Garcia-Gil, M., & Albi, E. (2021). Cholesterol and Sphingolipid Enriched Lipid Rafts as Therapeutic Targets in Cancer. *International Journal of Molecular Sciences, 22*(2), 726. DOI: https://doi.org/10.3390/ijms22020726.

215. Carotenuto, A. R., Lunghi, L., Piccolo, V., Babaei, M., Dayal, K., Pugno, N., Zingales, M., Deseri, L., & Fraldi, M. (2020). Mechanobiology predicts raft formations triggered by ligand-receptor activity across the cell membrane. *Journal of the Mechanics and Physics of Solids, 137*, Article 103974. DOI: https://doi.org/10.1016/j.jmps.2020.103974.

216. Akimov, S. A., Volynsky, P. E., Galimzyanov, T. R., & Kuzmin, P. I. (2017). Pore formation in lipid membrane II: Energy landscape under external stress. Scientific Reports, 7, 12509. DOI: https://doi.org/10.1038/s41598-017-12749-x.

APPENDIX

A1 Abbreviations and Chemical Acronyms

ANOVA:	Analysis of Variance
APS:	Ammonium Persulfate
BSA:	Bovine Serum Albumin
CTCs:	Circulating Tumor Cells
Cx43:	Connexin 43
DHPE:	1,2-Dihexadecanoyl-sn-Glycero-3-Phosphoethanolamine
DMPC:	Dimyristoylphosphatidylcholine
DOTAP:	Dioleoyl-3-trimethylammoniumpropane
DPBS:	Dulbecco's Phosphate-Buffered Saline
FBS:	Fetal Bovine Serum
FITC:	Fluorescein Isothiocyanate
FSC-A:	Forward Scatter-Area
FWHM:	Full Width at Half Maximum
GP:	Generalized Polarization
GUV:	Giant Unilamellar Vesicle
HUVEC:	Human Umbilical Vein Endothelial Cells
JAMs:	Junctional Adhesion Molecules
KLFs:	Krüppel-like Factors
Laurdan:	6-Dodecanoyl-2-Dimethylaminonaphthalene
MAPKs:	Mitogen-Activated Protein Kinases
MLV:	Multilamellar Vesicle
MMPs:	Matrix Metalloproteinases
NO:	Nitric Oxide
PKC:	Protein Kinase C
ROS:	Reactive Oxygen Species
TEMED:	Tetramethylethylenediamine
VE:	Vascular Endothelial
WGA:	Wheat Germ Agglutinin

A2 Tables of used Instruments and Materials

Devices		
Name	Manufacturer	Country of Origin
Ibidi Pump System	Ibidi	Germany
Stellaris 5 Confocal Microscope	Leica Microsystems	Germany
Axiovert 200M	Carl Zeiss	Germany
Axio Observer 7	Carl Zeiss	Germany
Zetasizer Ultra	Malvern Panalytical	United Kingdom
CytoFlex	Beckman Coulter Life Sciences	United States
Ultimaker S5 3D Printer	Ultimaker	Netherlands

Cells and Cell Culture Components		
Name	Manufacturer	Country of Origin
Early Passage HUVEC pooled	Pelobiotech	Germany
HeLa CCL-2	American Type Culture Collection (ATCC)	United States
EASY Endothelial Cell Growth Medium	Pelobiotech	Germany
Dulbecco's Modified Eagle's Medium	Bio&SELL	Germany
Penicillin/Streptomycin (Pen/Strep)	Bio&SELL	Germany
FBS Superior stabil	Bio&SELL	Germany
Dulbecco’s phosphate buffered saline	Sigma-Aldrich	Germany
Trypsin/EDTA (0.25%/0.02% w/v) in DPBS	Bio&SELL	Germany
Accutase/Biotase Solution	Bio&SELL	Germany
Collagen Type I, Rat (4,63 mg/ml)	Corning	United States
Acidic acid	Honeywell International	United States
µ-Slide I Luer 0.4	Ibidi	Germany
µ-Slide I Luer 0.8	Ibidi	Germany
Perfusionset red	Ibidi	Germany
Perfusionset yellow-green	Ibidi	Germany

Fluorescent Substances		
Name, Excitation/Emission	Manufacturer	Country of Origin
Wheat Germ Agglutinin (Alexa Fluor 555) 555 nm/565 nm	Invitrogen	United States
Laurdan (6-Dodecanoyl-2-Dimethylaminonaphthalene) 350–380 nm/440–490 nm	Sigma Aldrich	Germany
Red Fluorescent Silica Nanoparticles, 50 nm 569 nm/ 585 nm	DiagNano	United States
NucBlue Live ReadyProbes (Hoechst 33342) 350 nm/ 461 nm	Invitrogen	United States
Texas Red 1,2-Dihexadecanoyl-sn-Glycero-3-Phosphoethanolamine, Triethylammonium Salt 595 nm/615 nm	Invitrogen	United States
Fluoreszeinisothiocyanat–Dextran 4 kDa 495 nm/519 nm	Sigma Aldrich	Germany
Fluoreszeinisothiocyanat–Dextran 10 kDa 495 nm/519 nm	Sigma Aldrich	Germany
VE-cadherin Antibodies (F-8) (Alexa Fluor 647) 650 nm/665 nm	Santa Cruz Biotechnology	United States

Lipids		
Name	Manufacturer	Country of Origin
DMPC (14:0 PC)	Avanti Polar Lipids	United States
DOTAP (18:1 TAP)	Avanti Polar Lipids	United States

Chemical Substances and Consumables		
Name	Manufacturer	Country of Origin
Dimethylsulfoxide	American Type Culture Collection (ATCC)	United States
Acrylamide Solution (40%) - Mix 29:1 for Molecular Biology	AppliChem	Germany
N, N'-Methylenebisacrylamide, 2% Solution (Bisacrylamide)	Alfa Aesar	United States
N',N',N',N'-Tetraacetylethylenediamine (TEMED)	Sigma Aldrich	Germany
Ammonium Peroxodisulfate (APS)	AppliChem	Germany
Gelatin, powdered	AppliChem	Germany
Dulbecco's Modified Eagle's Medium 10X	Bio&SELL	Germany
Silicone paste KORASILON high viscosity	Carl Roth	Germany
Spinal cannula 1,10 x 90 mm	M. Schilling Medical Products	Germany
Cannula 1,60 x 25 mm	Dispomed	Germany

A3 Script used in Glycocalyx Staining Experiments

Available on Github: https://github.com/manuelsirch/dissertation/blob/main/glycocalyx_staining

```
import os
import numpy as np
import matplotlib.pyplot as plt
import csv

input_folder = "Input"
output_folder = "Output"

def create_histogram(input_folder, output_folder):
    # List of files in the input folder
    file_list = os.listdir(input_folder)

    os.makedirs(output_folder, exist_ok=True)

    # Loop through the files
    for file_name in file_list:
        if file_name.endswith('.tif'):
            input_file_path = os.path.join(input_folder, file_name)
            output_file_path = os.path.join(output_folder,
file_name.replace('.tif', '.csv'))

            # Read the images and convert to grayscale if necessary
            image = plt.imread(input_file_path)
            if len(image.shape) == 3:
                image = np.mean(image, axis=2)

            # Calculate the histogram
            histogram, bin_edges = np.histogram(image, bins=256, range=(0, 256))

            # Calculate the total number of pixels in the image
            total_pixels = np.sum(histogram)

            # Save the total and normalized histogram in a CSV file
            with open(output_file_path, mode='w', newline='') as csv_file:
                writer = csv.writer(csv_file)
                writer.writerow(['pixel value', 'frequency', 'frequency in
percent'])

                for value, frequency in zip(bin_edges[:-1], histogram):
                    percentage = (frequency / total_pixels) * 100 if total_pixels >
0 else 0
                    writer.writerow([int(value), int(frequency),
"{:.16f}".format(percentage)])

create_histogram(input_folder, output_folder)
```

A4 Script used for Cell Segmentation and Vesicle Adhesion

Available on Github: https://github.com/manuelsirch/dissertation/blob/main/segmentation_and_tracking

```
# --- Start of main.py ---

import os

import glob
from PIL import Image

import cellpose.plot
import matplotlib.pyplot as plt
import imagefunctions as imf
import skimage.io
from Cell import Cell
from AdherentCell import AdherentCell
import programrun_functions as prf

os.environ["KMP_DUPLICATE_LIB_OK"] = "TRUE"     # Suppress warning when program is
run on different computer

""" Run program for already created masks/diams, create new ones or run on test
images to find parameters for cell
detection? """
new_or_use_or_test = input("Create NEW masks, USE already created masks, run on
TEST images, find masks/diams for \
MULTIPLE data, determine CONFLUENCE or find adherent cells for FILTERED areas? \n[n
/ u / t / m / c / f]: ")

# Create new masks:
if new_or_use_or_test == "n":
    # get images from user
    path_input = input("Path of '.tif'-images: ")
    imgs = imf.read_tifs(path_input)

    # get parameters for cell detection from user
    cellprob_threshold, flow_threshold = prf.get_celldet_params()

    # create new directory for the data with the selected 'cellprob_threshold' and
'flow_threshold'
    path_output_cells_diams = os.path.join(path_input, "celladhesion_" + 'cpt' +
str(cellprob_threshold) + 'ft' + str(flow_threshold))
    os.mkdir(path_output_cells_diams)

    # run 'find_cells' method and save masks and diams (names: include
'cellprob_threshold' and 'flow_threshold')
    masks, diams = Cell.run_cellpose(imgs, cellprob_threshold=cellprob_threshold,
flow_threshold=flow_threshold)
    cells = Cell.find_cells(masks)
    masks_name = 'masks_' + 'cpt' + str(cellprob_threshold) + 'ft' +
str(flow_threshold)
    Cell.safe_masks(masks, path_output_cells_diams, masks_name)
    diams_name = 'diams_' + 'cpt' + str(cellprob_threshold) + 'ft' +
str(flow_threshold)
    Cell.safe_diams(diams, path_output_cells_diams, diams_name)

    # get parameters for adherent-cell detection from user
    time_for_adherent, delay, images_threshold, compare_threshold =
prf.get_adhcelldet_params(diams)

    # search adherent cells
    number_adherent_cells, number_cells_total, adherent_cells =
AdherentCell.find_adherent_cells(cells, diams,
```

```
images_threshold,

compare_threshold)
    # find number of adherent cells on each image
    nr_adherent_cells_on_img =
AdherentCell.nr_adherent_cells_on_img(adherent_cells, len(imgs))

    # create new subdirectory for data with the selected time and tolerance
    path_output_adherent = os.path.join(path_output_cells_diams, 'time' +
str(time_for_adherent) + 's_tolerance' + str(compare_threshold))
    os.mkdir(path_output_adherent)

    # create '.txt'-file to save data
    txtfile = open(os.path.join(path_output_adherent, 'celladhesion_' + 'time' +
str(time_for_adherent) + 's_tolerance'
                                + str(compare_threshold) + '.txt'), 'w+')

    # save the used masks, diams and parameters in the text file
    prf.save_params_in_txtfile(txtfile, masks_name, diams_name, time_for_adherent,
delay, images_threshold,
                               compare_threshold)

    # save the information found about the adherent cells in the text file
    prf.save_adh_in_txtfile(txtfile, number_adherent_cells, number_cells_total,
adherent_cells, cells,
                            nr_adherent_cells_on_img)

    # overlay outlines of the detected cells on the input images and mark the
adherent cells
    overlay = imf.overlay_outlines(imgs, masks)
    # 'overlay_adherent_squares' can only be done if list contains 'adherent_cell'-
objects
    if isinstance(adherent_cells[0], AdherentCell):
        overlay = imf.overlay_adherent_squares(overlay, adherent_cells, 30)

    # show created images and save them in the subdirectory
    prf.show_and_save_result_imgs(overlay, path_output_adherent, "celladhesion")

# use already created masks
elif new_or_use_or_test == "u":
    # get images from user
    path_imgs = input("Path of '.tif'-images: ").replace('\\', '/')
    imgs = imf.read_tifs(path_imgs)

    # get masks/diams from user
    path_input = input("Path where masks and diams are saved: ").replace('\\', '/')
    masks_name = str(input("Name of '.npy'-file with masks (without ending): ")) +
'.npy'
    masks = imf.load_masks(os.path.join(path_input, masks_name))
    diams_name = str(input("Name of '.txt'-file with diameters (without ending):
")) + '.txt'
    diams = imf.load_diams(os.path.join(path_input, diams_name))

    while True:
        # get parameters from user
        time_for_adherent, delay, images_threshold, compare_threshold =
prf.get_adhcelldet_params(diams)

        # create new subdirectory for the data with the selected time and tolerance
        path_output_adherent = os.path.join(path_input, 'time' +
str(time_for_adherent) + 's_tolerance' + str(compare_threshold))
        os.mkdir(path_output_adherent)

        # find cells and adherent cells
        cells = Cell.find_cells(masks)
        number_adherent_cells, number_cells_total, adherent_cells =
AdherentCell.find_adherent_cells(cells, diams,
```

```
images_threshold,

compare_threshold)
        # find number of adherent cells on each image
        nr_adherent_cells_on_img =
AdherentCell.nr_adherent_cells_on_img(adherent_cells, len(imgs))

        # create '.txt'-file to save the data
        txtfile = open(os.path.join(path_output_adherent, 'celladhesion_' + 'time'
+ str(time_for_adherent) + 's_tolerance'
                                    + str(compare_threshold) + '.txt'), 'w+')

        # save the used masks, diams and parameters in the text file
        prf.save_params_in_txtfile(txtfile, masks_name, diams_name,
time_for_adherent, delay, images_threshold,
                                   compare_threshold)

        # save the found information about the adherent cells in the text file
        prf.save_adh_in_txtfile(txtfile, number_adherent_cells, number_cells_total,
adherent_cells, cells,
                                nr_adherent_cells_on_img)

        # save number of adherent cells on image in a '.csv'-file
        prf.number_adh_on_image_to_csv(nr_adherent_cells_on_img,
os.path.join(path_output_adherent, 'adh_on_img.csv'))

        # overlay outlines of the detected cells on the input images and mark the
adherent cells
        overlay = imf.overlay_outlines(imgs, masks)
        # 'overlay_adherent_squares' can only be done if list contains
'adherent_cell'-objects
        if isinstance(adherent_cells[0], AdherentCell):
            overlay = imf.overlay_adherent_squares(overlay, adherent_cells, 30)

        # show created images and save them in the subdirectory
        prf.show_and_save_result_imgs(overlay, path_output_adherent,
"celladhesion")

        # check if user wants to overlay the adherent cells on an image of the call
layer
        cells_on_phc = input("\nOverlay adherent cells on image of the cell layer?
[y / n]: ")
        if cells_on_phc == "y":

            # get path and image of the cell layer
            path_phc = input("Path where image of cell layer is saved:
").replace('\\', '/')
            name_phc = str(input("Name of '.tif'-file of cell layer (without
ending): ")) + '.tif'
            img_phc = imf.read_single_img(os.path.join(path_phc, name_phc))

            # create new subdirectory for the overlayed images
            path_output_phc = os.path.join(path_output_adherent,
'celladhesion_overlayPhc')
            os.mkdir(path_output_phc)

            # overlay adherent cells on the image and save the result images in the
directory
            adh_over_phc = imf.adherent_cells_over_phasecontrast(img_phc, masks,
adherent_cells)
            prf.show_and_save_result_imgs(adh_over_phc, path_output_phc,
"overlayPhc")

            determine_confluence = input("\n Determine confluence of the cell
layer? [y / n]: ")
            if determine_confluence == "y":
                # get new parameters for cell detection from user and find mask +
confluence
```

```
                print("\nSet new parameters for cell detection on the cell layer:
")
                cellprob_threshold_layer, flow_threshold_layer =
prf.get_celldet_params()
                mask_layer, diams_layer = Cell.run_cellpose(img_phc,
flow_threshold=flow_threshold_layer,

cellprob_threshold=cellprob_threshold_layer)
                confluence = Cell.determine_confluence(mask_layer)

                # print and safe confluence
                prf.save_confluence_in_txtfile(txtfile, cellprob_threshold_layer,
flow_threshold_layer, confluence)

                # set name for output image
                name_output = name_phc
                if name_output.endswith('.tif'):
                    name_output = name_output[:-4]
                # plot masks over image and show/save the result
                img_output = cellpose.plot.mask_overlay(img_phc, mask_layer)
                prf.show_and_save_result_imgs(img_output, path_phc, "confluence_" +
str(confluence) + "_ "+ name_output)

        # check if user wants to rerun or stop the program
        rerun = input("Rerun? [y / n]: ")
        # if no, break out of the loop to stop the program
        if rerun == "n":
            break
        else:
            # if yes, check if user wants to use the same masks as before or new
ones
            new_or_same_masks = input("Use NEW or SAME masks? [n / s]: ")
            # if the user chooses new ones, get new images, masks and diameters
            if new_or_same_masks == "n":
                print("\n\n")
                # get images from user
                path_imgs = input("Path of '.tif'-images: ").replace('\\', '/')
                imgs = imf.read_tifs(path_imgs)

                # get masks/diams from user
                path_input = input("Path where masks and diams are saved:
").replace('\\', '/')
                masks_name = str(input("Name of '.npy'-file with masks (without
ending): ")) + '.npy'
                masks = imf.load_masks(os.path.join(path_input, masks_name))
                diams_name = str(input("Name of '.txt'-file with diameters (without
ending): ")) + '.txt'
                diams = imf.load_diams(os.path.join(path_input, diams_name))


# run on test images to find parameters for cell detection
elif new_or_use_or_test == "t":
    # get test-images from user
    path_imgs = input("Path of '.tif' test-images: ").replace('\\', '/')
    imgs = imf.read_tifs(path_imgs)

    while True:
        # get parameters for cell detection from user
        cellprob_threshold, flow_threshold = prf.get_celldet_params()

        # run 'find_cells' method, overlay cell outlines
        masks, diams = Cell.run_cellpose(imgs,
cellprob_threshold=cellprob_threshold, flow_threshold=flow_threshold)
        cells = Cell.find_cells(masks)
        overlay = imf.overlay_outlines(imgs, masks)

        # show images
        for i in range(len(overlay)):
            skimage.io.imshow(overlay[i])
```

```
            plt.title("testimg{0},  cpt={1}, ft={2}          ".format(i,
cellprob_threshold, flow_threshold))
            skimage.io.show()

        # check if user wants to rerun with different parameters
        rerun = input("Rerun? [y / n]: ")
        if rerun == "n":
            break
        else:
            print("Set new parameters.")

# Run Code to find masks and diams for multiple data inputs
elif new_or_use_or_test == "m":
    path_input = list()
    imgs = list()
    cellprob_threshold = list()
    flow_threshold = list()
    while True:
        path_input_temp = input("Path of '.tif'-images or 'stop', if no more paths
shall be read: ")
        if path_input_temp == "stop":
            break
        path_input.append(path_input_temp)
        imgs.append(imf.read_tifs(path_input_temp))
        cellprob_threshold_temp, flow_threshold_temp = prf.get_celldet_params()
        cellprob_threshold.append(cellprob_threshold_temp)
        flow_threshold.append(flow_threshold_temp)
        print("\n")

    for data_nr in range(len(path_input)):
        # create new directory for the data with the selected 'cellprob_threshold'
and 'flow_threshold'
        path_output_cells_diams = os.path.join(path_input[data_nr],
                                               "celladhesion_" + 'cpt' +
str(cellprob_threshold[data_nr]) + 'ft' + str(
                                                   flow_threshold[data_nr]))
        os.mkdir(path_output_cells_diams)

        # run 'find_cells' method and save masks and diams (names: include
'cellprob_threshold' and 'flow_threshold')
        masks, diams = Cell.run_cellpose(imgs[data_nr],
cellprob_threshold=cellprob_threshold[data_nr],
                                         flow_threshold=flow_threshold[data_nr])
        masks_name = 'masks_' + 'cpt' + str(cellprob_threshold[data_nr]) + 'ft' +
str(flow_threshold[data_nr])
        Cell.safe_masks(masks, path_output_cells_diams, masks_name)
        diams_name = 'diams_' + 'cpt' + str(cellprob_threshold[data_nr]) + 'ft' +
str(flow_threshold[data_nr])
        Cell.safe_diams(diams, path_output_cells_diams, diams_name)

elif new_or_use_or_test == "c":
    # get path and image of the cell layer
    path_phc = input("Path where image of cell layer is saved: ").replace('\\',
'/')
    name_phc = str(input("Name of '.tif'-file of cell layer (without ending): ")) +
'.tif'
    # read cell layer image
    img_phc = imf.read_single_img(os.path.join(path_phc, name_phc))

    # get parameters for cell detection from user and find mask + confluence
    cellprob_threshold, flow_threshold = prf.get_celldet_params()
    mask, diam = Cell.run_cellpose(img_phc, flow_threshold=flow_threshold,
cellprob_threshold=cellprob_threshold)
    confluence = Cell.determine_confluence(mask)

    # print confluence
    print("confluence: {0}%".format(confluence))

    # set name for output image
```

```
    name_output = name_phc
    if name_output.endswith('.tif'):
        name_output = name_output[:-4]
    # plot masks over image and show/save the result
    img_output = cellpose.plot.mask_overlay(img_phc, mask)
    prf.show_and_save_result_imgs(img_output, path_phc, "confluence_" +
str(confluence) + "_ "+ name_output)


elif new_or_use_or_test == "f":
    path_imgs = input("Path of '.tif'-images: ").replace('\\', '/')
    imgs = imf.read_tifs(path_imgs)

    # get masks/diams from user
    path_input = input("Path where masks and diams are saved: ").replace('\\', '/')
    masks_name = str(input("Name of '.npy'-file with masks (without ending): ")) +
'.npy'
    masks = imf.load_masks(os.path.join(path_input, masks_name))
    diams_name = str(input("Name of '.txt'-file with diameters (without ending):
")) + '.txt'
    diams = imf.load_diams(os.path.join(path_input, diams_name))
    #background_mask_name = str(input("Name of '.npy'-file with background masks
(without ending): ")) + '.npy'
    background_mask_name = str(input("Name of '.png'-file with background masks
(without ending): ")) + '.png'
    background_mask = skimage.io.imread(os.path.join(path_input,
background_mask_name))
    #background_mask = imf.load_masks(os.path.join(path_input,
background_mask_name))

    while True:
        # get parameters from user
        time_for_adherent, delay, images_threshold, compare_threshold =
prf.get_adhcelldet_params(diams)

        # create new subdirectory for the data with the selected time and tolerance
        path_output_adherent = os.path.join(path_input,
                                            'time' + str(time_for_adherent) +
's_tolerance' + str(compare_threshold) + '_filtered')
        os.mkdir(path_output_adherent)

        # find cells and adherent cells
        cells = Cell.find_cells(masks)
        filtered_cells = list()
        for i in range(len(cells)):
            filtered_cells.append(Cell.filter_for_position(cells[i],
background_mask))
        number_adherent_cells, number_cells_total, adherent_cells =
AdherentCell.find_adherent_cells(filtered_cells, diams,

images_threshold,

compare_threshold)
        # find number of adherent cells on each image
        nr_adherent_cells_on_img =
AdherentCell.nr_adherent_cells_on_img(adherent_cells, len(imgs))

        # create '.txt'-file to save the data
        txtfile = open(
            os.path.join(path_output_adherent, 'celladhesion_' + 'time' +
str(time_for_adherent) + 's_tolerance'
                         + str(compare_threshold) + '.txt'), 'w+')

        # save the used masks, diams and parameters in the text file
        prf.save_params_in_txtfile(txtfile, masks_name, diams_name,
time_for_adherent, delay, images_threshold,
                                   compare_threshold)

        # save the found information about the adherent cells in the text file
```

```
        prf.save_adh_in_txtfile(txtfile, number_adherent_cells, number_cells_total,
adherent_cells, cells,
                                nr_adherent_cells_on_img)

        # save number of adherent cells on image in a '.csv'-file
        prf.number_adh_on_image_to_csv(nr_adherent_cells_on_img,
os.path.join(path_output_adherent, 'adh_on_img.csv'))

        # overlay outlines of the detected cells on the input images and mark the
adherent cells
        overlay = imf.overlay_outlines(imgs, masks)
        # 'overlay_adherent_squares' can only be done if list contains
'adherent_cell'-objects
        if isinstance(adherent_cells[0], AdherentCell):
            overlay = imf.overlay_adherent_squares(overlay, adherent_cells, 30)

        # show created images and save them in the subdirectory
        prf.show_and_save_result_imgs(overlay, path_output_adherent,
"celladhesion")

        # check if user wants to overlay the adherent cells on an image of the call
layer
        cells_on_phc = input("\nOverlay adherent cells on image of the cell layer?
[y / n]: ")
        if cells_on_phc == "y":
            # get path and image of the cell layer
            path_phc = input("Path where image of cell layer is saved:
").replace('\\', '/')
            name_phc = str(input("Name of '.tif'-file of cell layer (without
ending): ")) + '.tif'
            img_phc = imf.read_single_img(os.path.join(path_phc, name_phc))

            # create new subdirectory for the overlayed images
            path_output_phc = os.path.join(path_output_adherent,
'celladhesion_overlayPhc')
            os.mkdir(path_output_phc)

            # overlay adherent cells on the image and save the result images in the
directory
            adh_over_phc = imf.adherent_cells_over_phasecontrast(img_phc, masks,
adherent_cells)
            prf.show_and_save_result_imgs(adh_over_phc, path_output_phc,
"overlayPhc")

        # check if user wants to rerun or stop the program
        rerun = input("Rerun? [y / n]: ")
        # if no, break out of the loop to stop the program
        if rerun == "n":
            break
        else:
            # if yes, check if user wants to use the same masks as before or new
ones
            new_or_same_masks = input("Use NEW or SAME masks? [n / s]: ")
            # if the user chooses new ones, get new images, masks and diameters
            if new_or_same_masks == "n":
                print("\n\n")
                # get images from user
                path_imgs = input("Path of '.tif'-images: ").replace('\\', '/')
                imgs = imf.read_tifs(path_imgs)

                # get masks/diams from user
                path_input = input("Path where masks and diams are saved:
").replace('\\', '/')
                masks_name = str(input("Name of '.npy'-file with masks (without
ending): ")) + '.npy'
                masks = imf.load_masks(os.path.join(path_input, masks_name))
                diams_name = str(input("Name of '.txt'-file with diameters (without
ending): ")) + '.txt'
                diams = imf.load_diams(os.path.join(path_input, diams_name))
```

```
# --- End of main.py ---

# --- Start of AdherentCell.py ---

import numpy as np

from Cell import Cell


class AdherentCell(Cell):
    """
    Subclass of Cell with extra attributes 'first_appearance' and
'number_appearances' needed for adherent adherent_cells
    """
    adherent_cellcounter = 0  # number of created 'AdherentCell'- objects

    def __init__(self, pos, radius, first_appearance, number_appearances):
        """

        :param pos: array
                1-dim array representing pixel positions x and y of cell center:
[x, y] (x and y: int)
        :param first_appearance: int
                image number of first appearance; e.g. if image with first
appearance is first image in the image
                folder, first_appearance will be 0 (image is imgs[0])
        :param number_appearances: int
                number of consecutive images where adherent cell is detected
        """
        super().__init__(pos, radius)
        self.__first_appearance = first_appearance
        self.__number_appearances = number_appearances

        AdherentCell.adherent_cellcounter += 1

    def get_first_appearance(self):
        return self.__first_appearance

    def set_first_appearance(self, first_appearance):
        self.__first_appearance = first_appearance

    def get_number_appearances(self):
        return self.__number_appearances

    def set_number_appearances(self, number_appearances):
        self.__number_appearances = number_appearances

    @staticmethod
    def reset_adherent_cellcounter():
        AdherentCell.adherent_cellcounter = 0

    @staticmethod
    def get_adherent_cellcounter():
        return AdherentCell.adherent_cellcounter

    def __str__(self):
        return "Pos.: {0}, Radius: {1}, Imgnr. first appearance: {2}, Nr.
appearances: {3}".format(self.get_position(),

self.get_radius(),

self.get_first_appearance(),

self.get_number_appearances())

    @staticmethod
    def find_adherent_cells(cells, diams, threshold_imgs, tolerance):
```

```
        """
        Returns number of adherent adherent_cells (adherent_cells that hold their
position on at least 'threshold_imgs'
        consecutive images). Position of a cell is compared to the position, where
the cell was first detected (rolling
        cells may not be detected as adherent cells)

        :param cells: list
                    list containing cell objects for each image:
list[img_index][cell_index]
        :param diams: list
                    list of cell diameters (float)
        :param threshold_imgs: int, >=2
                    number of consecutive images (for example threshold_imgs = 3,
if cell needs to be in same position
                    on three consecutive images)
        :param tolerance: int
                    tolerance radius for Cells.compare method

        :return number_adherent_cells: int
                    total number of adherent adherent_cells with given parameters
        :return number_cells_total: int
                    total number of adherent_cells
        :return adherent_cells: list
                    list of 'AdherentCell' objects
        """
        if threshold_imgs < 2:
            print("threshold_imgs has to be greater than or equal to 2")
            return "error", "error", "error"
        """elif float(tolerance) > min(diams) / 2:
            print("tolerance has to be smaller than estimated cell size")  #
prevent overlapping of adherent_cells
            return "error", "error", "error" """

        AdherentCell.reset_adherent_cellcounter()   # reset adherent_cellcounter
every time the method is called
        number_adherent_cells = 0  # complete number of adherent adherent_cells
        number_cells_total = 0  # complete number of adherent_cells

        adherent_cells_doubles = list()  # auxiliary variable to prevent multiple
counts for one cell
        adherent_cells = list()          # list with 'AdherentCell'-objects

        # iterate every image (ignore last image where no more new adherent
adherent_cells can be found)
        for img_number in range(len(cells) - 1):

            # iterate every cell on image 'img_number'
            for cell_number in range(len(cells[img_number])):
                number_consecutive_imgs = 1  # auxiliary variable that represents
number of images in which cell keeps its position

                # prevent multiple counts for one cell by checking if it's already
in 'adherent_cells_doubles'-list
                if not (cells[img_number][cell_number] in adherent_cells_doubles):

                    # iterate every image after 'image_number' to find adherent
adherent_cells
                    for check_img_number in range(img_number + 1, len(cells)):
                        """Boolean used to make sure no more images are searched
for  adherent_cells[img_number][cell_number] if
                        one image 'check_image_number' doesn't contain an adherent
cell"""
                        cell_found = False

                        # iterate every cell on image 'check_img_number'
                        for check_cell_number in
range(len(cells[check_img_number])):
```

```
                            # compare cell position
                            if
cells[img_number][cell_number].compare(cells[check_img_number][check_cell_number],
                                                                   tolerance):
                                """if true, raise 'number_consecutive_imgs' and add
cell to 'adherent_cells_doubles'

(adherent_cells[check_img_number][check_cell_number] is same cell as the one on
                                image 'img_number' -> doesn't have to be counted
twice)"""
                                number_consecutive_imgs += 1

adherent_cells_doubles.append(cells[check_img_number][check_cell_number])
                                cell_found = True
                                break
                        if not cell_found:
                            break  # no cell found on image 'check_img_number'
                            # -> jump to next cell cell[img_number][cell_number]

                # cell is only considered adherent, if it keeps position on at
least 'threshold_imgs' images
                if number_consecutive_imgs >= threshold_imgs:
                    number_adherent_cells += 1

adherent_cells.append(AdherentCell(cells[img_number][cell_number].get_position(),

cells[img_number][cell_number].get_radius(), img_number,
                                                        number_consecutive_imgs))

        """calculate total number of adherent_cells by counting all cell objects
and subtracting the doubled
        adherent_cells (saved in 'adherent_cells_doubles'-list)"""
        for i in range(len(cells)):
            for j in range(len(cells[i])):
                number_cells_total += 1
        number_cells_total -= len(adherent_cells_doubles)

        if not adherent_cells:  # prevent ValueError if 'adherent_cells'-list is
empty
            return number_adherent_cells, number_cells_total, ["No adherent cells
found"]
        else:
            return number_adherent_cells, number_cells_total, adherent_cells

    @staticmethod
    def find_adherent_cells2(cells, diams, threshold_imgs, tolerance,
missing_cell_threshold=0):
        """
        Same as 'AdherentCell.find_adherent_cells', but with an optional parameter
'missing_cell_threshold'.
        Returns number of adherent adherent_cells (adherent_cells that hold their
position on at least 'threshold_imgs'
        consecutive images). Position of a cell is compared to the position, where
the cell was first detected (rolling
        cells may not be detected as adherent cells)

        :param cells: list
                    list containing cell objects for each image:
list[img_index][cell_index]
        :param diams: list
                    list of cell diameters (float)
        :param threshold_imgs: int, >=2
                    number of consecutive images (for example threshold_imgs = 3,
if cell needs to be in same position
                    on three consecutive images)
        :param tolerance: int
                    tolerance radius for Cells.compare method
        :param missing_cell_threshold: int
```

```
                    if one cell is not found on 'missing_cell_threshold' images,
but on enough other consecutive images,
                    the cell will still be detected as adherent

        :return number_adherent_cells: int
                    total number of adherent adherent_cells with given parameters
        :return number_cells_total: int
                    total number of adherent_cells
        :return adherent_cells: list
                    list of 'AdherentCell' objects
        """
        if threshold_imgs < 2:
            print("threshold_imgs has to be greater than or equal to 2")
            return "error", "error", "error"

        AdherentCell.reset_adherent_cellcounter()  # reset adherent_cellcounter
every time the method is called
        number_adherent_cells = 0  # complete number of adherent adherent_cells
        number_cells_total = 0  # complete number of adherent_cells

        adherent_cells_doubles = list()  # auxiliary variable to prevent multiple
counts for one cell
        adherent_cells = list()  # list with 'AdherentCell'-objects

        # iterate every image (ignore last image where no more new adherent
adherent_cells can be found)
        for img_number in range(len(cells) - 1):

            # iterate every cell on image 'img_number'
            for cell_number in range(len(cells[img_number])):
                number_consecutive_imgs = 1  # auxiliary variable that represents
number of images in which cell keeps its position

                # prevent multiple counts for one cell by checking if it's already
in 'adherent_cells_doubles'-list
                if not (cells[img_number][cell_number] in adherent_cells_doubles):
                    missing_cell_counter = 0

                    # iterate every image after 'image_number' to find adherent
adherent_cells
                    for check_img_number in range(img_number + 1, len(cells)):
                        """Boolean used to make sure no more images are searched
for  adherent_cells[img_number][cell_number] if
                        one image 'check_image_number' doesn't contain an adherent
cell"""
                        cell_found = False

                        # iterate every cell on image 'check_img_number'
                        for check_cell_number in
range(len(cells[check_img_number])):

                            # compare cell position
                            if
cells[img_number][cell_number].compare(cells[check_img_number][check_cell_number],
                                                                   tolerance):
                                """if true, raise 'number_consecutive_imgs' and add
cell to 'adherent_cells_doubles'

(adherent_cells[check_img_number][check_cell_number] is same cell as the one on
                                image 'img_number' -> doesn't have to be counted
twice)"""
                                number_consecutive_imgs += 1

adherent_cells_doubles.append(cells[check_img_number][check_cell_number])
                                cell_found = True
                                break
                        if not cell_found:
                            missing_cell_counter += 1  # no cell found on image
'check_img_number'
```

```
                        if missing_cell_counter > missing_cell_threshold:
                            """ jump to next cell cell[img_number][cell_number], if
number of images with a missing
                                cell is greater than the missing_cell_threshold """
                            break

                            # cell is only considered adherent, if it keeps
position on at least 'threshold_imgs' images
                if number_consecutive_imgs >= threshold_imgs:
                    number_adherent_cells += 1

adherent_cells.append(AdherentCell(cells[img_number][cell_number].get_position(),
img_number,
                                                    number_consecutive_imgs))

        """calculate total number of adherent_cells by counting all cell objects
and subtracting the doubled
        adherent_cells (saved in 'adherent_cells_doubles'-list)"""
        for i in range(len(cells)):
            for j in range(len(cells[i])):
                number_cells_total += 1
        number_cells_total -= len(adherent_cells_doubles)

        if not adherent_cells:  # prevent ValueError if 'adherent_cells'-list is
empty
            return number_adherent_cells, number_cells_total, ["No adherent cells
found"]
        else:
            return number_adherent_cells, number_cells_total, adherent_cells

    @staticmethod
    def nr_adherent_cells_on_img(adherent_cells, nr_imgs):
        """
        Returns how many of the 'adherent_cells' are located on which image

        :param adherent_cells: list
                    list of 'AdherentCell' objects
        :param nr_imgs: int
                    total number of images

        :return: nr_adherent_cells_on_img: array
                    1-dim array where each element represents one image. 'int'
value of element is the number of
                    adherent cells on the image
        """
        # create 1-dim array where default number of adherent cells on each image
is 0
        nr_adherent_cells_on_img = np.zeros((nr_imgs,), dtype=int)

        if adherent_cells:
            for cell_number in range(len(adherent_cells)):      # iterate all
adherent cells in 'adherent_cells' list
                cell = adherent_cells[cell_number]              # simplify calling
the cell
                try:
                    # iterate 'number_appearances'-attribute of the cell to count
the appearances for all images
                    for number_appearance in range(cell.get_number_appearances()):
                        # raise the adherent cells counter for the respective image
                        nr_adherent_cells_on_img[cell.get_first_appearance() +
number_appearance] += 1
                except:
                    print("No adherent cells")

        return nr_adherent_cells_on_img

# --- End of AdherentCell.py ---

# --- Start of Cell.py ---
```

```
import os.path
import cellpose.models
import numpy as np
import imagefunctions as imf


class Cell:
    """ Object 'Cell' for each mask returned by 'cellpose' representing one cell
"""
    cellcounter = 0   # number of created 'Cell'-objects

    def __init__(self, pos, radius):
        """
        creates Object 'Cell' with given parameters

        :param pos: array
                1-dim array representing pixel positions x and y of cell center:
[x, y] (x and y: int)
        :param radius: int
                radius of the cell

        """

        self.__position = pos
        self.__radius = radius

        Cell.cellcounter += 1

    def get_position(self):
        return self.__position

    def set_position(self, pos):
        self.__position = pos

    def get_radius(self):
        return  self.__radius

    def set_radius(self, radius):
        self.__radius = radius

    @staticmethod
    def reset_cellcounter():
        Cell.cellcounter = 0

    @staticmethod
    def get_cellcounter():
        return Cell.cellcounter

    def __str__(self):
        return "Pos.: {0}, Radius: {1}".format(self.get_position(),
self.get_radius())

    @staticmethod
    def calculate_radius(number_pixels):
        # calculates the radius of an approximately round cell with an area of
'number_pixels'
        return int(round(np.sqrt(number_pixels / np.pi)))


    """   OLD VERSION
    @staticmethod

    def find_cells(imgs, flow_threshold=0.4, diameter=None, model_type='cyto'):

        Uses 'cellpose' to find masks on images 'imgs' where each mask represents
one cell and returns
        list of 'Cell' objects
```

```
        :param imgs: list
                containing 'ndarray' of each image
        :param flow_threshold: float (optional, default 0.4)
                flow error threshold (all adherent_cells with errors below
threshold are kept)
        :param diameter: float (optional, default None)
                diameter for each image (only used if rescale is None),
                if diameter is None, set to diam_mean
        :param model_type: str (optional, default 'cyto')
                'cyto'=cytoplasm model; 'nuclei'=nucleus model
        :return adherent_cells: list
                list containing cell objects for each image:
list[img_index][cell_index]



            cellpose returns 'masks': list of 2D arrays; labelled
            image, where 0=no masks; 1,2,...=mask labels
        model = cellpose.models.Cellpose(gpu=False, model_type=model_type)
        masks, flows, styles, diams = model.eval(imgs, diameter=None,
channels=[0,0],
                                         flow_threshold=0.4, do_3D=False)
        masks = np.asarray(masks)

        adherent_cells = list()

        for img_index in range(masks.shape[0]):             # walk through all
images in 'imgs'
            cells_on_img = list()                           # temporary list object
for each image
            for cell_index in range(1, masks[img_index].max() + 1):     # iterate
through all masks

                x_tot = 0           # counter for pixel x-position to calculate
center of cell
                y_tot = 0           # counter for pixel y-position to calculate
center of cell
                pixel_counter = 0       # counter for overall pixel number
                for y in range(masks[img_index].shape[0]):   # walk every pixel
                    for x in range(masks[img_index].shape[1]):
                        if masks[img_index][y][x] == cell_index:    # find pixels
of each mask 'cell_index'
                            x_tot += x
                            y_tot += y
                            pixel_counter += 1
                x_center = int(round(x_tot / pixel_counter))    # calculate center
                y_center = int(round(y_tot / pixel_counter))
                pos = np.array([x_center, y_center])
                cells_on_img.append(Cell(cell_index, pos))      # initialize Cell
object with 'cell_index' and center position 'pos'
            adherent_cells.append(cells_on_img)

        return adherent_cells
    """


    @staticmethod
    def run_cellpose(imgs, flow_threshold=0.4, cellprob_threshold=0.0,
diameter=None, model_type='cyto', min_size=15):
        """ Uses Uses 'cellpose' to find masks on images 'imgs' where each mask
represents one cell

        :param imgs: list
                containing 'ndarray' of each image
        :param flow_threshold: float (optional, default 0.4)
                flow error threshold (all adherent_cells with errors below
threshold are kept)
        :param cellprob_threshold: float (optional, default 0.0)
```

```
                cell probability threshold (all pixels with prob above threshold
kept for masks)
        :param diameter: float (optional, default None)
                diameter for each image (only used if rescale is None),
                if diameter is None, set to diam_mean
        :param model_type: str (optional, default 'cyto')
                'cyto'=cytoplasm model; 'nuclei'=nucleus model
        :param min_size: int
                minimum number of pixels per mask, can turn off with -1

        :return masks: list of 2D arrays; labelled
                image, where 0=no masks; 1,2,...=mask labels
        :return diams: list
                list of cell diameters (float)
        """

        model = cellpose.models.Cellpose(gpu=False, model_type=model_type)
        masks, flows, styles, diams = model.eval(imgs, diameter=diameter,
channels=[0, 0],
                                                 flow_threshold=flow_threshold,

cellprob_threshold=cellprob_threshold, do_3D=False, min_size=min_size)
        # change data types
        masks = np.asarray(masks)
        diams = [float(i) for i in diams]

        return masks, diams

    @staticmethod
    def find_cells(masks):
        """
        Creates 'Cell' object for each cellpose mask and returns them as a list
item

       :param masks: list of 2D arrays; labelled
                image, where 0=no masks; 1,2,...=mask labels

        :return cells: list
                list containing cell objects for each image:
list[img_index][cell_index]
        """

        Cell.reset_cellcounter()  # reset cellcounter every time the method is
called
        cells = list()

        for img_index in range(masks.shape[0]):             # walk through all
images in 'imgs'
            cells_on_img = list()                           # temporary list object
for each image
            number_of_cells = masks[img_index].max()        # number of cells
(=highest mask label)
            x_tot = np.zeros(number_of_cells + 1)           # arrays to calculate
center of cell
            y_tot = np.zeros(number_of_cells + 1)
            pixel_counter = np.zeros(number_of_cells + 1)
            for y in range(masks[img_index].shape[0]):      # walk every pixel
                for x in range(masks[img_index].shape[1]):
                    vap = masks[img_index][y][x]            # value at pixel

                    # if mask-pixel, add position to 'y_tot' and 'x_total' , index
is mask-label number
                    if vap != 0:
                        y_tot[vap] += y
                        x_tot[vap] += x
                        pixel_counter[vap] += 1

            for i in range(1, number_of_cells + 1):         # create position array
with center pos for each cell/mask
```

```
                pos = np.array([int(round(x_tot[i] / pixel_counter[i])),
int(round(y_tot[i] / pixel_counter[i]))])
                radius = Cell.calculate_radius(pixel_counter[i])
                cells_on_img.append(Cell(pos, radius))           # add to temporary
list for each image
            cells.append(cells_on_img)                      # add to complete cells
list

        return cells

    def compare(self, cell2, tolerance):
        """ Checks if position of two 'Cell'-objects match within given 'tolerance'
radius:
            equal if ((x2-x1)^2 + (y2-y1)^2 < tolerance^2)  """
        return (cell2.get_position()[0] - self.get_position()[0]) ** 2 + \
               (cell2.get_position()[1] - self.get_position()[1]) ** 2 <= tolerance
** 2

    @staticmethod
    def safe_masks(masks, path, filename):
        """ Save 'masks' as a '.npy'-file under the name 'filename' at given 'path'
        :param masks: list of 2D arrays
        labelled image, where 0=no masks; 1,2,...=mask labels
        :param path: string
                Format: "...:/.../..."
        :param filename: string
                without '.npy' ending
        """

        masks_array = np.asarray(masks)
        open(os.path.join(path, (filename + '.npy')), 'w+')     # create file
        np.save(os.path.join(path, (filename + '.npy')), masks_array)

    @staticmethod
    def safe_diams(diams, path, filename):
        """ Save 'diams' as a '.txt' file under the name 'filename' at given 'path'
        :param diams: list
                list of cell diameters (float)
        :param path: string
                Format: "...:/.../..."
        :param filename: string
                without '.txt' ending
        """

        txtfile = open(os.path.join(path, (filename + '.txt')), 'w+')
        txtfile.write("\n".join(str(item) for item in diams))

    @staticmethod
    def determine_confluence(mask):
        """
        Determines the confluence (percentage of the surface of a culture dish that
is covered by adherent cells) of the
        cells, represented by the mask

        :param mask: 2D array; labelled
                image, where 0=no masks; 1,2,...=mask labels

        :return confluence: int
                confluence of cells on img, given in percent
        """

        pixels = 0              # total number of pixels
        pixels_cells = 0        # number of pixels belonging to a cell (mask)

        for y in range(mask.shape[0]):          # iterate whole image
            for x in range(mask.shape[1]):
                pixels += 1                     # count pixels
                if mask[y][x] != 0:             # if mask pixel, increase
pixel_cells counter
```

```
                    pixels_cells += 1
        confluence = round((pixels_cells / pixels) * 100)   # calculate confluence

        return confluence

    @staticmethod
    def filter_for_position(cells, background_mask):
        """
        Filters an given 'cells' list, so that only those cells that have the same
position as the cells on an
        'background_mask' will remain. Use this function to consider cell adhesion
only for those cells, that have a
        certain position, determined by the background mask.

        :param cells: list
                list containing cell objects: list[cell_index]
        :param background_mask: 2D array; labelled
                image, where 0=no masks; 1,2,...=mask labels
        :return: filtered_cells: list
                list containing only the cells whose position matches the
background mask

        """

        filtered_cells = list()     # new list for the results

        for cell_nr in range(len(cells)):       # iterate all cells
            cell = cells[cell_nr]               # simplify cell call
            # check if the center of the cell already matches the background mask
            if background_mask[cell.get_position()[1]][cell.get_position()[0]] !=
0:
                filtered_cells.append(cells[cell_nr])       # if yes, add the cell
to the result list
            else:
                radius = cell.get_radius()      # simplify radius call
                match_found = False             # used to make sure, each cell is
added to 'filtered_cells' only once
                # iterate over all pixels in a square around the cell (side length:
2 * cell_radius)
                for y in range(cell.get_position()[1] - radius,
cell.get_position()[1] + radius):
                    for x in range(cell.get_position()[0] - radius,
cell.get_position()[0] + radius):
                        # prevent adding cell to 'filtered_cells' more than once
                        if not match_found:
                            # only check pixels of the actual cell (approx. circle
with radius  of the cell)
                            if (y - cell.get_position()[1]) ** 2 + (x -
cell.get_position()[0]) ** 2 <= radius:
                                # make sure the pixel is part of the background img
(relevant for cells on edges of the img)
                                if (0 <= y <= background_mask.shape[0]) and (0 <= x
<= background_mask.shape[1]):
                                    # if the position of the pixel matches a mask
pixel, add the cell to list
                                    if background_mask[y][x] != 0:
                                        match_found = True
                                        filtered_cells.append(cells[cell_nr])

        return filtered_cells


# --- End of Cell.py ---

# --- Start of config.py ---

"""Configuration file for the needed parameters"""

# cell detection parameters for 'cellpose' functions
```

```
celldet = {
    "cellprob_threshold": 0.0,  # float: (between 0.0 and 1.0, higher: less masks
will be found)
    "flow_threshold": 0.4,      # float: (between 0.0 and 1.0, lower: less masks
will be found)
}

# adherent cell detection parameters
adhcelldet = {
    "time_for_adherent[s]": 60,    # int or float: time [s] to be detected as
adherent
    "delay[s]": 30,                # int or float: delay [s] between images
    "images_threshold": 3,
    "tolerance": 10             # int: tolerance radius for comparing cell
positions (pixels)
}

# --- End of config.py ---

# --- Start of imagefunctions.py ---

import skimage.io
import skimage.segmentation
import os
import numpy as np
import cv2
import glob
from natsort import os_sorted


"""def read_tifs(folder):

    Reads '.tif'-files from the given folder
    :param folder: folder directory (...:/.../.../)
    :return: list containing ndarray of each '.tif'-file in the folder

    files = [os.path.join(root, filename)   # creates list of every filename
             for root, dirs, files in os.walk(folder)
             for filename in files
             if filename.lower().endswith('.tif')]

    imgs = [skimage.io.imread(f) for f in files]

    return imgs"""


def read_tifs(folder):
    """
    Reads '.tif'-files from the given folder
    :param folder: folder directory (...:/.../.../)
    :return: list containing ndarray of each '.tif'-file in the folder
    """

    # read the images and make sure the reading order is the same es the one in the
windows explorer ('os_sorted()')
    imgs = [skimage.io.imread(file) for file in
os_sorted(glob.glob(os.path.join(folder, "*.tif")))]

    return imgs


def read_pngs(folder):
    """
     Reads '.png'-files from the given folder
    :param folder: folder directory (...:/.../.../)
    :return: list containing ndarray of each '.png'-file in the folder
    """
    # read the images and make sure the reading order is the same es the one in the
windows explorer ('os_sorted()')
```

```
    imgs = [skimage.io.imread(file) for file in
os_sorted(glob.glob(os.path.join(folder, "*.png")), key=os.path.getmtime)]

    return imgs


def read_test_tifs():
    """
    Reads '.tif'-test-files from the test-folder
    :return: list containing ndarray of each .'tif'-test-file in the folder
    """
    folder = 'C:/Users/woerl/Documents/Physik/WS 21-
22/Bachelorarbeit/Python/celladheison/celladhesion/testimages'
    files = [os.path.join(root, filename)
             for root, dirs, files in os.walk(folder)
             for filename in files
             if filename.lower().endswith('.tif')]

    imgs = [skimage.io.imread(f) for f in files]

    return imgs


def read_single_img(path):
    # Read a single image from given path
    img = skimage.io.imread(path)
    return img


def load_masks(path):
    # load '.npy' masks from given path
    masks = np.load(path, allow_pickle=True)
    return masks


def load_test_masks():
    testmasks = np.load('testmasks.npy')
    return testmasks


def load_diams(path):
    # load diameters from '.txt' file at given path
    with open(path, 'r') as filehandle:
        diams = [current_diam.rstrip() for current_diam in filehandle.readlines()]
    return list(np.float_(diams))


def load_test_diams():
    # open file and read the content in a list
    with open('testdiams.txt', 'r') as filehandle:
        diams = [current_diam.rstrip() for current_diam in filehandle.readlines()]
    return list(np.float_(diams))


def overlay_outlines(imgs, masks):
    """
    Generates red outline overlay in 'imgs'

    :param imgs: list
                containing 'ndarray' of each image
    :param masks: list of 2D arrays; labelled
                image, where 0=no masks; 1,2,...=mask labels
    :param colour: array
                Float array with values from 0.0 to 1.0 for the three RGB channels
    :return overlay: list of RGB images
                RGB images with coloured outlines
    """
    if isinstance(imgs, list):
        overlay = list()
```

```
        for img_number in range(len(imgs)):     # iterate all images in 'imgs'
            # Create outlines of the masks with 'find_boundaries' function from
'skimage' package:
            outlines = skimage.segmentation.find_boundaries(masks[img_number],
mode='outer').astype(np.uint8)
            # Check if image is already RGB
            if len(imgs[img_number].shape) != 3:
                # convert image to RGB, divide by maximum value to show image in
full range:
                # img_rgb = np.stack((imgs[img_number] /
imgs[img_number].max(),)*3, axis=-1)
                img_rgb = np.stack((imgs[img_number],)*3, axis=-1)
            else:
                # img_rgb = imgs[img_number] / imgs[img_number].max()
                img_rgb = imgs[img_number]
            # iterate over every pixel and set colour of image to red, if pixel is
part of an outline:
            for y in range(masks[img_number].shape[0]):
                for x in range(masks[img_number].shape[1]):
                    if outlines[y][x] == 1:
                        img_rgb[y][x] = [imgs[img_number].max(), 0, 0]
            overlay.append(img_rgb)     # add new image with outlines to list
        return overlay

    else:
        outlines = skimage.segmentation.find_boundaries(masks,
mode='outer').astype(np.uint8)
        # Check if image is already RGB
        if len(imgs.shape) != 3:
            # convert image to RGB, divide by maximum value to show image in full
range:
            img_rgb = np.stack((imgs / imgs.max(),) * 3, axis=-1)
        else:
            img_rgb = imgs / imgs.max()
        # iterate over every pixel and set colour of image to red, if pixel is part
of an outline:
        for y in range(masks.shape[0]):
            for x in range(masks.shape[1]):
                if outlines[y][x] == 1:
                    img_rgb[y][x] = [1.0, 0, 0]
        overlay = img_rgb  # add new image with outlines to list
    return overlay


def overlay_adherent_squares(imgs, adherent_cells, square_length, colour=[0, 0.54,
0.27]):
    length = int(square_length / 2)
    imgs_rgb = list()
    for img_number in range(len(imgs)):
        # Check if image is already RGB
        if len(imgs[img_number].shape) != 3:
            # convert image to RGB, divide by maximum value to show image in full
range:
            # imgs_rgb.append(np.stack((imgs[img_number] / imgs[img_number].max(),)
* 3, axis=-1))
            imgs_rgb.append(np.stack((imgs[img_number],) * 3, axis=-1))
        else:
            imgs_rgb.append(imgs[img_number] / imgs[img_number].max())

    for cell_number in range(len(adherent_cells)):
        cell = adherent_cells[cell_number]
        try:
            pos = cell.get_position()
            pos_top = [pos[0] - length, pos[1] - length]
            pos_bottom = [pos[0] + length, pos[1] + length]
            first_appearance = cell.get_first_appearance()
            for consecutive_img_number in range(cell.get_number_appearances()):
```

```
                # imgs_rgb[first_appearance + consecutive_img_number] =
cv2.rectangle(imgs_rgb[first_appearance + consecutive_img_number], pos_top,
pos_bottom, color)
                imgs_rgb[first_appearance + consecutive_img_number] =
cv2.circle(imgs_rgb[first_appearance + consecutive_img_number], pos, 40, colour)
                """
                for x_top in range(-length, length):
                    imgs_rgb[first_appearance + concsecutive_img_number][pos[1] +
length][pos[0] + x_top] = [0, 0.54, 0.27]
                for x_bottom in range(-length, length):
                    imgs_rgb[first_appearance + concsecutive_img_number][pos[1] -
length][pos[0] + x_bottom] = [0, 0.54, 0.27]
                for y in range(-length, length):
                    imgs_rgb[first_appearance + concsecutive_img_number][pos[1] +
y][pos[0] + length] = [0, 0.54, 0.27]

                for y in range(-length, length):
                    imgs_rgb[first_appearance + concsecutive_img_number][pos[1] +
y][pos[0] - length] = [0, 0.54, 0.27]
                """



                """
                for y in range(-5, 5):
                    for x in range(-5, 5):
                        imgs_rgb[first_appearance + concsecutive_img_number][pos[1]
+ y][pos[0] + x] = [0, 0.54, 0.27]
                    """
        except:
            print("No adherent cells")

    return imgs_rgb


def time_to_nrimgs(time, delay):
    return 1 + int(round(time/delay, 0))


def filter_masks(masks, adherent_cells):
    """
    Filters the given masks for the adherent cells -> deletes all masks that do not
belong to an adherent cell

    :param masks: list of 2D arrays
                labelled image, where 0=no masks; 1,2,...=mask labels
    :param adherent_cells: list
                list of 'AdherentCell' objects
    :return: filtered_masks: list of 2D arrays
                same as masks, but only contains the masks that belong to adherent
cells
    """

    """for img_nr in range(len(masks)):
        if adherent_cells[img_nr]:
            pos = adherent_cells[img_nr][0].get_position()
            mask_number = masks[img_nr][pos[0]][pos[1]]
            adherent_mask_numbers[0] = mask_number
            for cell_nr in range(1, len(adherent_cells[img_nr])):
                pos = adherent_cells[img_nr][cell_nr].get_position()
                mask_number = masks[img_nr][pos[0]][pos[1]]
                adherent_mask_numbers.append(mask_number)
        for y in range(masks[img_nr].shape[0]):
            for x in range(masks[img_nr].shape[1]):
                if masks[img_nr][y][x] not in adherent_mask_numbers:
                    masks[img_nr][y][x] = 0
    filtered_masks = masks"""

    """zero_list = [0]
    adherent_mask_numbers = list()
```

```
    for i in range(len(masks)):
        adherent_mask_numbers.append(zero_list)
    print(adherent_mask_numbers)

    for cell_number in range(len(adherent_cells)):
        cell = adherent_cells[cell_number]
        first_app = adherent_cells[cell_number].get_first_appearance()
        pos = adherent_cells[cell_number].get_position()
        for consecutive_img_number in range(cell.get_number_appearances()):
            mask_nr = masks[first_app + consecutive_img_number][pos[1]][pos[0]]
            adherent_mask_numbers[first_app +
consecutive_img_number].append(mask_nr)"""

    # create list where the mask numbers belonging to adherent cells for each image
will be saved
    adherent_mask_numbers = list()

    # create copy of masks that will be edited
    filtered_masks = masks

    for img_nr in range(len(masks)):    # iterate all images/masks of all images
        temp_list = [0]                 # temporary list to safe adherent mask
numbers for one image
        for cell_nr in range(len(adherent_cells)):  # iterate all adherent cells
            cell = adherent_cells[cell_nr]
            first_app = cell.get_first_appearance()
            # iterate all appearances of an adherent cell
            for consecutive_img_number in range(cell.get_number_appearances()):
                # check, if the image number of the current appearance equals the
image number (outer iteration)
                if img_nr == first_app + consecutive_img_number:
                    # if yes, get position of the adherent cell
                    pos = cell.get_position()
                    # get number (pixel value) of the related mask
                    mask_nr = masks[first_app +
consecutive_img_number][pos[1]][pos[0]]
                    # add number to the temporary list
                    temp_list.append(mask_nr)
        # add temporary list to adherent_mask_numbers list
        adherent_mask_numbers.append(temp_list)

    # iterate all images
    for img_nr in range(len(filtered_masks)):
        # iterate all pixels on image
        for y in range(filtered_masks[img_nr].shape[0]):
            for x in range(filtered_masks[img_nr].shape[1]):
                # if value at pixel (mask) does not belong to an adherent mask,
delete the mask pixel (set value to 0)
                if filtered_masks[img_nr][y][x] not in
adherent_mask_numbers[img_nr]:
                    filtered_masks[img_nr][y][x] = 0

    return filtered_masks


def adherent_cells_over_phasecontrast(phc_img, masks, adherent_cells, colour):
    """
    Overlays outlines only of the adherent cells on one single image

    :param phc_img: ndarray
                Image on which the outlines of the adherent cells will be plotted
    :param masks: list of 2D arrays
                labelled image, where 0=no masks; 1,2,...=mask labels
    :param adherent_cells: list
                list of 'AdherentCell' objects
    :param colour: array
                Float array with values from 0.0 to 1.0 for the three RGB channels
    :return: adh_over_phc: list of RGB images
                RGB images with red outline where adherent cells are located
```

```
    """

    adherent_masks = filter_masks(masks, adherent_cells)
    imgs = list()
    for i in range(len(masks)):
        imgs.append(phc_img)
    adh_over_phc = overlay_outlines(imgs, adherent_masks)

    return adh_over_phc


def background_mask_over_img(imgs, background_masks):
    """
    Overlays outlines of the background mask over the images

    :param imgs: list
                list of 2D images
    :param background_masks: 2D array or list of 2d arrays
                labelled image, where 0=no masks; 1,2,...=mask labels
    :param colour: array
                Float array with values from 0.0 to 1.0 for the three RGB channels
    :return: background_over_img: list of RGB images
                RGB images with coloured outlines
    """
    masks = list()
    # if background mask is a list with more than one image
    if (isinstance(background_masks, list)) and (len(background_masks) > 1):
        masks = background_masks
    # if background mask is a list with just one image
    elif isinstance(background_masks, list):
        for i in range(len(imgs)):
            masks.append(background_masks[0])
    # if background mask is a single image
    else:
        for i in range(len(imgs)):
            masks.append(background_masks)

    background_over_img = overlay_outlines(imgs, masks)

    return background_over_img


def find_intensity_complete(img):
    """
    Determines the intensity of all pixel values of an given image

    :param img: ndarray
            image of which the intensity shall be determined
    :return: intensity: float
            intensity of the picture
    """
    pixels = 0  # total number of pixels
    intensity_counter = np.float64(0)   # total intensity of all pixels

    for y in range(img.shape[0]):   # iterate image
        for x in range(img.shape[1]):
            intensity_counter += img[y][x]  # raise value of the intensity by the
value of the pixel
            pixels += 1     # raise pixel counter

    intensity = round(intensity_counter / pixels, 2)   # calculate intensity,
normalized with the total number of pixels
    return intensity


def find_intensity_mask(img, background_mask):
    """
    Determines the intensities of those pixels on an image, that match with the
pixels of an background mask
```

```
    :param img: ndarray
            image of which the intensity shall be determined
    :param background_mask: 2D array
            labelled image, where 0=no masks; 1,2,...=mask labels
    :return: intensities: dictionary
            dictionary that contains the intensity (float) of all pixels matching a
mask, the intensity of all the other pixels
            and the confluence (percentage of the image surface covered by masks).
Key words: "mask", "rest",
            "confluence"
    """

    pixels_mask = 0     # variable to count the number of mask pixels
    pixels_rest = 0     # variable to count all other pixels
    intensity_mask_counter = np.float64(0)  # total intensity of mask pixels
    intensity_rest_counter = np.float64(0)  # total intensity of other pixels

    for y in range(img.shape[0]):   # iterate image
        for x in range(img.shape[1]):
            if background_mask[y][x] != 0:  # mask pixel, if value is not zero
                intensity_mask_counter += img[y][x]     # -> raise total mask
intensity
                pixels_mask += 1    # -> raise mask pixel counter
            else:   # else: no mask pixel
                intensity_rest_counter += img[y][x]     # -> raise rest mask
intensity
                pixels_rest += 1    # -> raise rest pixel counter

    # calculate intensity (normalized with the total number of pixels) of the mask
and rest pixels
    intensity_mask = round(intensity_mask_counter / pixels_mask, 2)
    intensity_rest = round(intensity_rest_counter / pixels_rest, 2)
    # calculate confluence of the background mask
    confluence = round((pixels_mask / (pixels_mask + pixels_rest)) * 100)

    # save values in a dictionary
    intensities = {"mask": intensity_mask, "rest": intensity_rest, "confluence":
confluence}

    return intensities


def find_intensity(imgs, background_mask=None):
    """
    Determines the intensities of one or more images. If an image with a background
mask is handed over, the intensities
    of those pixels on the images, that match with the pixels of the background
mask, are calculated separately.
    The function uses 'find_intensity_complete' and 'find_intensity_mask' functions
to do so.

    :param imgs: list or ndarray
            list containing 'ndarray' of each image ore one single ndarray
    :param background_mask: 2D array or list of 2d arrays
            labelled image, where 0=no masks; 1,2,...=mask labels
    :return: intensity: float or dictionary
            intensity value (for single image input) or list of intensity values
(for multiple image input)
            If a background mask is used, the intensity is a dictionary that
contains the intensity (float) of all
            pixels matching a mask, the intensity of all the other pixels and the
confluence (percentage of the image
            surface covered by masks). Key words: "mask", "rest", "confluence".
            Otherwise, the intensity is a single float value.
    """
    # version without background mask
    if background_mask is None:
        # multiple images
        if isinstance(imgs, list):
```

```
            intensities = list()    # list needed for multiple images
            for img_nr in range(len(imgs)):     # find intensity for every image
                intensities.append(find_intensity_complete(imgs[img_nr]))
            return intensities
        # single image
        else:
            intensity = find_intensity_complete(imgs)   # find intensity for single
image
            return intensity
    # version with background mask
    else:
        # multiple images
        if isinstance(imgs, list):
            intensities = list()    # list needed for multiple images
            for img_nr in range(len(imgs)):
                # if function gets a list of background_masks (one for every
image): use the specific background_mask[img_nr]
                if (isinstance(background_mask, list)) and (len(background_mask) >
1):
                    intensities.append(find_intensity_mask(imgs[img_nr],
background_mask[img_nr]))
                # otherwise use the same background mask for every image
                else:
                    intensities.append(find_intensity_mask(imgs[img_nr],
background_mask[0]))
            return intensities
        # single image
        else:
            intensity = find_intensity_mask(imgs, background_mask)
            return intensity


# --- End of imagefunctions.py ---

# --- Start of programrun_functions.py ---

import json

import imagefunctions as imf
from AdherentCell import AdherentCell
import skimage.io
import os.path
import csv
import config


def change_celldet_params():
    """ Changes the cell detection parameters in the config file"""

    # load the current configuration
    with open("config.json", "r") as jsonFile:
        config = json.load(jsonFile)

    while True:
        try:
            config["celldet"]["cellprob_threshold"] =
float(input("cellprob_threshold (between 0.0 and 1.0, higher: less masks will be
found): "))
            break
        except ValueError:
            print("cellprob_threshold not valid")
    while True:
        try:
            config["celldet"]["flow_threshold"] = float(input("flow_threshold
(between 0.0 and 1.0, lower: less masks will be found): "))
            break
        except ValueError:
            print("flow_threshold not valid")
```

```
    # write the new parameters to the config file
    with open("config.json", "w") as jsonFile:
        json.dump(config, jsonFile)
    jsonFile.close()


def change_adhcelldet_params():
    """ Changes the cell detection parameters in the config file"""

    # load the current configuration
    with open("config.json", "r") as jsonFile:
        config = json.load(jsonFile)

    while True:
        try:
            config["adhcelldet"]["time_for_adherent[s]"] = float(input("time [s] to
be detected as adherent: "))
            break
        except ValueError:
            print("time not valid")
    while True:
        try:
            config["adhcelldet"]["delay[s]"] = float(input("delay [s] between
images: "))
            break
        except ValueError:
            print("delay not valid")

    config["adhcelldet"]["images_threshold"] =
imf.time_to_nrimgs(config["adhcelldet"]["time_for_adherent[s]"],

config["adhcelldet"]["delay[s]"])
    while True:
        try:
            config["adhcelldet"]["tolerance"] = int(input("tolerance radius for
comparing cell positions: "))
            break
        except ValueError:
            print("tolerance radius not valid")

    # write the new parameters to the config file
    with open("config.json", "w") as jsonFile:
        json.dump(config, jsonFile)
    jsonFile.close()


"""def get_celldet_params():
    # get parameters for cell detection from user
    while True:
        try:
            cellprob_threshold = float(input("cellprob_threshold (between 0.0 and
1.0, higher: less masks will be found): "))
            break
        except ValueError:
            print("cellprob_threshold not valid")
    while True:
        try:
            flow_threshold = float(input("flow_threshold (between 0.0 and 1.0,
lower: less masks will be found): "))
            break
        except ValueError:
            print("flow_threshold not valid")
    return cellprob_threshold, flow_threshold"""


"""def get_adhcelldet_params(diams):
    # get parameters for adherent-cell detection from user
    while True:
        try:
```

```
            time_for_adherent = float(input("time [s] to be detected as adherent:
"))
            break
        except ValueError:
            print("time not valid")
    while True:
        try:
            delay = float(input("delay [s] between images: "))
            break
        except ValueError:
            print("delay not valid")
    images_threshold = imf.time_to_nrimgs(time_for_adherent, delay)
    while True:
        try:
            """"""compare_threshold = int(input(
                "tolerance radius for comparing cell positions: ".format(
                    min(diams) / 2)))""""""
            compare_threshold = int(input("tolerance radius for comparing cell
positions: "))
            break
        except ValueError:
            print("tolerance radius not valid")

    return time_for_adherent, delay, images_threshold, compare_threshold"""


"""def save_params_in_txtfile(txtfile, masks_name, diams_name, time_for_adherent,
delay, images_threshold,
                              compare_threshold):
    # save the used masks, diams and parameters in the text file
    txtfile.write("masks={0}, diams={1}, time_for_adherent[s]={2}, delay[s]={3},
images_threshold={4}, \
    tolerance={5}\n".format(masks_name, diams_name, time_for_adherent, delay,
images_threshold, compare_threshold))"""


def save_config_in_txtfile(txtfile, masks_name, diams_name, config):
    # save the used masks, diams and parameters in the text file
    txtfile.write("masks={0}, diams={1}\n".format(masks_name, diams_name))
    txtfile.write("Cell detection parameters:")
    txtfile.write(str(config["celldet"]))
    txtfile.write("\nAdherent Cell detection parameters:")
    txtfile.write(str(config["adhcelldet"]))

txtfile.write("\n_____________________________________________________________________
_____________________\n\n")


def save_adh_in_txtfile(txtfile, number_adherent_cells, number_cells_total,
adherent_cells, cells,
                        nr_adherent_cells_on_img):
    # save the information found about the adherent cells in the text file
    # number adherent cells
    print("Number adherent cells: ", number_adherent_cells)
    txtfile.write("Number adherent cells: {0}\n".format(number_adherent_cells))

    # number cells total
    print("Number cells total: ", number_cells_total)
    txtfile.write("Number cells total: {0}\n".format(number_cells_total))

    # number generated Cell objects
    cellcounter = 0
    for img_nr in range(len(cells)):
        for cell_nr in range(len(cells[img_nr])):
            cellcounter += 1
    print("Number generated Cell objects: {0}".format(cellcounter))
    txtfile.write("Number generated Cell objects: {0}\n\n".format(cellcounter))

    # number cells on first image
```

```
    print("\nNumber cells on first image: {0}".format(len(cells[0])))
    txtfile.write("\n\nNumber cells on first image: {0}".format(len(cells[0])))

    # number adherent cells on each image
    print("\nNumber adherent cells on each image: \n")
    txtfile.write("\n\nNumber adherent cells on each image: \n")
    for i in range(len(nr_adherent_cells_on_img)):
        print("    Image {0}:  {1}".format(i, nr_adherent_cells_on_img[i]))
        txtfile.write("\n    Image {0}:  {1} ".format(i,
nr_adherent_cells_on_img[i]))

    # adherent cells
    print("\n\nAdherent cells: \n")
    txtfile.write("\n\nAdherent cells: \n\n")
    for i in range(len(adherent_cells)):
        print("    {0}".format(adherent_cells[i]))
        txtfile.write("    {0}".format(adherent_cells[i].__str__()))
        txtfile.write("\n")

    # number generated AdherentCell objects
    print("\nCreated AdherentCell-objects: ",
AdherentCell.get_adherent_cellcounter())
    txtfile.write("\n\nCreated AdherentCell-objects:
{0}\n".format(AdherentCell.get_adherent_cellcounter()))


print("\n_____________________________________________________________________________
_________________\n\n")

txtfile.write("\n\n_____________________________________________________________________
_____________________________\n\n")


def save_confluence_in_txtfile(txtfile, mask_name, confluence):
    print("Confluence: {0}% \n\n".format(confluence))
    txtfile.write("\n\n\nConfluence (Used background mask: {0}): {1}%
\n\n\n".format(mask_name, confluence))


def show_and_save_result_imgs(imgs, path, name):
    # show images and save them in the directory under a given name
    if isinstance(imgs, list):
        for i in range(len(imgs)):
            skimage.io.imshow(imgs[i])
            skimage.io.show()
            filename = name + str(i) + ".jpg"
            skimage.io.imsave(os.path.join(path, filename),
skimage.util.img_as_ubyte(imgs[i]))
    else:
        skimage.io.imshow(imgs)
        skimage.io.show()
        filename = name + ".jpg"
        skimage.io.imsave(os.path.join(path, filename),
skimage.util.img_as_ubyte(imgs))


def number_adh_on_image_to_csv(nr_adherent_cells_on_img, path):
    # saves the nr_adherent_cells_on_img ('int'-list) in csv file
    with open(path, 'w', newline='') as csv_1:
        csv_out = csv.writer(csv_1)
        csv_out.writerows([nr_adherent_cells_on_img[index]] for index in range(0,
len(nr_adherent_cells_on_img)))


def celladhesion_to_csv(confluence, nr_adherent_cells, nr_on_first,
nr_adherent_cells_filtered, nr_on_first_filtered,
                        path):
    with open(path, 'w') as csv_1:
        csv_out = csv.writer(csv_1)
```

```
        csv_out.writerow(['Confl', 'adhC', 'Cfirst', 'adhC/Cfirst', 'adhC_filter',
'Cfirst_filter',
                          'adhC/Cfirst_filter'])
        csv_out.writerow([str(confluence).replace('.', ','),
str(nr_adherent_cells), str(nr_on_first),
                          str(round(nr_adherent_cells / nr_on_first,
2)).replace('.', ','),
                          str(nr_adherent_cells_filtered),
str(nr_on_first_filtered),
                          str(round(nr_adherent_cells_filtered /
nr_on_first_filtered, 2)).replace('.', ',')])
    csv_1.close()


def intensities_to_csv(intensity, path):

    with open(path, 'w') as csv_1:
        csv_out = csv.writer(csv_1)
        # single image, no background mask
        if isinstance(intensity, float):
            csv_out.writerow(['Intensity'])
            csv_out.writerow([str(intensity).replace('.', ',')])
        # single image, background mask
        elif isinstance(intensity, dict):
            csv_out.writerow(['Confluence', 'Intensity Mask', 'Intensity Rest',
'Diff.', 'Diff. Norm.'])
            csv_out.writerow([str(intensity["confluence"]).replace('.', ','),
                              str(intensity["mask"]).replace('.', ','),
                              str(intensity["rest"]).replace('.', ','),
                              str(intensity["mask"] -
intensity["rest"]).replace('.', ','),
                              str((intensity["mask"] - intensity["rest"]) /
(intensity["mask"] + intensity["rest"])).replace('.', ',')])
        # multiple images
        else:
            # no background mask
            if isinstance(intensity[0], float):
                csv_out.writerow(['Image Nr.', 'Intensity'])
                for i in range(len(intensity)):
                    csv_out.writerow([i, intensity[i]])
                csv_out.writerow([''])
                csv_out.writerow(['Images', 'Intensity Diff.'])
                for i in range(len(intensity) - 1):
                    csv_out.writerow([str(i + 1) + ' - ' + str(i),
                                      intensity[i + 1] - intensity[i]])
            # background mask
            else:
                # create lists for the results (simplify writing to the csv file)
                confluence = list()
                mask = list()
                rest = list()
                diff = list()
                diff_norm = list()

                csv_out.writerow(['Image Nr.', 'Confluence', 'Intensity Mask',
'Intensity Rest', 'Diff.', 'Diff. Norm.'])
                for i in range(len(intensity)):
                    # add results to the lists
                    confluence.append(intensity[i]["confluence"])
                    mask.append(intensity[i]["mask"])
                    rest.append(intensity[i]["rest"])
                    diff.append(mask[i] - rest[i])
                    diff_norm.append((mask[i] - rest[i]) / (mask[i] + rest[i]))
                    csv_out.writerow([i,
                                      str(confluence[i]).replace('.', ','),
                                      str(mask[i]).replace('.', ','),
                                      str(rest[i]).replace('.', ','),
                                      str(diff[i]).replace('.', ','),
                                      str(diff_norm[i]).replace('.', ',')])
```

```
                csv_out.writerow([''])
                csv_out.writerow(['Images', 'Intensity Diff.', 'Intensity Diff.
Norm.'])
                for i in range(len(intensity) - 1):
                    csv_out.writerow([str(i + 1) + ' - ' + str(i),
                                      str(diff[i + 1] - diff[i]).replace('.', ','),
                                      str(diff_norm[i + 1] -
diff_norm[i]).replace('.', ',')])

    csv_1.close()

# --- End of programrun_functions.py ---
```

A5 Script used in Macromolecule Diffusion through the Endothelial Layer

Available on Github: https://github.com/manuelsirch/dissertation/blob/main/macromolecule_diffusion

```
from PIL import Image
import numpy as np
from tkinter import Tk
from tkinter.filedialog import askdirectory
import os
import matplotlib.pyplot as plt
import csv
import time
import pandas as pd
import re

timestr = time.strftime("%Y-%m-%d-%H-%M-%S")

rootdir = askdirectory(title='Select Folder')
print(rootdir)

for dirs in os.listdir(rootdir):
    if os.path.isdir(os.path.join(rootdir, dirs)):

        foldername = os.path.basename(os.path.normpath(dirs))

        df=pd.DataFrame()

        dfname = './' + foldername + '_' + timestr + '.csv'

        length = np.arange(0, 634.88, 0.62)

        df['Abstand'] = length


        for files in os.listdir(os.path.join(rootdir, dirs)):

            filename = os.path.join(dirs, files)
            print(filename)

            if files.endswith(".jpg"):
                img = Image.open(filename).convert('L')
                filename = os.path.basename(filename)
                number = re.findall(r'\d+', filename)
                time = (int(number[0]) * 15) - 15
                new_filename = str(time).zfill(3) + ' s'
                WIDTH, HEIGHT = img.size
                pix = img.load()
                data = np.asarray(img.getdata())
                data = data.reshape((HEIGHT,WIDTH))
                reduced_data = data.mean(axis=1)
                maximum = max(reduced_data)
                reduced_data[:] = [x / maximum for x in reduced_data]
                reduced_data = reduced_data[::-1]
                #filename = os.path.basename(filename)
                df[new_filename] = reduced_data.flatten()
                #df = df.join(pd.DataFrame(reduced_data, columns = [filename]))
                #if not os.path.exists(dfname):
                    #with open(csvname, 'w', neewline='') as file:
                        #spamwriter = csv.writer(file, delimiter = ',')

        df = df.sort_index(axis = 1)
        first_column = df.pop('Abstand')
        df.insert(0, 'Abstand', first_column)
        df.to_csv (dfname, index = False, header = True)
```

LIST OF PUBLICATIONS

P1. Manuel M. Sirch, Andrej Kamenac, Simon V. Neidinger, Achim Wixforth, and Christoph Westerhausen, Phase-state-dependent silica nanoparticle uptake of giant unilamellar vesicles, The Journal of Physical Chemistry B, Volume 128, Issue 29, July 12, 2024, 7172–7179, https://doi.org/10.1021/acs.jpcb.4c02383.

P2. Manuel M. Sirch, David Wörle, Marina G. Huber, and Christoph Westerhausen, Enhanced Adhesion of positively charged Vesicles to Endothelial Cells with shed Glycocalyx, accepted. ACS Omega, https://doi.org/10.1021/acsomega.4c10054.

P3. Manuel M. Sirch, Marina G. Huber, Serap Demir, Dominik Richter, David Wörle, Torsten Gloe, and Christoph Westerhausen, Glycocalyx Formation and Degradation strongly regulate the Uptake of Nanoparticles and Molecules in Endothelial Cells, under review.

SUPERVISED BACHELOR'S AND MASTER'S THESES

- David Wörle, Adhäsion von Lipidmembranen an Zellen unter Fluss, Bachelorarbeit, 2022
- Lara Clemen, Die Rolle des Scherflusses bei der Aufnahme von Nanopartikeln, Masterarbeit, 2023
- Serap Demir, Nanopartikelaufnahme in Endothelzellen, Bachelorarbeit, 2023
- Yannic Schmidt, Optimierung von Hydrogelen für die Zellkultur unter Fluss, Bachelorarbeit, eingereicht 2023.
- Niklas Kugelmann, Untersuchung des Phasenzustandes von unter Fluss kultivierten Endothelzellen, Bachelorarbeit, 2023
- Marina Gabriela Huber, Analyse der Glykokalyx und Morphologie von Endothelzellen in vitro unter verschiedenen Flussbedingungen durch Fluoreszenzmikroskopie, Masterarbeit, 2024

ACKNOWLEDGMENTS

First and foremost, I would like to express my deepest gratitude to Prof. Dr. Christoph Westerhausen for his exceptional supervision of my doctoral research. Your trust in my abilities and the freedom you granted me to independently shape my research have been invaluable. This opportunity allowed me to grow not only as a scientist but also as an individual.

To all my colleagues and students, thank you for your unwavering support and camaraderie. You have transformed the everyday life in the lab and office into more than just work—it has been a genuine community of friends, filled with laughter, collaboration, and encouragement.

I am also sincerely grateful to Prof. Dr. Janina Bahnemann, whose advice and collaboration I deeply value. I eagerly look forward to the exciting projects and fruitful cooperation that lie ahead.

Lastly, I extend my heartfelt thanks to my parents, Heike and Arnold Sirch, for their unwavering support and for always standing by my side. Your encouragement and the stability you provided have been the foundation upon which this journey was built.